# Analysis of slope and surface displacements on Mars using high-resolution satellite imagery

**Master Thesis**

**Author(s):**
Bickel, Valentin (iD)

**Publication date:**
2017

**Permanent link:**
https://doi.org/10.3929/ethz-b-000461971

**Rights / license:**
In Copyright - Non-Commercial Use Permitted

**ETH**zürich

**D**ERDW
EARTH SCIENCES

MSc Thesis

# Analysis of slope and surface displacements on Mars using high-resolution satellite imagery

Valentin Tertius Bickel

**Supervisors:**

Dr. Andrea Manconi

Dr. Andrea Wolter

Zurich, September 14, 2017

# SUMMARY

The acquisition of high-resolution imagery by orbiting satellites has revealed active surface processes such as migrating dunes and frost avalanches on planet Mars. Digital Image Correlation techniques (DIC) are able to exploit multitemporal image stacks while tracking and quantifying ongoing displacements, potentially revealing yet unknown surface and slope deformation mechanisms on Mars. The first part of this thesis assessed and validated the qualitative and quantitative performance of three different DIC algorithms with GNSS measurements of an active landslide in Cuolm da Vi (CdV), Swiss Alps. Further, customized improvements were implemented into the algorithms and an optimized processing pipeline was established. The second part of this work applied the validated DIC codes in selected Areas of Interest on Mars, such as dunes, slopes, and volcanoes to answer the two predominant scientific questions of this thesis, whether there is any evidence for recent slope or surface deformation on Mars and whether it can be detected and measured with DIC and available high-resolution imagery.

Best validation results in CdV compared to the GNSS data were achieved with a frequency-based DIC algorithm (FFT) and an overall RMSE of 1 m and a StD of 0.85 m (0.54 resp. 0.38 m after outlier removal), while larger search window sizes and appropriate pre- and post-processing enhanced the quality of the DIC results. Results of previous studies on Martian dune field migration rates of ~ 1 m/a with DIC were reproduced in the range of ~ 0.8 to 1.4 m/a using all three validated codes. Global application of DIC on Mars revealed that occurring deformations are either below the minimum sensitivity of ~ 0.6 m/a or non-existent resp. inactive. Using complementary change detection methods, avalanche activity close to the North pole was monitored and measured over 8 years, resulting in a detailed conceptual kinematic model, proposing several parallels to glacial processes on Earth. Contributions of this work could be used to improve current and future data acquisition strategies to optimize data usability for change detection purposes within the frame of planetary surface exploration missions.

---

# ACKNOWLEDGEMENTS

Finally, I would like to thank my colleagues and friends at ETHZ, who accompanied me during the last two adventurous years. There were many particularly tough moments and I am very happy and proud that we mastered all of them together. Let's see what comes next!

In the end, my gratitude belongs to my family and to Meli, whose unlimited and unconditional support encouragement and patience from the very beginning enabled me to get to the point, where I am right now. Vielen Dank!

Für Max Pilot.

# TABLE OF CONTENTS

# LIST OF FIGURES

# LIST OF TABLES

# TABLE OF ABBREVIATIONS

| CODE | MEANING |
| --- | --- |
| AoI | Area of interest |
| ASP | Ames Stereo Pipeline |
| CCD | Charged Coupled Device |
| CdV | Cuolm da Vi |
| COSI Corr | Co-Registration of Optically Sensed Images and Correlation |
| CRISM | Compact Reconnaissance Imaging Spectrometer for Mars |
| CTX | Context Camera |
| CVP | Camera View Plane |
| DEM | Digital Elevation Model |
| DIC | Digital Image Correlation |
| DSGSD | Deep Seated Gravitational Slope Deformation |
| EDR | Experimental Data Record |
| FFT | Fast Fourier Transform |
| FOV | Field Of View |
| GLF | Glacier Like Feature |
| GNSS | Global Navigation Satellite System |
| GSD | Ground Sampling Distance |
| HiRISE | High Resolution Imaging Science Experiment |
| HRSC | High Resolution Stereo Camera |
| IR | Infrared |
| IRB | Infrared Blue |
| ISIS3 | Integrd. Software for Imagers and Spectrometers |
| LOS | Line Of Sight |
| MEX | Mars Express |
| MOLA | Mars Orbiter Laser Altimeter |
| MRO | Mars Reconnaissance Orbiter |
| NCC | Normalized Cross-Correlation |
| RGB | Red Green Blue |
| RMSE | Root Mean Square Error |
| SHARAD | Shallow Subsurface Radar |
| SNR | Signal to Noise Ratio |
| StD | Standard Deviation |
| VNIR | Visible Near Infrared |

# APPLIED SOFTWARE

| SOFTWARE | MEANING | DEVELOPER |
|---|---|---|
| **ArcGIS 10.4.1** | Arc Geographic Information System | ESRI |
| **ASP 2.5.2** | Ames Stereo Pipeline | NASA Intelligent Systems Division |
| **COSI-Corr release 10-23-14** | Co-Registration of Optically Sensed Images and Correlation | Caltech Tectonics Observatory |
| **ENVI 5 Classic** | Environment for Visualizing Images | ITT Exelis |
| **HiView 1.5.0-zeta** | HiRISE View | University of Arizona |
| **ISIS3 3.5.0.7383** | Integrated Software for Imagers and Spectrometers | United States Geological Survey |
| **JMars 3.7.4** | Java Mission-planning and Analysis for Remote Sensing | Arizona State University Mars Space Flight Facility |
| **Matlab R2016a** | Math Laboratory | MathWorks |

# 1. INTRODUCTION & SCIENTIFIC QUESTIONS

Remote Sensing is a category of technologies and techniques which gathers and obtains information about distant objects using reflected or emitted electromagnetic radiation, acoustic energy, potential fields or geochemical measurements (Prost, 2013). Since the invention of the eyeglass by Roger Bacon in the 13th century remote sensing techniques have become increasingly important in Earth observation and for the solution of Earth Science problems. Its applications include topographic mapping of the Earth's surface using photogrammetry, environmental monitoring, natural hazard recognition and many more (Prost, 2013). In addition, remote sensing has always been a key element in extraterrestrial exploration: optical photographs helped to understand that craters on the Moon are caused by impacts and not by Lunar volcanism, radar technology enabled us to see through Venus's dense atmosphere while mapping the underlying surface, and imaging spectrometers allowed us to draw geological interpretations of planetary bodies in our solar system without touching or sampling them (Prost, 2013).

A part of remote sensing is focused on the identification of time-dependent deformations. One of the available techniques for this purpose is called Differential Synthetic Aperture Radar Interferometry (DInSAR), which uses the phase change of a reflected electromagnetic microwave to determine changes in the distance between the radar antenna and the reflector, normally a topographic surface, at two or more different points in time (Moreira et al., 2013). These phase changes can be transferred to line-of-sight (LOS) surface displacements, as it has been done e.g. for subsidence monitoring in Mexico City or monitoring of volcanic activity of the Sierra Negra Caldera on the Galápagos Islands (Moreira et al., 2013) (Casu et al., 2011).

Another technique for remote change detection is called Digital Image Correlation (DIC, also known as feature-tracking or sub-pixel offset), and is a technique to identify and quantify deformations orthogonal to the LOS of the camera using multitemporal digital imagery. This is a versatile technique which has not only been applied for geological mapping, but in numerous other fields such as industrial process control or biological growth monitoring (Michael et al., 2009). As DIC algorithms can be used on amplitude data of all kinds, possible source data includes for example ground-, air- or space borne optical imagery (Scambos et al., 1992), ground-, air- or space borne radar images (Casu et al., 2011) or thermal images (Walter et al., 2013). There are numerous different algorithms which utilize the DIC principle, normally tailor-made for a certain field of application (Michael et al., 2009). In particular, the most popular algorithms are the so called Normalized Cross Correlation (NCC) code, a Fast Fourier Transformation (FFT) implementation and an approach combining NCC and FFT called COSI-Corr (Leprince et al., 2007). Per Heid & Kääb (2012) a NCC algorithm operates in the spatial domain, while a FFT algorithm works in the frequency domain; COSI-Corr uses both domains for different calculation steps. Similar codes have been applied before in various locations on Earth, but also on Mars, where the time-dependent movement of dunes was investigated by Bridges et al. (2012) using COSI-Corr. Generally, the application of DIC codes is convenient, as they can be used on a great variety of data and as their theoretical registration accuracy can range down to one-hundredth of the pixel size (Guizar-Sicairos et al., 2008), which may detect 2D surface displacements with a sub-centimeter accuracy,

depending on the spatial resolution of the used input acquisitions. Their potential can be further enhanced if the quality of the underlying acquisitions is improved by applying certain pre- and post-processing steps, such as e.g. a radiometric correction with a dynamic contrast enhancement or appropriate result de-noising with specific filters. The potential of this technique is remarkable and enables surface change detection not only in accessible areas on Earth, but also in inaccessible terrestrial or even in extraterrestrial areas. As ground truthing and validation of the results derived with DIC, is not yet possible on other planets, a detailed analysis and assessment of the selected algorithms has to be performed within the frame of a controlled case study in an accessible area. Besides the comparison of the qualitative and quantitative accuracy of the codes to the true deformation, measured with another technique, this assessment is also expected to reveal the optimal setup of the DIC input parameters. With the optimal code setup as well as the quantitative accuracy known, the respective algorithms can then be applied in a place other than Earth.

The latest exploration missions by the National Aeronautics and Space Administration (NASA) and the European Space Agency (ESA) on planet Mars keep returning large quantities of optical, radar and multispectral imagery with spatial resolutions up to 30 cm per pixel or even less (cf. HiRISE, n.d.). Enhanced by recent findings which describe Mars as a dynamic planet with avalanches (NASA, 2015), potentially moving Glacier-Like-Features (GLFs) (Hubbard et al., 2014) or potential subsurface volcanic activity (Mitchell & Wilson, 2003) (Dohm et al., 2008) a systematic investigation of recent Martian surface deformations using DIC appears particularly interesting and promising, in order to support or withdraw the state-of-the-art assumptions. The application of DIC algorithms for selected Areas of Interest (AoIs) on Mars is therefore the main intention of this thesis research, in order to answer the predominant scientific questions of this work:

- Is there any evidence for recent and ongoing slope or surface deformations on Mars?

- Can these recent deformations on Mars be detected and measured by exploiting DIC algorithms on availably satellite imagery?

- Are the predisposing and driving factors of slope or surface deformations on Mars similar to the ones which can be observed on Earth?

Proper and expressive results of a DIC application and the identification of recent surface deformations on Mars could have significant influence on the interpretation of the past and recent geological Martian history. In addition, the same technique could be used to search for and to quantify recent surface deformations on other planets, moons or even comets.

# 2. METHODS

## 2.1 Digital Image Correlation

Digital Image Correlation (DIC), also known as feature tracking or sub-pixel offset, is a technique to identify and quantify deformations using multitemporal digital imagery. Thus, DIC applies algorithms that first geometrically align two or more images of the same area, acquired at different times, by relying on control points (Wang et al., 2015). Subsequently, DIC evaluates internal misalignment of sub-portions of the analyzed images as a potential deformation of the investigated area along the two directions orthogonal to the camera sight (i.e. the camera view plane, CVP). Out-of-CVP deformation cannot be measured with DIC.

More specifically, DIC algorithms consider search windows of a specific size, which run over both images synchronously while measuring the degree of radiometric correlation of the in-window pixel values between both search windows. In theory, the biggest possible search window would be equal to the dimensions of the used input images, while the smallest possible size would be a square of two by two pixels. Delacourt et al. (2007) and Travelletti et al. (2012) state that the dimensions of the window are a compromise between the desired accuracy of the displacement measurement and the spatial resolution of the displacement field. A larger search window will facilitate the identification of matches while assuring a good signal-to-noise ratio (SNR), but the accuracy on the displacement estimates decreases because they are averaged over a larger correlation window.

There are various algorithms that apply these methods. Example of applications to monitor surface displacements include Travelletti et al. (2012), who used DIC for the ground-based monitoring of continuously active landslides and Heid and Kääb (2012), who measured glacier surface velocities. In this work, three implementations of different algorithms were selected. In the following, the main characteristics of these algorithms will be outlined.

### 2.1.1 Normalized Cross Correlation (NCC)

The Normalized Cross-Correlation algorithm operates in the spatial domain of the input images. Its application is versatile and widespread due to the simplicity of the code itself (Heid & Kääb, 2012). In this study, the Matlab R2016a built-in normxcorr2 code from the Image Processing Toolbox was utilized, which is implemented using a formula from Lewis (1995) with the correlation factor γ as:

$$\gamma(u,v) = \frac{\sum_{x,y}[f(x,y) - \bar{f}_{u,v}]\,[t(x-u,y-v) - \bar{t}]}{\left\{\sum_{x,y}[f(x,y) - \bar{f}_{u,v}]^2 \sum_{x,y}[t(x-u,y-v) - \bar{t}]^2\right\}^{0.5}} \qquad (2.1.1-1)$$

with $f$ as the image, $\bar{t}$ as the mean of the template and $\bar{f}_{u,v}$ as the mean of $f(x,y)$ in the region under the template.

The algorithm computes the normalized cross correlation of a square template window from the older or master image and a square search window from the newer or slave image, with γ ranging from -1 (anti-correlation) to 1 (perfect match). The search window has to be larger than the template for the correlation to be meaningful, as the code is searching for the maximum or peak correlation between the template and a tile with equal dimensions, moving within the search window. If the position of the template and the identified best-fit tile is the same in the master and the slave image, no shift and therefore no deformation occurred. If deformation took place, its change in the image will be expressed by a x and a y component. During the processing, the template and the search window are simultaneously moved over the master and the slave (Lewis, 1995); their shift is performed line-wise (horizontally) and follows the Nyquist-Shannon sampling theorem to capture all information from a continuous-time signal of finite bandwidth (Olshausen, 2000) with steps of

$$sampling \; shift \; (x,y) = \frac{window \; size}{2} \qquad (2.1.1 - 2)$$

in x and y direction (as indicated by figure 1).
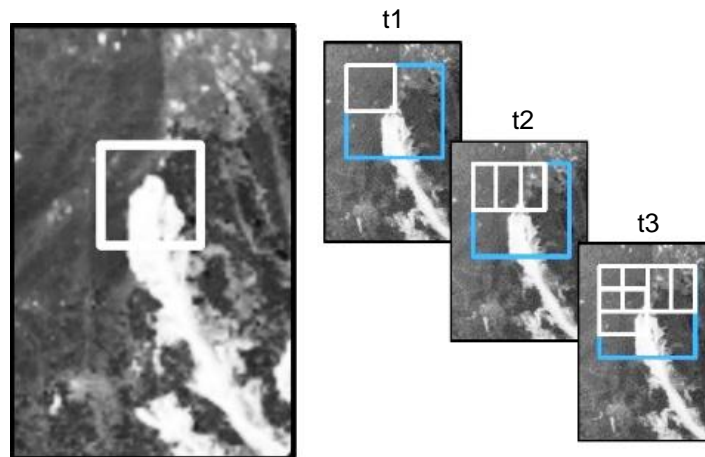


Figure 1: Master image on the left (large), slave image on the right (small); sketch illustrates the template window (white) shifting scheme inside the larger search window (blue) on the slave at three different points in time (t1, t2, t3).

As the cross-correlation is normalized, the comparison between images with different illumination angles is facilitated and the correlation coefficients from different correlation attempts can be compared. Further the application of NCC is generally time intensive, as the code applies a spatial-domain convolution operation – a frequency domain based code will outperform NCC (Heid & Kääb, 2012).

Another potential disadvantage of NCC is mentioned by Heid & Kääb (2012) as the inequality of occurring contrasts in the master and the slave. This means that the code could create erroneous matches if features in the image are changing non-systematically (e.g. irregular moving snow patches or rolling rocks on a systematically moving glacier), as the code is looking for contrasts to perform the matching. High contrasts enhance image correlation, but high non-systematic intensity changes will

confuse a NCC code. Travelletti et al. (2012) also name rotation of features in the time between two acquisitions as possible reason for matching failure, as NCC struggles to recognize rotation.

## 2.1.2 Fast Fourier Transform (FFT)

The selected algorithm by Guizar-Sicairos, Thurman & Fienup (2008) operates in the frequency domain and obtains an initial estimate of the cross-correlation peak between master and slave within square search windows using a Fast Fourier Transform, while also following the Nyquist-Shannon sampling theorem (Olshausen, 2000) for the search window movement pattern. Subsequently, the shift estimation is refined by an up-sampling of the Discrete Fourier Transform in a small neighborhood of that estimate by means of a matrix multiplication. By using this approach, all image points are used to calculate the up-sampled cross correlation. The output contains the x and y component of the measured shifts.

According to Heid & Kääb (2012), FFT performs faster than NCC, but does not transform a normalization to the frequency domain easily – this could cause mismatches if illumination conditions change during the acquisitions. A way to approximate normalization with FFT is to consider only the phase information of an image; this ignores the differences in the intensity of the images. The cross-correlation *CC* is then expressed as:

$$CC(i,j) = IFFT\left(\frac{F_0(u,v)G_0^*(u,v)}{|F_0(u,v)G_0^*(u,v)|}\right) \qquad (2.1.2-1)$$

with $IFFT$ being the inverse of the Discrete Fourier Transform, $F(u,v)$ the FFT of the matching window from the image at time = 1 and $G(u.v)$ the FFT of the matching window from the image at time = 2; * denotes a complex conjugate.

Heid and Kääb (2012) hypothesize that DIC codes operating in the frequency domain, such as the FFT and COSI Corr, achieve worse matching quality on small window sizes compared to spatial domain methods such as the NCC, due to the Heisenberg's uncertainty principle. The current study enables a superficial investigation of this hypothesis.

The FFT code that has been used for this thesis was implemented for Matlab R2016a by Dr. Andrea Manconi based on Guizar-Sicairos, Thurman, & Fienup (2008).

## 2.1.3 Co-Registration of Optically Sensed Images and Correlation (COSI Corr)

The third image matching code operates in both, the spatial and in the frequency domain, and is called Co-Registration of Optically Sensed Images and Correlation (COSI-Corr). This collection of algorithms and image processing codes is based on work by Leprince et al. (2007) and is distributed for free (for research) by the Caltech Tectonics Observatory on its webpage. It was implemented in ENVI 5 Classic

as the release version from October 23$^{rd}$ 2014 and its output was transferred to Matlab R2016a to assure the direct comparability of the results of the three applied codes.

With COSI Corr, the image registration and correlation is achieved with an iterative unbiased processor, which estimates the phase plane in the Fourier domain to detect sub-pixel shifts (Leprince et al., 2007). However, the estimated phase difference between master and slave is not transformed back to the spatial domain to find the maximum *CC*. By using a robust and iterative function for its measurements, COSI Corr is less sensitive to radiometric outliers (Heid & Kääb, 2012). COSI Corr uses a bell-shaped search window, which gives more weight to the inner part of the window than to the outer part, thus avoiding edge effects. By doing so, the misinterpretation of outliers within the search window – which could lead to erroneous results – is less probable. At the same time, pixels in the search window have to move very coherently for COSI-Corr to retrieve a correct match – this could lead to problems in areas with many (different) deformations (Heid & Kääb, 2012). COSI Corr has already been applied for Martian dune migration detection and quantification (cf. Bridges et al. (2012) and Ayoub et al. (2014)).

## 2.1.4 DIC input parameters

All three DIC codes require two input parameters that directly control the processing and the results: the search window size and the oversampling factor.

The search window (*wi*) has an *m* by *m* shape and is measured in pixels. Common sizes are e.g. 32 by 32 pixels or 128 by 128 pixels. The square length is always increased or decreased in steps of a power of two to meet the requirements by the Nyquist-Shannon sampling theorem and the movement pattern of the template. As described before, the dimensions of the window are a compromise between the desired accuracy of the displacement measurement and the spatial resolution of the displacement field. If the search window is larger (e.g. 128 by 128 pixels) the matching will be easier and the SNR will be enhanced, but the theoretical accuracy of the measurement is lower as it is averaged over a larger area (Delacourt et al.,2007) (Travelletti et al., 2012).

The oversampling factor (*os*) determines whether there is an oversampling during the pixel offset analysis and how large the oversampling is. In general, oversampling is the process of sampling a signal with a sampling distance smaller than the critical Nyquist distance or rate. This procedure does not reveal more information about the sampled signal, but improves the SNR (SVI, n.d.). In the simplest case, oversampling additionally increases the spatial (pixel) resolution of an image by a previously chosen interpolation type between the already existing pixels. Here, an oversampling factor of 1 indicates no oversampling, an *os* of 2 indicates an increase of pixels by a factor of 4 (from 4 to 16 pixels), and so on (cf. figure 2). For example, Heid and Kääb (2012) recommend the application of an oversampling factor of 2 for codes operating in the spatial domain and no oversampling for frequency domain-based algorithms.
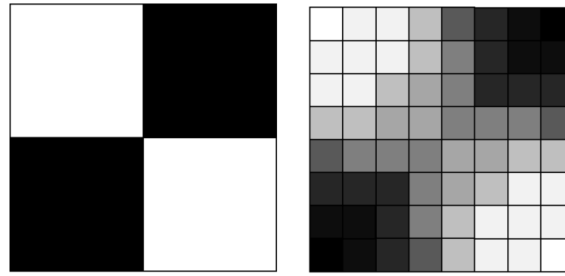
*Figure 2: Principle of linear oversampling in 2D from 4 to 64 pixels, oversampling factor is 4, newly generated matrix has the same dimensions as the original matrix, while the spatial resolution is virtually improved.*

The idea of oversampling is to increase the accuracy of the DIC to a sub-pixel scale, as done by Leprince et al. (2007) with COSI Corr down to 1/20 of the initial pixel size. Theoretically, in an image with a spatial resolution of 25 cm per pixel, deformations of down to 1.25 cm could be recognized. A disadvantage of oversampling is the significantly increased processing time, as the number of pixels is much larger, depending on the *os* factor.

COSI Corr does not offer an opportunity to manually set the oversampling factor, as this is performed by default. Additionally, a robustness iteration (*ri*) with values from 1 to 5 can be applied for the matching, which determines how many times a frequency mask is adaptively re-computed, increasing the overall SNR with the cost of a longer computation time (Ayoub et al., 2015).

## 2.1.5 DIC output

After the correlation process, DIC algorithms provide two deformation matrices with positive and negative numbers, i.e. the mean of the measured deformation in x and in y direction in (sub)pixels for each search window (cf. to figure 3). In this study, the x component is always the horizontal or East-West component (EW), while the y component is always the vertical or North-South component (NS). By dividing those matrices by the spatial resolution of the input images, one can obtain the deformation components in meters or centimeters. The FFT code additionally provides an internal measure for the quality of the correlation in the form of an additional matrix, which can be visualized as well (cf. to figure 3). The quality is expressed as a Root Mean Square Error (RMSE) of the correlation. A collection and visualization of COSI Corr's log-cross spectrum threshold filter has not been written and implemented for this study, but is generally possible. As not all codes have an identical internal measure to compare the matching quality, an external source needs to be exploited for validation, such as e.g. GNSS data.

The measurement of deformation with DIC is only possible in the camera viewing plane, which is the plane orthogonal to the sensor's line of sight (LOS). Consequently, when utilizing orthorectified air- or space borne imagery, the detection of elevation changes is not possible.
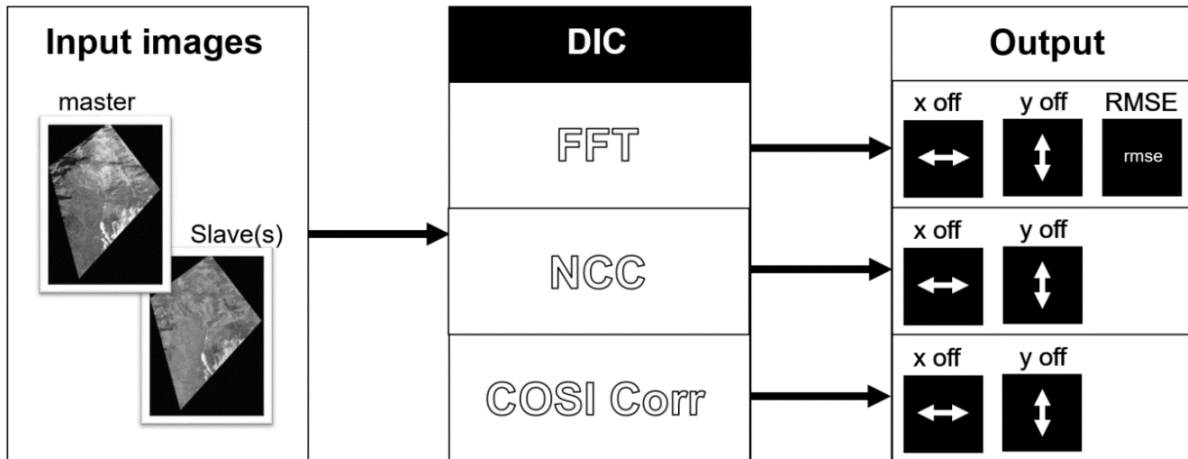
*Figure 3: Visualization from input images over DIC to the output matrices. As only FFT provides an internal measure for the matching quality (RMSE), an external evaluation tool needs to be used to compare all three codes.*

## 2.2 DIC input, Pre- & Post-processing

The primary inputs are the master and the slave images from the area of interest (AoI). As DIC algorithms are highly sensitive to the movement of pixels within the input images, all used acquisitions must be acquired from the exact same position in space to retrieve unbiased results, e.g. using a fixed camera. If this is not possible, as for example for air- or space borne imaging systems, the images need to be orthorectified to remove the influence of the surface topography, the acquisitions should be in map view to maintain the required acquisition quality. It is important to note that for the DIC analysis to be meaningful, the geometric stability of the images must be at the highest possible level. Generally, the same sensor should be used for both acquisitions, although the used sensor need not be the same, if several requirements are met.

All DIC codes used for this thesis work with single band imagery, which could e.g. be a panchromatic band or any other band. Therefore, the radiometric resolution becomes important as well, i.e. how many different increments of the backscattered intensity the sensor can distinguish and save. Another consequence is the increased dependency of the matching success on the lighting conditions in the master and the slave images; in the best case, they should be exactly the same in both to avoid mismatching due to changing shadows or reflection intensities.

As it is not always possible to meet these requirements, certain pre-processing steps can be taken to minimize negative influences in the input acquisitions and to enhance matching success. Sub-optimal radiometric properties and the influence of varying lighting conditions can be modified by invoking a radiometric correction resp. a dynamic range optimization. This process is also called contrast or edge enhancement and can be performed using e.g. a Wallis filter. According to Baltsavias (1991), this filter forces the local mean and contrast under a search window, which runs over the original image, to fit to

some defined target values, which assures that different parts of the image have a similar dynamic range, thus facilitating matching. This operation is expressed as

$$f(m,n) = \big[g(m,n) - m_g\big]c * \frac{s_f}{cs_g + (1-c) * s_f} + bm_f + (1-b)m_g \qquad (2.2-1)$$

with $g$ and $f$ as the original and the filtered image, $m$ for the local mean as well as $s$ for the local standard deviation of the pixels within the window. $c$ and $b$ are, respectively, the contrast expansion constant and the brightness forcing constant. If the six input parameters are not carefully set, the dynamic range modification could also lead to negative effects such as a saturation of pixels or to a disadvantageous distribution along the image histogram. In the best case, a post-filter histogram would have a Gaussian shape with no saturation at its ends. For this study, a Wallis filter has been written and implemented for single band images in Matlab R2016a, based on Wallis (Baltsavias, 1991), which does not alter the original Ground Sampling Distance (GSD) of the input images. It produces 8 bit single band images with an optimized dynamic range, ready for introduction into the DIC codes (cf. figure 4).
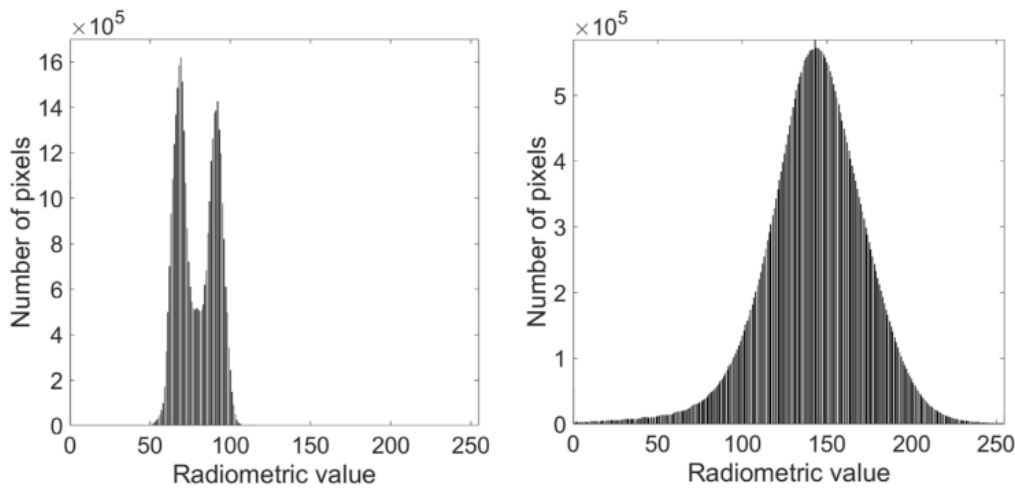


*Figure 4: Example for results obtained by using the implemented Wallis filter – dynamic range of the original 8 bit image on the left, Wallis filtered 8 bit image with the same spatial resolution on the right; the Gaussian shape is clearly visible, thus the dynamic range has been improved and contrast has been enhanced.*

In order to ensure an optimal geometric alignment of the master and the slave, both acquisitions should be co-registered before used for DIC. Thus, a co-registration guarantees that the observed displacement is true displacement and not caused by a poor alignment of master and slave. This is achieved by a comparison of either intensity values or features in both images using correlation metrics. The best global fit, i.e. the best global correlation on average, of both images is then used to align the slave onto the master.

Co-registration is usually performed by applying an oversampling factor (*co_os*), which can increase the accuracy of the matching to a sub-pixel scale. The procedure is equivalent to the one applied for DIC. To further increase the accuracy of the co-registration, master and slave can be sub-divided into smaller tiles, which are then co-registered in isolation from each other; subsequently, the average of the registration of all single tiles is then calculated and applied on the entire slave image. This process is called splitting (*sp*) and should theoretically increase the accuracy of the co-registration. A co-

registration algorithm was implemented by Dr. Andrea Manconi for Matlab R2016a using parts of Guizar-Sicairos, Thurman & Fienup (2008) and was used for NCC as well as FFT input pre-processing. COSI Corr uses a built-in co-registration algorithm by default.

After invoking a DIC code, there are several possibilities to enhance the quality of the resulting deformation matrices by applying post-processing methods, also called output filters. In general, a filter tries to identify and delete data points from an image matrix, that contain wrong or poor information. Five of them were used for this study: an RMSE threshold filter, a log-cross spectrum filter, a vector filter, a mean filter and a median filter. The threshold filter was implemented in Matlab R2016a only for the FFT code by Dr. Andrea Manconi using parts from Guizar-Sicairos, Thurman & Fienup (2008). It utilizes the translation invariant normalized RMSE derived from the correlations between master and slave. This value ranges from 0 to 1 and is an indicator of the reliability of the correlation, with smaller numbers representing more reliable matches. The filter cuts off all correlated search windows with RMSEs that are too low, allowing only good or true, correlations pass (cf. figure 5). The cutoff value can be defined by the user. COSI Corr uses its own threshold filter by allowing a masking of the frequencies according to the amplitude of the log-cross spectrum (Ayoub et al., 2015). Still, the general procedure is comparable to the one described above.
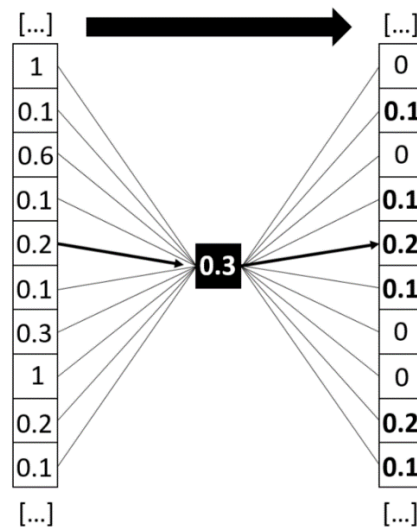


*Figure 5: Principle of the RMSE threshold filter, on the left are raw DIC output RMSE values, in the middle is the defined cap size criterion, on the right are the threshold-filtered RMSE values. All poor values which are above the chosen cap will be replaced by zero; only the sufficient values will be used to build up the final output image.*

The vector filter was written and implemented in Matlab R2016a and can be used for all three DIC algorithms. It operates in the spatial domain of the images (i.e. in 2D) and exploits both deformation matrices as well as the calculated resultant, i.e. the magnitude of the x and y offsets. The intention of the filter is to remove noisy and obviously wrong correlations, which are identified based on their deviating direction and magnitude. To do so, every correlation cell is compared to a specified amount of neighboring correlation cells and if it deviates from their average, either by deformation magnitude or -direction, it is removed by the filter. These cutoff values of the filter can be defined manually or are connected to the search window size, which has been used during the preceding DIC run. By default, the magnitude deviation is capped with

$$magcap = \frac{window\ size}{2} \qquad\qquad (2.2-2)$$

while the directional deviation is capped with

$$x\ or\ ycap = \frac{window\ size}{10} \qquad\qquad (2.2-3).$$

This means that if either the deviation in magnitude or direction of a correlation cell is larger than its respective cap, the entire cell will be filtered out and will be replaced by a zero. These caps were derived deterministically using a trial and error approach (cf. figure 6).
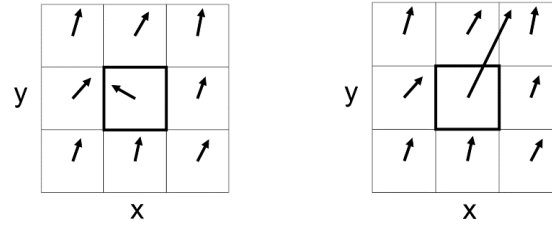


*Figure 6: Principle of the 2D spatial vector filter for effective noise reduction, on the left for the directional deviation, on the right for the magnitude deviation; in both cases, the tested correlation cell in the middle would exceed the caps due to their deviation from the mean of the surrounding cells (by direction or by magnitude) while being replaced by a zero.*

The vector filter can be expressed in the form:

$$x_{Def\_filt,ij} = \left| x_{Def,ij} - \frac{\sum_{a=1}^{n} x_{Def}}{n} \right| \leq xcap \qquad\qquad (2.2-4)$$

$$y_{Def\_filt,ij} = \left| y_{Def,ij} - \frac{\sum_{a=1}^{n} y_{Def}}{n} \right| \leq ycap \qquad\qquad (2.2-5)$$

$$mag_{Def\_filt,ij} = \left| mag_{Def,ij} - \frac{\sum_{a=1}^{n} mag_{Def}}{n} \right| \leq magcap \qquad\qquad (2.2-6)$$

Besides the two selective filters described above, two filters were written and implemented for Matlab R2016a that modify the deformation matrices to enhance the results. One of them is a mean filter, which re-calculates the value of each correlation cell based on the mean of its surrounding cells – the number of influencing cells can be defined by the user. Optionally, a loose cut off sequence can be performed prior to removing extreme outliers, which could otherwise negatively influence the calculation of a representative average. The mean filter will smooth the deformation matrices, while reducing noise but also sacrificing some resolution of the determined deformation field, similar to a low-pass filter (cf. figure 7).

| | | | | | | |
|---|---|---|---|---|---|---|
| 55 | 59 | 65 | | 55 | 59 | 65 |
| 58 | **53** | 49 | ➡ | 58 | **56** | 49 |
| 54 | 52 | 61 | | 54 | 52 | 61 |

x

*Figure 7: Principle of mean filter, on the left is the unfiltered matrix, on the right is the recalculated matrix; the new value of the center cell is the mean of the cell itself as well as of its 8 neighbors.*

Finally, a median filter has been assessed for post-processing, which performs the same operation as the mean filter, but calculates the median of the neighborhood instead of the average. Thus, outliers have less influence on the derivation of the new correlation cell value. The only input parameter is the size of the applied window and advantages resp. disadvantages are similar to the mean filter (cf. figure 8).

| | | | | | | |
|---|---|---|---|---|---|---|
| 55 | 59 | 65 | | 55 | 59 | 65 |
| 58 | **53** | 49 | ➡ | 58 | **55** | 49 |
| 54 | 52 | 61 | | 54 | 52 | 61 |

x

*Figure 8: Principle of median filter, on the left is the unfiltered matrix, on the right is the recalculated matrix; the new value of the center cell is the median of the cell itself as well as of its 8 neighbors.*

The following pipeline visualizes the entire workflow from pre-processing through DIC and post-processing to output visualization:
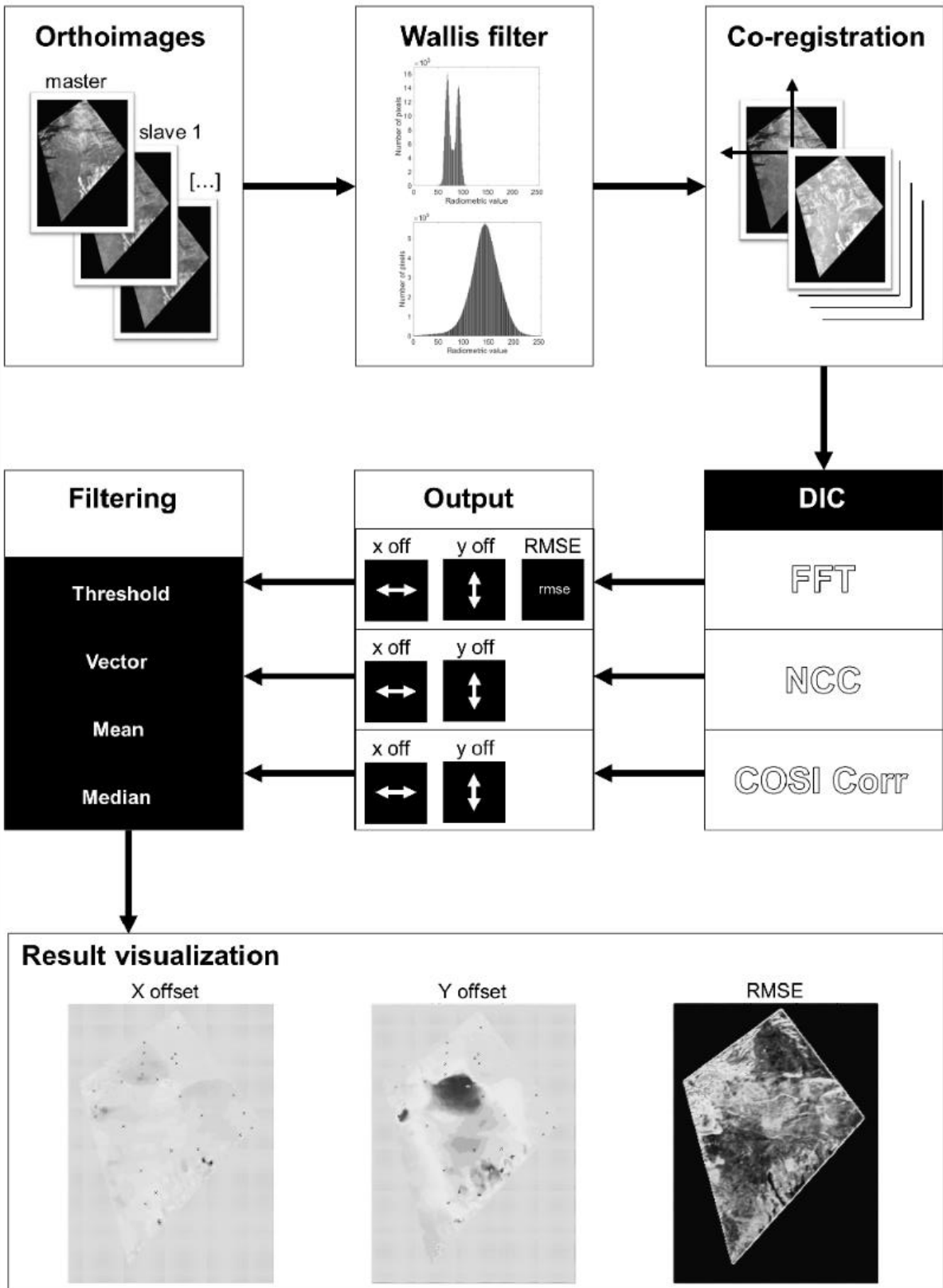
*Figure 9: Complete DIC processing pipeline.*

# 3. ASSESSMENT OF DIC CODES

The three selected DIC codes were assessed on a study site located on Earth, more specifically in the Swiss Alps, prior to any extra-planetary application. This enabled a DIC performance assessment and a validation in a controlled environment. The outcomes were then used to plan and execute a change detection campaign on Mars.

## 3.1 Study site

The chosen validation area was Cuolm da Vi (CdV) in the Canton Graubünden, Switzerland, which hosts a deep-seated gravitational slope deformation (DSGSD). CdV is situated on a south-facing mountain slope north of the town Sedrun in the Central Alps, on the southern boundary of the Aar Massif (figure 10).
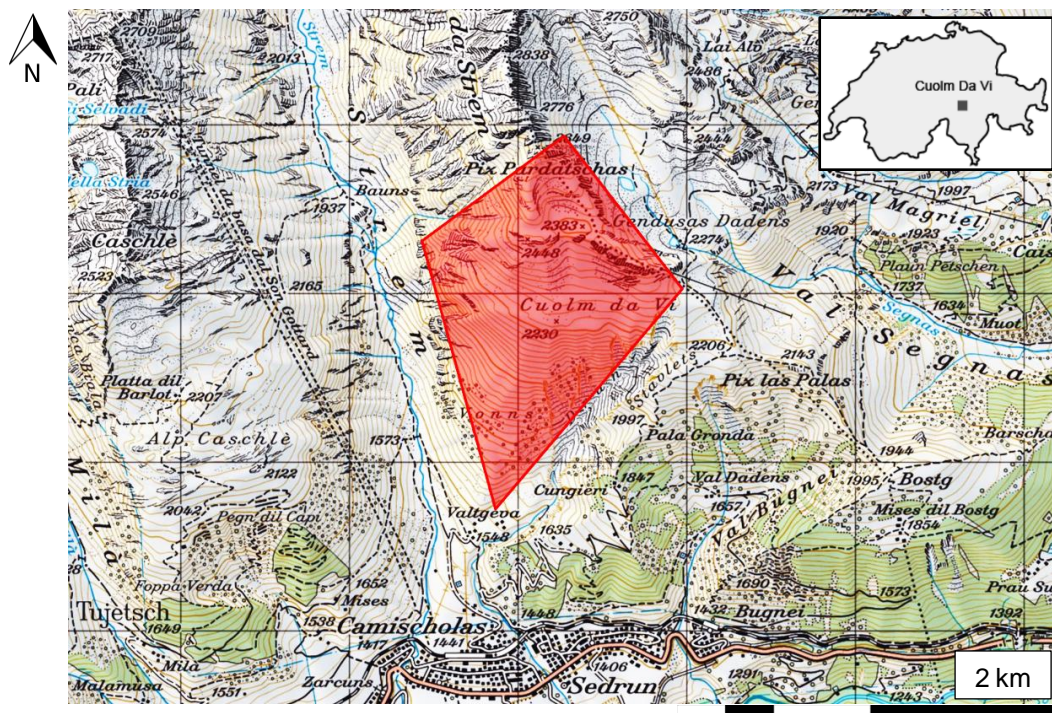


*Figure 10: Topographical map of Cuolm da Vi and the town of Sedrun in Graubünden, Switzerland. The AoI is marked in red (Swiss Geoportal, n.d., Manconi et al., 2016).*

Slope angles in the AoI range from 15° to 70° with an average of 40° to 45° while the relief ranges from 1750 masl (meters above sea level) to 2450 masl. The unstable volume is estimated as roughly 150 million cubic meters, consisting of granitic gneisses with E-W trending mylonitic and kakiritic shear zones. The toe of the DSGSD comprises a weak, thick kakirite band, which hosts active gullying processes. The ongoing deformation is expressed on the surface by tension cracks, antiscarps, graben and sagging structures, which indicate a gravitational displacement along inherited tectonic structures, especially in the upper part of the area (Manconi et al., 2016, Amann, 2006). Photographs of such

surface features from 1952 and 2003 are found in the supplementary information section (S 4). Amann (2006) classified the occurring processes as i) a southern downslope failure zone, which is defined by fragmented material and brittle, surficial toppling, ii) a slope shoulder with shallower slope angles and EW trending antiscarps and sagging structures, and iii) an upslope region with distinctive graben and extension crack features. Manconi et al. (2016) describes the main kinematic failure mechanism as a southeast to westward toppling. Slope deformations in Cuolm da Vi have been monitored since 1942 with traditional techniques such as tachymeters, extensometers and GNSS (Global Navigation Satellite System). According to Manconi et al. (2016) and Amann (2006) the average displacement rates across the area range from 4.7 to 67 cm per year. Lower displacement rates are presumed to be caused by global, deep-seated (> 30 m depth) movements, whereas higher rates represent local, shallow movements. The general trend of deformation is controlled by the orientation of the tectonic and morphological structures and varies between W and SE (Manconi et al., 2016). In recent years, Manconi et al. (2016) applied DIC codes in this area and found not only that displacements measured with this technique are compatible with results from standard methods, but also identified portions of an unknown and accelerating unstable zone. On March 14th, 2016, this part failed, with an estimated volume of about $2 \times 10^5$ cubic meters. A geological map of the area is shown in figure S 2 in the supplementary information section.

## 3.2 Available data

We considered orthorectified aerial photographs as well as GNSS data from the AoI. The aerial images were acquired and processed in the years 1999, 2003, 2010, 2013 and 2015 under snow- and cloud-free conditions by Swisstopo resp. Swissphoto, the Bonanomi AG and Donatsch + Partner AG. The camera system of the 1999 acquisition is not known, but is likely to be an airborne camera; the 2015 image was captured with an "ebee" fixed-wing drone produced by the company Sensefly, presumably equipped with a Canon S 110 RGB. Both images are RGB and have a GSD of 0.25 m per pixel. This spatial resolution exactly matches the GSD of one of the sensors, that has been planned to be utilized for the DIC exploration campaign on Mars. This should enhance the intention to directly apply the conclusions of the CdV case study for the subsequent work. For this study, the 1999 and 2015 images were selected, providing the maximal temporal baseline, i.e. the longest possible time difference of 16 years, as well as the best GSD. Both images can be reviewed in the supplementary information section (S 5). Due to logistical and temporal constraints, the effects of the application of different cameras for DIC input image acquisition could not be investigated; technically, a control area without any deformation should be used to verify DIC code operability. For this work however, potential influences by use of different sensors were dismissed as unlikely and were neglected. Due to the given acquisition mode and image shape of the 1999 image, the 2015 photograph has been cropped to the same rhombohedral shape to facilitate data handling and image matching. After the application of the DIC algorithms, deformation results are compared to the available GNSS time series from 1999 to 2015, derived by Bonanomi AG and Donatsch + Partner AG, acquired at specific locations. This dataset contains the CdV

displacement field in NS, EW and elevation (3D) at 23 measurement points across the instability; the corresponding map can be considered in the supplementary information section (S 1). The average error of the logging has been derived as 6 mm horizontally and 11 mm vertically; figure S 3 in the supplementary section illustrates the principle of the GNSS measurement in CdV as performed by the ETH MSC Engineering Geology class 2015/17 during a field trip in 2016. Due to the mode of measurement, operator or other errors cannot be excluded.

## 3.3 Investigation plan

The two chosen orthoimages were used for a systematic application with the selected DIC algorithms, following a defined scheme to produce an ample and expressive set of outputs, based on varying pre- and post-processing steps as well as DIC input parameters. These outputs were then compared with the GNSS data, which were treated as representing the true deformation of the CdV DSGSD. The intention was to validate and compare the applicability and accuracy of DIC codes for qualitative and quantitative slope deformation detection with high-resolution images, in order to identify the advantages and limitations for an application on a foreign planet, where ground truthing is no longer possible. To assess possible post-processing steps, i.e. result filters, all four described possibilities were applied during the case study. In addition, the influence of oversampling was investigated by applying an $os$ of 1, 4 and 8. As oversampling cannot be manually set for COSI Corr, the robustness iteration was instead evaluated for values of 1, 4 and 5. Further, a variation of the window size was tested with $wi$ as 32 by 32, 64 by 64 and 128 by 128 pixels. The effect of pre-processing was investigated by applying all mentioned parameters to two different pairs of input images, one without pre-processing at all and one which had been Wallis-filtered. All these steps were conducted for the NCC, the FFT and the COSI Corr codes, resulting in a total number of 144 different DIC runs, 48 for each code; table 1 illustrates the workflow and all parameters.

*Table 1: CdV DIC workflow scheme, displaying all parameters that were subject to the investigation and were therefore systematically changed during the 144 DIC runs.*

| Code | COSI Corr / FFT / NCC | | | | | | | | | | | | |
|------|--------|--------|--------|--------|--------|--------|--------|--------|--------|--------|--------|--------|--------|
| Image | ORIGINAL | | | | | | | | | | | | |
| wi | 32 | | | | 64 | | | | 128 | | | | |
| os / ri | 1 / 1 | | 4 / 4 | | 1 / 1 | | 4 / 4 | | 1 / 1 | | 4 / 4 | | 8 / 5 |
| Filter | Median | Vector | Median | Vector | Median | Vector | Median | Vector | Median | Vector | Median | Vector | Vector |
| | Mean | Thres. | Mean | Thres. | Mean | Thres. | Mean | Thres. | Mean | Thres. | Mean | Thres. | |
| Image | WALLIS | | | | | | | | | | | | |
| wi | 32 | | | | 64 | | | | 128 | | | | |
| os / ri | 1 / 1 | | 4 / 4 | | 1 / 1 | | 4 / 4 | | 1 / 1 | | 4 / 4 | | 8 / 5 |
| Filter | Median | Vector | Median | Vector | Median | Vector | Median | Vector | Median | Vector | Median | Vector | Vector |
| | Mean | Thres. | Mean | Thres. | Mean | Thres. | Mean | Thres. | Mean | Thres. | Mean | Thres. | |

In order to reduce the extent of testing, some parameters of interest were deterministically defined prior to the case study, such as the co-registration split and oversampling as well as the default values for all filters. For the accuracy of the NCC code, it was determined that the use of a co-registration split of 4 and an oversampling of 1 for original input images, and a *sp* of 1 and a *co_os* of 1 for Wallis-filtered images, yields the best results. The FFT algorithm performs best with no *sp* and *co_os* (equal to 1) at all for both input acquisition types (cf. tables S T 5 & S T 6 in the supplementary information section). In this case, the identification of the best results is based on the comparison of a quantification of the different DIC results using a RMSE-based approach, while following a specific procedure; this method will be further described in the following paragraphs. It has to be noted that the CdV input images were already co-registered prior to any processing within the frame of this study, but only in a very slight and conservative way; its influence on this assessment is assumed as being slight. The best threshold filter value was identified as 0.5 for a raw input image and as 0.6 for a Wallis-filtered input image, while for COSI Corr the default value of 0.90 for the log-cross spectrum filter was used. The vector filter caps showed best results with a magnitude cap of *wi*/2 and directional caps as *wi*/10 for both types of images. The mean filter yielded the best results with a window size of 6 by 6 pixel, while the median post-processing achieved best quality with a 5 by 5 pixels window. Here, the best results were found using a trial and error approach in combination with a visual comparison of the quality of the returned spatial coverage. These findings were set during all test runs of this case study and were not altered.

After each DIC run, the produced NS and EW deformation matrices had to be compared to the GNSS NS and EW (true) deformation in a quantitative sense. To do so, the point values of the DIC NS and EW matrices closest to each of the 23 GNSS measurement locations were gathered and used for a quantitative comparison of the deformation. Following a trial and error approach, the utilization of the closest 12 DIC correlation cells around each single GNSS measurement point were identified best for the quantitative comparison, using the calculated RMSE of all options as an indicator. Twelve points achieve the best compromise between a good SNR and an acceptable accuracy, as the deformation is averaged over a larger area (cf. figure 11 and table S T 1 in the supplementary section). Using only the closest point or closest 4 points proved to be very susceptible to noise, while not enhancing the accuracy of the comparison. Using the closest 24 points, however, decreased the accuracy, as the respective average is taken over too large of an area.
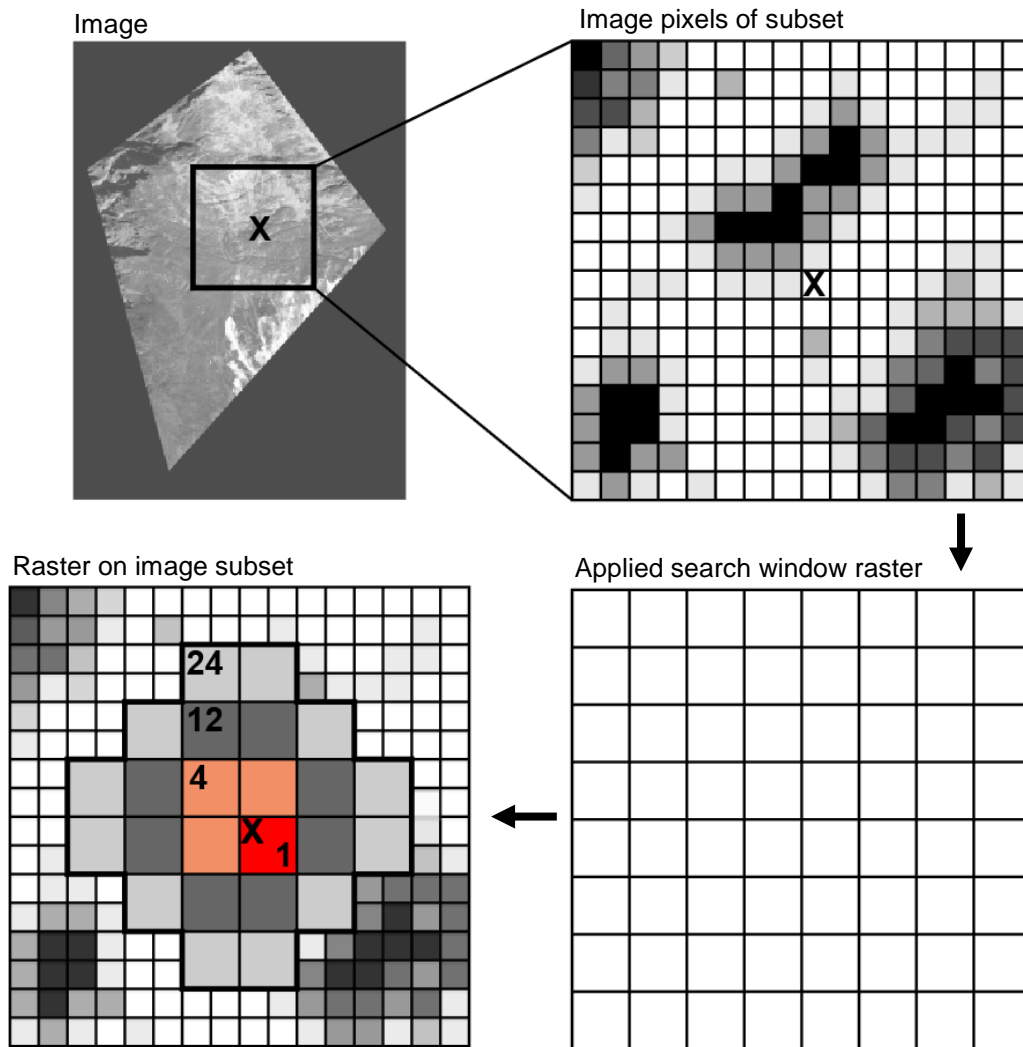
*Figure 11: Top-down view scheme of vicinity-point offset data extraction, black X is the GNSS measurement point of interest. Subset illustrates how the image is built by pixels, while the search window raster (here 2 by 2 pixels) is applied during DIC onto the image. For the quantitative comparison the closest 1, 4, 12, and 24 GNSS point vicinity raster cells were used.*

With the NS and EW deformation component at each GNSS measurement point extracted from the DIC results, a direct quantitative comparison between all runs could be performed. In a first step, the mean RMSE and the mean standard deviation (StD) of the NS, EW and NS-EW-resultant of the pixoff data from the GNSS data were derived and added to a master table, to give a global overview of the accuracy and precision of the performed run. Additionally, a linear regression was executed and plotted for each one of the 23 GNSS points to visualize the accuracy of each run's NS, EW and resultant, utilizing the calculated RMSE value.

Using an external Matlab R2016a function implemented by D'Errico (2006) called gridfit, the magnitude of the deformation, i.e. the NS-EW-resultant, was interpolated between the 23 measurements. This mask was then compared to the deformation resultant derived from the DIC codes, giving the residual or remaining deformation as an additional indicator for the accuracy of the respective DIC run. Additionally, a subtraction of both input orthoimages after a precise co-registration could allow conclusions about the general differences between both images, i.e. reflectance intensities, and could unveil deformations. Large differences in the reflectance intensity could cause DIC mismatches, which

means that in the best case, the subtraction of both images would lead to a matrix consisting of zeros – in areas without any change. This basic change detection operation could therefore contribute to a sophisticated and comprehensive analysis and an operational code has been written and implemented in Matlab R2016a.

The computation operations were performed on a personal notebook with advanced performance hardware, i.e. double core 2.40 GHz CPU and 16 GB DDR4 RAM. Due to the occasionally immense hardware requirements of some operations, particularly the NCC calculations with small search windows and high oversampling, these operations had to be performed in parallel on several sophisticated desktop computers with up to 8 cores CPU and 32 GB RAM, allocated by the Institute of Geodesy and Photogrammetry of ETH Zurich, Campus Hönggerberg.

## 3.4 Results

The interpolated GNSS deformation magnitude, i.e. the EW – SW resultant, is plotted in figure 12. All GNSS positions are marked with black crosses.
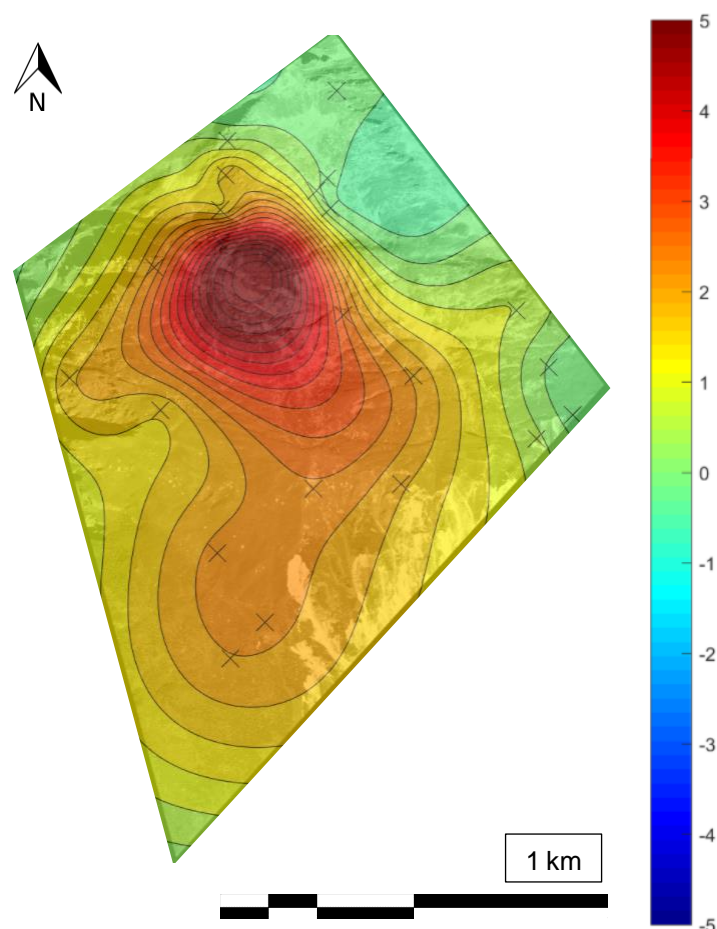


*Figure 12: Interpolated GNSS offset magnitude using gridfit, the black crosses indicate the 23 GNSS measurement point locations. Scale is in [m].*

Figure 13 illustrates a sample visual output of the DIC codes after post-processing using a window size of 64 pixels and a vector filter, with the NS component to the left and the EW component to the right. Additionally, figure 14 shows the xy resultant or magnitude of the DIC derived deformation. While a greenish color indicates no deformation, a blueish color in the NS (up – down) image indicates a movement to the North; in the EW plot (left – right), it indicates a movement to the West. A reddish color indicates a movement to the South or to the East, respectively. The black crosses indicate the 23 GNSS measurement points across the AoI.
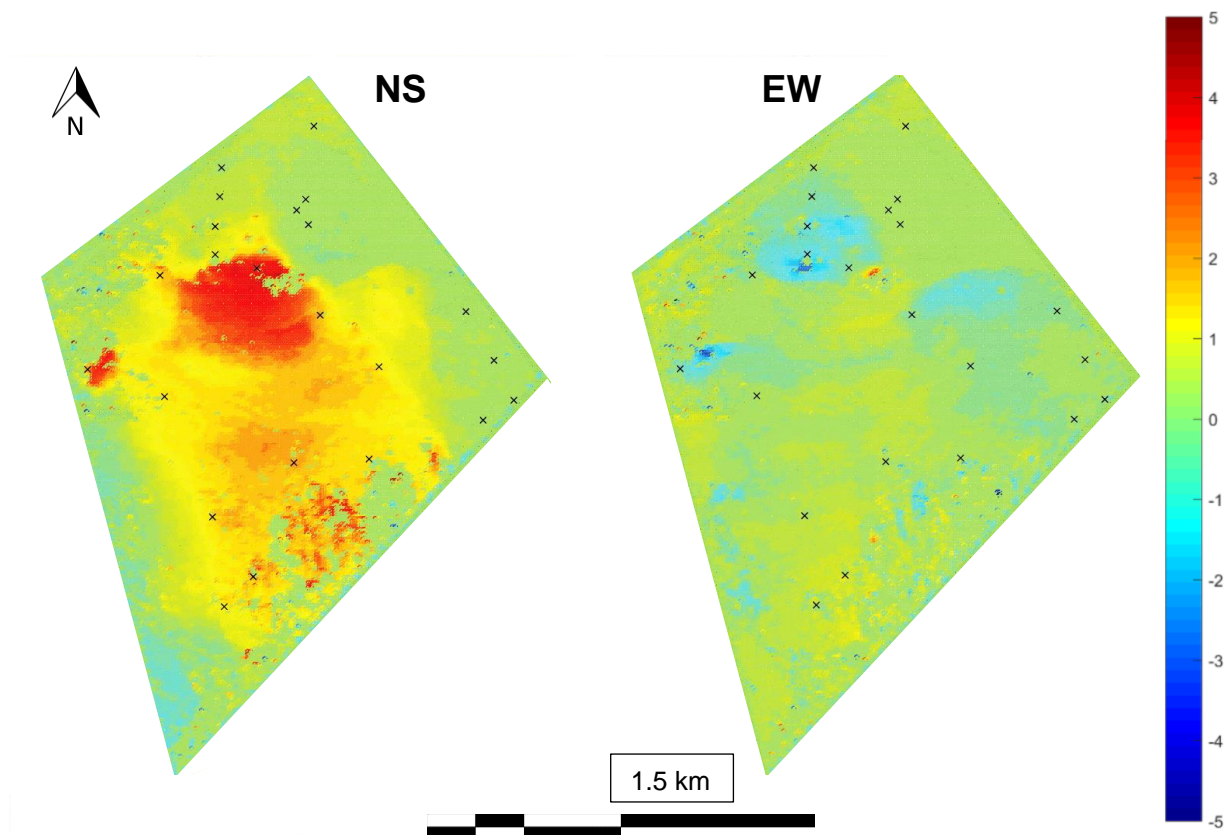


*Figure 13: Exemplary visualization of the results by a DIC run with the FFT code, using a wi of 64 pixels and a vector filter for post-processing. Black crosses indicate the locations of the GNSS measurement points. Scale is in [m] and ranges from red (+5 m) to blue (-5 m).*
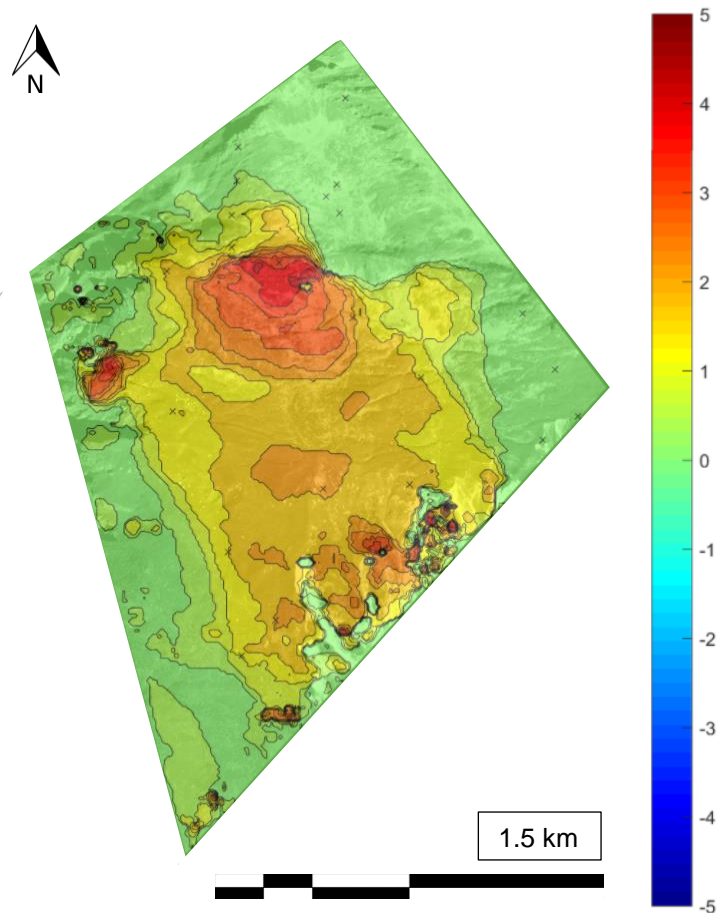
*Figure 14: DIC offset magnitude of a FFT run with wi of 64 pixels and a vector filter. Scale is in [m].*

Plot 15 illustrates the deformation resultant with vectors, thus enhancing the visualization of the occurred deformation. The length of the vectors does not reflect the total displacement at that point, but rather gives an impression of the relative magnitude of the deformation at each point.
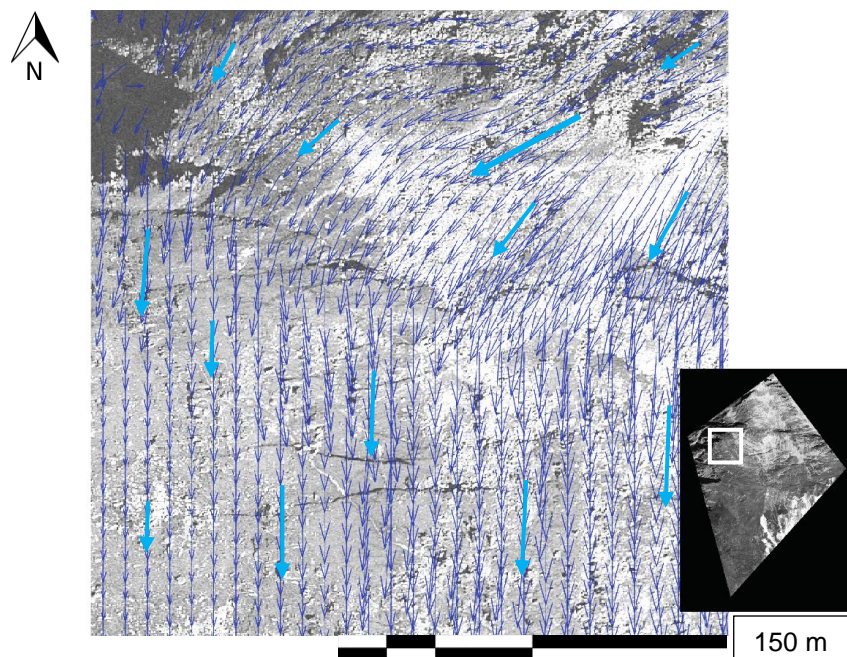


*Figure 15: Zoom into a DIC-derived (wi 64 pixel, vector filtered) deformation direction, plotted with vectors in blue on top of the master input image from 1999; overview with AoI marked in white on the right side. Scarp and graben features are visible in the background image, striking +/- EW.*

A comparison between the output quality of a raw and a Wallis-filtered input image after post-processing is shown in figure 16.
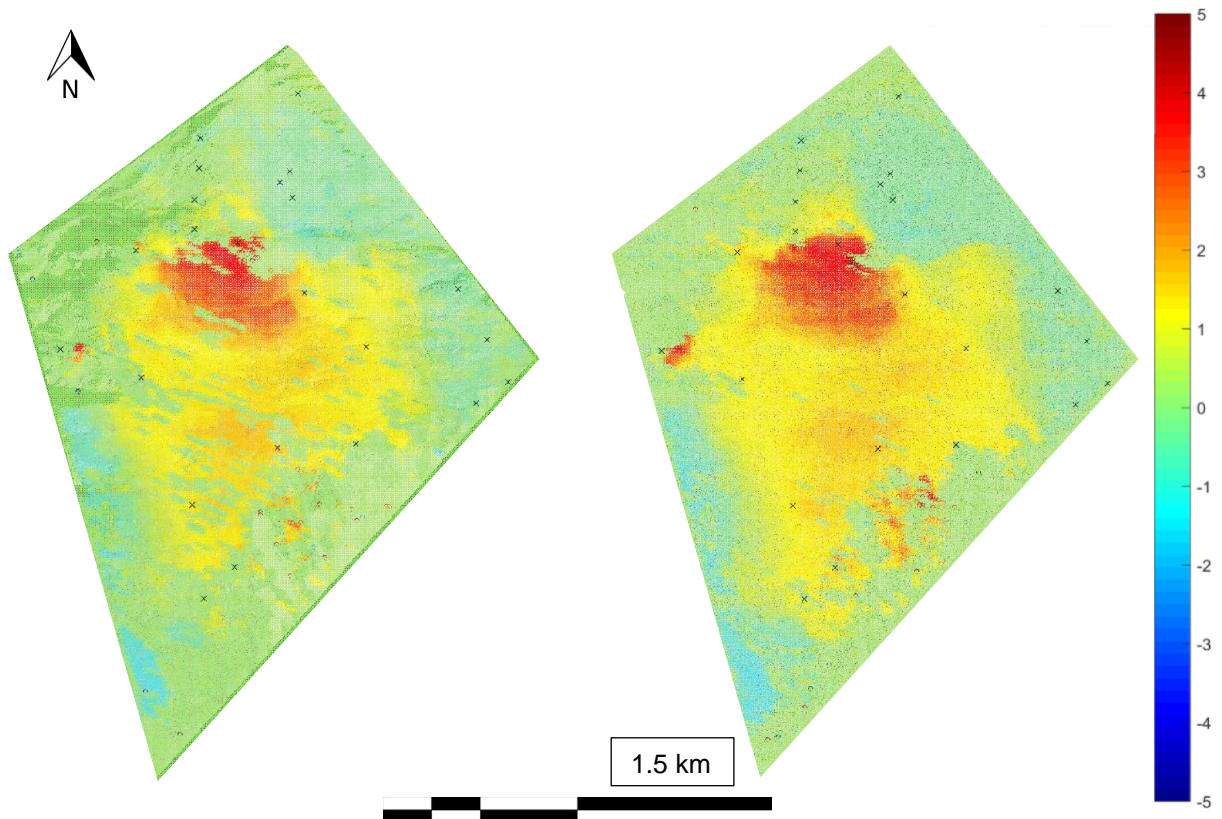


*Figure 16: Comparison of the quality of the returned spatial coverage (i.e. matching quality) of two DIC runs with NCC and identical input parameters, but with an original input image on the left and Wallis-filtered input image on the right. Scale is in [m]. Grid effects in the left plot are caused by an interference of the circles indicating each correlation cell; this optical effect is enhanced by the black background of the underlying image.*

As the NS components of the derived DIC displacements are the most prominent and representative, they were used to visualize the quality of the spatial coverage of each single run of this case study, to enable a visual comparison of the applied input parameters and utilized codes, in tables 2, 3, and 4. Only plots with oversampling of 1 have been selected for this purpose, as an increased oversampling did not improve the spatial coverage. Due to space limitations and the varying quality, the representation of data in this chapter has been limited to results derived using the vector and the median filter. Results derived with the other two post-processing techniques has been incorporated into the supplementary information section (S T 2, S T 3, S T 4), to allow a direct comparison.

*Table 2: CdV NS DIC-output visualization for NCC on original and Wallis images with different window sizes as well as median and vector filter. Colorbar and coding are equal to the one used for DIC NS and EW output plotting before (e.g. figure 13). Differences in color intensity are caused by different densities of the used search windows, 32 appears brighter than 128, or by filter action resp. pre-processing filter action. North is up, not to scale.*
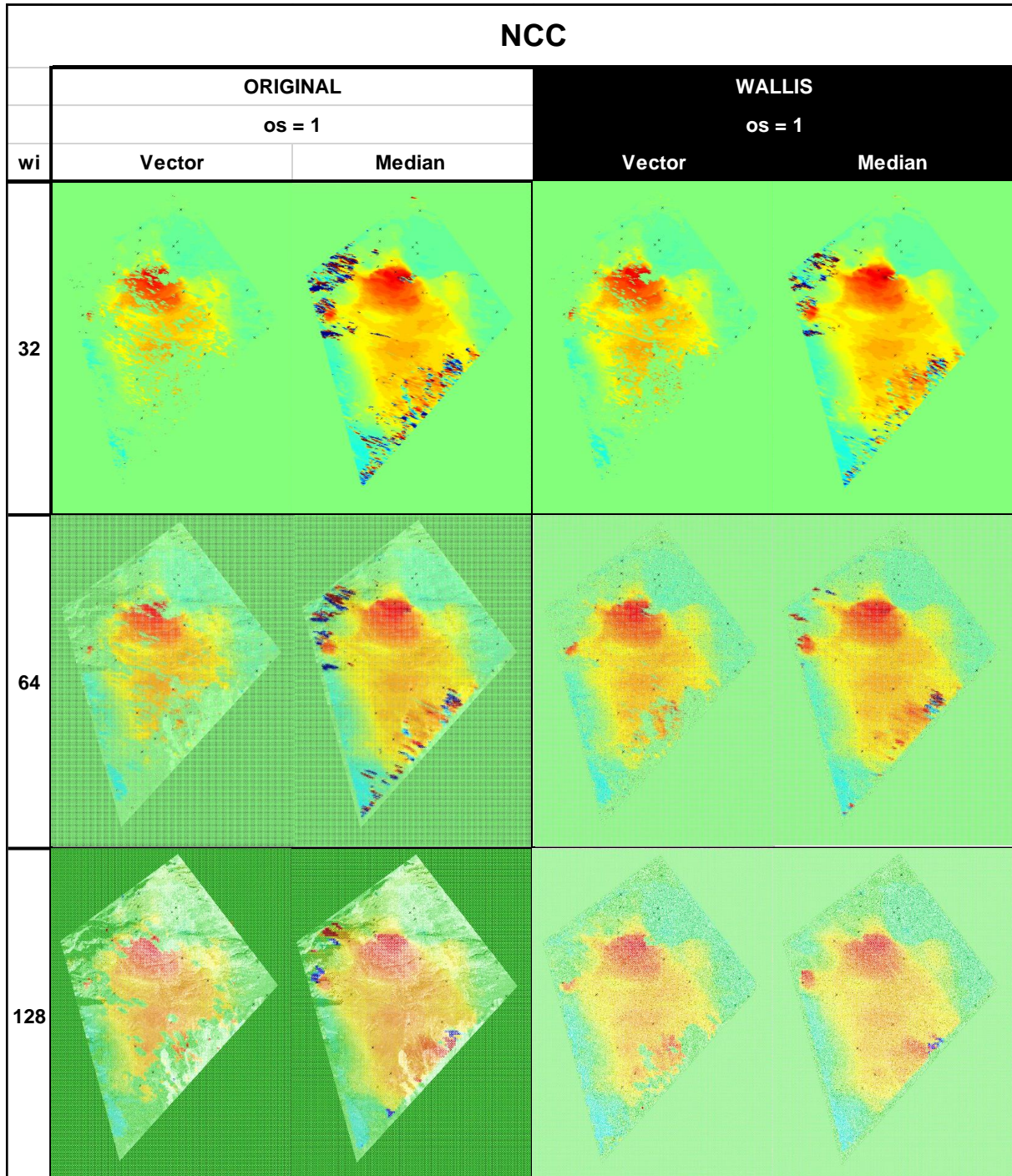
*Table 3: CdV NS DIC-output visualization for COSI Corr on original and Wallis images with different window sizes as well as median and vector filter. Colorbar and coding are equal to the one used for DIC NS and EW output plotting before (e.g. figure 13). Differences in color intensity are caused by different densities of the used search windows, 32 appears brighter than 128, or by filter action resp. pre-processing filter action. North is up, not to scale.*
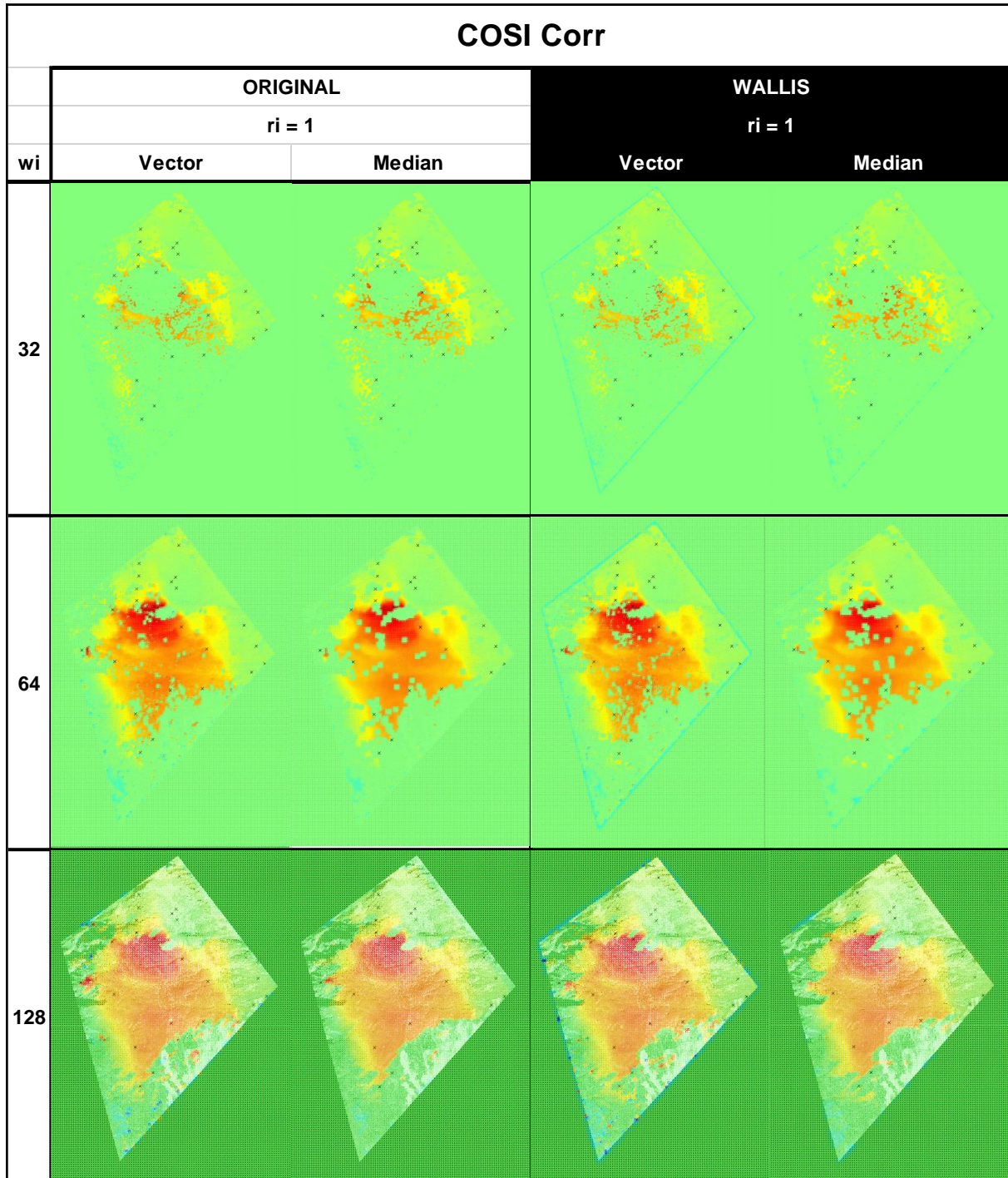
*Table 4: CdV NS DIC-output visualization for FFT on original and Wallis images with different window sizes as well as median and vector filter. Colorbar and coding are equal to the one used for DIC NS and EW output plotting before (e.g. figure 13). Differences in color intensity are caused by different densities of the used search windows, 32 appears brighter than 128, or by filter action resp. pre-processing filter action. North is up, not to scale.*
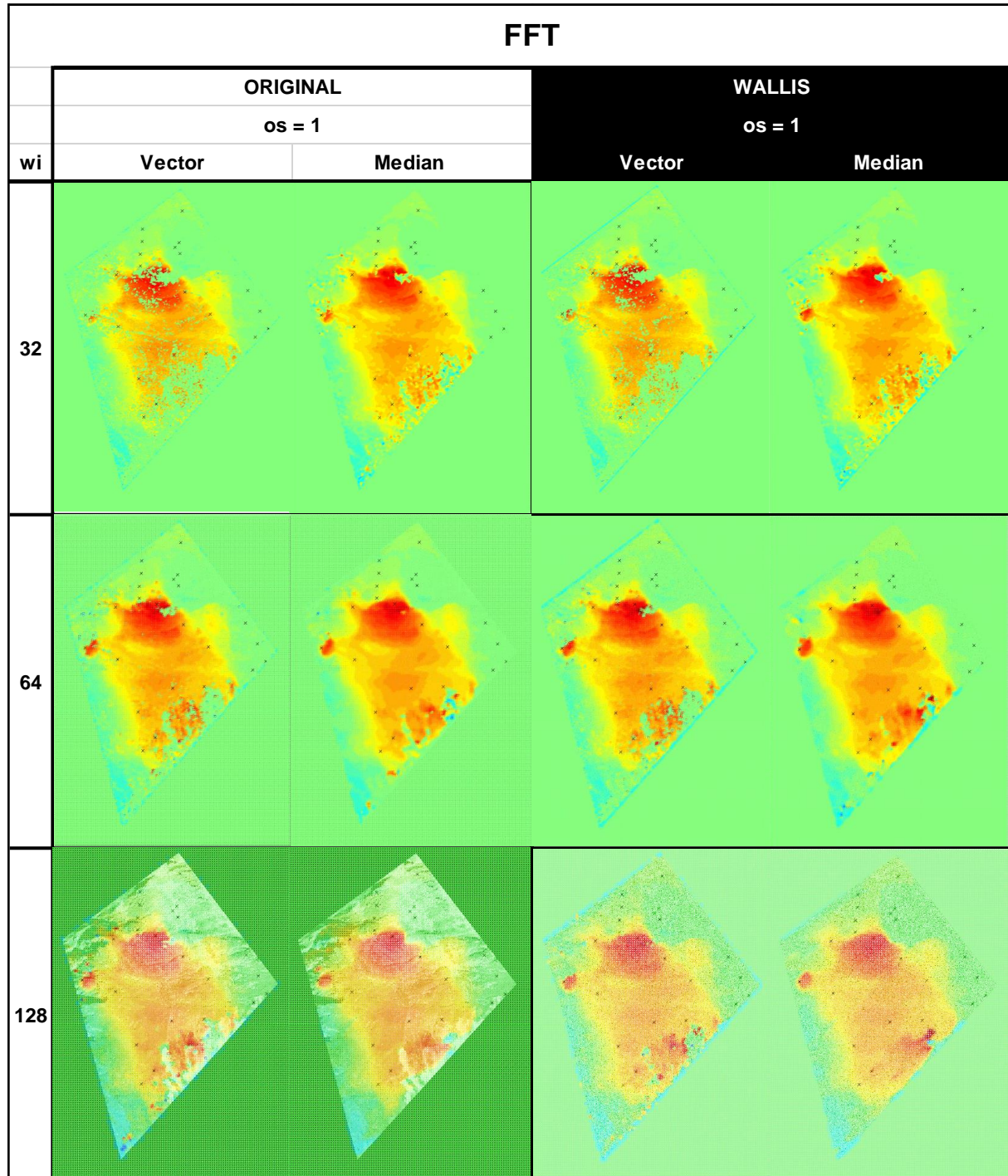


Computation time estimates and approximations for the ~ 30 MB CdV input orthophotos for all three codes with the described computers and with various window sizes and oversampling factors are listed in table 5, while figure 17 gives a graphical visualization of the time required for each separate processing step for the FFT and the NCC codes. The pie charts underline the relative differences in computation power consumption. COSI Corr has not been plotted, as time information cannot be extracted from the toolbox.

*Table 5: Mean computation times for all codes using different search windows and oversampling factors for the CdV data set using a personal computer.*

| wi \| os (ri) | COSI Corr | FFT | NCC |
|---|---|---|---|
| **32 \| 1 (1) / 4 (4) / 8 (5)** | 45s / 90s / 180s | 3min / 30min / 90min | 1.5h / 4h / 12h |
| **64 \| 1 (1) / 4 (4) / 8 (5)** | 30s / 60s / 100s | 2min / 20min / 60min | 1h / 2.5h / 9h |
| **128 \| 1 (1) / 4 (4) / 8 (5)** | 15s / 30s / 60s | 0.5min / 5min / 15min | 0.5h / 1.5h / 6h |
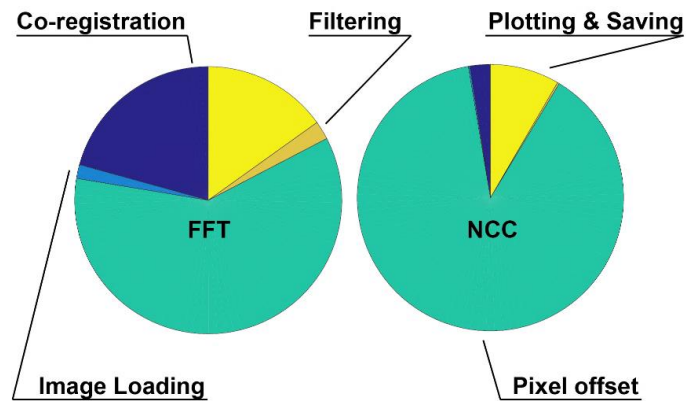


*Figure 17: Relative computation time consumption for FFT (left) and NCC (right).*

The resultant of a FFT run with window size of 64 pixel (figure 13) was subtracted from the previously interpolated GNSS magnitude mask (figure 12) to derive a residual map; figure 18 shows a sample result of this procedure.
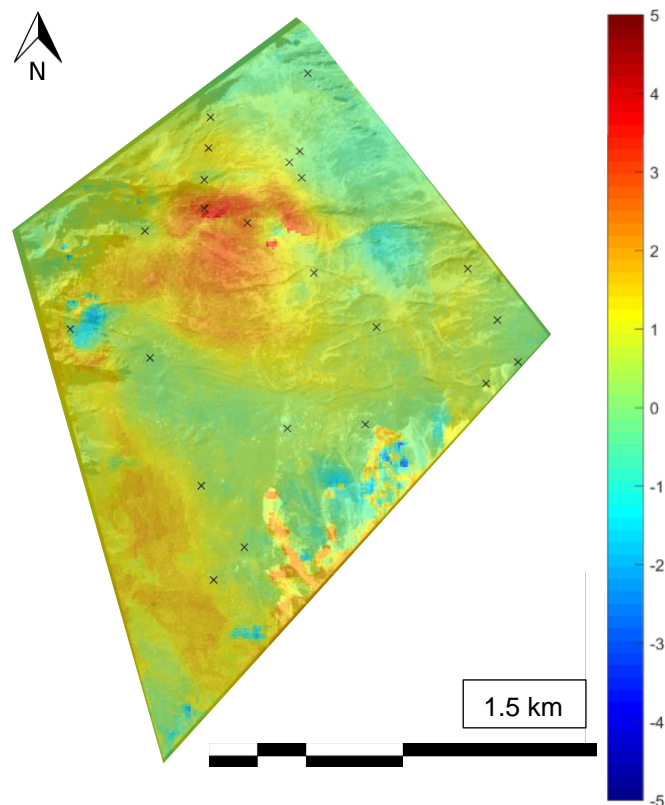


*Figure 18: Plot of the GNSS magnitude subtracted from the DIC derived magnitude for a FFT run with wi 64 pixels and vector filtering. Difference in measured deformation is plotted. Scale is in [m].*

Additionally, the precisely co-registered original orthoimages were subtracted from each other, in order to perform a basic quality check and to potentially identify deformations. The results were plotted as a binary mask, using a weak median filter to reduce noise level caused by radiometric differences (figure 19).
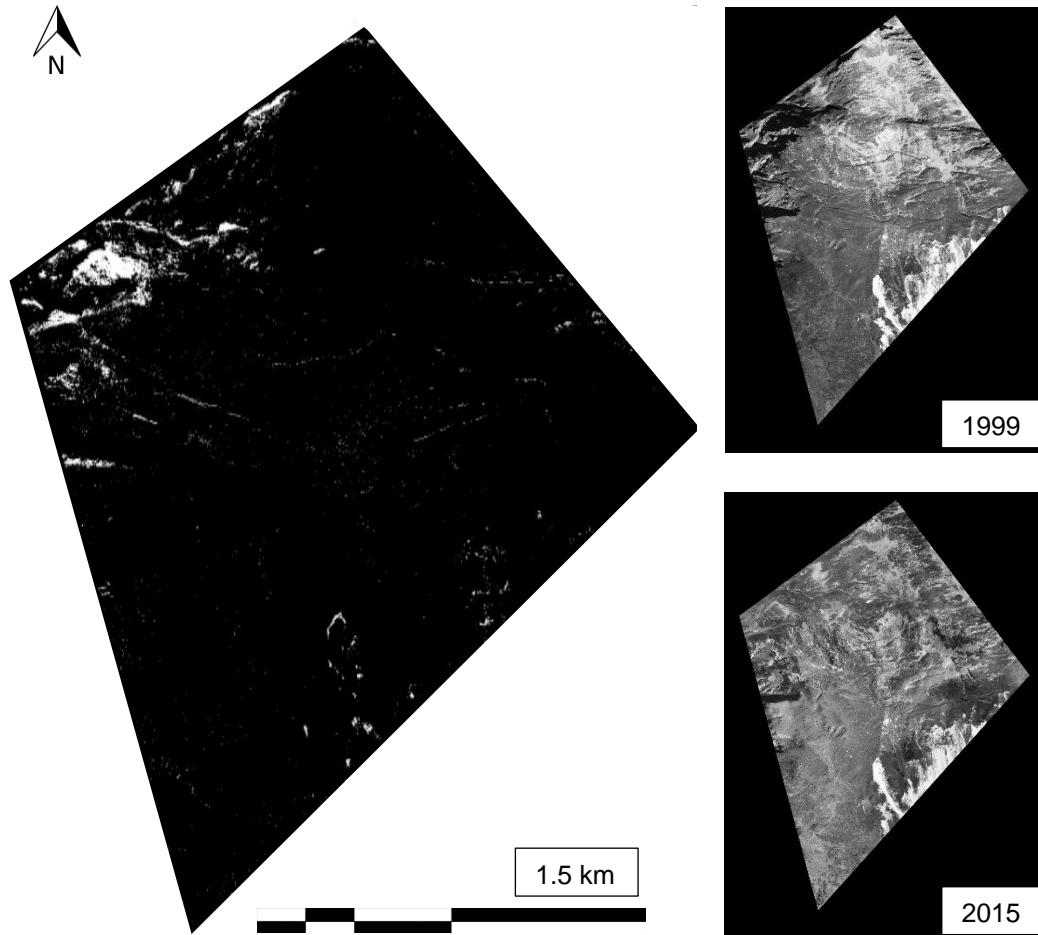


*Figure 19: Smoothed binary plot of input image subtraction from 1999 and 2015 using a binary threshold of 80 bit. Occurred changes are displayed with black pixels (0 bit) indicating no change and white pixels indicating differences (255 bit). Original images as interpretation support on the right.*

Tables 6, 7, and 8 represent a visualization overview of the calculated linear regressions of the NS-EW-resultant with the RMSE values of the conducted runs with the vector and the median filter, with GNSS magnitude on the y axis and the pixel offset magnitude on the x axis. The colored dots represent the 23 measurement points, where data from both methods as well as their spatial distribution can be directly compared. Each run's respective magnitude RMSE is noted within its individual subplot and due to ambiguity reasons the potential outliers were included, but marked with black arrows in the first subplot.

*Table 6: Overview of calculated linear regressions of the NS-EW-magnitude for selected runs with NCC using the closest 12 DIC points, with GNSS resultant on the y axis and the pixel offset resultant on the x axis in [m]. The colored dots represent the 23 measurement points, where data from both methods has been directly compared. Respective RMSE in [m] is noted within its subplot, potential outliers marked with black arrows, GNSS point ID 11 in dark green, point ID 17 in light green.*

| | NCC | | | |
|---|---|---|---|---|
| | **ORIGINAL** | | **WALLIS** | |
| **wi / os** | **Vector** | **Median** | **Vector** | **Median** |
| **32  1** | 1.078 | 1.117 | 1.089 | 1.094 |
| **32  4** | 1.101 | 1.111 | 1.079 | 1.085 |
| **64  1** | 1.092 | 1.091 | 1.055 | 1.081 |
| **64  4** | 1.097 | 1.089 | 1.053 | 1.082 |
| **128  1** | 1.065 | 1.163 | 1.076 | 1.129 |
| **128  4** | 1.048 | 1.028 | 1.072 | 1.13 |
| **128  8** | 1.047 | | 1.071 | |
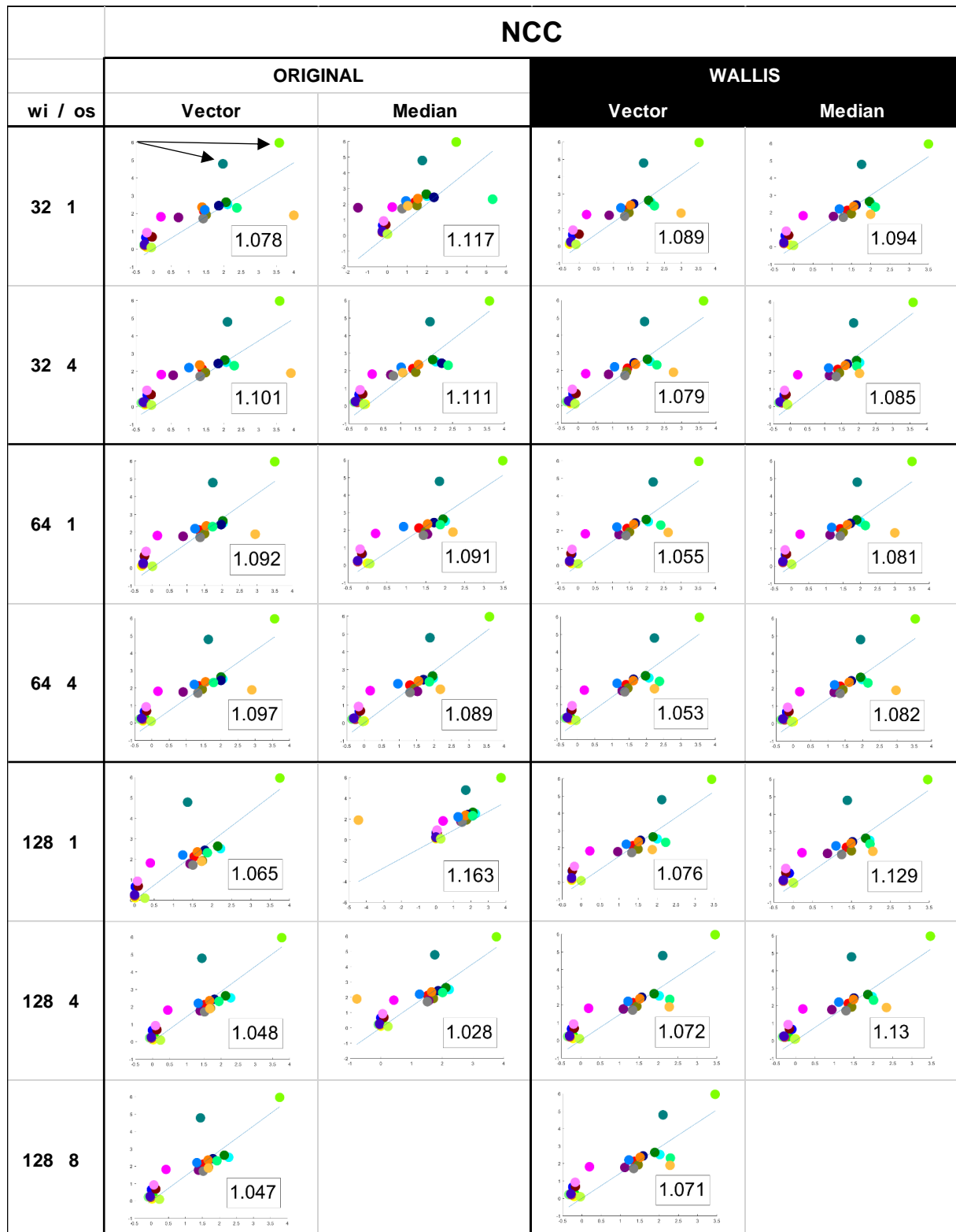
*Table 7: Overview of calculated linear regressions of the NS-EW-magnitude for selected runs with COSI Corr using the closest 12 DIC points, with GNSS resultant on the y axis and the pixel offset resultant on the x axis in [m]. The colored dots represent the 23 measurement points, where data from both methods has been directly compared. Respective RMSE in [m] is noted within its subplot, potential outliers marked with black arrows, GNSS point ID 11 in dark green, point ID 17 in light green.*



| wi / ri | COSI Corr | | | |
| | ORIGINAL | | WALLIS | |
| | Vector | Median | Vector | Median |
| 32  1 | 1.796 | 2.141 | 1.8 | 2.076 |
| 32  4 | 1.798 | 2.141 | 1.786 | 2.076 |
| 64  1 | 0.903 | 1.445 | 0.94 | 1.621 |
| 64  4 | 0.901 | 1.445 | 0.936 | 1.622 |
| 128  1 | 0.929 | 1.279 | 0.874 | 1.257 |
| 128  4 | 0.929 | 1.28 | 0.874 | 1.257 |
| 128  5 | 0.925 | | 0.871 | |
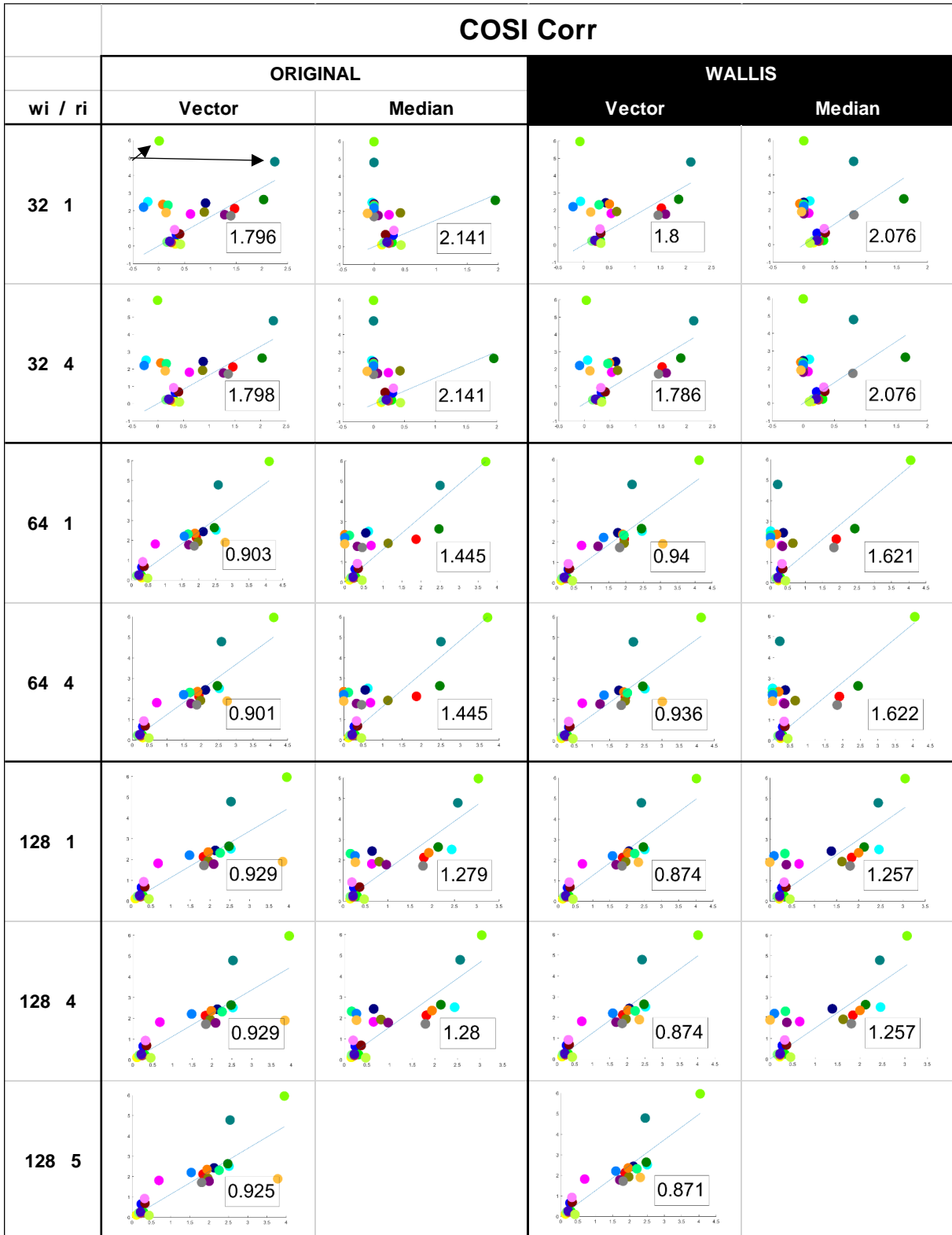
*Table 8: Overview of calculated linear regressions of the NS-EW-magnitude for selected runs with FFT using the closest 12 DIC points, with GNSS resultant on the y axis and the pixel offset resultant on the x axis in [m]. The colored dots represent the 23 measurement points, where data from both methods has been directly compared. Respective RMSE in [m] is noted within its subplot, potential outliers marked with black arrows, GNSS point ID 11 in dark green, point ID 17 in light green.*

| | FFT | | | |
|---|---|---|---|---|
| | ORIGINAL | | WALLIS | |
| wi / os | Vector | Median | Vector | Median |
| 32  1 | 1.141 | 1.061 | 1.003 | 1.014 |
| 32  4 | 1.136 | 1.057 | 0.994 | 1.022 |
| 64  1 | 1.007 | 1.017 | 0.986 | 1.005 |
| 64  4 | 0.996 | 0.996 | 0.971 | 0.996 |
| 128  1 | 1.033 | 1.035 | 0.982 | 1.016 |
| 128  4 | 1.005 | 1.024 | 0.969 | 1.001 |
| 128  8 | 1.011 | | 0.972 | |
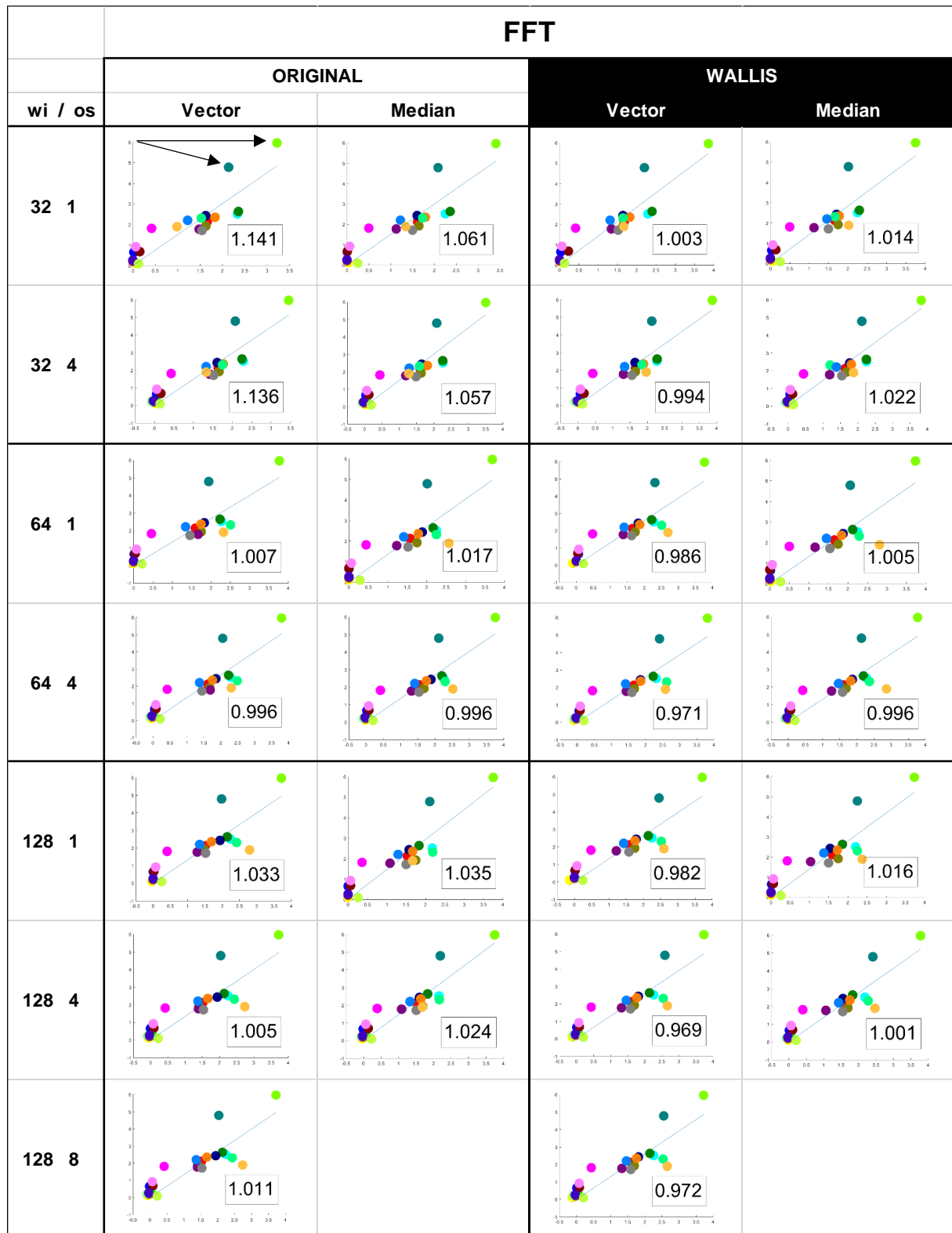
By plotting the derived RMSE values for each measurement point side by side, figure 20 has been retrieved. The black bars represent the GNSS deformation in meters, the white ones the DIC displacement. The x axis lists the IDs of all 23 points from left to right. The NS component plot indicates a deformation to the South with the bar being larger than zero and a movement to the North with the bar going below zero; the EW component plot is shown in the supplementary information section (S 7).
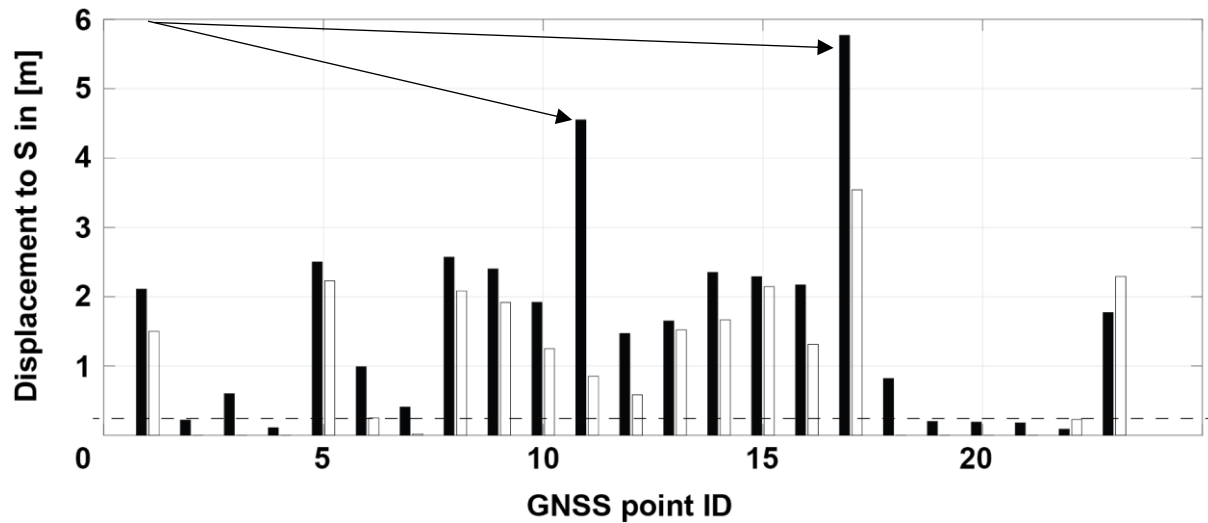


*Figure 20: Bar chart comparison of measured displacement towards South at all 23 points in [m] with GNSS in black and an exemplary DIC run with FFT wi 64 pixels and vector filtering in white. The dashed line represents the apparent minimum sensitivity of FFT with this particular window size. Black arrows indicate the potential outliers.*

Finally, tables 9 and 10 contain a selection of the quantitative comparison between all three algorithms using varying input parameters, with the original input image on its left side and the Wallis image on the right side. Displayed numbers are in meters and RMSE as well as StD results for all applied post-processing methods are listed. As described before, COSI Corr uses *ri* instead of *os*:

Table 9: Overview of the quantitative comparison between all algorithms using varying input parameters; original input image on the left side, Wallis image on the right side. Displayed RMSE values are in [m].

| Setup | wi | os / ri | Filter | RMSE mag | StD mag | wi | os / ri | Filter | RMSE mag | StD mag |
|---|---|---|---|---|---|---|---|---|---|---|
| COSI Corr | 32 | 1 | Median | 2.14 | 1.56 | 32 | 1 | Median | 2.08 | 1.48 |
|  |  |  | Vector | 1.80 | 1.42 |  |  | Vector | 1.80 | 1.42 |
|  |  | 4 | Median | 2.14 | 1.56 |  | 4 | Median | 2.08 | 1.48 |
|  |  |  | Vector | 1.80 | 1.42 |  |  | Vector | 1.79 | 1.40 |
|  | 64 | 1 | Median | 1.44 | 1.02 | 64 | 1 | Median | 1.62 | 1.23 |
|  |  |  | Vector | 0.90 | 0.82 |  |  | Vector | 0.94 | 0.85 |
|  |  | 4 | Median | 1.44 | 1.02 |  | 4 | Median | 1.62 | 1.23 |
|  |  |  | Vector | 0.90 | 0.82 |  |  | Vector | 0.94 | 0.85 |
|  | 128 | 1 | Median | 1.28 | 1.00 | 128 | 1 | Median | 1.26 | 1.01 |
|  |  |  | Vector | 0.93 | 0.87 |  |  | Vector | 0.87 | 0.78 |
|  |  | 4 | Median | 1.28 | 1.00 |  | 4 | Median | 1.26 | 1.01 |
|  |  |  | Vector | 0.93 | 0.87 |  |  | Vector | 0.87 | 0.78 |
|  |  | 5 | Vector | 0.93 | 0.86 |  | 5 | Vector | 0.87 | 0.78 |
| FFT (ORIGINAL) | 32 | 1 | Median | 1.06 | 0.82 | 32 | 1 | Median | 1.01 | 0.81 |
|  |  |  | Vector | 1.14 | 0.90 |  |  | Vector | 1.00 | 0.79 |
|  |  | 4 | Median | 1.06 | 0.82 |  | 4 | Median | 1.02 | 0.80 |
|  |  |  | Vector | 1.14 | 0.91 |  |  | Vector | 0.99 | 0.80 |
|  | 64 | 1 | Median | 1.02 | 0.82 | 64 | 1 | Median | 1.01 | 0.84 |
|  |  |  | Vector | 1.01 | 0.85 |  |  | Vector | 0.99 | 0.83 |
|  |  | 4 | Median | 1.00 | 0.81 |  | 4 | Median | 1.00 | 0.83 |
|  |  |  | Vector | 1.00 | 0.84 |  |  | Vector | 0.97 | 0.81 |
|  | 128 | 1 | Median | 1.04 | 0.78 | 128 | 1 | Median | 1.02 | 0.80 |
|  |  |  | Vector | 1.03 | 0.84 |  |  | Vector | 0.98 | 0.81 |
|  |  | 4 | Median | 1.02 | 0.78 |  | 4 | Median | 1.00 | 0.79 |
|  |  |  | Vector | 1.00 | 0.83 |  |  | Vector | 0.97 | 0.80 |
|  |  | 8 | Vector | 1.01 | 0.83 |  | 8 | Vector | 0.97 | 0.81 |
| NCC | 32 | 1 | Median | 1.12 | 0.94 | 32 | 1 | Median | 1.09 | 0.86 |
|  |  |  | Vector | 1.08 | 0.94 |  |  | Vector | 1.09 | 0.91 |
|  |  | 4 | Median | 1.11 | 0.86 |  | 4 | Median | 1.09 | 0.85 |
|  |  |  | Vector | 1.10 | 0.94 |  |  | Vector | 1.08 | 0.90 |
|  | 64 | 1 | Median | 1.09 | 0.86 | 64 | 1 | Median | 1.08 | 0.89 |
|  |  |  | Vector | 1.09 | 0.90 |  |  | Vector | 1.06 | 0.87 |
|  |  | 4 | Median | 1.09 | 0.86 |  | 4 | Median | 1.08 | 0.89 |
|  |  |  | Vector | 1.10 | 0.91 |  |  | Vector | 1.05 | 0.86 |
|  | 128 | 1 | Median | 1.16 | 1.06 | 128 | 1 | Median | 1.13 | 0.89 |
|  |  |  | Vector | 1.06 | 0.84 |  |  | Vector | 1.08 | 0.86 |
|  |  | 4 | Median | 1.03 | 0.80 |  | 4 | Median | 1.13 | 0.89 |
|  |  |  | Vector | 1.05 | 0.84 |  |  | Vector | 1.07 | 0.87 |
|  |  | 8 | Vector | 1.05 | 0.84 |  | 8 | Vector | 1.07 | 0.87 |

(Left side: ORIGINAL; Right side: WALLIS)

*Table 10: Addendum to the quantitative comparison between all algorithms using varying input parameters and mean and threshold filters; original input image on the left side, wallis image on the right side. Displayed RMSE and StD values are in [m].*

| Setup | wi | os / ri | Filter | RMSE mag | StD mag | wi | os / ri | Filter | RMSE mag | StD mag |
|---|---|---|---|---|---|---|---|---|---|---|
| COSI Corr | 32 | 1 | Mean | 2.19 | 1.55 | 32 | 1 | Mean | 2.16 | 1.50 |
| | | 1 | Thres | 1.90 | 1.41 | | 1 | Thres | 1.83 | 1.35 |
| | | 4 | Mean | 2.19 | 1.55 | | 4 | Mean | 2.16 | 1.50 |
| | | 4 | Thres | 1.91 | 1.42 | | 4 | Thres | 1.05 | 1.34 |
| | 64 | 1 | Mean | 1.65 | 1.16 | 64 | 1 | Mean | 1.70 | 1.26 |
| | | 1 | Thres | 1.05 | 0.87 | | 1 | Thres | 1.05 | 0.88 |
| | | 4 | Mean | 1.65 | 1.16 | | 4 | Mean | 1.70 | 1.26 |
| | | 4 | Thres | 1.05 | 0.87 | | 4 | Thres | 1.05 | 0.88 |
| | 128 | 1 | Mean | 1.32 | 0.99 | 128 | 1 | Mean | 1.34 | 1.04 |
| | | 1 | Thres | 0.80 | 0.74 | | 1 | Thres | 0.96 | 0.85 |
| | | 4 | Mean | 1.32 | 0.99 | | 4 | Mean | 1.34 | 1.04 |
| | | 4 | Thres | 0.80 | 0.74 | | 4 | Thres | 0.96 | 0.85 |
| FFT | 32 | 1 | Mean | 1.27 | 0.95 | 32 | 1 | Mean | 1.14 | 0.87 |
| | | 1 | Thres | 1.29 | 1.04 | | 1 | Thres | 1.25 | 0.98 |
| | | 4 | Mean | 1.30 | 0.97 | | 4 | Mean | 1.16 | 0.88 |
| | | 4 | Thres | 1.23 | 0.98 | | 4 | Thres | 1.30 | 1.02 |
| | 64 | 1 | Mean | 1.08 | 0.84 | 64 | 1 | Mean | 0.99 | 0.78 |
| | | 1 | Thres | 1.01 | 0.85 | | 1 | Thres | 1.12 | 0.93 |
| | | 4 | Mean | 1.08 | 0.85 | | 4 | Mean | 0.99 | 0.78 |
| | | 4 | Thres | 0.99 | 0.84 | | 4 | Thres | 1.06 | 0.88 |
| | 128 | 1 | Mean | 1.01 | 0.74 | 128 | 1 | Mean | 0.98 | 0.76 |
| | | 1 | Thres | 1.03 | 0.81 | | 1 | Thres | 1.03 | 0.90 |
| | | 4 | Mean | 1.01 | 0.74 | | 4 | Mean | 0.98 | 0.76 |
| | | 4 | Thres | 1.00 | 0.80 | | 4 | Thres | 1.02 | 0.90 |
| NCC | 32 | 1 | Mean | 1.24 | 0.94 | 32 | 1 | Mean | 1.19 | 0.93 |
| | | 1 | Raw | 1.30 | 1.32 | | 1 | Raw | 1.29 | 1.07 |
| | | 4 | Mean | 1.23 | 0.94 | | 4 | Mean | 1.16 | 0.95 |
| | | 4 | Raw | 1.28 | 1.24 | | 4 | Raw | 1.22 | 0.99 |
| | 64 | 1 | Mean | 1.00 | 1.00 | 64 | 1 | Mean | 1.12 | 1.02 |
| | | 1 | Raw | 1.77 | 1.79 | | 1 | Raw | 1.32 | 1.30 |
| | | 4 | Mean | 1.02 | 1.00 | | 4 | Mean | 1.15 | 1.04 |
| | | 4 | Raw | 1.70 | 1.71 | | 4 | Raw | 1.25 | 1.21 |
| | 128 | 1 | Mean | 1.64 | 1.62 | 128 | 1 | Mean | 1.08 | 0.82 |
| | | 1 | Raw | 4.93 | 4.34 | | 1 | Raw | 1.08 | 0.86 |
| | | 4 | Mean | 1.43 | 1.45 | | 4 | Mean | 1.10 | 0.91 |
| | | 4 | Raw | 4.43 | 3.99 | | 4 | Raw | 1.64 | 1.62 |

(Left side: ORIGINAL; right side: WALLIS)

## 3.5 Discussion

The interpolation of the GNSS magnitude reveals a certain trend of the deformation within the years 1999 and 2015. The plot indicates an area to the North, which shows a locally restricted, but strong deformation of more than 6 m. This local cell slightly extents towards the SW, but particularly towards the S and SE, showing gradual magnitude changes from about 2 to 4 m. It should be noted that the GNSS data only reveals a single hotspot with deformation magnitudes around 6 m in the upper part of the slope towards the North, in contrast to the results derived with DIC, which indicate two hotspots. Due to a lack of data and a boundary condition towards the borders of the AoI, the magnitude slowly drops to 0 radially, driven by the interpolation by gridfit. In any case, the interpolated magnitude map should be considered carefully, particularly close to the edges, as only 23 point measurements were extrapolated over a large area.

By plotting the DIC NS and EW components as in figure 13, similarities to the GNSS magnitude are recognizable. The major peak in deformation is marked in the North, with fringes extending towards the SE and W and SW. The measured peak displacement of around 4 m is much smaller than the one suggested by the GNSS data, however. Remarkably, the results indicate that the main displacement component is NS, whereas EW displacement is limited. Interestingly, the plot suggests a sharp ending of the slope instability towards the NE, striking NW - SE; this almost straight line cannot be straightforwardly identified with the naked eye in the morphology of CdV and is not specifically marked or mentioned in the detailed dissertation study by Amann (2006), although some smaller faults and open fissures mapped by Amann (2006) seem to strike in a similar way, just West of the cable car station on the outer Eastern rim of the input images (cf. S 1). This border of deformation strikes in a considerably different direction than all other mapped major discontinuities in the CdV AoI. The available aerial imagery suggests a scarcely visible feature striking the same way as observed in the DIC output (cf. S 5). Potentially, DIC could reveal a yet unknown displacement in this sub-part of the CdV DSGSD and a yet unidentified subsurface structure, such as a fault or a kakiritic band, which might express itself on the surface of the slope in the future. The framework of this project does not allow a further investigation of this phenomenon, but a more detailed examination would be an interesting topic for a future study.

Parts of the slope in the northern peak area as well as in the western displacement zone and in the southwestern gully area show an abrupt change in color from darker reddish to green; this indicates the effect of the used filter, a vector filter in this case, which removed these areas and marked them as zero, because it identified them as noisy. A reason for this initial noise level at these locations could be an influence by shadows causing mismatches, if one considers the master image for a direct comparison, or the occurrence of failure-related surface changes, such as gully activity in the SE. The offset information close to the edge is likely to be negatively influenced by correlation mismatches resp. search window interferences and is not credible. Generally, DIC appears to resolve slow to moderately fast and coherent deformations very well, but struggles to match non-systematic occurrences, such as rapid movements or failures.

Utilizing vectors to plot the DIC derived deformation resultant facilitates the visual interpretation of the measured displacement (figure 15). This visualization illustrates the complexity and the small-scale changes in magnitude and direction of slope processes, while enabling conclusions to be drawn about the genesis of the observed morphological features such as the back-scarps. The vectors of the resultant seem to always cross features orthogonally, which supports the explanation of scarps being formed by the DSGSD through tensional forces caused by toppling.

The detection of displacements by DIC in general seems to be facilitated by applying an appropriate pre-processing to the input data, as figure 16 suggests. The contrast enhanced image delivers better results with less noise, less mismatches and therefore a better spatial coverage of the deformation and less susceptibility to shadows. However, the recognition of the quality and quantity of the deformation seem to remain equal. Due to this, a pre-processing with the Wallis filter appears to be an effective measure to not only enhance the performance of all DIC codes in general, but to negate some of their disadvantages, such as the high susceptibility of the NCC algorithm to irregular contrast changes or of the FFT algorithm to changing illumination conditions. However, Wallis filtering does not have any positive influence on the matching quality of COSI Corr, for a yet unknown reason; the results are different, but none is distinctively better or worse.

Considering figures x, y and z, the assessed algorithms and input parameters can be investigated in terms of the quality of the returned NS deformation field. Besides the positive effect of pre-processing on the FFT and NCC codes, as well as its neutral to slightly negative influence on COSI Corr, the importance of the used search window size is apparent. For all codes, a larger window size delivers a smoother and less noisy spatial coverage, at the price of a poorer resolution of the deformation matrices. Larger window sizes seem to be favorable to detect unknown displacements at larger spatial scales, as they enable a better interpretation. The oversampling factor does not have any influence on the visual output from the DIC codes, for any of the assessed codes or input parameters. Generally, the FFT performs the lowest number of mismatches and therefore delivers the best coverage of the deformation fields, for all tested window sizes, which is particularly clear for smaller windows such as 32 by 32 pixels. NCC produces slightly poorer coverage, while COSI Corr's performance in smaller window sizes is very poor and does not allow further use of the output. This means that the results of this study do not implicitly agree with Heid and Kääb (2012), which state that frequency domain-based DIC codes achieve worse matching quality for small window sizes due to Heisenberg's uncertainty principle. This seems to be true for COSI Corr, but the FFT algorithm produces fewer mismatches than the spatial domain NCC code. If this assertion cannot be proven, the selection of DIC algorithms for specific tasks, such as e.g. detection of very small-scale deformations, which require small search windows, could be made more effective, as certain codes could be excluded at the start of investigations. In regards of computation time, figure 17 and table 5 show that COSI Corr operates in an order of seconds, FFT in an order of minutes and NCC in an order of hours. Although DIC processing time has no influence on the produced quality, faster codes could be preferred for large scale or global applications of DIC, where multitemporal image stacks are exploited.

Considering additional figures S T 2, S T 3, and S T 4 from the supplementary information section, the effect of the four different post-processing alternatives can be assessed. As shown by the data, the

threshold filter for the FFT is not able to completely remove noisy areas from the output images, in contrast to the other filters, which all completely denoise the results. In return, the threshold filter's or even raw outputs can also be considered as useful and enable alternative interpretations, e.g. an association of contained noise with vegetated areas, fast surface deformations or even failures. This cannot be done with filtered data, because the noise information is lost. The mean and median filters show a worse resolution of the deformation, as the matrices are smoothed resp. multi-looked; this has the advantage of a noise elimination and of an improved visualization, but reduces the expressivity of the entire output, because noise blurs into the true deformation, impeding robust interpretations due to the mixed state of signal and noise. Locally, the median filter even produces outputs which strongly resemble coherent areas of deformation only based on noise; using this filter for the detection of unknown displacements could therefore lead to erroneous interpretations of noise. The vector filter does not modify the data and effectively removes noise from the images. Based on the visual representation, no disadvantage of this filter can be perceived, other than the loss of the possibility of noise interpretation and a locally too coarse removal of noise for the results of the NCC and COSI Corr codes.

The NS-EW-resultant derived with DIC traces the GNSS magnitude interpolation very well; both agree on the major hotspot in the North, as well as with the fringing towards the SE, S and SW. However, the DIC code delivers a much smaller peak magnitude of only around 4 m, compared to the ~6 m of the GNSS, for an unknown reason. Still, the fringes show the same magnitude in both maps, more or less. Due to the nature of their generation, the DIC derived magnitude map has a significantly higher spatial resolution, which introduces noise in the SE, where very fast surface changes were occurring, resp. where the DIC code had trouble to match. Besides rapid changes, reasons for this locally poor correlation include decorrelation due to growing or moving vegetation, as it can be identified in the input images. Importantly, the DIC codes recognized an ongoing deformation in the West, which cannot be extracted from the GNSS data; as mentioned before, this part of the slope failed on March 14th, 2016 (Manconi et al., 2016).

By subtracting the interpolated GNSS magnitude- from the DIC magnitude a residual map was derived, showing the overall difference or the error of the DIC application. The visualization of this calculation supports the previous findings of the direct comparison: the DIC underestimates the northern peak deformations, while overestimating the displacements in the W and SE. However, the GNSS data are punctual, not spatial, and interpolation may introduce erroneous values. These overestimations in the W and SE are therefore no mistakes, but might lie in fact closer to reality than the GNSS interpolation. This is highlighted by the round artefacts from the subtraction in the SE and SW, where the interpolation is presumably quite poor due to a lack of data points and a boundary condition. Still, a large part of the residual map indicates a good match between DIC and GNSS, which are mainly parts with a slow to moderate speed of deformation. This result showcases the potential of DIC techniques to collect deformation data form large areas with relatively high accuracy.

Considering figure 19, conclusions about the basic differences between both orthoimages used can be drawn, i.e. the measured surface reflectivity. A black color suggests that the subtraction is almost perfect and that almost no change of reflectivity of this pixel occurred and no change of the surface. In turn, a white color represents a pixel, at which a significant change took place. While the vast majority of the

AoI is covered with darkish pixels, suggesting a high coherence of the image intensities, several of the observed white pixels can be directly related to observed changes, either in the DIC output or even with the naked eye in the images. In the NW, the shadows caused by different lighting conditions are marked by lighter pixels, just as numerous back-scarps or graben structures, which were moving significantly between the two acquisitions, are (cf. 13). Further, gully activity in the SE is indicated by a contour of whitish pixels, where the surface changed drastically due to erosion along the rim of the gully. Thus, image subtraction proposes that changes occurred, although no quantification of these processes is possible. Remarkably, the majority of the whitish areas in figure 19 can be, at least partially, related to noisy areas in the DIC results, as displayed by tables 2 to 4, probably because DIC algorithms struggle to process the large differences in the dynamic range domain. Thus, a quick input image subtraction with a smoothed thresholding binary mask prior to DIC could help in the identification of hard-to-match resp. noise susceptible areas; these insights could then be utilized to automatically adapt the DIC parameters at these locations by increasing the window size to facilitate the matching. This could be a step towards DIC codes, that autonomously optimize their search routines to adapt to the expected matching success, while enhancing performance and quality.

The calculation of RMSE and StD allows a quantitative comparison of all performed runs in terms of accuracy and precision. A visual representation of these results is shown in tables 6, 7, and 8, where a linear regression series was performed and plotted. Generally, the scatter of points is limited and the resulting shape is close to linear, indicating a good matching accuracy of the DIC codes in comparison to the GNSS data; however, there are two outliers throughout the dataset. These two points have the IDs 11 & 17 and significantly underestimate the true displacement with differences of up to 3.5 m and cause the relatively high RMSE of around 0.8 to 1.0 m, i.e. 3 to 4 pixels, which is worse than expected, considering the GSD of 0.25 m of the input images in combination with a subpixel co-registration. Hereby, point 11 adds the largest error. Ignoring the outliers, the global RMSE per run is around 0.50 m or less, i.e. two pixels, which is two times the assumed sensitivity limit of the applied technique. It has to be pointed out that although 23 GNSS points were used for the quantitative assessment, the accuracy and precision of all tested DIC codes was decreased by around 50% due to the two points, which are expected to be outliers. By considering tables 6 to 8, both outlying points 11 and 17 are situated almost systematically well outside a good matching location in almost each subplot for all codes. This fact further illustrates that the relatively poor RMSE derived with DIC is not caused by a noise influence, but mainly by two apparently poor correlation points. The sensitivity limit, suggested by figure 20, defines what minimum deformation is necessary for the DIC code to recognize a displacement at all. The data further suggests that COSI Corr is able to achieve a lower limit of sensitivity, reaching a level of subpixel detection. However, a better sensitivity does not improve the general accuracy of the measurements. The outlying GNSS measurement points are situated in the upper slope towards the North, where peak deformations occur (cf. figure 21). This underestimation of the deformation has also been observed in the comparison of the GNSS and DIC magnitude resp. their residual map.

Potentially, the DIC codes struggle to quantify too large deformations in a precise way, i.e. the accuracy of DIC measurements would drop with an increasing speed of deformation. Unfortunately, this hypothesis could not be tested within the frame of this thesis, but remains an interesting question for

further research. Still, there is the possibility for incorrect GNSS measurements at those positions. Potential operator or technical errors cannot be excluded. Nevertheless, the accuracy of the major part of the DIC derived deformation is in the order of one pixel or 25 cm compared to the GNSS deformation field, while offering a complete spatial coverage of the AoI, instead of only point measurements.
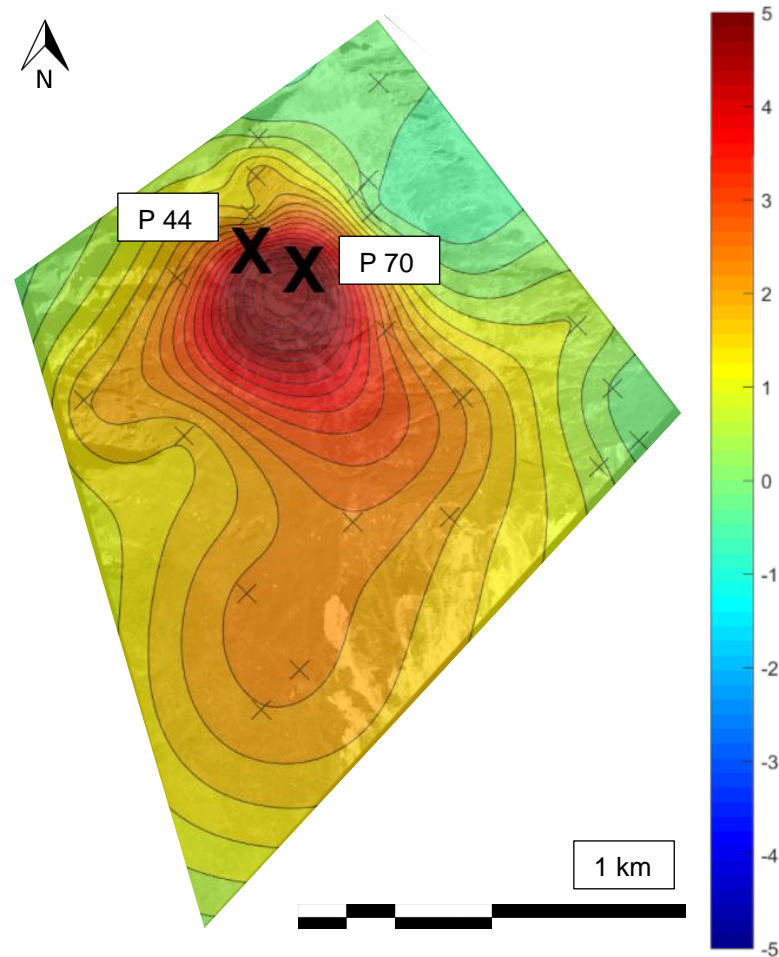


*Figure 21: Interpolated GNSS deformation magnitude map, identifying outliers (points 44 and 70, i.e. IDs 11 & 17 in figure 20). Scale for the GNSS magnitude is in [m].*

The exact performance of each code in combination with certain parameters can be retrieved from table 9 and 10. Due the current ambiguity about their origin, both outliers have been considered throughout the quantitative analysis and comparison, but theoretical results without their consideration are presented in brackets () as well. The FFT code provided the best global accuracy and precision with the lowest RMSE average of 1.06 m (0.54 m) and the lowest mean StD of 0.84 m (0.38 m). In addition, the stability of the RMSE and StD is remarkably high, i.e. FFT will deliver results with a low RMSE relatively independent from the used input parameters. The data show that the application of a Wallis filter further enhanced the mean accuracy and precision of the FFT code by smoothing. This means that with a Wallis filter, the achieved RMSE and StD are slightly lower, where a measurement without pre-processing delivered poor accuracy, but also higher, where increased accuracy was achieved. Still, the absolute accuracy is slightly better with a Wallis filter with a mean RMSE of 1.04 m (0.53 m), compared to 1.07 m (0.56 m) without pre-processing, i.e. an improvement of ~4 %. Therefore, a Wallis filter seems to increase the stability and reliability of the DIC measurements. For FFT, a window size of 128 pixels

delivered the lowest RMSE and StD values of 1.01 m (0.52 m) and 0.80 m (0.37 m) on average. Further, oversampling only increased the accuracy by 0.01 m, i.e. 0.1 %, but raised the computation time by a factor of 4. While this time is < 5 minutes without oversampling and for medium window sizes using the 30 MB CdV input images, it increases to > 20 minutes when oversampling is applied. Table 10 further shows that post-processing with the mean filter achieved a mean RMSE of 1.04 m, with the median filter of 1.02 m, with the threshold filter of 1.11 m and with the vector filter of 1.02 m. As a consequence, for maximum performance a FFT code should be used with a Wallis filtered input image, a window size of 128 by 128 pixels, no oversampling and a vector or median filter.

The NCC algorithm achieved RMSE values of 1.33 m (0.65 m) on average and a mean StD of 1.15 m (0.45 m). The stability of the derived RMSE. i.e. the accuracy, is also relatively high, but not as distinct as for the FFT code. Remarkably, the application of Wallis improves the average RMSE by ~23 % from 1.50 (0.66) to 1.15 m (0.59 m), by removing the occurrence of single, outlying, particularly poor measurements, but also generally. Pre-processing thus significantly enhances the performance of the NCC code, which confirms the intention of using the dynamic contrast enhancement procedure to counter some of the limiting properties of a NCC code. A window size of 32 by 32 pixels achieved the best mean RMSE and StD values of 1.16 m (0.60 m) and 1.05 m (0.44 m), with 64 by 64 pixel windows performing almost equally. Remarkably, NCC algorithms achieve the highest accuracy with smaller window sizes, in contrast to the frequency-domain-based FFT and COSI Corr codes, which perform best with larger search windows. The application of oversampling improved the mean RMSE by 0.02 m, or by 1.5 %, but increased the processing time. Remarkably, the computation time of NCC is very poor even without oversampling, as the 30 MB CdV images require < 60 minutes for medium window sizes, while an application of oversampling increases this number to > 2 hours or more. The computation time could be optimized by more effective programming and parallel computation, within certain limits. The table indicates that filtering with a mean filter delivered a mean RMSE of 1.20 m, with a median filter of 1.10 m, without any filter of 1.93 m and with a vector filter of 1.08 m. Hence, NCC should be used with a Wallis-filtered input image, a window size of 32 by 32 pixels, no oversampling and a vector or median filter, to achieve the best results.

COSI Corr performed poorest with a mean RMSE of 1.46 m (0.70 m) and a poor StD of 1.13 m (0.57 m) on average. Its overall derived RMSE values are relatively stable, similar to the ones produced with the NCC code. Interestingly, a Wallis-filtered input image raises the mean RMSE by ~1.5 % from 1.45 (0.69) to 1.47 m (0.70 m). Unlike the NCC and the FFT, pre-processing does not enhance the results of the DIC. With a mean RMSE of 1.09 m (0.45 m) and a mean StD of 0.91 m (0.40 m), a window of 128 pixels performed best and 45 % better than a window of 32 pixels. This illustrates that COSI Corr has to be utilized in combination with larger window sizes, as spatial coverage quality, accuracy and precision are significantly reduced for small search windows. As the COSI Corr graphical user interface (GUI) does not allow manual setup of the oversampling factor, its effects on the accuracy of the matching could not be assessed. However, the robustness iterations were altered, but this did not have a significant effect on the accuracy or the precision of the DIC. COSI Corr has a prompt processing time of <1 minute for the 30 MB CdV input, which is by far the shortest and potentially enables the processing of much larger data sets, e.g. images with a better resolution, in the same time. By using a mean filter, an average

RMSE of 1.73 m was derived, while a median filter produced a mean RMSE of 1.64 m, a threshold filter of 1.26 m and a vector filter of 1.21 m. Thus, for peak performance, COSI Corr, should be used without pre-processing, a large window size such as 128 by 128 pixels and a vector or median filter. Additional data from the NCC and FFT codes suggests that there are diminishing returns in improvement regarding a further increase of the *os* factor to 8, i.e. an increase in the oversampling of more than 4 does not further enhance the accuracy or precision of the DIC. Similarly, by applying a more robust iteration with a factor of 5 for COSI Corr, the accuracy resp. precision are only occasionally and slightly improved, in the order of half a centimeter. It has to be noted that besides its particularly negative influence on the computation time of the FFT code and even COSI Corr, oversampling of 8 in combination with the NCC algorithm demands a significantly increased processing time of > 10 hours for the 30 MB CdV images. Quantitative accuracy is important to measure a deformation, but good coverage of the AoI is decisive as well, especially for the detection and interpretation of unknown processes, like on Mars or a remote place on Earth. As a consequence, none of the codes should be used with a window size of 32 pixels at first, because the SNR does not allow a good and reliable coverage, at least for input images with a GSD of 0.25 m. As a window size of 128 pixels does not perform more poorly in a quantitative sense, there is no disadvantage. However, a medium size such as 64 pixels could help to detect small-scale deformations, like rockfalls. If only one larger correlation cell covers and indicates such a feature, it would be removed as noise – if the correlation cells are smaller, more of them will cover and indicate deformation, which will increase the likelihood of their detection as well as inhibit their removal due to the increased coherence.

Ayoub et al. (2015) recommend choosing a window with a size of at least twice the expected deformation magnitude. Using the CdV GNSS peak deformation of 6 m equal to 24 pixels as an example, the window size should be at least 48 pixels wide, which appears to be confirmed by the CdV results, where 64 by 64 pixels performed significantly better than 32 by 32 pixels windows. Moreover, this study's results suggests that the window size should rather be selected according to this modified formula

$$wi \, [pixel] \geq 5 * expected \, deformation \, [pixel] \qquad (3.5-1)$$

to maximize qualitative and quantitative accuracy as well as to optimize spatial coverage. Further, the derived DIC sensitivity of around one pixel of the NCC and FFT codes and a slightly lower one for COSI Corr suggests that even with the application of sub-pixel co-registration and sub-pixel DIC codes the recognition of very slow deformation is limited by the spatial resolution of the applied imagery. This lower threshold could be written as

$$detectable \, deformation \, [m] \left(t_{0-1}, v_{Def}\right) \geq GSD \, [m] \qquad (3.5-2)$$

while the detectable deformation is subject to the time passed *t* between the two used acquisitions resp. their deformation velocity. This formula suggests that sensors with a poorer spatial resolution cannot resolve slow displacements, resp. that they need a larger difference in time between the acquisitions to detect a slow displacement. Cameras with a smaller GSD need less time difference to detect the same change. It is important to note that in theory sensors with large GSDs are capable of detecting the same deformations as cameras with small GSDs, if the temporal baseline is sufficiently long. Yet, cameras with a large GSD will struggle to identify displacements with a spatial footprint smaller than their spatial

resolution, independent of the magnitude of the deformation. The recommendation for window size by Ayoub et al. (2015) as well as the modification on behalf of the author still requires at least an estimate of the scale and magnitude of the expected deformation. This estimate might be difficult or impossible to derive, particularly if unknown processes with unknown kinematics and velocities on foreign planets or planetary bodies without a possibility of ground truthing are targeted. As observed deformation might be non-linear or only active under certain conditions, an application of DIC can be further exacerbated, because the used input imagery must have a sufficient temporal baseline, which covers actual deformation with, at the same time, a potentially detectable speed of displacement. Therefore, the use of different sensors with varying GSDs as well as the application of input data with a maximum temporal baseline in combination with differing search window sizes, starting from the recommendations given by the discussed formulas, is proposed for a comprehensive exploration of unknown surface processes. As one of the assessed DIC codes had to be applied in such subject areas on Mars, the most reliable and robust code and parameters had to be selected, to assure a reliable analysis of the findings. Due to its particularly good coverage with all tested window sizes and its stable quantitative accuracy and precision, the FFT code in combination with Wallis-filtered images and larger window sizes was selected as the first choice for this task. The implementation of a Wallis pre-filtering is hereby recommended for any application and environment, if the FFT or NCC algorithm is applied; COSI Corr should operate on non-processed images to achieve its best performance. No oversampling should be used and post-processing should be conservative, using raw and vector filtered outputs for the result exploitation. The rapid computation time is another critical property, as the exploration of a foreign planetary surface requires the processing of large amounts of data.

In summary, the potential and aptitude of DIC codes to detect and measure slope and surface displacements has been positively assessed and the gained knowledge about DIC performance enables a novel application in remote places without access or the possibility of ground truthing, such as on planet Mars. Table 11 summarizes the identified DIC input parameters to achieve the highest accuracy and precision, as they were used for the exploration of Mars.

*Table 11: Summary of all findings of the CdV DIC assessment.*

|  |  | NCC | COSI Corr | FFT |
|---|---|---|---|---|
| **Pre-processing** | **sp** | 4 | Default | 1 |
|  | **co_os** | 1 | Default | 1 |
|  | **Wallis** | Yes | No | Yes |
| **DIC** | **wi** | $wi\,[pixel] \geq 5 * expected\ deformation\,[pixel]$ | | |
|  | **os / ri** | 1 | 1 | 1 |
| **Post-processing** | **Best accuracy** | Vector | Vector | Vector |
|  | **Best coverage** | Median | Median | Median |

# 4. DEPLOYMENT AND VALIDATION ON MARS

According to the main intention of this thesis, validated DIC codes were applied on Mars to investigate whether Earth's neighboring planet is host to dynamic slope or surface changes other than moving sand and dust devils.

## 4.1 Planet Mars

Mars is the outermost rocky planet in our solar system with a mean distance of around 228 million km to the Sun and around 78 million km to Earth. At the same time, the red planet's orbit has a high eccentricity of 0.0935, which is 5.6 times the eccentricity of Earth's orbit, meaning that the average distances are subject to significant changes over time. This is relevant for missions to Mars, as propellant for carrier systems is limited and distance in combination with time is a vital parameter. Due to orbital properties such as the obliquity, the length of a day on Mars is almost the same as on Earth, but the orbit around the sun takes more time, which results in a Martian year with roughly twice as many days as on Earth. This has to be considered, when analyzing data from Mars, as annual measurements will only be available in a two-Earth-year interval (Mars Fact Sheet, n.d.).

As its mass is only 10 % of Earth's, the gravitational acceleration amounts to only 3.69 m/s$^2$, i.e. ~ 38 % of what we are used to (Mars Fact Sheet, 2017). Presumably, this will affect the mode and velocity of surface and particularly slope deformations. The seasonal presence of liquid water and ice in the shallow subsurface or even on the surface of slopes facing the sun has been discovered and investigated by McEwen et al. (2014) and others, and could also have an influence on slope stabilities, as on Earth. Dynamic surface processes already discovered on Mars include moving dune fields (Bridges et al., 2012), dust devils or dust whirls (Whelley & Greeley, 2008), and so-called frost avalanches, released from steep cliffs at the North polar layered deposits (NASA, 2015). DIC could reveal that Mars's surface is active in ways, that have not yet been considered or detected. As Mars does not have any recent oceans, its datum or "sea level" has been re-defined by Smith et al. (2001) as the equipotential surface whose average value at the equator is equal to the mean radius as determined by MOLA (Mars Orbiter Laser Altimeter). The term mbmd therefore means meters below Mars datum, while the datum is zero elevation.

Mars's geologic history is divided into four different periods, the Pre-Noachian > ~ 4 Ga ago, the Noachian between ~ 4 and 3.7 Ga, the Hesperian from ~ 3.7 to 3 Ga and the Amazonian, until present (cf. figure 22). The main characteristics of the Pre-Noachian were the existence of a planetary magnetic field as well as the formation of large impact basins. The Noachian was dominated by high cratering and erosion rates as well as valley formation, while so called warm and wet conditions were met occasionally (Carr & Head, 2010). During the Hesperian, volcanic activity occurred with a relatively high average rate as well as water flood events, both altering the surface by processes such as canyon erosion. The

Amazonian featured a deceleration of all geologic processes and reshaping of the surface was only driven by canyon landslides and occasional small flood events. Most prominent, the Amazonian period led to the accumulation of ice, including the polar layered deposits and other features such as lobate debris aprons, gully erosion and Glacier Like Features (GLFs) (Carr & Head, 2010). Such GLFs are water or dry ice-dust mixtures presumably similar to terrestrial valley glaciers, which show signs of viscous downhill deformation as well as an expanded former extent. Their ice motion behavior could only be estimated, with values of around 7.5 mm per year. It remains unclear whether GLFs are currently moving (Hubbard et al., 2014). As volcanic activity dropped significantly since the Hesperian period, it is likewise uncertain, whether tectonic activity is still ongoing on Mars. Carr and Head (2010) propose that volcanism has been limited to the Tharsis and Elysium Montes provinces during the Amazonian. Both, GLFs and Tharsis or Elysium volcanoes, would be particularly interesting targets for a DIC investigation, potentially revealing recent deformation.
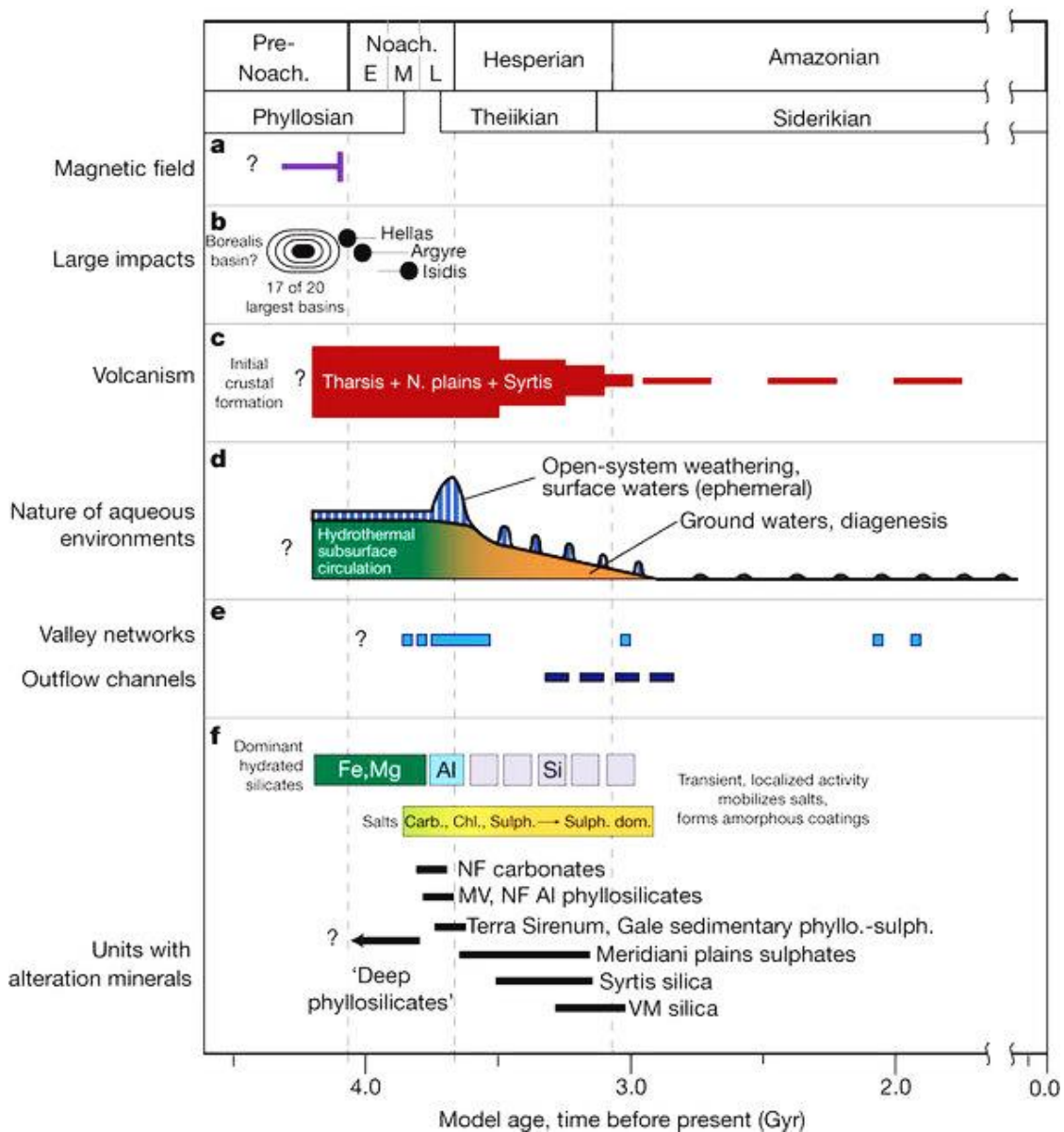


*Figure 22: Geological history of Mars from left to right, with remarkable events in different categories such as magnetic field, impacts, etc. (Ehlmann et al., 2011).*

## 4.2 Available data

Thanks to the latest planetary exploration missions such as those by the National Aeronautics and Space Administration (NASA) and the European Space Agency (ESA) to planet Mars, there is a large database of optical, radar and multispectral imagery which can be used for change detection analyses. The involved instruments are carried by two satellites, NASA's Mars Reconnaissance Orbiter (MRO) and ESA's Mars Express (MEX). MRO was launched on August 12th, 2005 and arrived in Martian orbit on March 10th, 2006. The mission's science phase started in the same year and is still ongoing (MRO, n.d.). Four of MRO's sensors are interesting as sources for either DIC input images or as interpretation support data: HiRISE, CTX, CRISM, and SHARAD.

The High Resolution Imaging Science Experiment (HiRISE) is a Charged Coupled Device (CCD) camera which operates in the visible and infrared (IR) wavelength range but with a telescopic lens, offering a red, a green-blue as well as an IR channel. The resolution of the acquired images reaches a pixel size of < 30 cm, which enables the recognition of very small surface objects with a size greater than ~ 1 m (MRO, n.d.). The Field of View (FOV) is very narrow with 1.14° x 0.18° and the swath width, i.e. the footprint of the image on the surface, is around 6 km wide and varies in length. Selected raw HiRISE acquisitions are semi-regularly processed by NASA and other institutions to Digital Elevation Models (DEMs) and map-projected orthoimages, which can be directly used for import into DIC codes, resp. pre-processing algorithms. About 400 DEMs with an extent of around 40 square kilometers each have been produced so far, severely limiting the possible area of exploration (HiRISE, n.d.). The Context Camera (CTX) is another CCD linescan camera which obtains greyscale images with a GSD of 6 m per pixel over a 30 km wide swath in a 6° FOV. CTX acquisitions are taken simultaneously with the HiRISE and CRISM sensors to facilitate an integration of the different scenes in a greater context. NASA does not offer any processed CTX data, which means that it must be produced prior to application for DIC (MRO, n.d.).

CRISM, or Compact Reconnaissance Imaging Spectrometer for Mars, delivers hyperspectral image information with resolutions ranging from 18 m to 200 m per pixel and an acquisition width of about 11 km, using a field of view of 2.06°. The possible spectral resolution ranges from 362 to 3920 nm, covering the IR and VNIR (visible near infrared) parts of the spectrum. CRISM outputs can be used to investigate the occurrence of specific minerals such as oxidized iron minerals or carbon hydroxide ice as well as their spatial distribution (MRO, n.d.) (JHUAPL, n.d.). The Shallow Subsurface Radar (SHARAD) images the distribution of Martian subsurface structures and ice bodies down to depths of 1 km, depending on the di-electric properties of the encountered soil or rock. By using a frequency of 15 to 25 MHz, SHARAD achieves a free-space horizontal resolution between 300 to 3000 m and a vertical resolution of 15 m – this improves to 10 m in the ground (MRO, n.d.). All MRO data can be browsed using the JMars software by Arizona State University's (ASU) Mars Space Flight Facility, which also provides direct links to NASA's and other's download pages for each desired product (Christensen et al., 2009). These pages are the HiRISE main site (HiRISE, n.d.) for HiRISE data and the ASU's Image Explorer (Image Explorer, n.d.) for CTX, CRISM and SHARAD data.

MEX was launched with a Soyuz rocket from Baikonur on June 2nd , 2003 as a joint mission by ESA and NASA. The mission's science phase started in 2003 as well and is continuing today. One sensor of MEX's payload is of particular interest for this thesis, the High Resolution Stereo Camera (HRSC). This stereoscopic and multispectral CCD camera was constructed by the German Aerospace Center (DLR) and images with 5 panchromatic and 4 narrow-band color channels, RGB as well as NIR. The swath width is around 52 km and the GSD is at 12.5 m per pixel, although this can decrease to 2 – 3 m per pixel in super resolution mode. The array of the 9 different CCD lines allows the derivation of a 3D surface on a single pass (along-track) and without rotation of the spacecraft, as the lines differ in pointing direction and incidence angle (HRSC DLR, n.d.) (JPL, n.d.). Numerous HRSC acquisitions are regularly processed from their raw state to level 4, which are orthorectified and map-projected images, sufficient to serve as DIC input. The Freie Universität Berlin Planetary Science Department offers a platform called HRSC Orbit Location Extractor, where available images can be viewed and downloaded (HRSC OLE, n.d.). Table 12 summarizes all instruments of interest, while figures 23 and 24 illustrate the effect of swath width and GSD.

*Table 12: Overview of all used sensors and their most important properties.*

|              | HiRISE | CTX | CRISM    | SHARAD        | HRSC     |
|--------------|--------|-----|----------|---------------|----------|
| **Type**     | CAM    | CAM | CAM      | RADAR         | CAM      |
| **GSD [m/pix]** | 0.25 | 6   | 18 - 200 | (300 – 3000)  | 2 – 12.5 |
| **Swath [km]** | 6    | 30  | 11       | /             | 52       |
| **Bands**    | 3      | 1   | up to 543| /             | 9        |
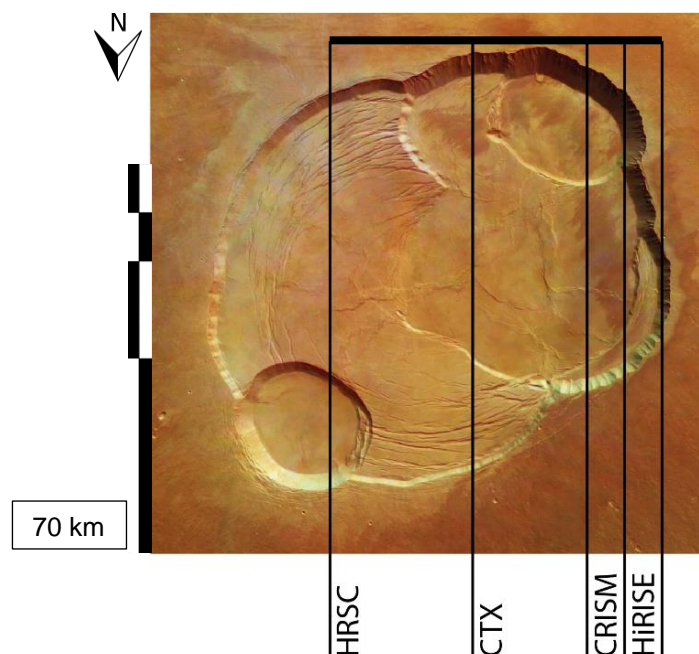


*Figure 23: Different swath widths of used sensors plotted for comparison. While the width (here left – right) is limited by the camera, the length (up – down) is only limited by the satellites' data processing & transmission capabilities. The background shows the caldera of Olympus Mons on Mars - the largest known volcano in the solar system - with a diameter of ~ 70 km (raw data from Image Explorer, n.d.).*
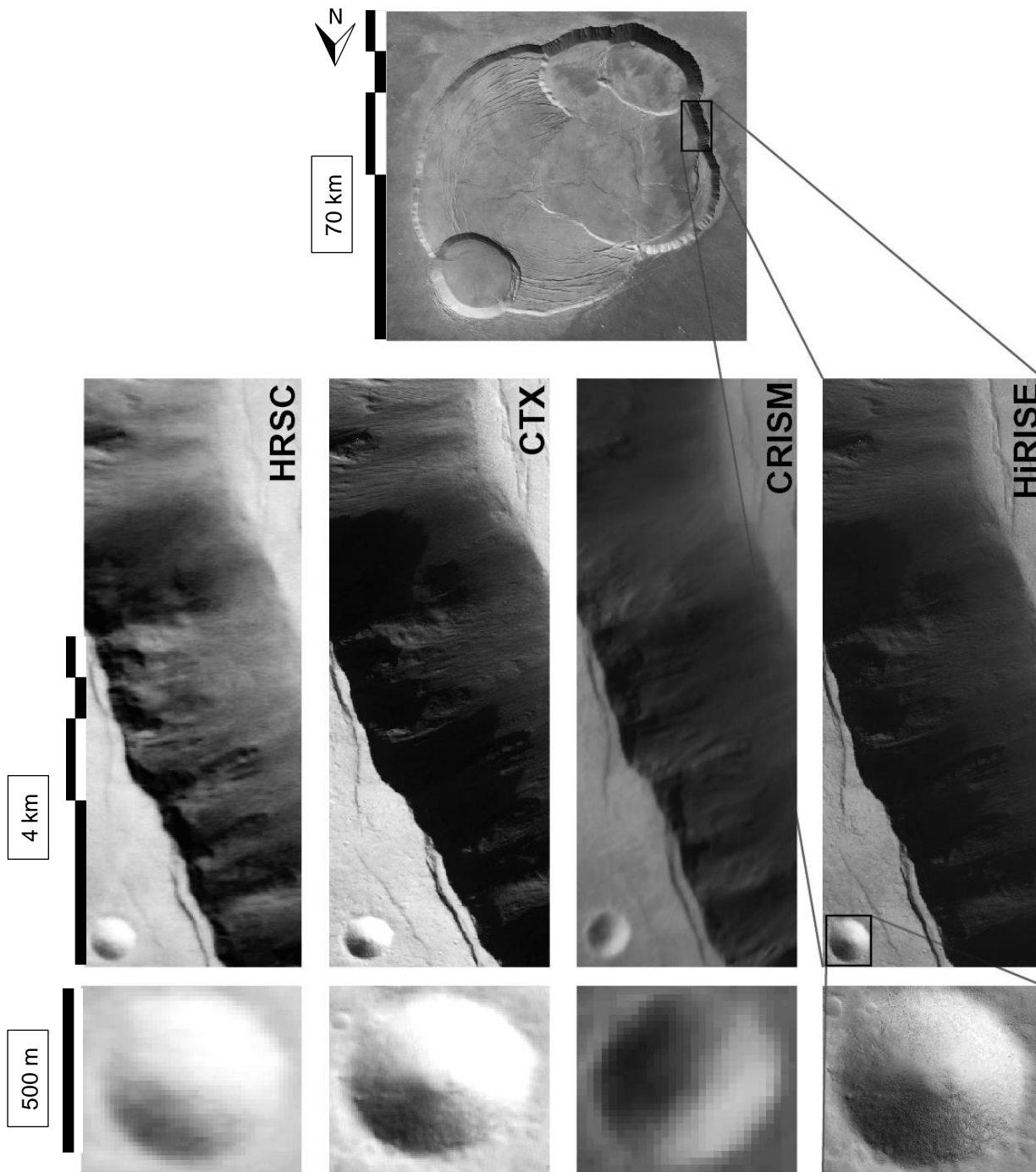
*Figure 24: Illustration of the GSD of each sensor for different zoom levels. Targeted cliff and the unnamed crater are situated in the Western Olympus Mons caldera (raw data from HiRISE, n.d., HRSC OLE, n.d. & Image Explorer, n.d.).*

Besides the instrument parameters, the availability of data for AoIs on the Martian surface is decisive for an appropriate selection of instruments. High temporal resolution, as well as adequate spatial resolution, are vital for change detection. This means, that images from the same AoI from different points in time are required. However, frequent observations of the same area contradict the basic intention of space probes to image and measure the entire surface of a planet, i.e. monitoring of specific areas on the ground is only performed, if these areas are of a major scientific interest. The general approach by Space Agencies is therefore to use low resolution images with larger swaths for global mapping and high-resolution acquisitions with smaller swaths for detailed studies. However, as the

footprint of sensors as HiRISE is too small, global coverage is not possible, which is why this instrument is only used for single, manually selected targets. Following this idea, NASA uses HiRISE to frequently re-visit specific AoIs on Mars's surface to observe ongoing processes, such as dune migration or Reoccurring Slope Lineae (RSLs). In contrast, HRSC aims for global coverage, which makes it difficult to find overlapping images, that can be used for DIC, as more overlap means less total coverage and is therefore minimized by the operators.

Further, the scale of the expected deformation is important, as the GSD of the used input images determines the degree of detail recognizable on the surface. With a resolution of 12.5 m per pixel, rockfall events won't be detectable, but with a GSD of 0.25 m and a small footprint on the ground large scale processes such as tectonics cannot be resolved in turn, simply because the entire image might be shifting continuously, which cannot be measured by DIC or will be interpreted as noise. A comprehensive exploration of Mars's unknown surface processes needs to contain multi-temporal input data sets from different sensors with varying GSDs and swath widths over the maximum possible timeframe in order to achieve valuable results. Data from instruments such as CRISM and SHARAD can then be used to support subsequent interpretations by allowing insights into the mineralogy and subsurface of the identified AoIs.

## 4.3 Investigation plan

The application of DIC codes to identify and measure potential slope and surface deformations on Mars has been implemented in two separate phases. First, already available and suitable data of potentially interesting sites on the ground was collected and used for a superficial and immediate analysis. Phase two was based on the preliminary findings and targeted exclusively previously detected and promising AoIs for a detailed study. The second stage also included processing of remote sensing raw data to improve the spatial and temporal resolution of the already existing datasets.

Stage one served multiple purposes: First, a preliminary exploration should clarify whether the DIC codes in combination with their determined optimum settings produce results of sufficient quality when using other input imagery, such as HiRISE and HRSC, and if they generally suffer from specific artefacts or noise. Further, the first phase should provide additional validation for the operability of DIC codes by an observation and survey of already proven and very fast surface processes on Mars such as moving dune fields, i.e. if the codes correctly identify those movements. On the other hand, verification that the DIC algorithms do not suggest any deformation in places, where presumably no displacements occurred, should be completed. In a best case, this would be proven with an image containing both a rapid deformation, such as a dune, and a static feature close by, such as a solid rock surface in an area without any relief, to enable a direct comparison. Subsequently, the investigation should show that all three DIC codes deliver the same results, which would finally validate their effectiveness for the research intention of this study. Finally, the preliminary exploration aimed to exploit the existing databases in order to derive the availability, spatial distribution, scale and magnitude of potentially occurring deformations on Mars. Based on this, future targets were prioritized, which were subject of phase two,

the detailed investigation of selected AoIs. In order to fulfill the intentions, preliminary exploration targets were selected and assigned to four different categories, aerial processes, slope processes, tectonic processes, and seasonal processes. As mentioned before, the availability of the high-quality products, which are required for DIC, such as DEMs and orthoimages, is limited and heavily influenced the selection of targets on the ground. Care has been taken to spread the campaign as evenly as possible over the entire planet. As only existing datasets were exploited during the first phase, only HiRISE and HRSC data was utilized. AoIs were selected based on a geological and geomorphological examination by the author using DEMs and greyscale images, which considered the expected scale and magnitude, as well as the type of potential displacement. In addition, preference was given to AoIs with high relief, fresh-looking scarps or surfaces. Analogous sites with almost identical settings were only processed for one chosen area to save processing time and as the observable mechanisms were expected to be very similar.

As explained above, dunes resp. aeolian processes were selected to further validate the DIC codes in direct comparison to work by Bridges et al. (2012) and Ayoub et al. (2014). Their work found evidence of dune migration rates on Mars e.g. with mean fluxes of 6.9 cubic meters per year and velocities of up to ~1 m per Earth year, both depending on the dune height, using COSI Corr. In addition to their research, which focused on dunes in Nili Patera; the targets of the study on hand investigated dune field migration in other areas to produce results with a certain spatial distribution on the surface of Mars. Further, this study used also NCC and FFT codes as well as an image subtraction method for dune migration detection, which enables a direct comparison of the results of Bridges et al. (2012) and Ayoub et al. (2014) with this study's conclusion using COSI Corr as well as two other DIC tools. Therefore, 3 AoIs for aeolian processes were investigated. A preliminary application of DIC in slope areas was meant to show whether the image processing applied by NASA, ESA, DLR and other institutions is capable of completely removing the distortions introduced by surface curvature during the orthorectification of HiRISE and HRSC acquisitions in steep terrain. Any imperfection during the challenging orthorectification, i.e. an imperfect subtraction of the original image's incidence angle, would amplify in the presence of distinctive topography during the map-projection and would cause artefacts during the DIC, which could potentially be misinterpreted as deformation. Therefore, a DIC indicating overall stable conditions without any noise or artefacts in hilly terrain would suggest sufficiently precise processing. Most importantly, the preliminary investigation was expected to point out whether slope processes are occurring on Mars, to what extent and in which locations. In total, 49 AoIs were processed.

Seasonal processes were investigated in a low relief area called Inca City close to Mars's South Pole. This location is the target of an ample monitoring campaign by HiRISE, as changes in season have distinctive effects there, such as blotches, opening cracks and fans, which form as the sun is heating up the subsurface ice and is thus creating gas pressure from underneath (HIRISE IC5, n.d.). The intention was to potentially identify horizontal deformations with DIC in this area. In total, 8 AoIs for seasonal processes were investigated. Even if high-resolution imagery such as HiRISE is not the best choice for detecting tectonic deformations due to its small footprint, some interesting areas with troughs and open cracks were investigated with DIC methods. The aim was to show whether the available temporal baseline in combination with the imagery could be sufficient to detect tectonic activity. The use of HRSC

data could have been more promising, but is impeded by the fact that almost no overlapping, orthorectified HRSC acquisitions exist. Given this, 16 AoIs were examined. Overall, a total of 76 AoIs were studied, which accounts for ~ 19 % of the maximum possible amount, using only pre-produced NASA orthoimages. The relatively small percentage reflects the effort to process similar geomorphological settings only once to save operating and computation time. Still, processing of all data for phase one demanded a computation effort of around 60 hours, excluding the required operator time. The workflow for phase one followed the identical pipeline as the CdV case study (cf. figure 9), but additionally applied the previously gained experiences. At first, appropriate input images were identified, i.e. acquisitions covering the AoI and with a maximum possible temporal baseline. These images were downloaded in a re-sampled version to optimize data size and processing speed, generally with a GSD of 0.75 to 1.0 m per pixel for HiRISE and 12.5 m per pixel for HRSC images. Subsequently, Wallis filtering as well as a sub-pixel co-registration was applied, before the data was processed with the FFT algorithm, using the determined optimum settings. Large and small window sizes were used successively to guarantee a detection of features with unknown spatial scales. Post-processing was very conservative, i.e. with no or a vector filter, to avoid missing actual deformation information and to not introduce fake displacements by running modifying filters. In the case of potential change detection, full resolution imagery was used to perform a visual investigation of the respective site. If positive, the ground truthing triggered a second run with the FFT code with the same pipeline and parameters as before, but with the full resolution orthoimages, i.e. 0.25 m per pixel for HiRISE. This significantly increased the required computation time, but delivered more precise and reliable results, especially for small-scale deformation processes. For HRSC, only the standard resolution of 12.5 m per pixel was applied, as no other pre-processed GSDs are available.

## 4.4 Results

To provide an overview, all targeted sites are marked on a MOLA elevation map of Mars in figure 25, aeolian processes in red, slope in blue, seasonal in green and tectonics in cyan.
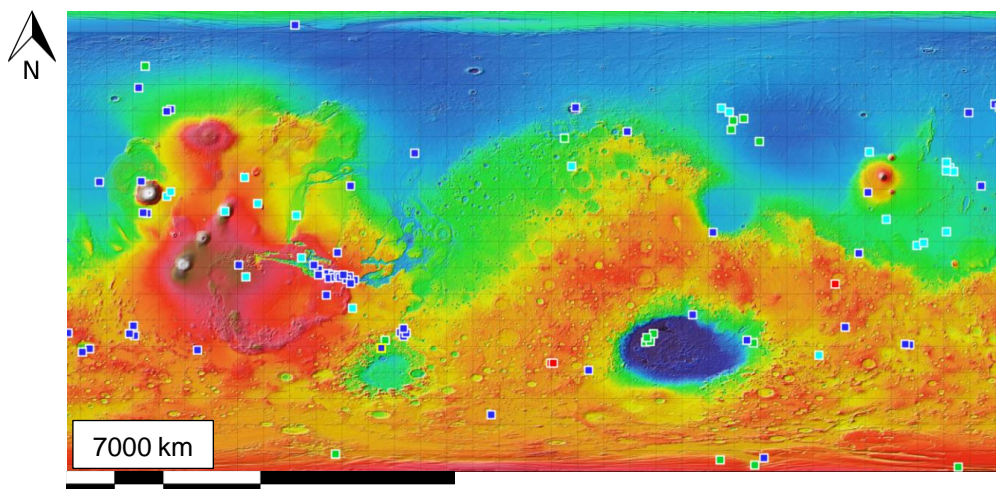


*Figure 25: MOLA colorized elevation map of Mars with all 76 AoIs marked in respective colors, blue for slope, green for seasonal, red for aeolian, and cyan for tectonic processes (Christensen et al., 2009).*

## 4.4.1 Results HiRISE camera

While investigating the general quality of the DIC outputs using pre-produced HiRISE orthoimages, some unexpected features were observed in the results. Occasionally, parts of the output deformation matrices are separated by straight lines or are streaked by linear artefacts, while the direction and magnitude of the erroneously displayed offset can alter, affecting both the NS as well as the EW matrix, but to a varying extent. Further, local patches of terrain in the input images show unusual shapes and edges, which always occurs in places of high relief, thus creating a peculiar response during DIC. Occasionally, a resulting DIC matrix also indicates a gradual change of deformation spreading over an entire image, independent of terrain and geomorphological features. Figure 26 displays all types.
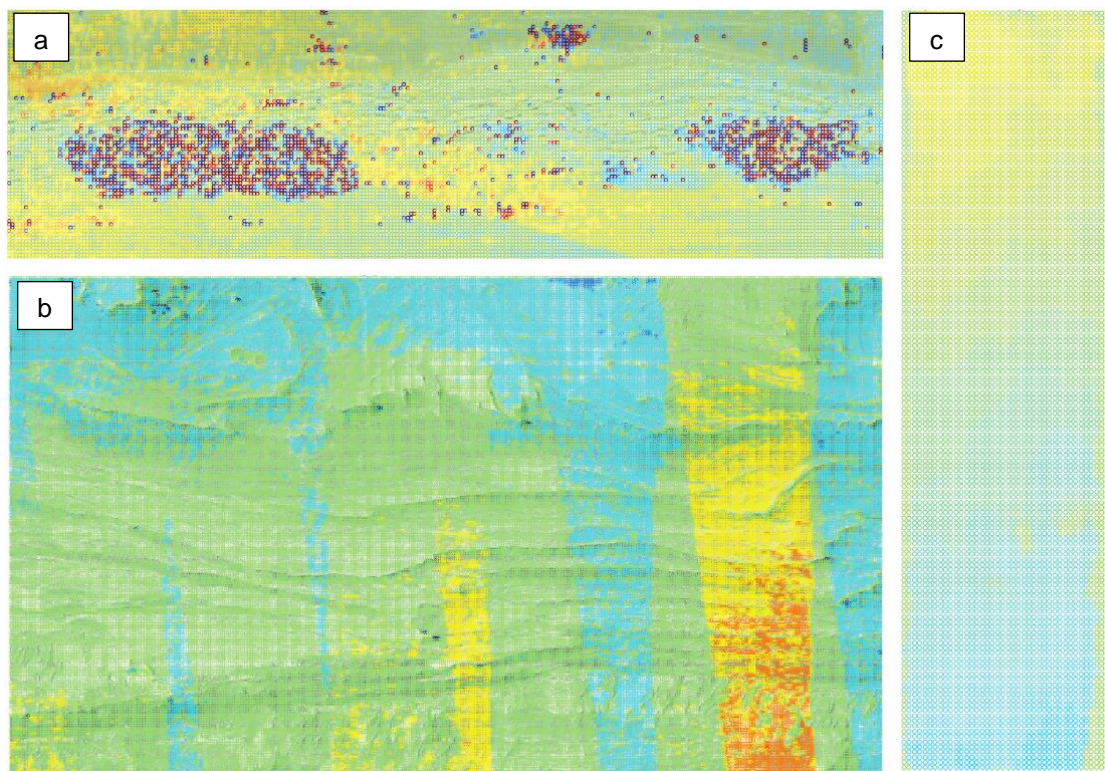


*Figure 26: Examples for the three most common artefacts using DIC with Martian imagery: a) irregular blobs of noise in places of high relief, b) linear resp. streaked artefacts, and c) gradual change of colors independent of topography. Not to scale, only for qualitative analysis (raw data from HRSC OLE, n.d., and from HiRISE, n.d.).*

Aeolian processes were investigated with COSI Corr as by Bridges et al. (2012), but also with NCC and FFT algorithms, in the Eastern Coprates Chasma, where sandy dunes run on an E-W axis through low relief terrain with exposed bedrock. Figure 27 shows the results of those runs with all three codes; displayed are the NS and EW deformation matrices of the same AoI. The temporal baseline was from January 2nd, 2014 until November 26th, 2015, i.e. ~ 22 Earth months.

*Figure 27: DIC validation with a Coprates Chasma dune field. 2.5D plot visualizes the terrain, isohypses have a 25 m vertical distance, elevation is slightly exaggerated to enhance visualization. DIC has been performed on the dune field in the depression, not on the slopes. On the left side, all EW results are presented, on the right side, all NS results. Measured deformation is in [pixel], while the GSD is 0.25 m per pixel. DIC runs were performed with wi 128 pixels except for COSI Corr, where 256 pixels had to be used to improve matching quality (raw data from HiRISE, n.d.).*

Figure 28 displays the results of a subtraction of the co-registered input images, using a 2-bit threshold and a binary mask representation.
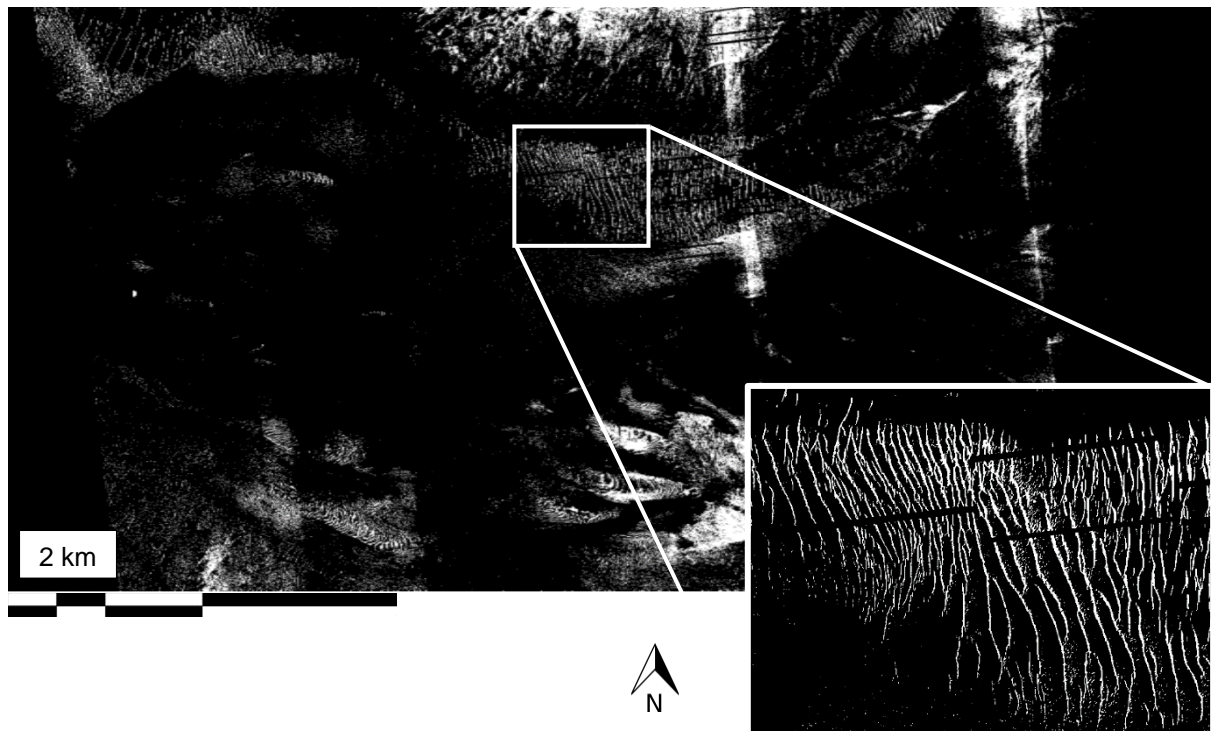


*Figure 28: Smoothed binary plot of input image subtraction from 2014 and 2015 using a binary threshold of 2 bit. Occurred changes are displayed with black pixels (0 bit) indicating no change and white pixels indicating differences (255 bit). Moving dune ridges are visible in the zoom window. Black and white linear features are CCD malfunctions of the HiRISE sensor.*

Another result was achieved with all codes for a Ganges Chasma dune field with a temporal difference from February 20th, 2012 until January 6th, 2015, i.e. ~ 34 Earth months. Here, dunes seem to move around hills and mountains of solid bedrock in different styles and shapes. Figure 29 displays the FFT derived NS and EW components:
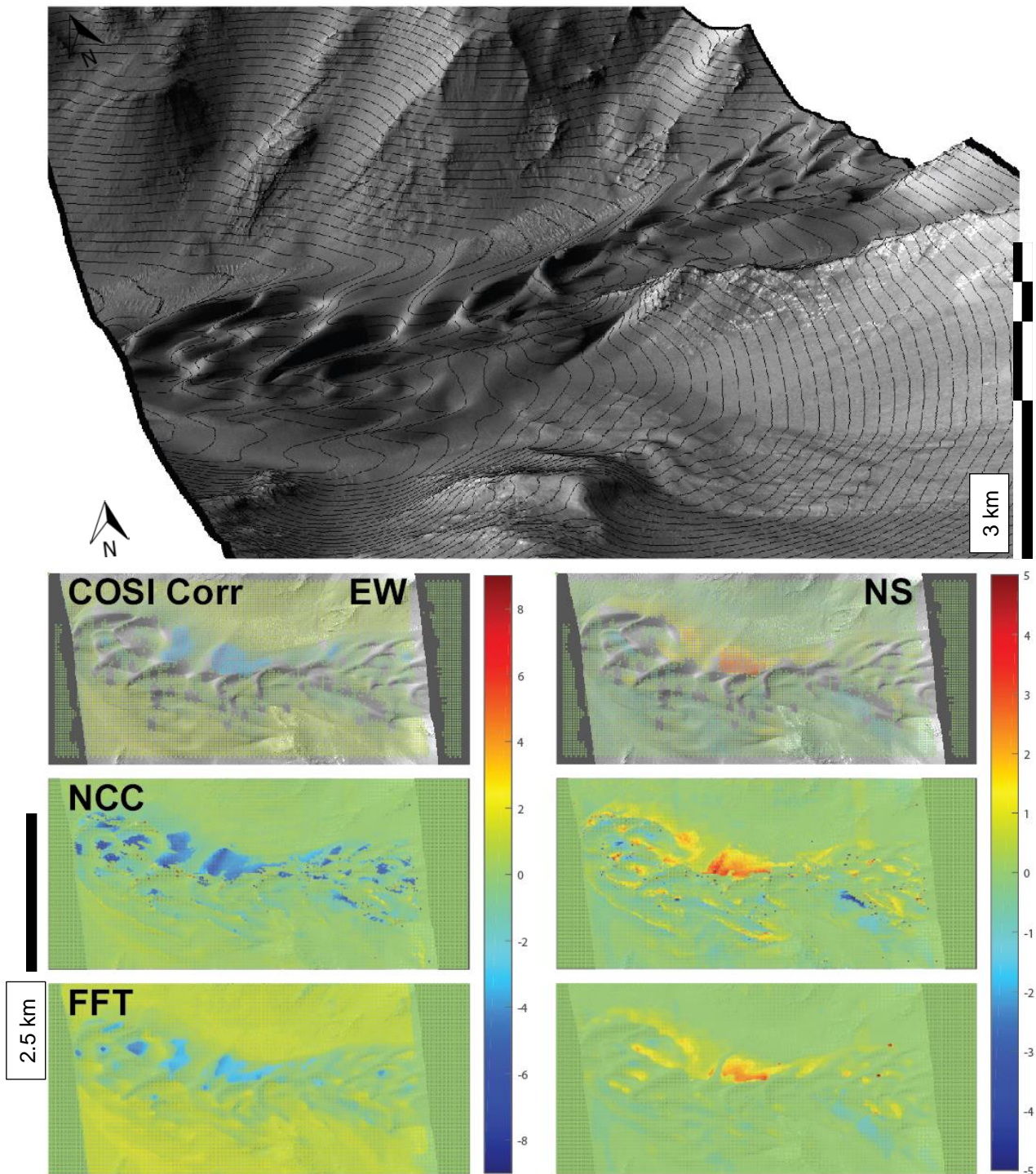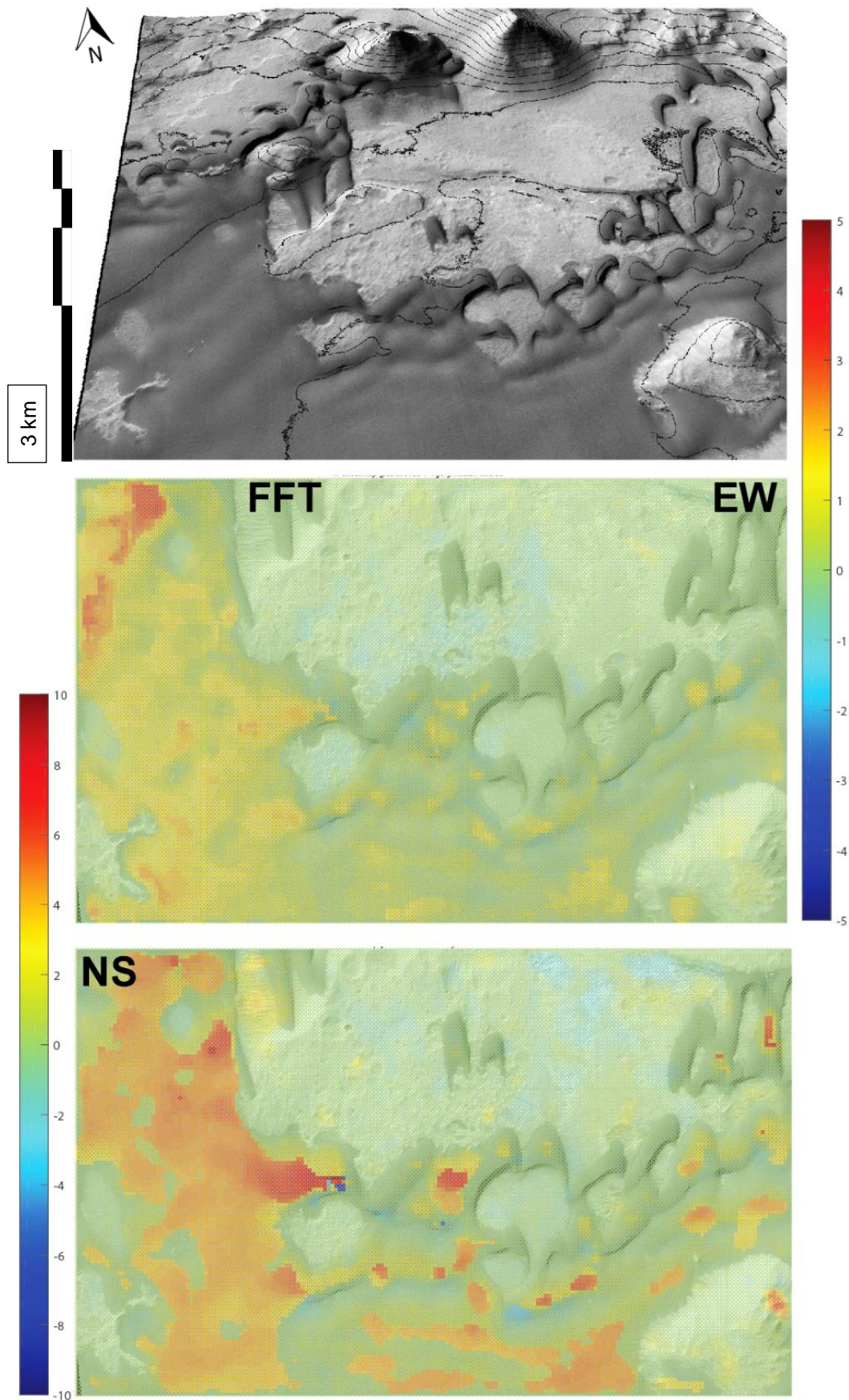
*Figure 29: DIC validation with a Ganges Chasma dune field. 2.5D plot visualizes the terrain, isohypses have a 25 m vertical distance, elevation is slightly exaggerated to enhance visualization. In the middle, the EW result is presented, at the bottom, the NS result. Measured deformation is in [pixel], while the GSD is 0.25 m per pixel. DIC run was performed with wi 128 pixels (raw data from HiRISE, n.d.).*

Another location has been identified, where aeolian processes seem to occur on the slopes of an apparently unnamed crater 300 km north of Yaren Crater. Temporal difference is from April 15th, 2011 to May 6th, 2011, i.e. 21 Earth days. Figure 30 displays these results with a vector plot to underline the observed deformation behavior and to illustrate the dynamics of the activity.
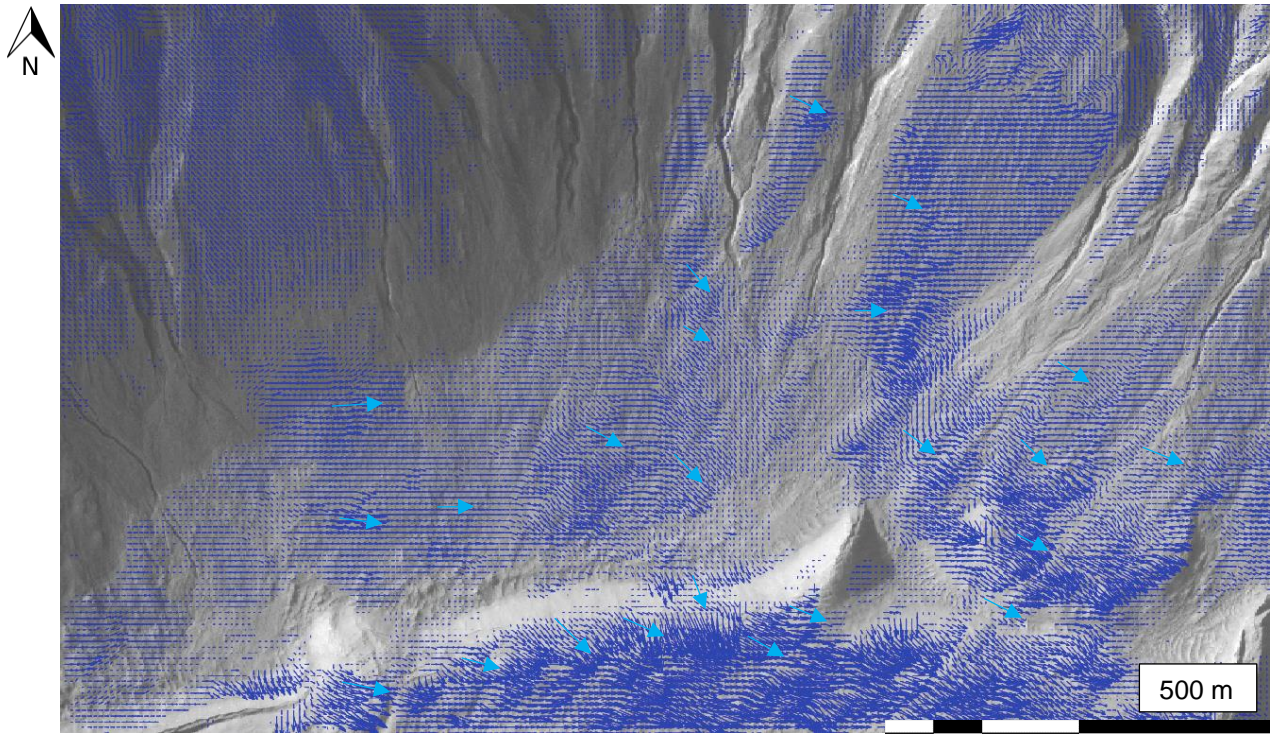


*Figure 30: DIC validation with dunes in an unnamed crater. Terrain drops from North to South, gullies are visible in the North. Measured offset is expressed with vectors, indicating the direction of the deformation as well as its dynamic and local variability. GSD of the image is 0.25 m per pixel. DIC run was performed with wi 128 pixels (raw data from HiRISE, n.d.).*

Figure 31 shows an exemplary result of the FFT code on the western slope of Palikir crater, where images indicate gullying processes as well as RSLs. The time difference ranges from December 30th, 2014 to January 21st, 2015, ~ 22 Earth days:
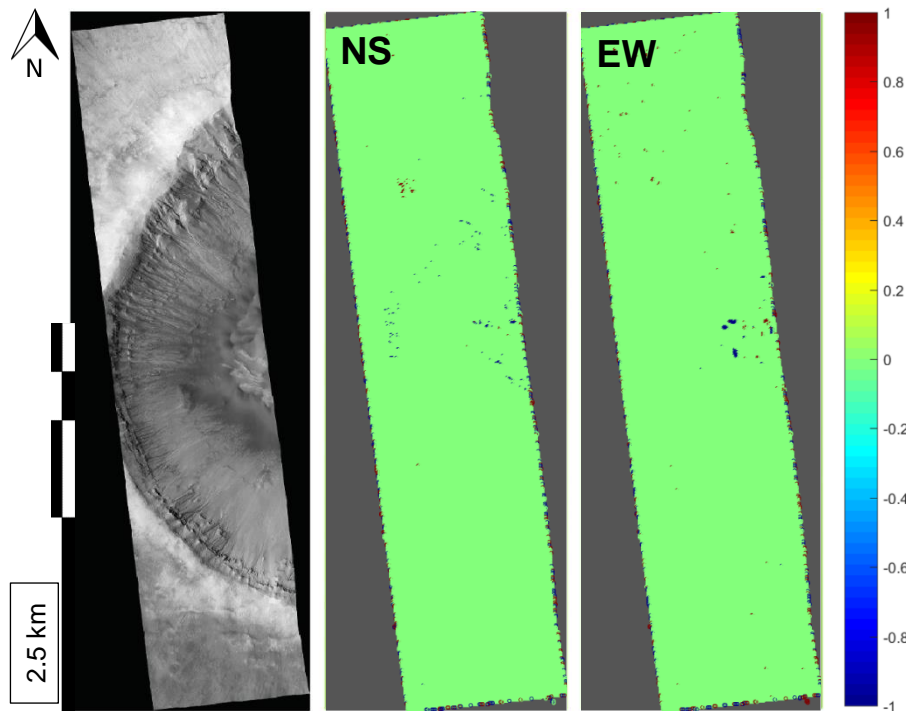
*Figure 31: DIC validation with slopes, gullies & steep terrain in Western Palikir crater. Elevation drops towards the East and into the crater. In the middle, the NS result is presented, on the right, the EW result. GSD is 0.25 m per pixel and the DIC run was performed with wi 64 pixels. Some noise can be seen in the results. Scale is in [m] (raw data from HiRISE, n.d.).*

Further, a steep cliff at the rim of the North polar layered deposits was investigated with FFT, exactly at the place where the so-called frost avalanches were imaged by HiRISE previously. The layered deposits are shaped like a plateau, while the drop of the cliff is very steep and up to 700 m deep. At the bottom, debris aprons can be identified. The temporal baseline was from August 10th, 2010 to September 8th, 2010, i.e. ~ 29 Earth days. Figure 32 shows a topographic overview and one of the imaged avalanches, while figure 33 provides the results of the DIC application.
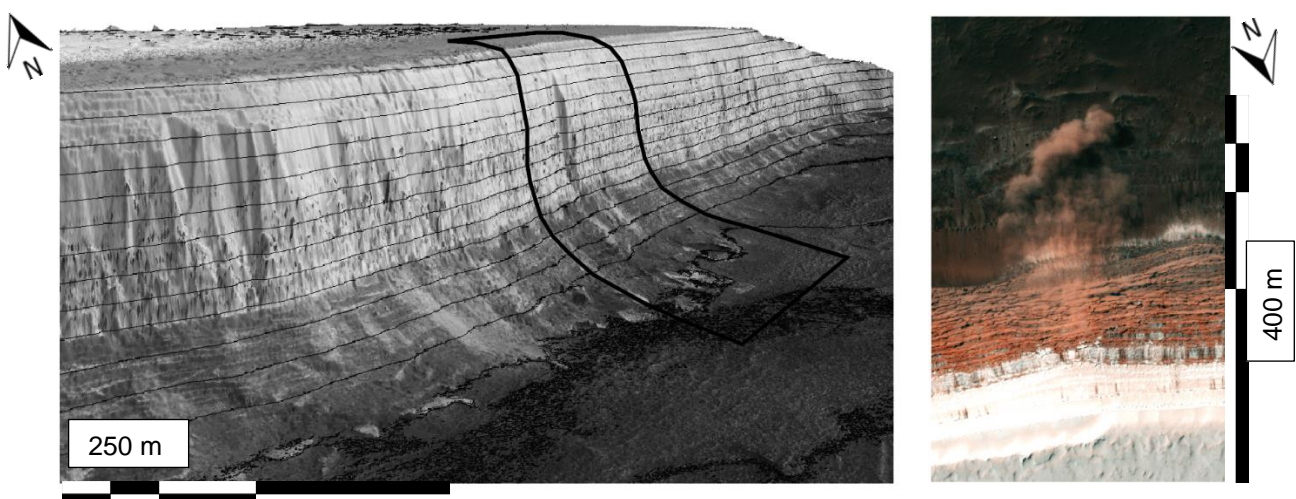


*Figure 32: 2.5D plot on the left visualizes the terrain, isohypses have a 50 m vertical distance, elevation is slightly exaggerated to enhance visualization, black box indicates the dimensions of the HiRISE image on the right; this image taken in 2008 by NASA MRO HiRISE shows an occurring avalanche (raw data from HiRISE, n.d., NASA, 2015).*
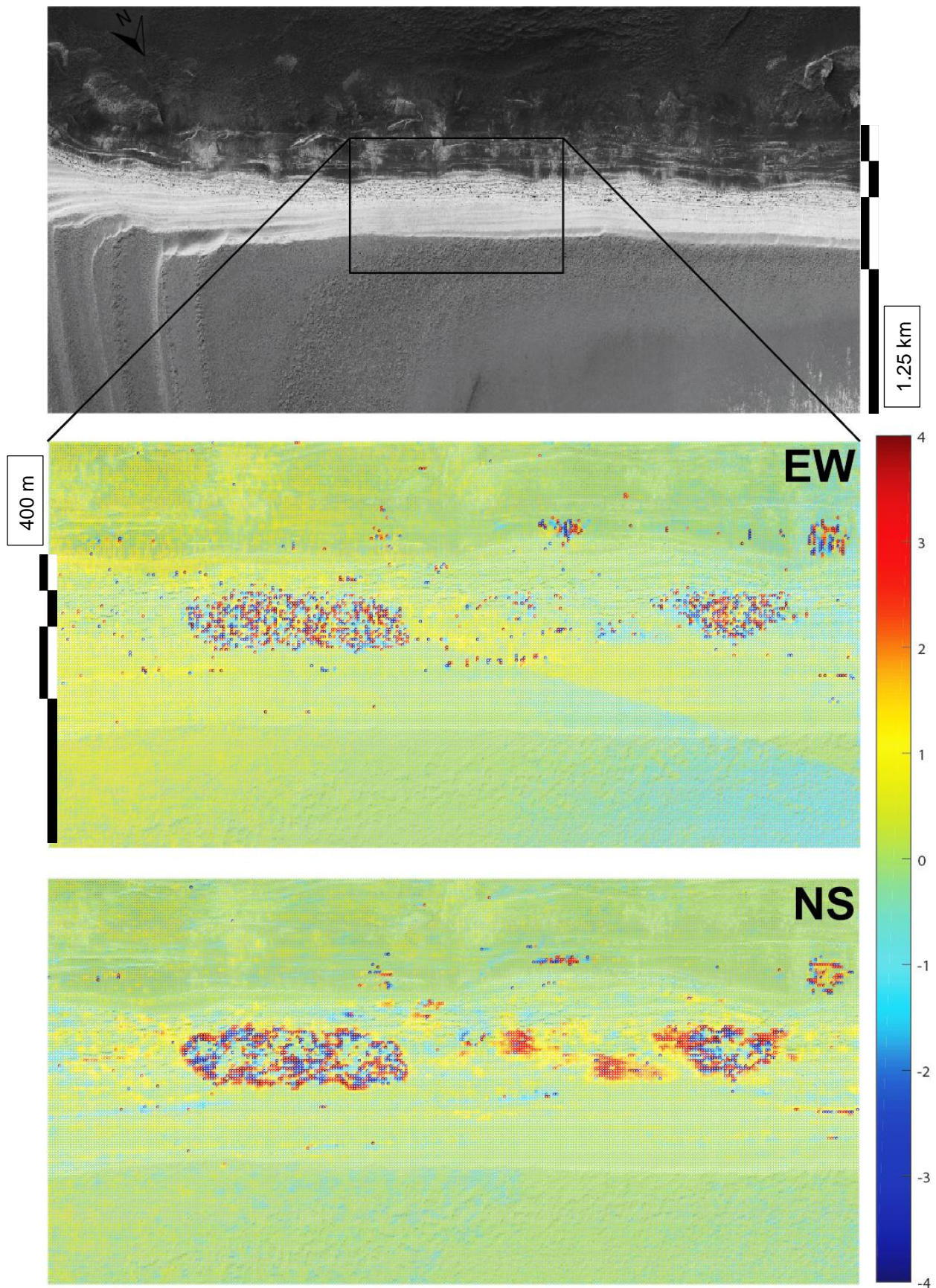
*Figure 33: DIC validation with a Rupes Tenuis cliff (i.e. the cliff where avalanches were imaged). In the middle, the EW result is presented, at the bottom, the NS result. Measured deformation is in [pixel], while the GSD is 0.25 m per pixel. DIC run was performed with wi 64 pixels. The EW plot features a linear artefact, striking NW-SE (raw data from HiRISE, n.d.).*

Seasonal activity has been studied in Inca City close to the Martian South Pole. Temporal baseline ranged from January 28th, 2007 until September 13th, 2012, i.e. ~ 5 Earth years and 7 Earth months. Figure 34 displays the output.
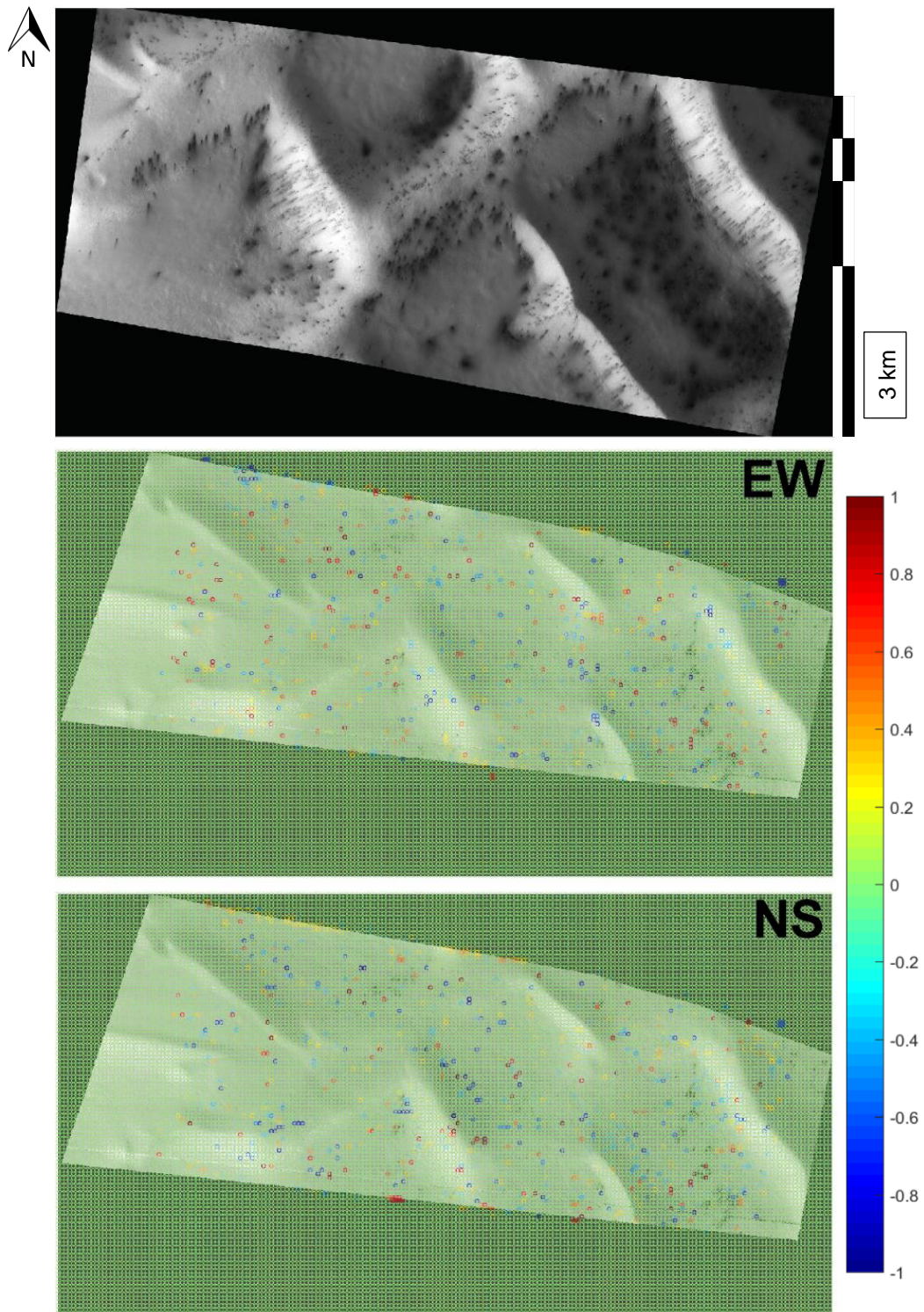


*Figure 34: DIC validation in Inca City close to the South Pole. Terrain is flat and locally hilly, dark spots in the top image are seasonal processes, such as gas outbursts, ice melt, etc. In the middle, the EW result is presented, at the bottom, the NS result. GSD is 0.25 m per pixel and the DIC run was performed with wi 128 pixels. Scale is in [m], noise resp. potential rapid changes are visible (raw data from HiRISE, n.d., HiRISE IC5, n.d.).*

Finally, figure 35 represents the results from FFT application on an inflation feature in Phlegra Dorsa with a time difference from November 26th, 2013 to February 1st, 2014, ~ 36 earth days.
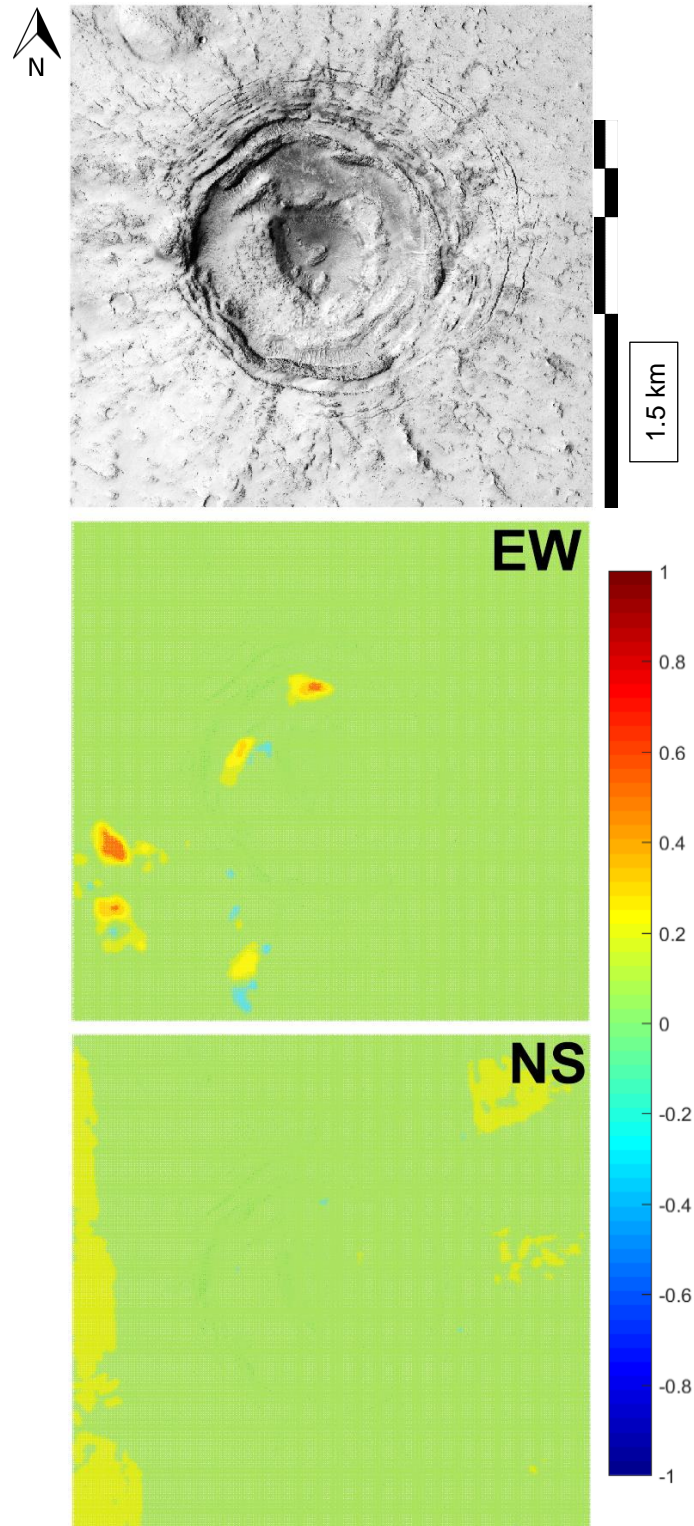


*Figure 35: DIC validation for an inflation feature in Phlegra Dorsa. Terrain is flat and the feature appears to have been subject to no inflation or subsidence, including radial scarps. In the middle, the EW result is presented, at the bottom, the NS result. GSD is 0.25 m per pixel and the DIC run was performed with wi 32 pixels. Scale is in [m], local patches of noise are visible, which are likely to be caused by shadows or poor pixels in one of the input images (raw data from HiRISE, n.d.).*

## 4.4.2 Results HRSC camera

Due to the lack of overlapping, pre-produced level 4 HRSC orthoimages, only one example AoI was investigated, a cross-section through the Southern Ganges Chasma valley wall. The site features the steep slope of the chasma as well as the deposits by an old landslide, presumably triggered of an impact crater close by. The temporal baseline is short due to the underlying imaging scheme by MEX and ranges from September 12th, 2015 to September 18th, 2015, i.e. 6 Earth days. Figure 36 shows the respective DIC results.
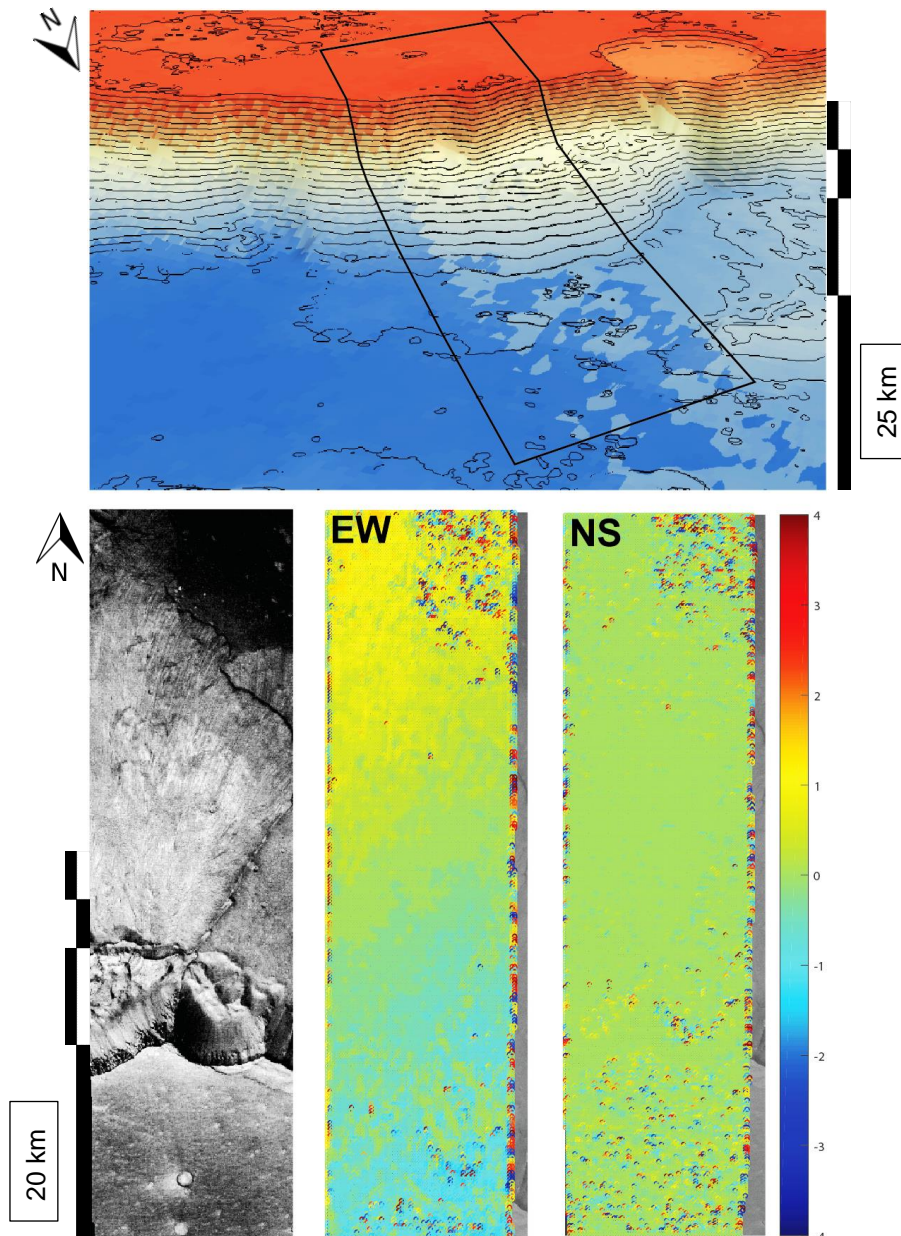


*Figure 36: DIC validation over an old landslide scarp in Ganges Chasma. Elevation model visualizes the terrain, red colors represent higher elevations, blue colors represent lower elevations, isohypses have a 200 m vertical distance, elevation is slightly exaggerated to enhance visualization. The black footprint outlines the dimensions of the used acquisitions. On the left, one of the input images is shown, in the middle, the EW result is presented, on the right, the NS result. Measured deformation is in [pixel], while the GSD is 12.5 m per pixel. DIC run was performed with wi 64 pixels (raw data from HRSC OLE, n.d.).*

## 4.5 Discussion

The application of the assessed DIC processing pipeline on Mars generally produced valuable results. This means that all selected DIC codes are able to operate on various input imagery, such as HiRISE, HRSC and the CdV cameras, while producing results with the same or very similar quality. Further, the elaborated input parameters for the detection of unknown features on foreign planetary surfaces seem to perform promisingly. Still, the data delivered by the Martian orbiters contains three types of systematic artefacts, which are revealed by DIC. As illustrated in figure 26, the HiRISE orthoimages appear to have linear artefacts, which run over the entire image, simulating deformation. Those features are probably introduced during the mosaicking of the HiRISE CCD's acquisition stripes and can be distinguished from noise and true deformation without difficulty. The introduced erroneous deformation is slight in a quantitative sense and any true, i.e. non-systematic, surface displacement will be recognizable through the noise; in such an area, the real deformation would be the measured deformation minus the systematic background noise. Secondly, HiRISE orthoimages locally contain patches of incorrectly projected terrain. This systematic error occurs solely in areas which express high relief, e.g. steep slopes. They are likely caused by meshing algorithms, which intend to fill holes and missing data values in these regions: possibly, the underlying DEM for the respective orthorectification was not perfect, comprising holes, which needed to be filled in order to continue the data production. As no data is available, the responsible algorithm might just have interpolated values over the holes, which subsequently leads to locally limited artefacts in the DIC matrices, caused by a poor map-projection during the orthorectification process. However, these minor errors can be recognized by performing a manual and visual validation of the utilized input data, if applicable by using hillshade plots. Finally, gradual changes of measured deformation such as in figure 26 are occasionally encountered and probably express insignificant errors in the camera calibration or during the bundle adjustment prior to orthorectification. As this is another systematic error, any non-systematic displacement will be detectable through the noise. In general, such systematic errors cannot be removed by filters, as they are too coherent; fortunately, they can be easily identified and avoided by a considerate operator. Yun et al. (2007) demonstrated a way to remove systematic artefacts by using the calculated offsets to correct the slave input image. Even if this would be an elegant solution to minimize noise in the DIC input images, the procedure requires operation and computation time and is not really necessary for this study, as all encountered artefacts can be recognized without difficulties.

To further assess the performance of all DIC codes, dunes in Eastern Coprates Chasma and Ganges Chasma were observed and measured. The respective results of all codes are particularly comprehensible concerning detected quality and quantity of deformation, which further underlines their effectiveness for this investigation. Indicated by the topography of the field in Coprates Chasma in figure 27, the area comprises a horizontally stretched dune field, migrating from East to West, derived from the geomorphology and dune shapes. This terrain is circumscribed by bedrock outcrops in the North and South. As described before, the expected deformation should only occur within the dunes, while the bare rock should be stable. Exactly this is reflected by the results shown by figure 27; all codes indicate local movement of dunes towards the West – Southwest with a mean resultant velocity calculated as ~

6 cm per Earth month and ~ 0.8 m per Earth year, whereas outcropping rock strata is green in color and therefore not moving. The derived local peak deformation magnitude ranges from ~ 5.3 m (COSI Corr & NCC) to ~ 5.8 m (FFT) in total for the observed 22 months, which is an acceptable deviation between the different codes, considering the application of different search windows as well as the findings of the CdV study. Interestingly, there seems to exist a hotspot of deformation in the center of the image, while displacement speed seems to peak close the ridges of dunes, just as would be expected based on experiences on Earth. As known from the CdV case study, COSI Corr appears to be unable to achieve a complete spatial coverage due to correlation mismatches.

Results derived by FFT and the other codes in Ganges Chasma support these findings (figure 28): The respective setting consists of a vast dune field which seems to travel around several mountains; horizontal bedrock is exposed locally. DIC analysis indicates a movement of the dunes towards the Southeast with a speed of ~ 0.12 m (FFT) per Earth month and ~ 1.4 m per Earth year, while all surrounding rock faces are stable. Results such as plotted in figure 29 additionally suggest that there is aeolian activity on Mars which drives sand and dust across or even up slopes with measurable magnitudes. Insights like those, derived by DIC, could lead to an optimization or improvement of atmospheric models at a local scale or potentially to a weekly monitoring of sand or dust behavior at certain points of interest, e.g. landers or rovers.

The observations of this work match the findings made by Bridges et al. (2012) and Ayoub et al. (2014), who derived dune migration rates on Mars with velocities of around 1 m per Earth year. All applied codes returned migration rates of around 0.8 to 1.4 m per Earth year for other areas of interest than covered by Bridges et al. (2012) and Ayoub et al. (2014). Therefore, slight deviations from the literature might be caused by local topography or different atmospheric conditions during the observations. As COSI Corr as well as NCC and FFT perform almost equally, and as their results can be directly linked to results by other studies using DIC, the goal of further validating DIC algorithms using past studies on Martian dune migration has been achieved. In the future, a quantitative and qualitative assessment of different DIC codes for sites on Mars, where COSI Corr was already applied, could enable a direct comparison on a foreign planet. Potentially, further assessment with other algorithms, such as FFT and NCC codes, could show that COSI Corr, although widespread amongst researchers worldwide, could be complemented or even replaced by other DIC codes, possibly benefitting the exploration of planetary surface processes in general.

By testing DIC on difficult Martian imagery, such as of high relief areas, the efficiency of topography removal has been assessed. Imperfections within the orthorectification could cause fake offsets, such as visible in figure 26; a pair of high-quality orthoimages would indicate absolutely no deformation in an area without actual displacement and relief. One chosen site to show this is situated in Western Palikir crater, where the surrounding ground elevation of ~ -250 mbmd drops down to ~ -1300 mbmd with a mean slope angle of ~ 18°. The resulting NS and EW offset illustrates that there is absolutely no deformation going on, which means that the orthorectification process appears to be close to perfect. This is one example showing that the data processing is apparently capable of producing input data of reliable and sufficient quality for DIC, even for more difficult geomorphological conditions.

Data gathered by HiRISE at another AoI on Mars's North Pole shows ongoing slope processes in the form of avalanches. An application of DIC codes in exactly this region and at the identical part of the cliff with a temporal baseline of around four Earth weeks delivers results as seen in figure 33. Both offset matrices indicate some kind of locally limited deformation at two hotspots in the middle to lower part of the cliff, whereas the displacement itself appears very noisy and a direction of movement cannot be determined. This type of noise could potentially indicate a slope failure, as the surface is completely altered and the DIC codes cannot match corresponding pixels anymore. In addition, two other, more coherent parts of the slope appear to move uphill, i.e. to the South. Further, some areas within the debris aprons display some noise; this could represent a fast surface change as well, e.g. by recently deposited avalanche material, completely altering the surface texture and reflectance. The noisy areas cover an area of $\sim$ 2 and $\sim$ 1 hectare ($10^4$ m$^2$), the southwards moving an area of around 3000 square meters, while apparently moving at $\sim$ 0.2 m per week. Some systematic artefacts can be seen in the EW offset matrix, but generally the used orthoimages seem to be of high quality, as suggested by the vast area of stable ground on the plateau as well as on the bottom of the cliff. These potential slope displacements occur only in the part of the slope with the highest relief and the measured DIC signature could therefore represent a pre- or post-failure behavior of this Martian slope, whose activity is proven by acquisitions of failures as well as the existence of distinct talus cones.

However, the discovered results raise questions. An uphill slope deformation in a very limited region cannot be explained by any conceptual geomechanical model. In addition, a visual investigation of the apparently active parts of the slope does not deliver any proof for an occurred change of the surface's texture, which would be necessary for a slope failure of that size. Moreover, the manual scan reveals the occurrence of severe artefacts at the locations of deformation, with a twisted and blurry appearance. Further, if the noise at the bottom of the slope would indicate fresh avalanche deposits, parts of the cliff above these locations should indicate failures as well; but this is not the case. By considering a hillshade of the underlying DEM more significant artefacts can be identified at the same positions as derived by the previous visual check, as visible in figure 37. Probably, those relicts were created by a meshing algorithm, which tried to fill holes in the DEM prior to orthorectification, as described before. Such holes are likely to occur in this terrain, as relief is very steep and surface changes seem to appear very frequently. It has to be noted that the introduced errors are not caused by the relief and a bad topography removal itself, but by a poor DEM meshing resp. sub-optimal underlying stereo correlation, probably caused by an inappropriate selection of stereopair images used to produce the underlying DEM. This type of artefact was already identified in other orthoimages by NASA, as described before and shown in figure 26, and therefore significantly decreases the credibility of the derived offset results, as the orthorectification introduced substantial fake deformations. Based on those findings, the quality as well as the amount and temporal baseline of the available data is not sufficient to detect a pre- or post-failure behavior of this polar cliff. As the apparently poor hole meshing is likely caused by stereo correlation mismatches, theoretical reasons for the decorrelation of the stereo algorithms besides relief, illumination and frost patches could also be substantial changes of the cliff caused by large failures. This possibility has been discarded by considering images of the AoI taken before and after the respective stereopair acquisitions, used by NASA for the production of the discussed DEM: All reviewed images did not confirm any change of the cliff at the locations, indicated by DIC using the poor DEM. Still, failures at

smaller scales are occurring with an unknown frequency, which makes this AoI a priority target for a more detailed and comprehensive DIC analysis in phase two.

Despite the fact that the applied algorithms by NASA and affiliated institutions deliver HiRISE DEMs and orthoimages with high quality over large portions of the surface of Mars, the same codes in combination with the selected stereopair images do not perform sufficiently for areas with distinct relief. Steps could be taken to adapt the utilized codes for such challenging areas on Mars, to guarantee consistent quality, as according to the HiRISE webpage (n.d.), similar artefacts are also known from several sites on the surface, further underlining the relevance of such an adaptation. A potential method of processing is described and illustrated in chapter 5.2 of this thesis.
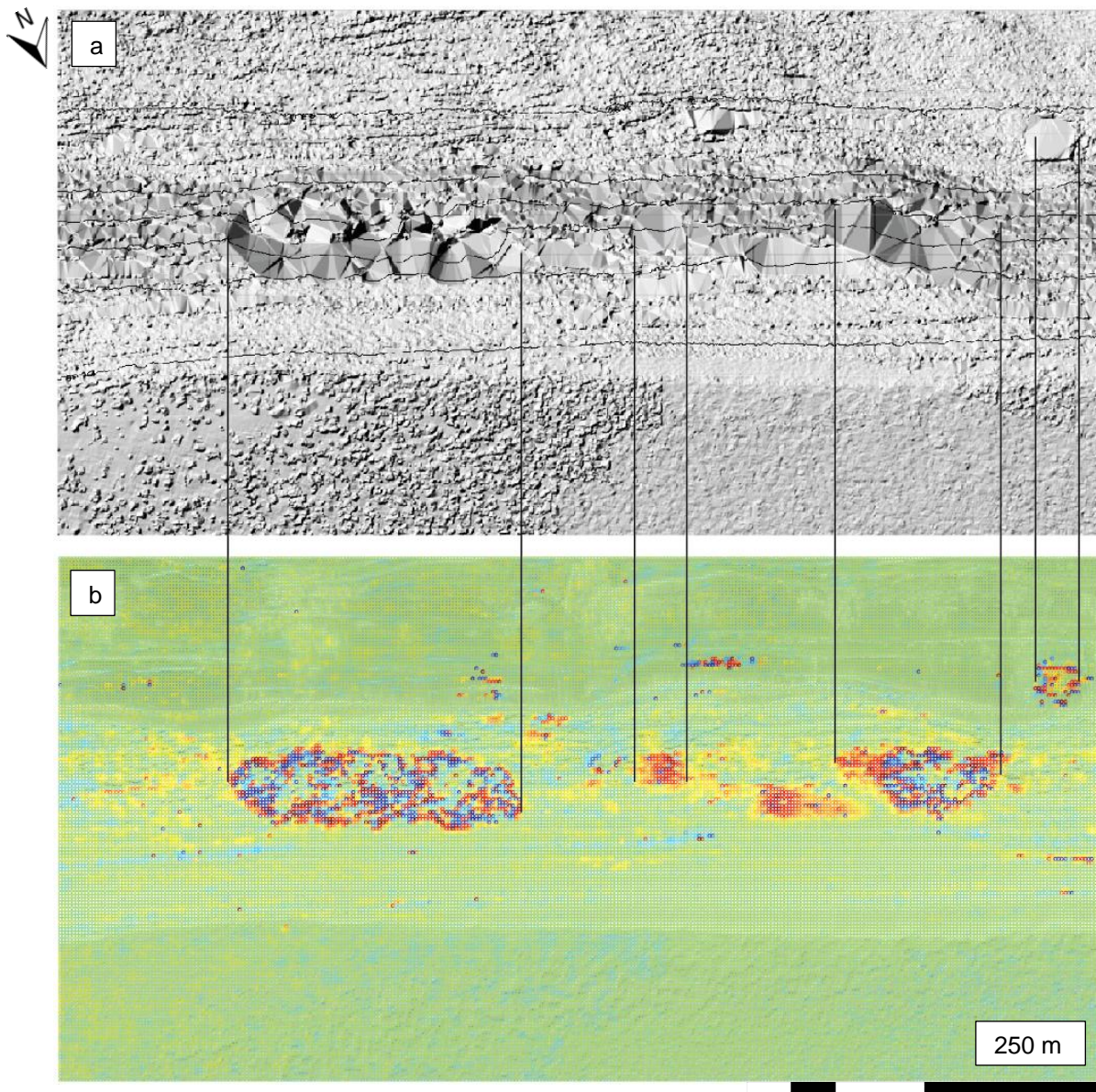


*Figure 37: Artefacts encountered at the Rupes Tenuis cliff close to the North Pole: a) Application of a hillshade on the NASA DEM reveals coarse areas in the elevation grid, probably caused by meshing algorithms which tried to fill holes caused by stereo correlation mismatches. b) poor hole filling introduces local pixel shifts which are not visible with the naked eye, but cause significant fake deformations during DIC. GSD of both images is 0.25 m per pixel. No scale is available, as plots are supposed to be used as qualitative information only (raw data from HiRISE, n.d.).*

Long-term temporal surface changes in connection with seasonal processes such as soil creep were investigated in Inca City close to Mars's South Pole. Despite the substantial time difference of around 5.5 Earth years the derived DIC offset matrices do not indicate any surface displacement in the camera plane, at least not in the used GSD. The visible scattered noise however could be related to the seasonal occurrence of surface alterations caused by the influence of the sun on subsurface ice: its melting is thought to build up a pressure, eventually cracking and deforming the overlying ice and soil mixture, creating so called spiders or fans (HIRISE IC5, n.d.). The supplementary information section contains a visual example of those Martian features (S 8). DIC codes are able to detect these features, but as they are not moving, resp. as they are moving along the LOS, the true potential of DIC cannot be utilized. Still, an application of DIC for e.g. automated seasonal change detection would be an interesting topic for further research.

Use of HiRISE images for remote detection of tectonic activity has been elaborated in Phlegra Dorsa, where potential inflation features occur. Those features do not allow an easy estimate of the occurred or occurring deformation and the retrieved offset data does not indicate any movement either. Only a few areas appear to show very limited displacement in the EW direction, but these zones are likely to be influenced by changing shadows in both used orthoimages and do not represent tectonic or other activity. Still, the available time difference of 36 Earth days is quite short for tectonic processes to take place and the results of this preliminary investigation should be considered with care. Unfortunately, longer baselines are not available using only pre-processed data by NASA or ESA. Still, potentially active zones on Mars remain a priority target for further measurements, while temporal baselines should be maximized.

By increasing the GSD by changing the used sensor, large scale displacements are more likely to be observed. This has been attempted in Ganges Chasma using the HRSC level 4 products with a short time difference of 6 Earth days. Although the scanned area entails a high relief as well as old landslide deposits, DIC does not indicate any displacement, only some noise and a systematic artefact in its EW component. However, the detection of large scale processes in very short time frames is not very likely, except for e.g. Marsquakes, and the GSD of 12.5 m per pixel is presumably too large to detect smaller changes. Unfortunately, HRSC is aspiring a full planetary coverage and is therefore minimizing overlaps or revisits, significantly constraining DIC applications. This unfavorable combination of preconditions is therefore impeding a substantial application of pre-processed HRSC imagery for further Martian change detection analyses at this time.

The preliminary investigation of the Martian surface with DIC and pre-processed imagery data has revealed regions, which require more sophisticated and comprehensive research. The critical factor was identified as the available temporal baseline between the acquisitions, i.e. the temporal resolution, which seems sufficient to detect fast surface changes such as moving dunes, but insufficient to expose slower processes, such as slope or tectonic deformations. Therefore, the intention for phase two was to autonomously produce orthoimages from selected AoIs in order to maximize the temporal resolution. Additionally, the potential of sensors with larger GSDs should be further examined, which also have a better temporal resolution, such as the MRO's CTX camera, due to larger overlaps related to an increased swath width. A combination of both intentions would enable an identification of slower

processes and of displacements with larger scales and would thus complete the first exploration of Martian surface processes with DIC. To do so, CTX images were used to study the behavior of two AoIs in a volcanic province, in a second attempt to detect tectonically driven displacements on Mars. In addition, CTX data was applied to monitor the potential movement of a GLF, which could not be done in phase 1, as pre-processed CTX data was not available. Thus, large scale creeping movements are also investigated in more detail. Finally, the already treated polar cliff which shows recent activity in the form of avalanches will be the main focus of phase two and subject to a thorough analysis using the maximum possible bandwidth of available HiRISE acquisitions from this area. So, potentially slow and small-scale slope processes on Mars could be identified.

# 5. EXPLORATION OF SURFACE DEFORMATIONS ON MARS

The second phase of the change exploration campaign on Mars focused on four specific AoIs, in order to complete the entire study, based on previous insights and conclusions.

## 5.1 Selected study sites

These four AoIs fall into three of the four previously defined categories, seasonal processes and creep, tectonic activity and slope processes. Selected targets are a GLF at the Eastern rim of Hellas Planitia, a volcano close to the Tractus Fossae as well as the caldera of Ascraeus Mons in the Tharsis Montes and a cliff of the Northern polar deposits in the Rupes Tenuis close to Olympia Undae. Dune activity will not be investigated here. Figure 38 shows the respective locations of all AoIs on the planet.
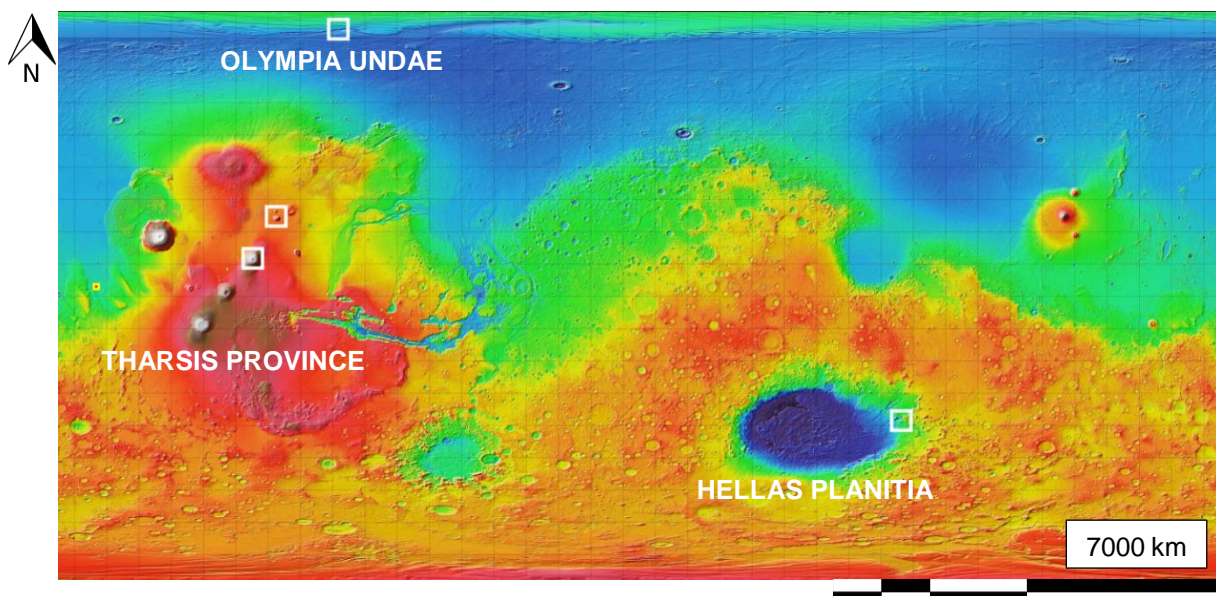


*Figure 38: MOLA colorized elevation map of Mars with all 4 final AoIs marked with white rectangles in the Olympia Undae, Hellas Planitia, and Tharsis Province (Christensen et al., 2009).*

### 5.1.1 Glacier Like Feature

The AoI is situated on the Eastern border of Hellas Planitia, around Penticton Crater between the Centauri and Hellas Montes. Figure 39 shows the area as a colorized elevation plot, based on Mars Orbiter Laser Altimeter data (MOLA) with a GSD of 300 m per pixel. The GLF appears to have been moving from the East towards the West, while partially entering Penticton Crater. Topography is relatively flat, with the GLF's altitude ranging from around – 1500 mbmd (meters below Mars datum) down to – 2000 mbmd, with an average gradient of around 2°. When considering a single band CTX

acquisition of the AoI, the surface of the GLF looks hummocky and appears to have been shaped or is still being shaped in a flow-like or viscous way, displaying curved features orthogonal to the assumed flow direction. Those structures look similar to crevassed parts of terrestrial valley glaciers, as already observed by Hubbard et al. (2014). Further, the GLF seems to have a distinct border towards the South of Penticton Crater, where potential displacement may be detected with DIC.

The underlying geological setting is mapped by the United States Geological Survey (USGS) Geological Map of Mars # 3292 (Tanaka et al., 2014) as a transition between an Amazonian resp. Hesperian impact unit (AHi), which consists of multi-lobed ejecta blankets with brecciated target rocks and sediments, locally showing impact melt, and an Amazonian resp. Noachian apron unit (ANa), which are ice-rich materials, transported by mass flow events as well as thermokarst processes. The GLF itself might either consist of particularly ice-rich parts of the Amazonian resp. Noachian apron unit or might just be an accumulation of water and dry ice, mixed with Martian regolith or dust, as described by Hubbard et al. (2014), or a heterogeneous mixture of both without clear distinction. Based on the information extracted from the MOLA DEM as well as from the CTX image, the GLF, if moving, would flow from the East towards Hellas Planitia in the West, while following the low gradient. Local deformation could be located in Penticton Crater, where the GLF appears to drop into the local depression in topography. Displacement velocities are assumed as being very small. A part of the geological map of the AoI can be reviewed for more details in the supplementary information section (S 9).

In order to perform the DIC analysis of this area, two CTX camera acquisitions from the area were selected and processed. Image P02_001714_1413_XI_38S263W was acquired in December 2006, while image J02_045453_1413_XN_38S263W was taken in April 2016, which defines a temporal baseline of around 9.5 Earth years. The GSD is CTX's default with 6 m per pixel. The incidence angles were 2° resp. 5.73° with very similar lighting conditions. These properties should assure a proper orthorectification procedure and a good input image quality for the DIC analysis.
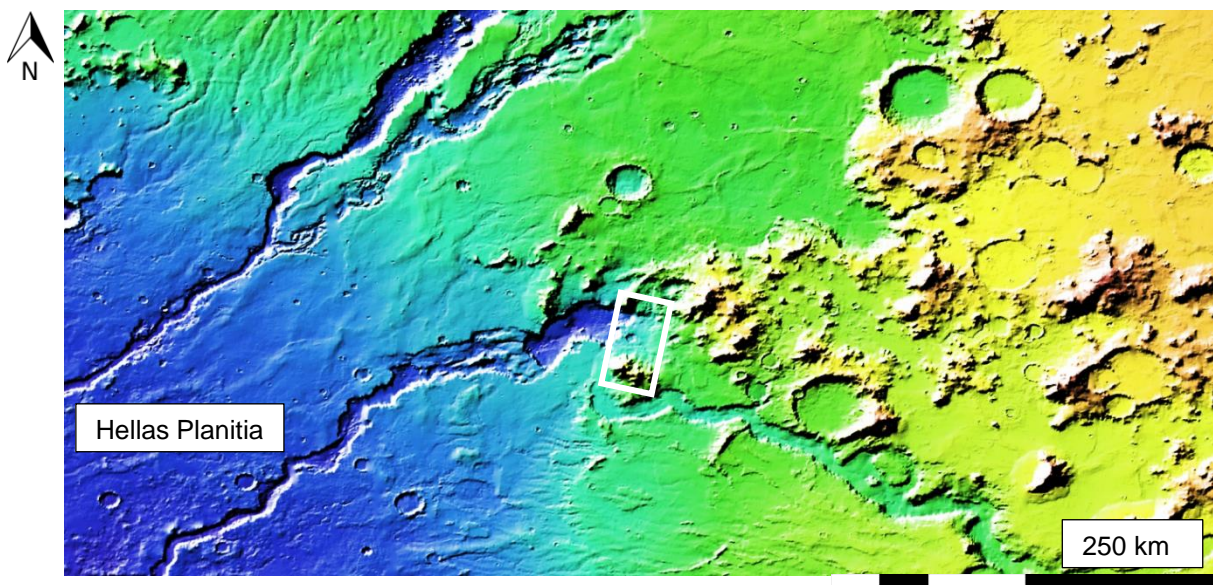


*Figure 39: MOLA colorized elevation map of Mars with the GLF AoI in Eastern Hellas Planitia marked with a white rectangle. Yellow colors indicate higher elevations, blue colors lower ones (Christensen et al., 2009).*

## 5.1.2 Volcanic region

Both targets are located in the Tharsis Montes West of the Lunae Planum and Northwest of Valles Marineris, as displayed by the MOLA map in figure 40. The volcano Ceraunius Tholus lies farther North and raises about 6500 m from the surrounding region with an average slope angle of 9°. With a diameter of ~ 100 km it is smaller compared to other Martian volcanoes, such as Olympus Mons or Arsia Mons. However, its size enables a complete diagonal coverage with a single image by the CTX camera, without the need to stitch mosaics. As visible in CTX imagery, the crater and flanks of Ceraunius Tholus are covered with small to medium sized impact craters, with several old lava flow channels visible as well. The satellite imagery does not directly suggest any ongoing activity in the area, but small tectonic deformations would not be visible with the naked eye. To the South, the volcano Ascraeus Mons raises around 14400 m above the surrounding region with a mean gradient of ~ 4.6° and a diameter of ~ 350 km. Due to its width, a single CTX acquisition is not able to cover the entire volcano, which is why the focus was set on Ascraeus Mon's caldera. The caldera's slope angle is about 12.4° on average and shows distinct radial scarps and cracks along the crater's rim, potentially expressing past or recent sacking or rotational displacements.

On the USGS Geological Map of Mars # 3292 (Tanaka et al., 2014) Ceraunius Tholus is marked as part of the Hesperian volcanic edifice unit (Hve), which features different combinations of lava flows and pyroclastic as well as volcaniclastic deposits, locally modified by collapses due to magma withdrawal and fluvial dissection. Ascraeus Mons belongs to the Amazonian volcanic edifice (Ave), which consists of volcanoes composed of lava flows and volcaniclastic rocks, potentially deformed by magma withdrawal or gravity spreading of flanks. By considering the MOLA DEM as well as the geomorphology displayed in the respective CTX images, potentially ongoing displacements of various kinds could occur, such as sub-circular inflation or deflation features, expressed on one of the volcano's flanks, or rotational slope instabilities in the caldera, as mentioned earlier. Generally, deformations in these areas are expected as being very slow, if existing. Sections of the geological map of both AoIs can be reviewed for more details in the supplementary information section (S 10).

Two CTX acquisitions from both AoIs were used for the orthorectification and DIC analysis in this volcanic region. Ceraunius Tholus was scanned with B04_011399_2045_XN_24N097W from December 2008 and J03_045829_2045_XN_24N097W from May 2016, i.e. with a baseline of around 7.5 years and incidence angles of 17.86° and 7.79° respectively. Ascraeus Mons was analyzed with P01_001510_1913_XN_11N104W in November 2006 and with F01_036361_1913_XN_11N104W in April 2014 and a time difference of ~ 7.5 years. The respective incidence angles were 0.09° and 2.92°. The spatial resolution was at its standard of 6 m per pixel whereas lighting conditions were as similar as possible to limit matching errors during the processing and the DIC application.
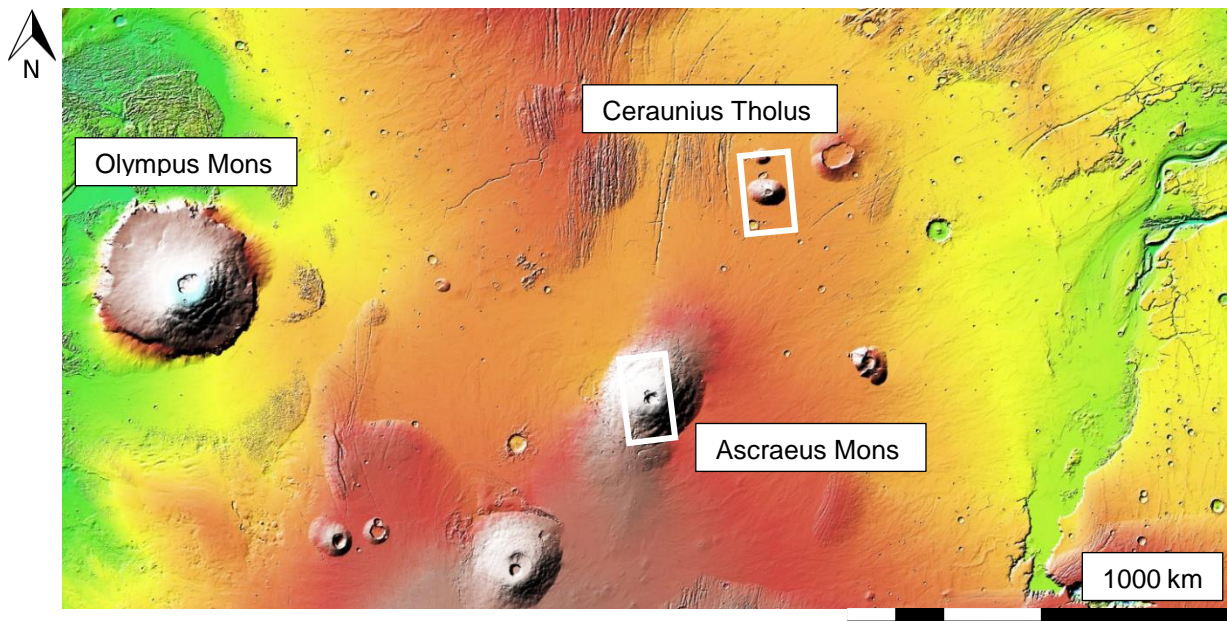
*Figure 40: MOLA colorized elevation map of Mars with the volcanic AoIs in the Tharsis Province marked with white rectangles, Olympus Mons on the left. White colors indicate higher elevations, green colors lower ones (Christensen et al., 2009).*

## 5.1.3 Polar cliff

The cliff of interest is situated close to Mars's North Pole in the Rupes Tenuis, between the Chasma Boreale and the Olympia Undae, as illustrated in figure 43. The general topography of this area is relatively flat, but with sharp and steep steps, which form a terrace-shaped morphology. HiRISE data indicates that the step, i.e. the cliff of interest, is about 700 m high, with a mean slope angle of around 65°. Optical images from the cliff show distinctive textures of the plateau and the bottom of the cliff: While asymmetric and flat shapes of potential ice and dust dominate on the plateau, the bottom terrace shows talus-shaped avalanche deposits, hummocky terrain and blocks with varying sizes of unknown composition. In the cliff itself alternating layers with thicknesses of up to several meters can be recognized, which eventually outcrop close to the lateral edge of the cliff. Further, the cliff appears to erode by forming disc-shaped blocks of varying size in the order of several meters, which potentially could fail in a toppling manner. NASA researchers described the dismantled material as blocks of carbon dioxide frost that dislodge from the cliff (NASA, 2015).

Using different combinations of HiRISE's bands, i.e. InfraRed Blue (IRB) and Red GreenBlue (RGB) composites as visible in figure 41, in connection to observation experiences by routinized operators (McEwen & Eliason, 2007), some additional conclusions about the observed materials can be drawn. Reddish colors in the RGB could indicate dust or dust-covered materials, as observable on the cliff itself, while frost and ice is normally blueish to whiteish in IRB and RGB, as visible on top of the cliffs plateau.
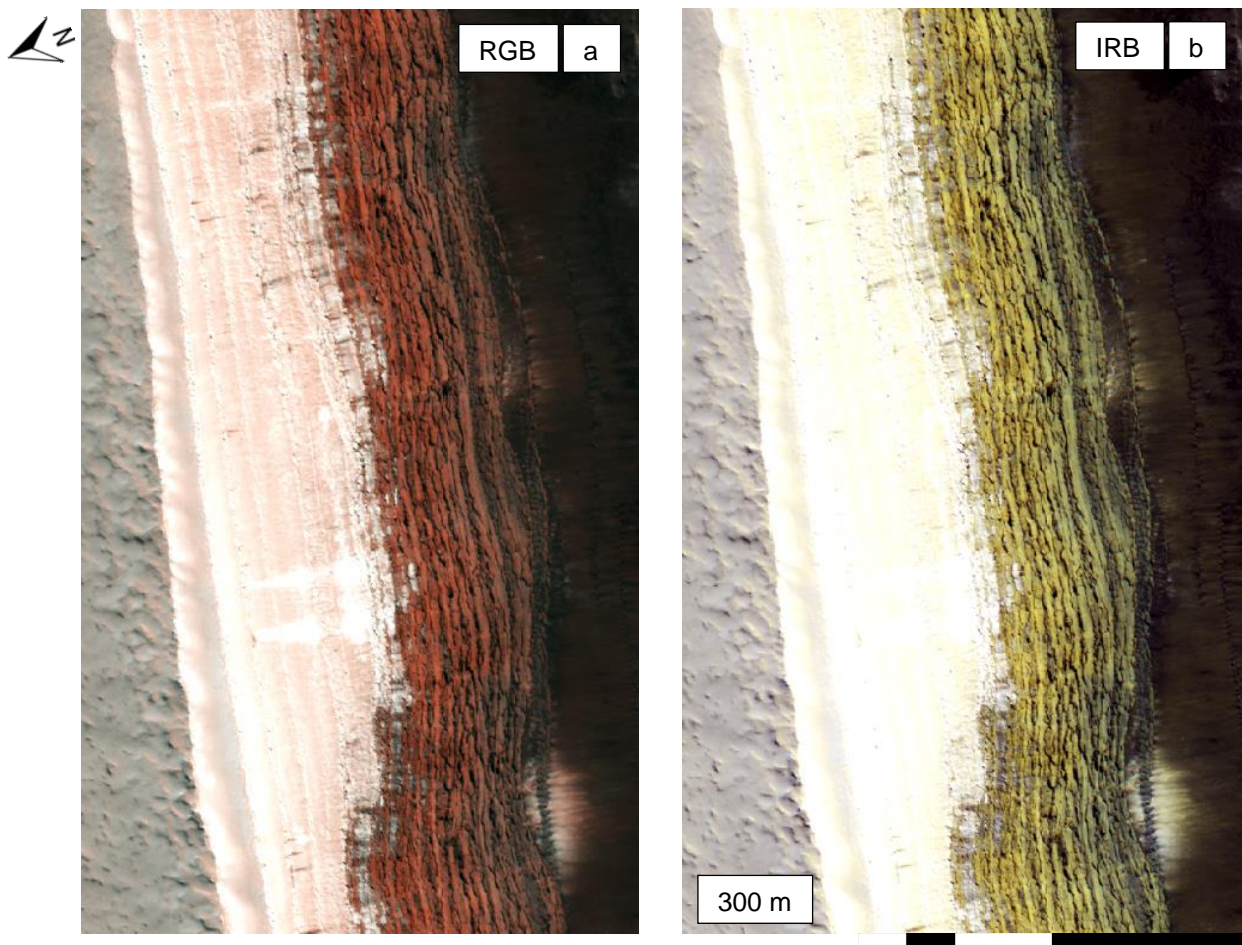
*Figure 41: Close-up of the cliff AoI: a) RGB false color, indicating a dust covered cliff (red colors) and an ice covered plateau on the left side of the image (white colors), b) IRB false color, supporting the interpretations using RGB (raw data from HiRISE, n.d., McEwen & Eliason, 2007).*

On a larger scale, the USGS map #3292 by Tanaka et al. (2014) classifies the area as Amazonian polar undivided unit (Apu) with moderate to low albedo, meters-thick layers and an overall thickness of up to 1000 m or more, consisting of ice with intermixed dust and local layers of frozen dunes with interbedded ice layers. SHARAD radargrams intersecting the cliff confirm the previous observation of a horizontal to sub-horizontal layering, as illustrated in figure 42. A section of the geological map of the AoI can be reviewed in the supplementary information section (S 11).

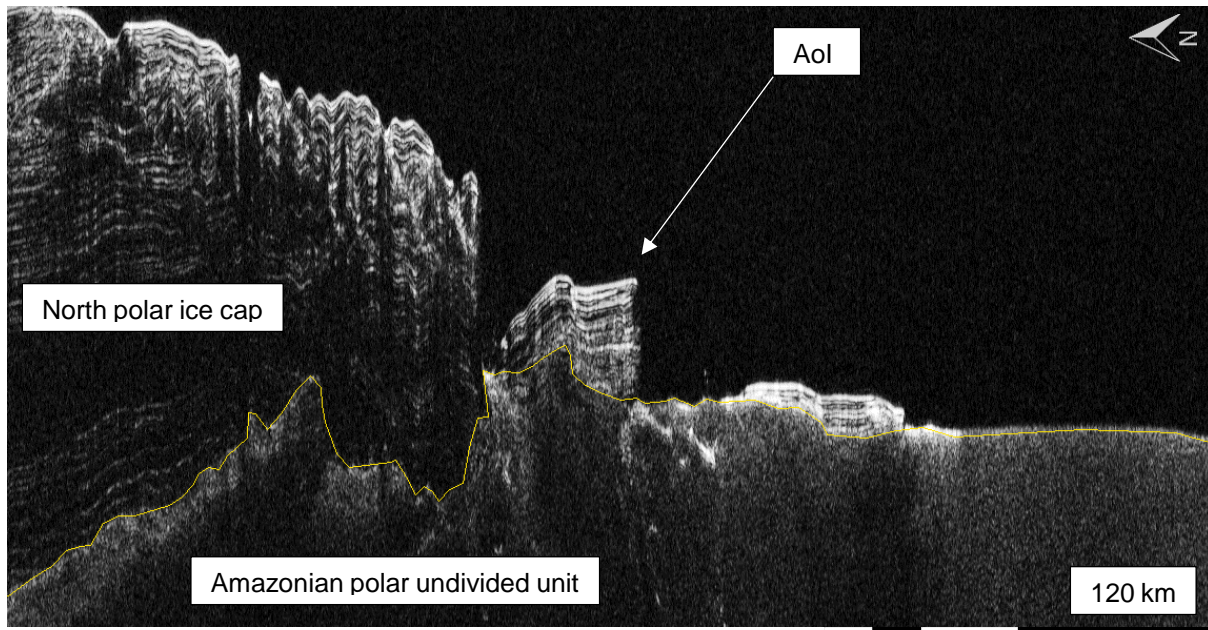*Figure 42: Vertical SHARAD radar line-profile through the Northern polar undivided deposits as well as the overlying ice cap. Yellow line suggests the contact between ice and strata. Scale is only applicable horizontally, as this is a radargram and the two-way-travel time is dependent on the di-electric properties of the medium. This data supports the idea of a sub-horizontal layering of the ice body within the AoI (white arrow) (Image Explorer, n.d.).*

From the data collected, the potential type of deformation could occur via a toppling and subsequent blockfall, which would complicate a detection with DIC, as rapid changes could be confused with noise due to their spatial incoherence. Still, DIC codes could reveal whether there might be other processes such as creep on top of the cliff or even pre-event indications of avalanches.

Besides the already applied data such as RGB and IRB composites and SHARAD radargrams, numerous HiRISE acquisitions cover the AoI, which can be utilized for input image generation and a DIC analysis. Due to the avalanche activity, NASA stated having a major interest in the cliff and manually monitors the frequency and extent of slope failures in the region. The temporal baseline is remarkable, with the first image taken in November 2006 and the latest image from April 2017, with a total of 100 images up to present. Time intervals between single images vary between days to weeks, while during Martian autumn and winter no acquisitions are made at all; it is assumed that the cliff's activity is bound to the seasons, which is why images are only taken during spring and summer. The quality of the images is generally high, although some data cannot be used due to CCD malfunctions. While the default GSD of HiRISE is 0.25 m per pixel, a significant amount of the images from this area are only available in 0.5 m per pixel spatial resolution for an unknown reason. Further, some images do not cover the entire AoI, which disqualifies them as input images for DIC codes. Those limitations reduce the effective sequence of usable images down to 54 acquisitions over 5 Martian seasons, i.e. Earth seasons 2007/08, 2009/10, 2011/12, 2013/14 and 2015/16. As HiRISE is a camera system with a very narrow field of view, images with a high emission or incidence angle are particularly difficult to utilize; this impediment further reduces the amount of usable images down to a number of 33. This is directly connected to the orthorectification process; details will be explained in the next chapter. CTX images were not used here, as the expected displacement scale is too small to be recognized with the large GSD of 6 m per pixel.
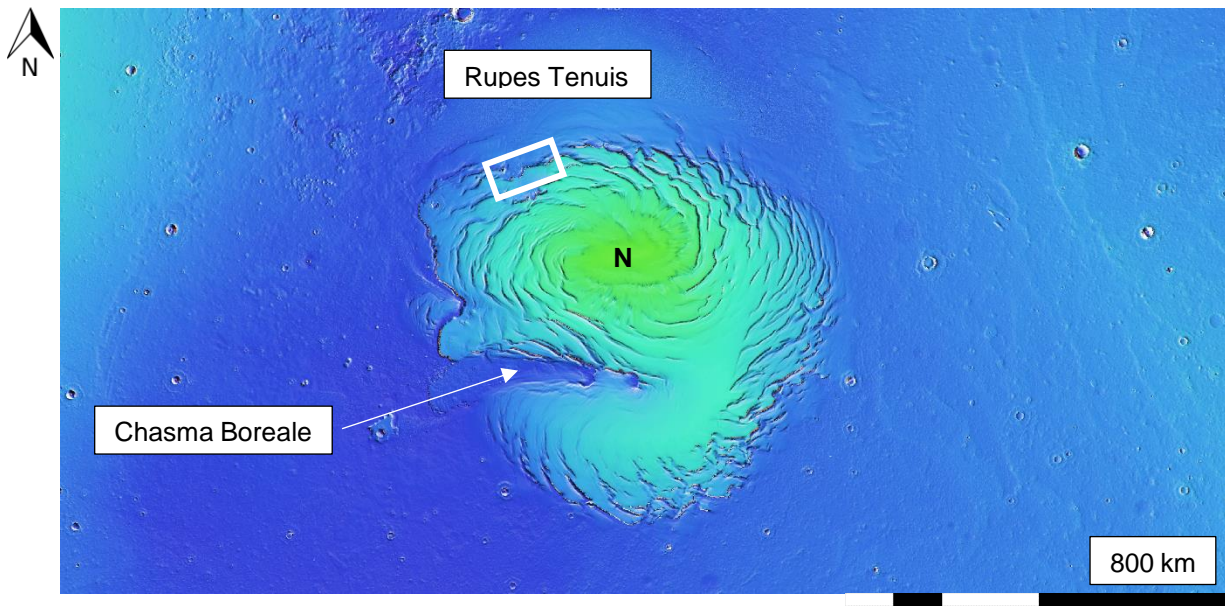
*Figure 43: MOLA colorized elevation map of Mars with the cliff AoI close to Chasma Boreale marked with a white rectangle. Green colors indicate higher elevations, blue colors lower ones (Christensen et al., 2009).*

## 5.2 Methods

Due to the limited amount of available pre-processed data, a more comprehensive second phase study requires the processing of raw imagery from Martian satellites, particularly from the MRO. This enables a greater degree of freedom in the selection of surface targets as well as the application of input images with maximized temporal resolution. However, MRO raw data processing is challenging and involves multiple processing steps as well as significant computation time, especially for the large HiRISE high-resolution imagery data sets.

### 5.2.1 Orthoimage production

In general, orthorectification is the process of projecting a raw image onto a surface, thus creating a nadir or top-down map view of the original image, which is to scale and reflects true distances on the photographed surface. In other words, an orthoimage theoretically lacks any influence by distortions such as surface curvature, incidence angle or camera parameters. As DIC requires input images taken from the exact same position, which is difficult using satellite imagery, orthorectification of all acquisitions is critical. Whereas factors such as incidence angle or camera parameters are precisely known or are the same for all different acquisitions, the relief of the scanned surface is likely to change. Thus, in order to remove influences by the topography, a precise DEM of the corresponding AoI with an appropriate spatial resolution is necessary, reflecting the elevation of the terrain.

The handling and processing of raw MRO data requires the use of special software tools. For the study on hand, ISIS3, or Integrated Software for Imagers and Spectrometers, by the USGS (Becker & Anderson, 2013) has been used in combination with ASP, or Ames Stereo Pipeline, by NASA (Shean et al., 2016). Raw data was retrieved online from the Caltech Jet Propulsion Laboratory's (JPL) Planetary Imaging Atlas (PDS). Finally, the quality analysis of the produced data was performed with ArcGIS 10.4.1 and Matlab R2016a. The CTX and HiRISE camera demand different steps of processing and computation time. As HiRISE's field of view is very narrow and the data volume of an image is very large due to the high spatial resolution, the manipulation is complicated and time-intensive. In turn, CTX acquisitions consume less computation and operator time.

The processing of a CTX orthoimage starts with the download of the demanded raw EDR (Experimental Data Record) .IMG file from the PDS, representing the level 0 data product without any pre-processing. Subsequently, the .IMG is input into ISIS3 while being transformed into a new file format, .cub. Further, the SPICE kernels of the image are initialized, which contains vital label data such as target name, date and time, spacecraft position or instrument pointing, before the .cub files are transferred to ASP. In order to enhance the accuracy of the produced output DEM and orthoimages, the error introduced by the satellite position and orientation has to be corrected prior to any other processing, a technique called bundle adjustment. It simultaneously adjusts the properties of involved cameras and the 3D locations of the objects they see in order to minimize the error between the estimated, back-projected pixel locations of the 3D objects and their actual measured locations in the captured images (Shean et al., 2016). Subsequently, two bundle adjusted CTX images of the same AoI are stereo correlated in order to produce a point cloud file, here using a parabola fitting algorithm. The application of this specific stereo correlation algorithm yielded best results in terms of matching quality and computation time in comparison to the simple affine correlator algorithm, offered by ASP: This code uses a Bayes Expectation Maximization (EM) mode without any noise removal for optimized speed and should achieve less mismatches, in theory. Due to this insight, the third available algorithm, a Bayes EM with noise removal, has not been evaluated, as it requires about five times as much processing time as the other codes and results were not expected to be better. A visual comparison of both stereo codes can be reviewed in the supplementary information section (S 15). During the stereo correlation, several sub-routines perform an image registration, pre-processing, disparity map initialization, sub-pixel refinement, outlier rejection, hole filling and finally triangulation. One output of this process is a GoodPixelMap, which gives insights into the overall quality of the cross-correlation. Next, the retrieved point cloud is meshed, producing a DEM of the AoI. The spatial resolution of the DEM is hereby manually set and was defined as a 24 m grid for this study, i.e. the original GSD times four. After a positive assessment of the DEM's quality, the bundle adjusted .cub files used for the stereo correlation are map-projected onto their DEM, which corresponds to their orthorectification. The final outputs are a DEM .tif file and two orthoimage .tif files of the AoI, ready for use with DIC codes. Figure 44 visualizes the processing pipeline. Using a personal computer with advanced performance, the entire processing cycle requires a computation effort of around 10 hours form the EDR to the output products.
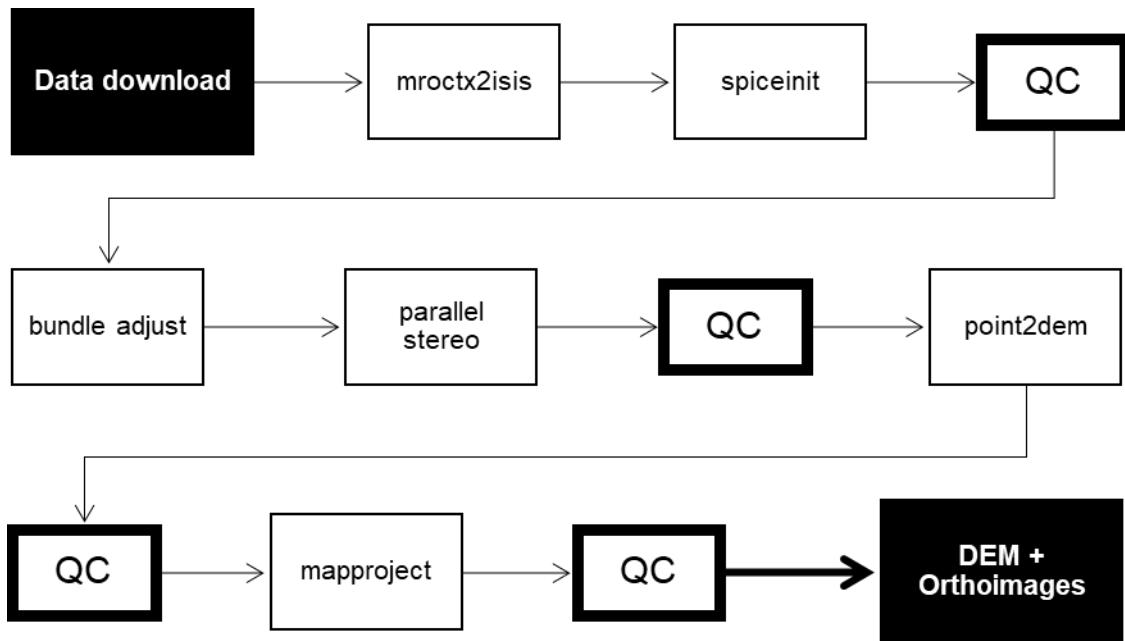
*Figure 44: CTX DEM & Orthoimage production pipeline for ISIS3 and ASP. QC means quality control and is performed regularly to assure optimized processing and results.*

As HiRISE acquires images using several CCD sensors instead of only one like CTX, all 20 image stripes from all CCDs need to be downloaded from the PDS, to start with the processing. Due to a CCD failure, the amount of image stripes reduced to 18 up to date. Next, an ASP algorithm needs to be invoked, which transforms the .IMG stripes to .cub and initiates the SPICE kernels. Additionally, it projects all single stripes in the perspective of CCD RED5 and performs a de-jittering, i.e. a correction of errors introduced by slight off-orbit deviations by the sensor causing problems in the reconstruction of the digital image data (Shean et al., 2016). Finally, all stripes are mosaicked and normalized, producing a single HiRISE output image. Due to the significant size of the mosaicked images, which can exceed 8 GB, the targeted AoI has to be cropped out of each mosaic, to reduce processing time. All subsequent steps are equal to the ones performed for CTX images, i.e. a bundle adjustment, stereo correlation, DEM meshing and a final map projection. The grid of the DEM was defined as 5 m, i.e. 20 times the original GSD to account for potential stereo mismatching errors and to increase stability. A comparison and assessment of different grid sizes can be reviewed in the supplementary information section (S 16). The final DEM product was saved as a stereographic projection, as this specific AoI is situated close to the North Pole and potential map-projection related distortions should be avoided. The outputs are the same as well, one DEM and two orthoimages. It has to be noted that computation time is significantly increased for HiRISE, even for cropped areas: With a personal computer and advanced performance hardware the complete procedure requires around 30 hours. Figure 45 illustrates the HiRISE processing pipeline.
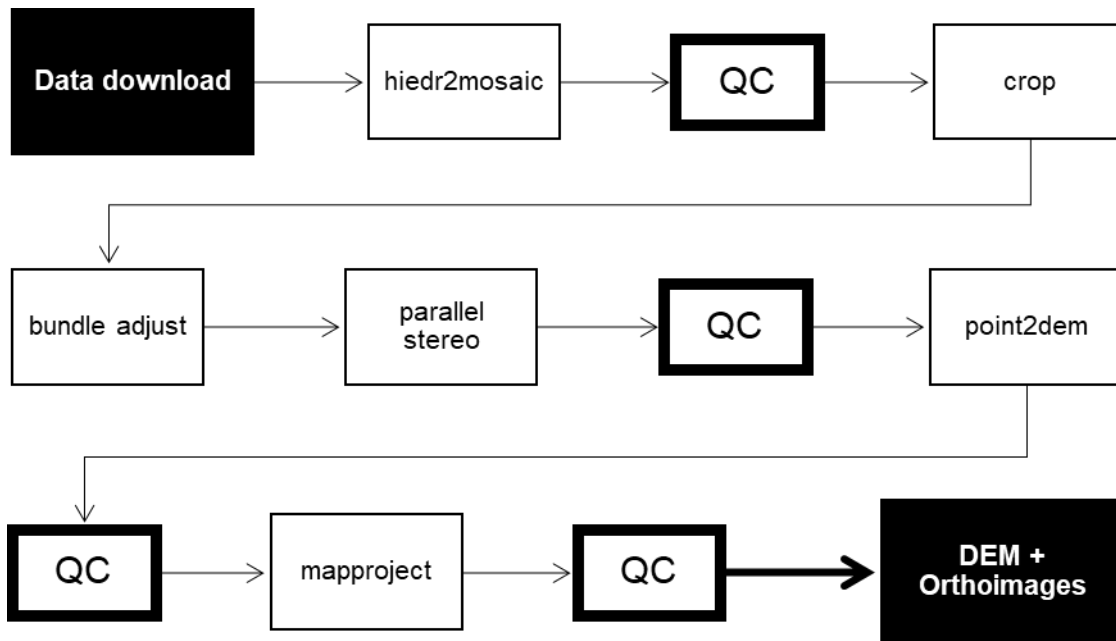
*Figure 45: HiRISE DEM & Orthoimage production pipeline for ISIS3 and ASP. QC means quality control and is performed regularly to assure optimized processing and results.*

Due to its larger GSD and wider field of view, CTX appears less susceptible to errors during the data processing. HiRISE, however, is subject to severe limitations, predetermined by its sensor properties. Particularly during the stereo correlation, deficiencies can occur in the form of correlation mismatches, subsequently causing holes in the resulting point cloud file. For example, the stereo algorithms struggle to match corresponding parts if the illumination conditions have changed from one input image to the other and identical objects on the surface cast different shadows. Further, input images with a large emission angle difference can cause mismatches, as the distance between corresponding parts in the images becomes just too wide due to geometric distortion. In the particular case of the Rupes Tenuis cliff, the steep relief exacerbates correlation, as the use of images with an unfavorable viewing direction and emission angle might not be able to picture the slope of the cliff, e.g. if it is sub-parallel in relation to the sensor's LOS. In such a case, stereo matching would also fail. Another property of the Martian cliff is its remarkable activity: any alteration of the surface texture or appearance by e.g. a slope failure will also cause correlation mismatches and therefore holes in the point cloud. All imperfections in the point cloud will reflect in the produced DEM mesh and will directly influence the orthorectification: all parts without elevation information in the DEM will not be used by the map projection algorithm to project the images, i.e. parts of the image might be missing. As these parts are likely to be situated in the slope of the cliff due to the described reasons, this image data would be useless for DIC, because the information of interest, i.e. the slope of the cliff with all potential deformation over time, is not contained in the image.

However, there is a possibility to account for poor stereo correlation by filling the holes in the DEM artificially, e.g. by extrapolating the vicinity values over the respective hole. Still, such a procedure does not represent the actual relief, but assumes one. This problem increases with increasing hole size, as the extrapolation will differ from reality more and more. Generally, DEM hole filling is considered as being very critical and potentially jeopardizing for the quality of the final orthoimages. For this study, only

very conservative hole filling was performed. The quality of the stereo correlation needs to be at an absolute maximum to guarantee an optimized orthorectification of the selected imagery.

The output data, i.e. the GoodPixelMaps, DEMs and orthoimages, are subject to a quality assessment prior to input into the DIC algorithms. As a first measure, a GoodPixelMap will indicate, whether the stereo correlation was successful and where holes in the point cloud exist. Only promising GoodPixelMaps were selected for further processing of the data. Figure 46 illustrates a comparison between a good and a poor PixelMap.
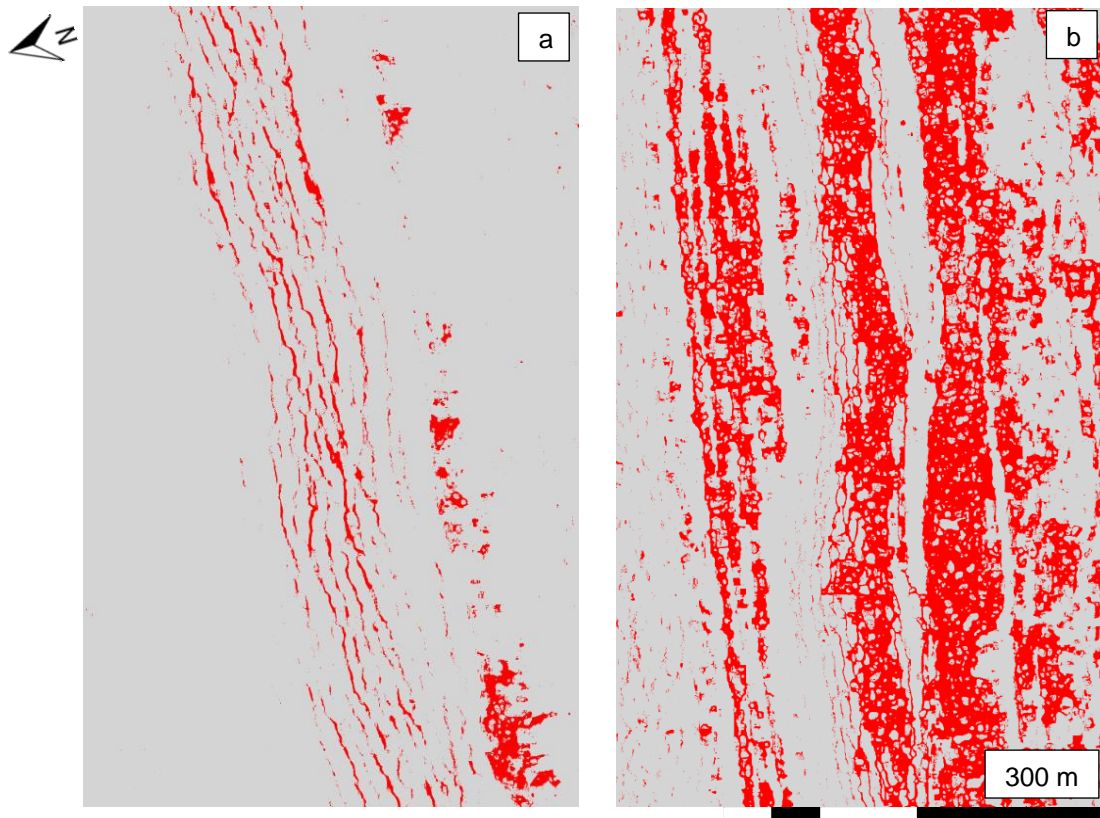


*Figure 46: GoodPixelMaps a) from 2008 with a good quality and b) from 2012 with a poor quality, red pixels indicate correlation mismatches. DEM meshing algorithms will struggle to process b), while a) is likely to deliver a high-quality DEM (raw data from HiRISE, n.d.).*

Meshed DEMs were reviewed with ArcGIS by a visual check of the elevation grid as well as by use of cross-sectional plots. Priority was given to an intact slope area as the main interest of this study. For unknown reasons, the talus and plateau areas are prone to be noisy and erroneous, but this does not affect the actual AoI, the slope of the cliff. Typical observed errors are therefore remaining holes in the DEM, extreme outlier values, poor hole fillings and apparently correct, but misleading and false stereo matches, mimicking incorrect topography. Imperfect hole fillings are likely to cause severe projection errors during orthorectification, while misleading stereo matches occur due to unknown reasons and lead to incorrect map projections as well. In addition, they could induce wrong conclusions about the evolution of the cliff over time. For these reasons, any occurrence of these errors in the slope area was not tolerated.
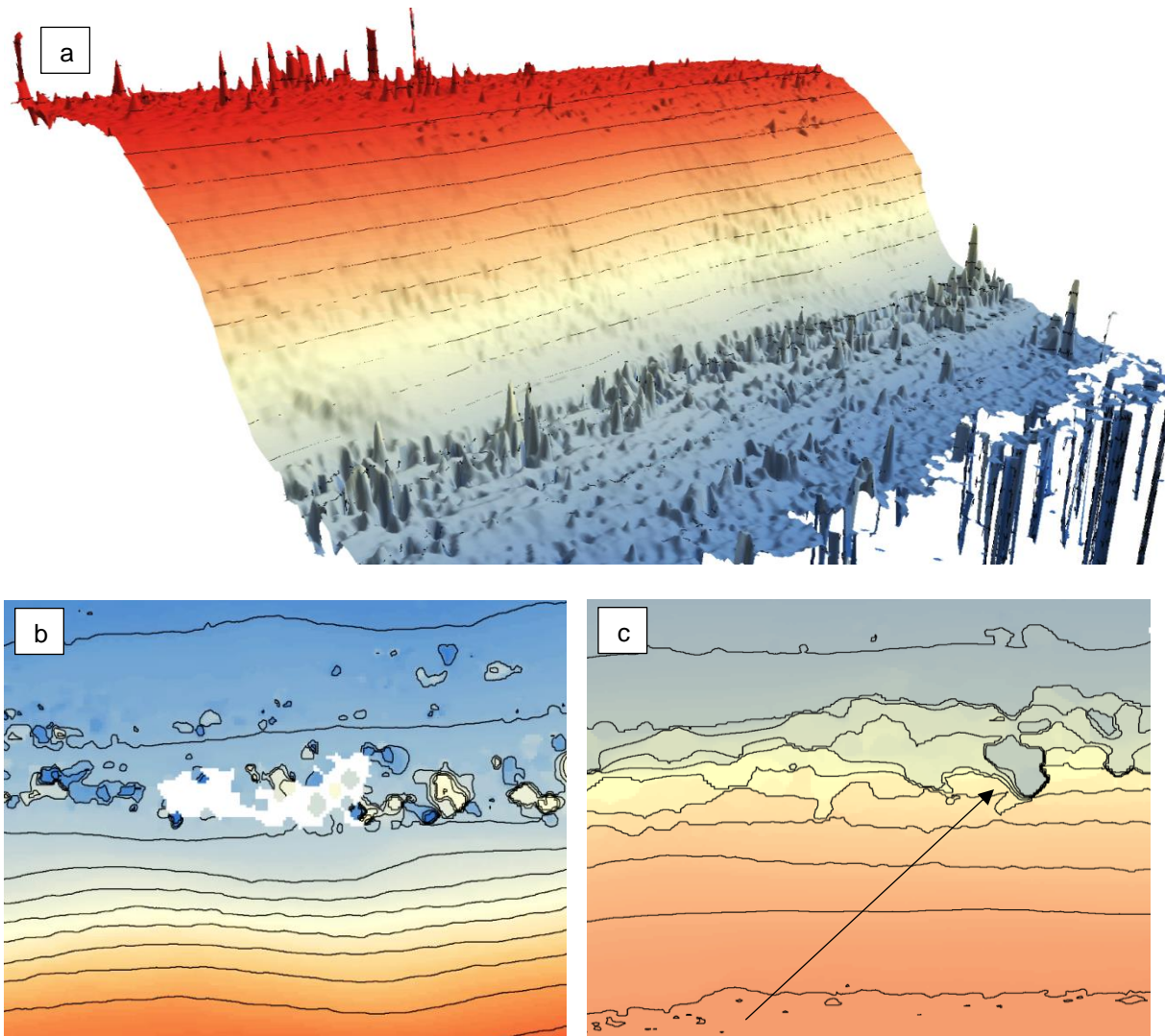
*Figure 47: Overview of the most common stereo correlation and DEM meshing failures & artefacts: a) mismatches lead to misinterpretations and finally to outliers, creating an extremely rough fake-terrain, b) poor stereo correlation and inappropriate hole filling lead to holes in the DEM (white area), c) bad stereo correlation leads to wrong terrain derivation, thus creating corrupt DEMs with incorrect and misleading topography (black arrow). Not to scale, only meant for qualitative analysis (raw data from HiRISE, n.d.).*

If not discovered or prevented, the mentioned imperfections in the DEM are likely to cause orthorectification errors. These features are shown in figure 48 and appear as blurred or twisted forms. Obviously, such structures will cause a detection of false deformations by the DIC codes and have to be avoided. During this work it was found that this type of artefact and its occurrence is only poorly understood, even by the ASP developers. This further underlines the challenge of producing high quality DEMs and orthoimages on Mars in areas where slope displacements could occur due to relief and gravity. Empirically, in map projections of .cub files with emission angles > ~7° these features need to be expected, which indicates that they form depending on the emission angle and locally poor quality of the underlying DEM. Thus, an optimization of the quality of the elevation model by selecting stereo pairs with short temporal difference and equal illumination conditions in combination with the application of low emission angle images assured a sufficient quality of the produced DEMs and orthoimages.
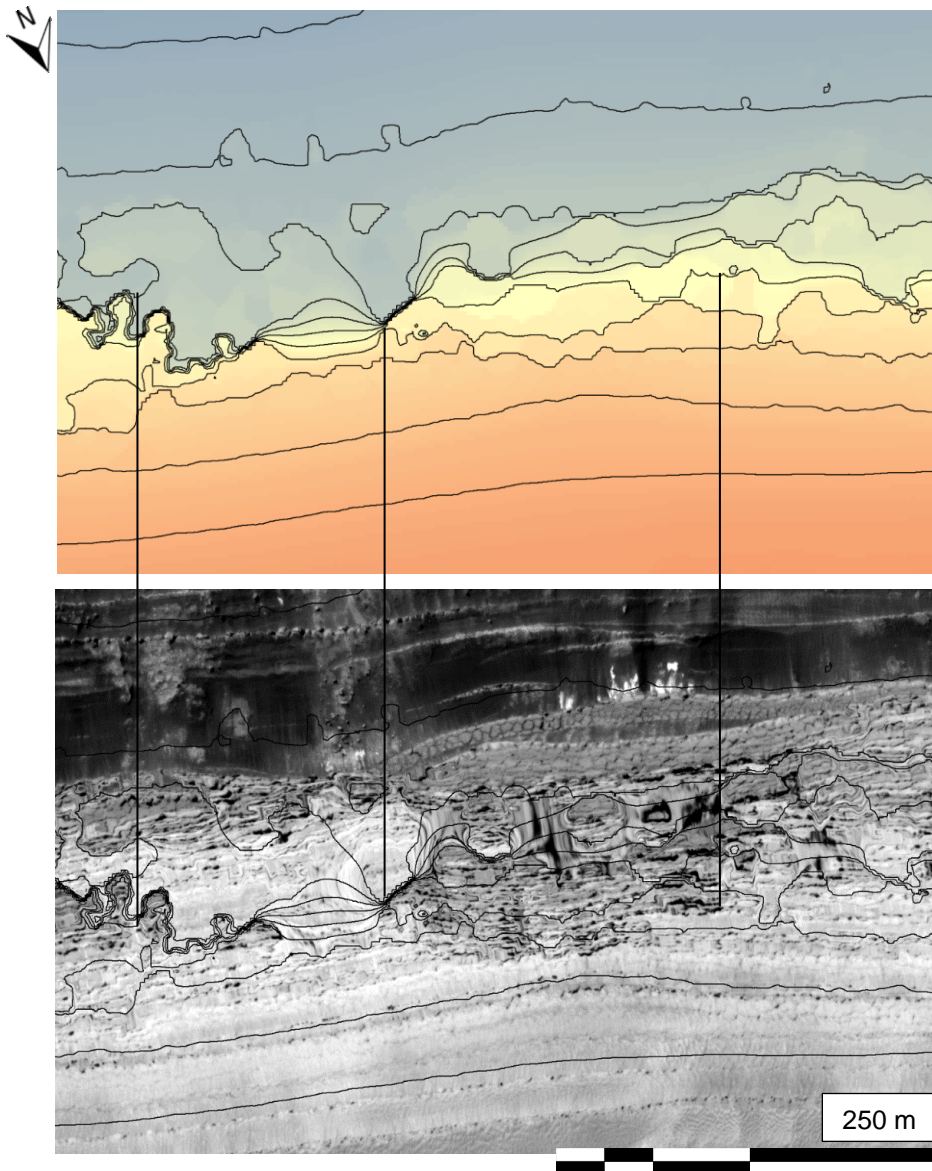
*Figure 48: Example of the influence of a poor DEM onto the orthorectification process. The resulting image is heavily deformed (black lines) and cannot be used for DIC analysis. Degree of image deformation is dependent on the emission angle of the map projected acquisition, a larger angle will further decrease the quality (raw data from HiRISE, n.d.).*

## 5.2.2 Investigation plan

The first phase of the exploration of Mars with DIC aimed to further validate the general procedure in combination with Martian imagery and to identify promising AoIs on the ground. During the second stage, these particular locations were targeted and detailed DIC research was performed. Hereby, a major part of phase two was the processing of Mars orbiter raw data, which can be utilized for DIC.

Finally, four AoIs were selected for phase two, which were promising for a DIC application and which have already been described in detail. However, for these areas no sufficient image data exists or has been processed by NASA or other institutions. By using HiRISE and CTX raw data from the MRO, high quality data products for a DIC application, i.e. DEMs and orthoimages, were produced, applying ISIS3

and ASP. To reach a sufficient level of quality, this data processing required an intensive trial and error approach, lasting over several months, caused by the complexity and computational effort of handling ultra-high resolution optical image data, particularly HiRISE acquisitions.

For the three AoIs covered by CTX, input image emission angles were not as decisive for the processing success as for HiRISE, which is why the selection process was almost exclusively based on criteria such as the available maximum temporal baseline in combination with similar illumination conditions. For the application of CTX only two images were selected and processed, to generally verify, whether the AoIs are deforming at all; in all three cases, the selected images represent the longest temporal baseline possible. Following DEM and orthoimage creation, both produced images were Wallis filtered to enhance the dynamic range and to improve DIC results, as found during the CdV case study. Finally, the FFT code was applied on the ortho pairs using different search window sizes and filters, in order to identify any recent surface processes. Following equation 3.5-1, window sizes with 32 by 32 and 64 by 64 pixels were used to optimize matching and quality.

For the cliff AoI, relevant information of all available acquisitions was collected at first, in order to perform a systematic selection of potential input images. Twelve images were selected from 100 acquisitions of the AoI, which were taken from the beginning of MRO's scientific interest in this region of Mars in 2008 until present. Due to the sensitivity of HiRISE image data and the selection and production of only the highest-quality output, ~90% of this imagery could not be used for processing (cf. to chapter 5.2.1 for details). Still, images from all five Martian years, i.e. Earth years 2007/08, 2009/10, 2011/12, 2013/14 and 2015/16, were utilized, although data availability and quality in 2012 was not sufficient to produce appropriate outputs for this year. As image sizes drastically increased the processing time, each input image was divided into two small sub-parts called Primary (P, the eastern half of the image) and Secondary (S, the western half of the image). Area P includes the part of the cliff, where the avalanche was captured by HiRISE in 2008 (cf. figure 32). Both tiles were processed independently, which decreased computation time remarkably. Figure 49 displays this tiling process of each input image.
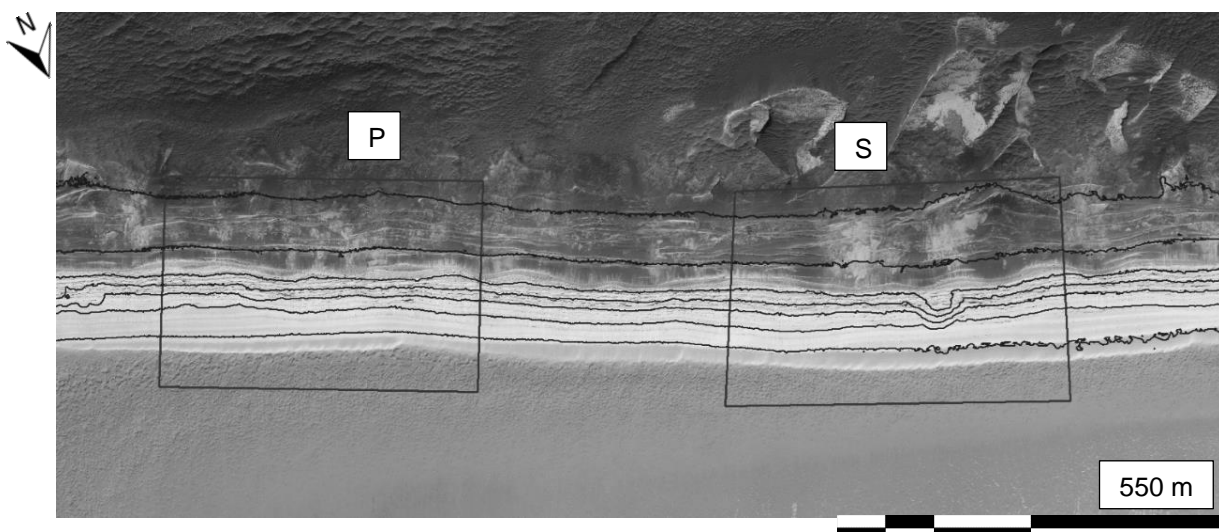


*Figure 49: Overview of the Primary (P) and Secondary (S) tiles for computation acceleration. The avalanche shown by figure 32 occurred in P in 2008 (raw data from HiRISE, n.d.).*

Finally, for 2007/08, 2 DEMs and 4 orthoimages, for 2009/10, 2 DEMs and 4 orthos, for 2013/14, 1 DEM and 2 orthos and for 2015/16, 1 DEM and 2 orthoimages were produced, i.e. a total of 6 DEMs and 12 orthorectified images over 8 Earth years. The creation of each DEM required the use of two input images, which were then orthorectified using the created DEM; therefore, for each created DEM, two orthoimages were produced using their "own" or "personal" DEM. Two orthoimages were produced twice, i.e. March 29th, 2008 and March 28th, 2010, but by using two different DEMs for each, resp. DEM 2829 and DEM 294 for the 2008 ortho and DEM 2228 and DEM 2819 for the 2010 ortho. Table 13 summarizes the image information.

*Table 13: Overview of selected imagery for ISIS3 and ASP processing, most important data for the selection procedure is shown, such as emission and illumination angle. The overlapping DEMs were used to produce two orthoimages with the same input image but a different DEM to perform a quality assessment subsequently.*

| ID | DEM ID | DEM ID | Year | Month | Day | Emission angle | Illumination angle | Resolution |
|---|---|---|---|---|---|---|---|---|
| PSP_007826_2640 | DEM 2829 | | 2008 | March | 28 | 6.2° | 65° | 0.25 m/pixel |
| PSP_007839_2640 | | DEM 294 | 2008 | March | 29 | 0.5° | 65° | 0.25 m/pixel |
| PSP_007918_2640 | | | 2008 | April | 4 | 2.7° | 64° | 0.25 m/pixel |
| ESP_017122_2640 | DEM 2228 | | 2010 | March | 22 | 4.2° | 61° | 0.25 m/pixel |
| ESP_017201_2640 | | DEM 2819 | 2010 | March | 28 | 0.7° | 61° | 0.25 m/pixel |
| ESP_017478_2640 | | | 2010 | April | 19 | 3.8° | 60° | 0.25 m/pixel |
| ESP_033842_2640 | DEM 1520 | | 2013 | October | 15 | 0.7° | 70° | 0.25 m/pixel |
| ESP_033908_2640 | | | 2013 | October | 20 | 2.7° | 69° | 0.25 m/pixel |
| ESP_042875_2640 | DEM 1925 | | 2015 | September | 19 | 0.6° | 67° | 0.25 m/pixel |
| ESP_042954_2640 | | | 2015 | September | 25 | 3.9° | 66° | 0.25 m/pixel |

After processing, the retrieved orthoimages were cropped to the same dimensions using a visually determined control point on the ground, then being Wallis filtered. The basic intention was to use the two overlapping orthoimages from March 29th, 2008 and the two orthos from March 28th, 2010, produced with identical input images but different DEMs, for an initial visualization of quality, by using DIC. As the two orthoimages should be perfectly identical, i.e. DIC would indicate entirely stable conditions (all green in NS and EW direction). If such stable conditions would be shown by DIC, the consequence would be that the orthorectification procedure itself produces a quality sufficient for the desired analysis, despite using different DEMs.

Subsequently, the complete image stack of 10 orthoimages was used for a complete DIC analysis, which profited from the different available temporal baselines from 1 day to more than 7.5 years. As for the CTX images, the same pipeline as for the CdV study was applied (cf. figure 9), using varying search window sizes. Following a systematic pattern of testing (figure 50), the available orthoimages were tested in all possible combinations, in order to retrieve information from different temporal baselines and to identify images with potentially poor or insufficient quality, which e.g. introduce fake deformations, that are only visible in all results produced with one particular image, but not in any other combination. The goal was to identify large or spatial, e.g. creeping parts, and small or object scale, e.g. rockfall, deformations of the observed Rupes Tenuis cliff.
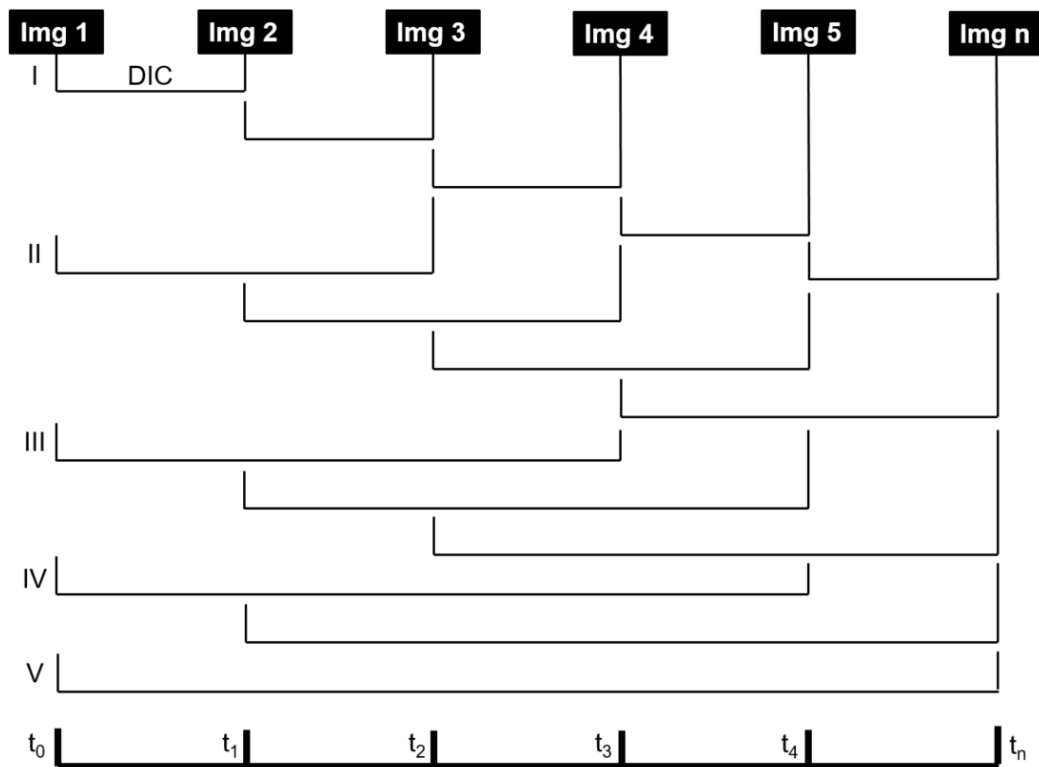
*Figure 50: Scheme for DIC stacking and testing for the cliff AoI. Images (Img) in black boxes were taken at different times, e.g. 2008 (Img 1), 2010 (Img 2) and 2014 (Img 3), and so on. Lines between the images indicate DIC runs with both respectively connected acquisitions. Testing of the longest possible temporal baseline (V) is possible by connecting Img 1 and Img n.*

Small scale failures, such as rock- or icefalls, were identified, counted and measured in terms of their dimensions in all available years, i.e. in between the respective Martian spring or summer times, namely 2007/08 to 2009/10, 2009/10 to 2011/12, 2011/12 to 2013/14 and 2013/14 to 2015/16. Only for this particular investigation, another image from January 19th, 2012 was produced. However, this image had to be map projected without bundle adjustment, as insufficient data were available for the same time period, which means that it contains severe geometric distortions, caused by a lack of camera parameter correction, and cannot be used for DIC. Still, any small-scale changes, such as cliff failures, could be recognized through the contained noise and artefacts, which is why its application for this specific task is acceptable. An image subtraction code written in Matlab R2016a has been utilized to generally investigate the occurrence of changes and to potentially support the findings of DIC by comparing input images from 2007/08 and 2015/16, using a binary mask visualization. Additionally, a code has been implemented in Matlab R2016a to co-register, adapt, smooth and subtract the respective DEMs of the listed years, in order to perform an elevation model-based change detection.

This enabled a further confirmation of failures, identified with DIC, and potentially allowed the derivation of 3D information about the failures, i.e. volume estimations. With this information, a coarse temporal distribution of cliff failures in combination with their magnitude was determined and the measured volumes were plotted against time, visualizing the activity of this Martian cliff. Finally, all gathered information was integrated to develop a conceptual kinematic model for this AoI, considering the topography, morphology, geology, avalanche activity and other parameters.

## 5.3 Results

### 5.3.1 Results CTX camera

The results of the DIC analysis of the CTX data for the GLF at the Eastern border of Hellas Planitia between the Centauri and Hellas Montes are shown in figure 51. Temporal baseline was ~ 9.5 years.
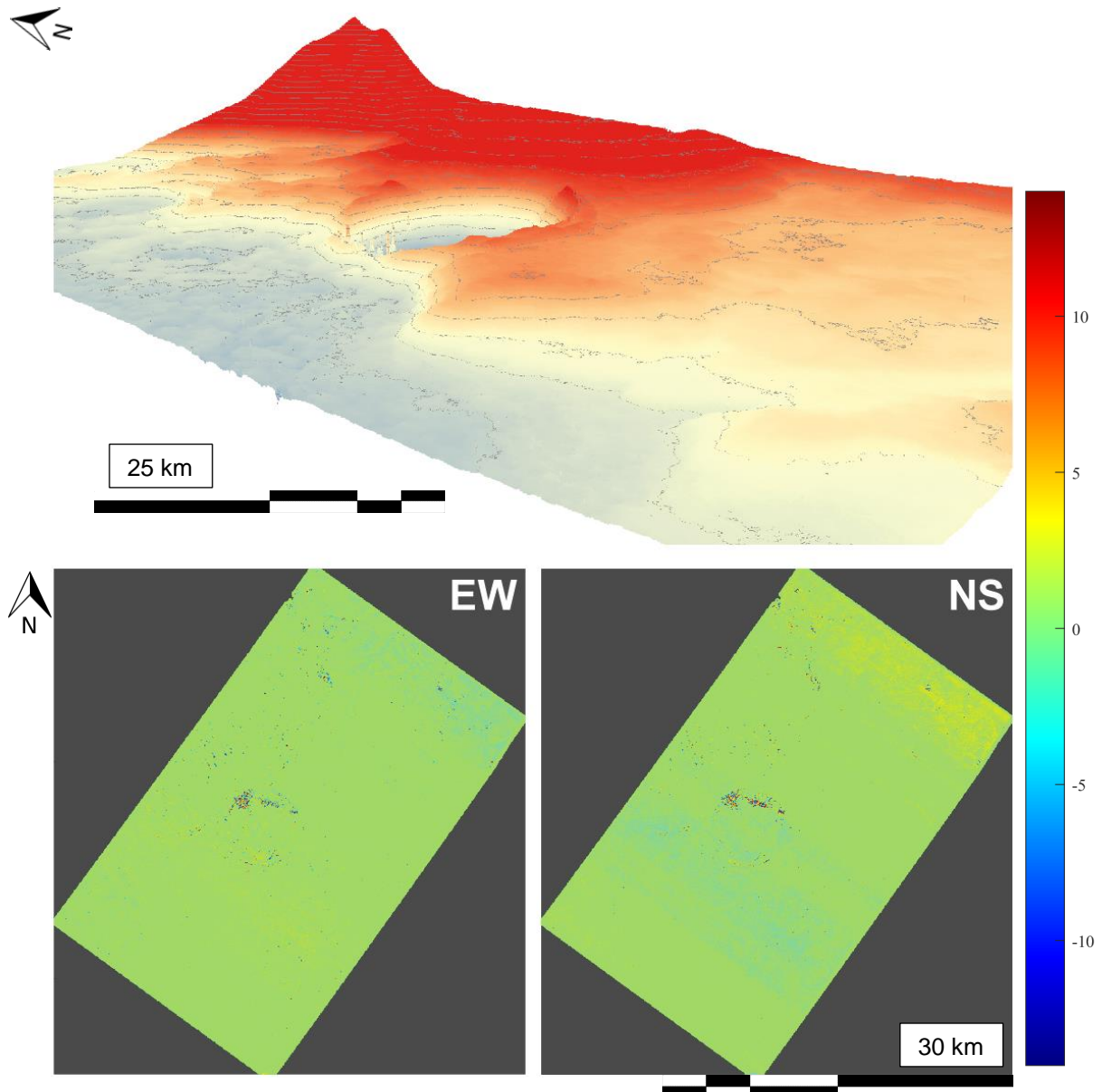


*Figure 51: DIC analysis of the GLF AoI. Elevation model shows the terrain, red colors represent higher elevations, blue colors represent lower elevations, isohypses have a 50 m vertical distance, elevation is slightly exaggerated to enhance visualization. In the center of the image, Pentincton crater is visible. On the bottom left, the EW result is presented, on the bottom right, the NS result. The GSD is 6 m per pixel and the DIC run was performed with wi 64 pixels. Scale is in [pixel] (raw data from Image Explorer, n.d.).*

The investigation of the volcanoes Ceraunius Tholus and Ascraeus Mons produced the results plotted in figures 52 and 53. The temporal baselines were ~ 7.5 years for both image pairs.
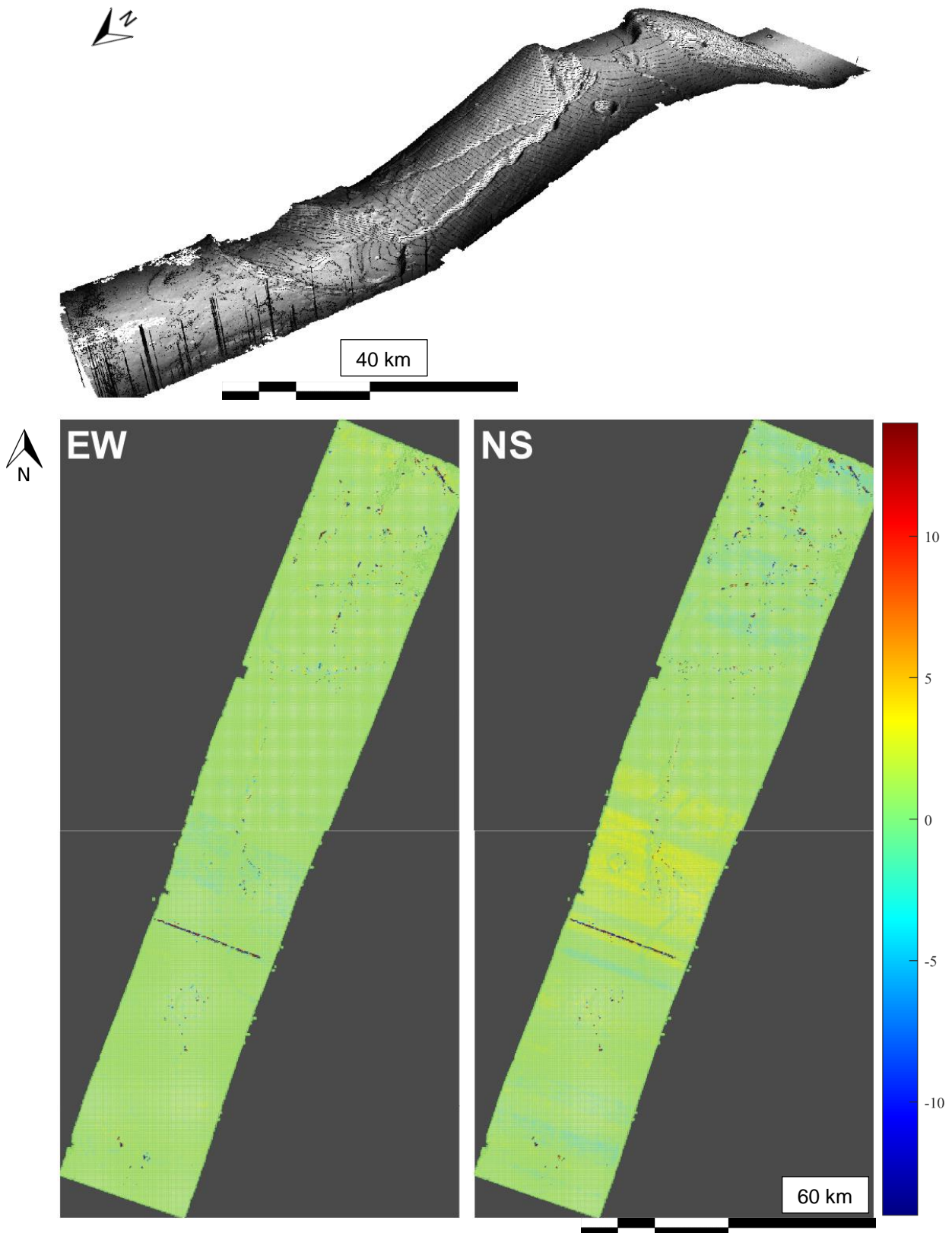
Figure 52: DIC analysis of the Ceraunius Tholus AoI. 2.5D model visualizes the terrain, isohypses have a 100 m vertical distance, elevation is slightly exaggerated to enhance visualization. Vertical artefacts in the DEM are introduced by edge effects and cannot be removed without performing a mosaic with a second DEM, which was not available. While the acquisition length is sufficient to cover the entire volcano, the width is not satisfactory to image the full volcanic edifice. On the bottom left, the EW result is presented, on the bottom right, the NS result. The GSD is 6 m per pixel and the DIC run was performed with wi 64 pixels while some linear artefacts are visible. Scale is in [pixel] (raw data from Image Explorer, n.d.).
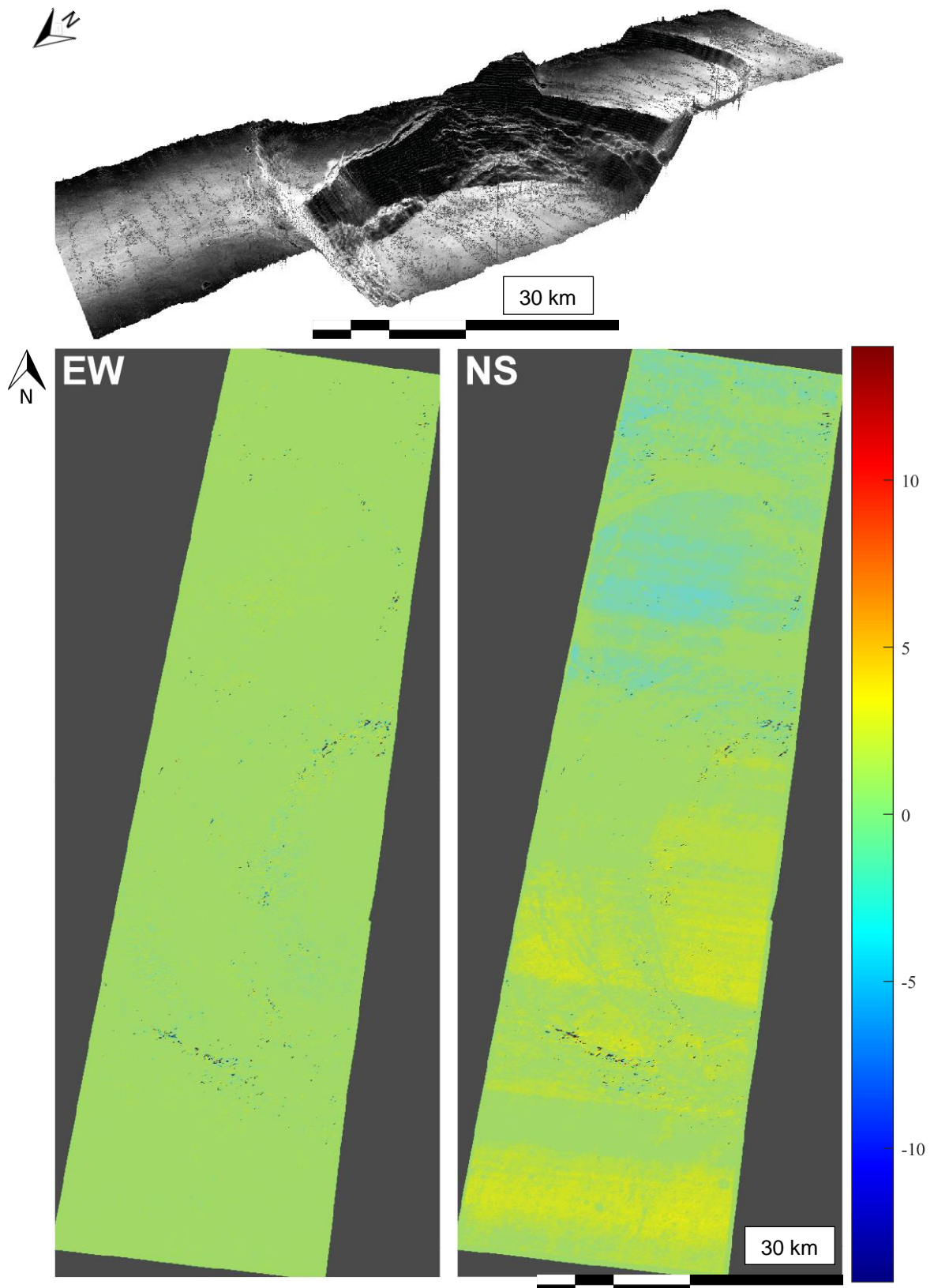
Figure 53: DIC analysis of the Ascraeus Mons caldera AoI. 2.5D model visualizes the terrain, isohypses have a 100 m vertical distance, elevation is slightly exaggerated to enhance visualization. Acquisition width is only sufficient to cover a part of the caldera. The slopes show large scarps and sacking structures. On the bottom left, the EW result is presented, on the bottom right, the NS result. The GSD is 6 m per pixel and the DIC run was performed with wi 64 pixels while some linear artefacts are visible. Noise in the offset matrices is related to changing shadows or other illumination issues. Scale is in [pixel] (raw data from Image Explorer, n.d.).

## 5.3.2 Results HiRISE camera

First, the quality of the produced orthoimages was tested by running the FFT code on two identical images, which were orthorectified using two different DEMs. Figure 54 represents the results of both test runs, for the 2007/08 pair as well as for the 2009/10 pair, but only for the P part of the acquisitions.
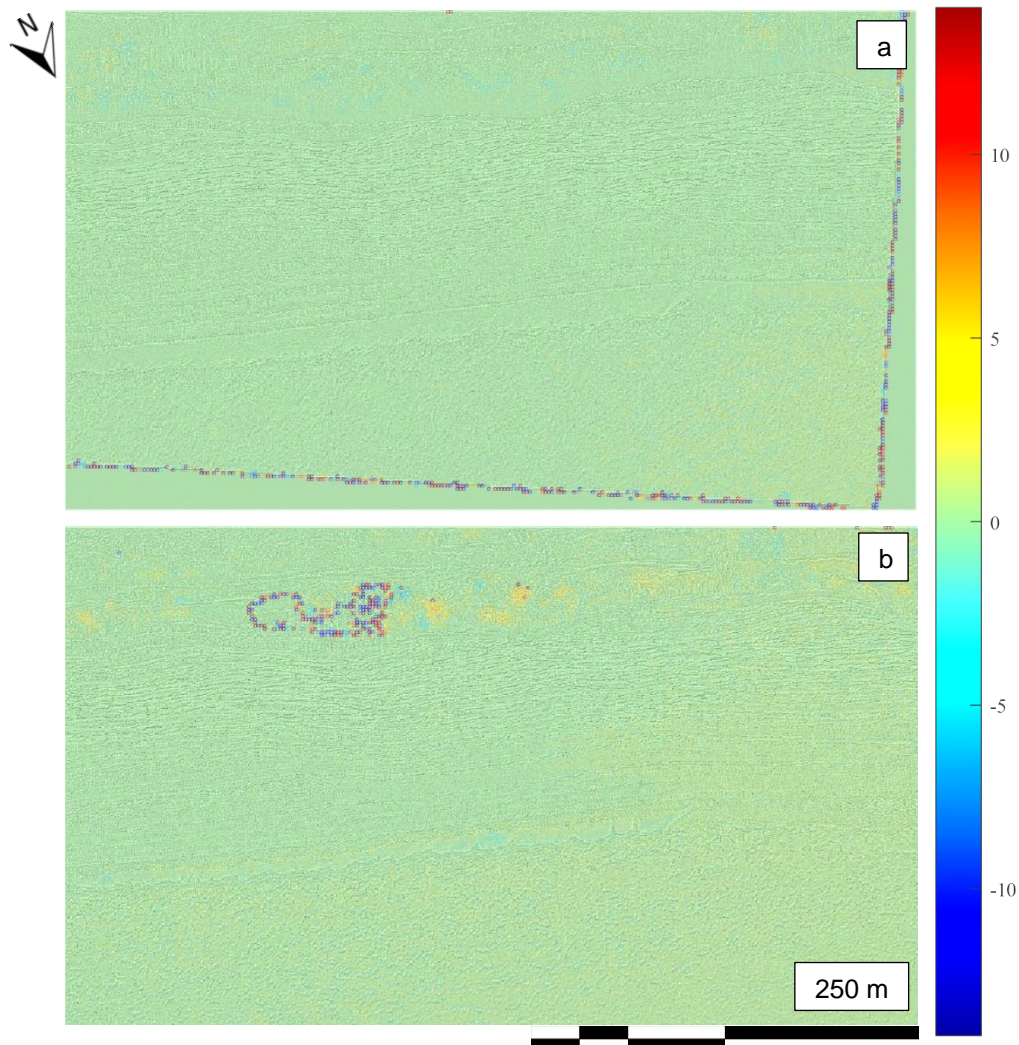


*Figure 54: Quality control of identical HiRISE images, projected on different DEMs for a) 2008 and b) 2010. Green color suggests no activity at all and therefore an almost perfect orthorectification procedure, only locally some minor noise is visible; such noise could be introduced by superficial changes (e.g. frost patches), as the original images for the DEM creation were taken with a certain time difference. Noise close to the image borders can be neglected, as can the feature in the 2010 result, which is caused by a hole in the DEM at this location. Scale is in [pixel] (raw data taken from HiRISE, n.d.).*

Some of the results of the complete DIC analysis with the FFT code are displayed in figures 55 and 56. Shown are the runs that were performed over the seasons, i.e. the 2007/08 to 2009/10, 2009/10 to 2011/12, 2011/12 to 2013/14 and 2013/14 to 2015/16 pairs as well as the run with the maximum temporal baseline. Only the y (NS) offsets of tile P are represented in figure 55, due to space limitations and due to the similarity of the EW – NS output visualizations: noise is equally reflected in both.
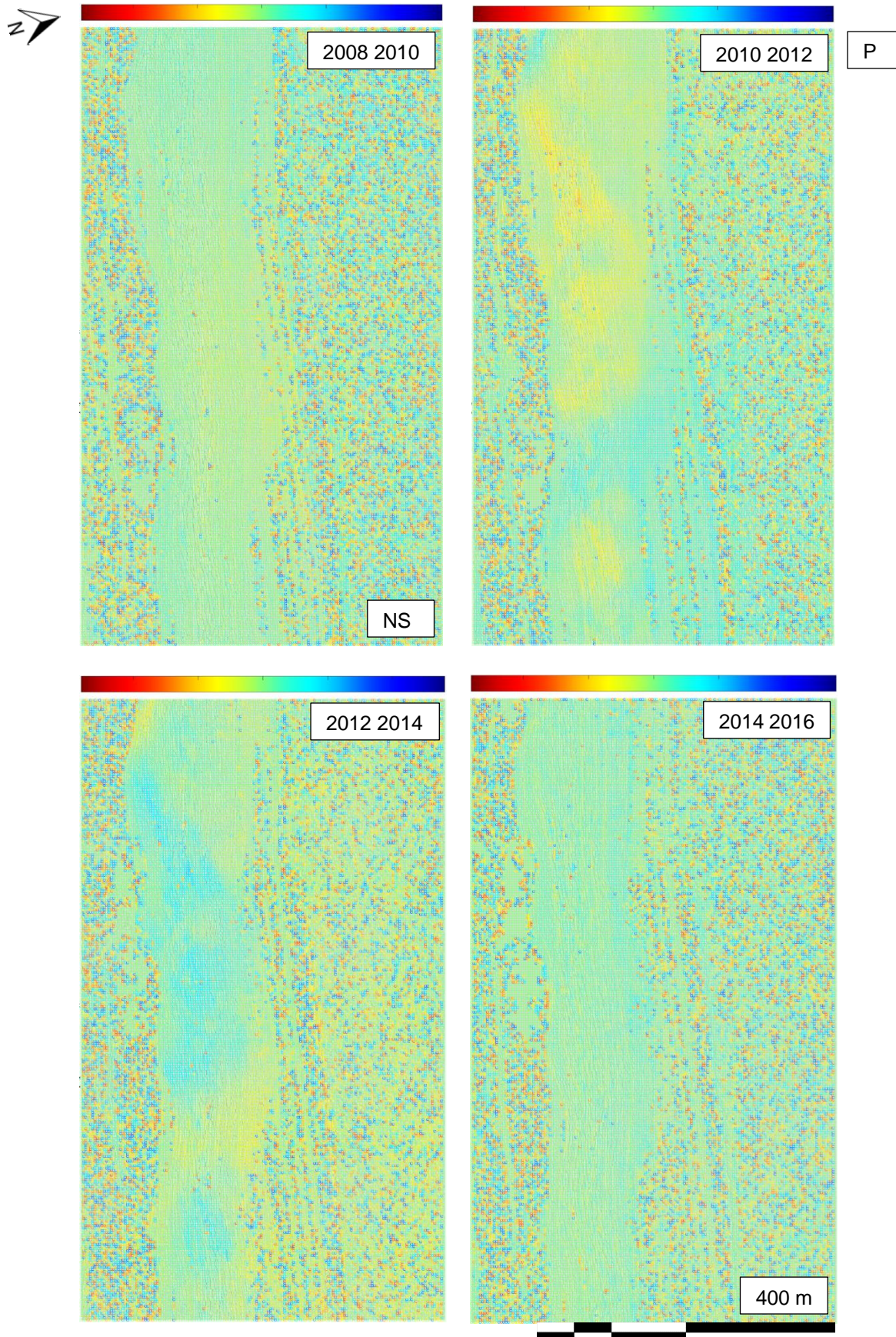
*Figure 55: DIC NS-offset results for tile P over the seasons from 2007/08 to 2015/16. Noisy and decorrelated areas are situated on the plateau and on the toe of the cliff. Scale bar is in [m], ranging from +2.5 m (red, northwards) to -2.5 m (blue, southwards) (raw data taken from HiRISE, n.d.).*
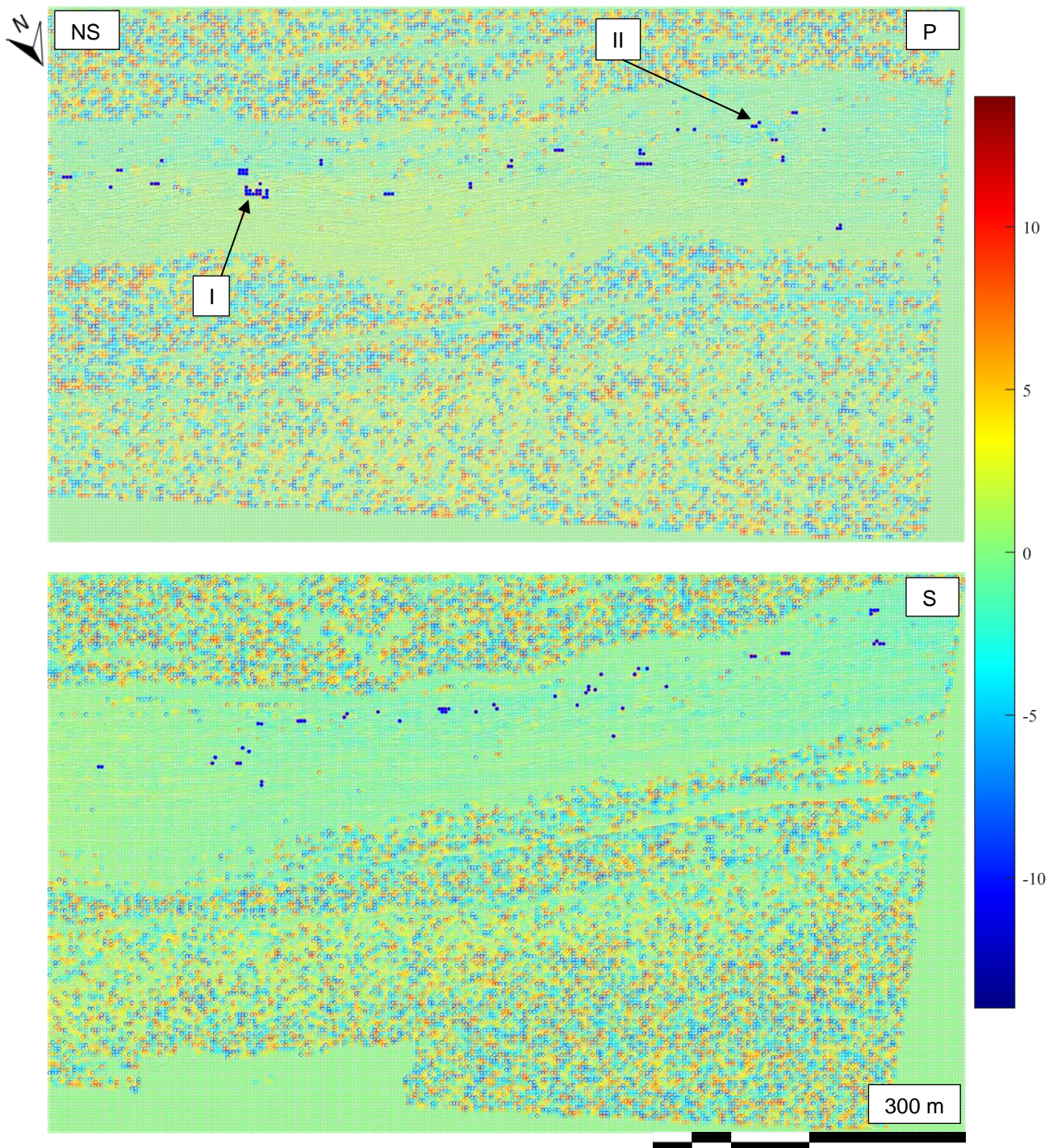
Figure 56: DIC NS-offset results for tile P and S over the maximum temporal baseline from 2007/08 to 2015/16. Noisy and decorrelated areas are situated on the plateau and on the toe of the cliff. Scale bar is in [pixel], ranging from +2.5 m (red, northwards) to -2.5 m (blue, southwards), 0.25 m per pixel resolution. Most prominent DIC detections in the cliff have been manually marked with blue dots to visualize the spatial distributions of occurred avalanche failures. I and II represent locations of two major failures, further shown in figure 58 (raw data taken from HiRISE, n.d.).

A co-registered input image subtraction has been performed for the maximum temporal baseline. A threshold of 20 bit has been used to create a binary mask, which has been additionally smoothed prior to plotting. Figure 57 represents the result:
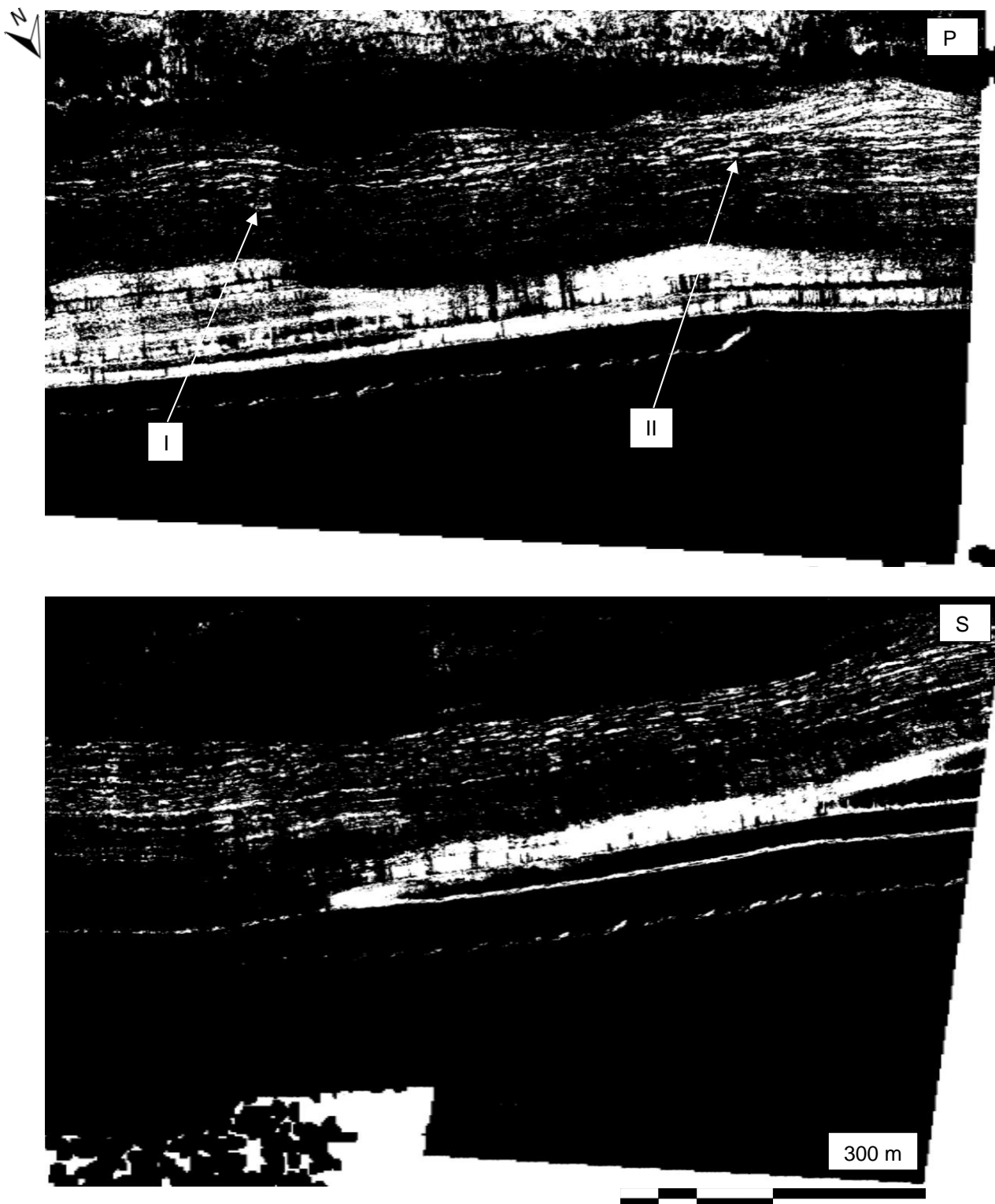
*Figure 57: Smoothed binary plot of input image subtraction from 2007/08 and 2015/16 using a binary threshold of 20 bit. Occurred changes are displayed with black pixels (0 bit) indicating no change and white pixels indicating differences (255 bit). White arrows indicate the sites I and II, which have been pointed out in figure 56 already (raw data from HiRISE, n.d.).*

Figure 58 displays some of the identified pre- and post-cliff failures using DIC, their respective locations are marked in figure 56 with white arrows and circles as well as with the corresponding ID code (I and II).
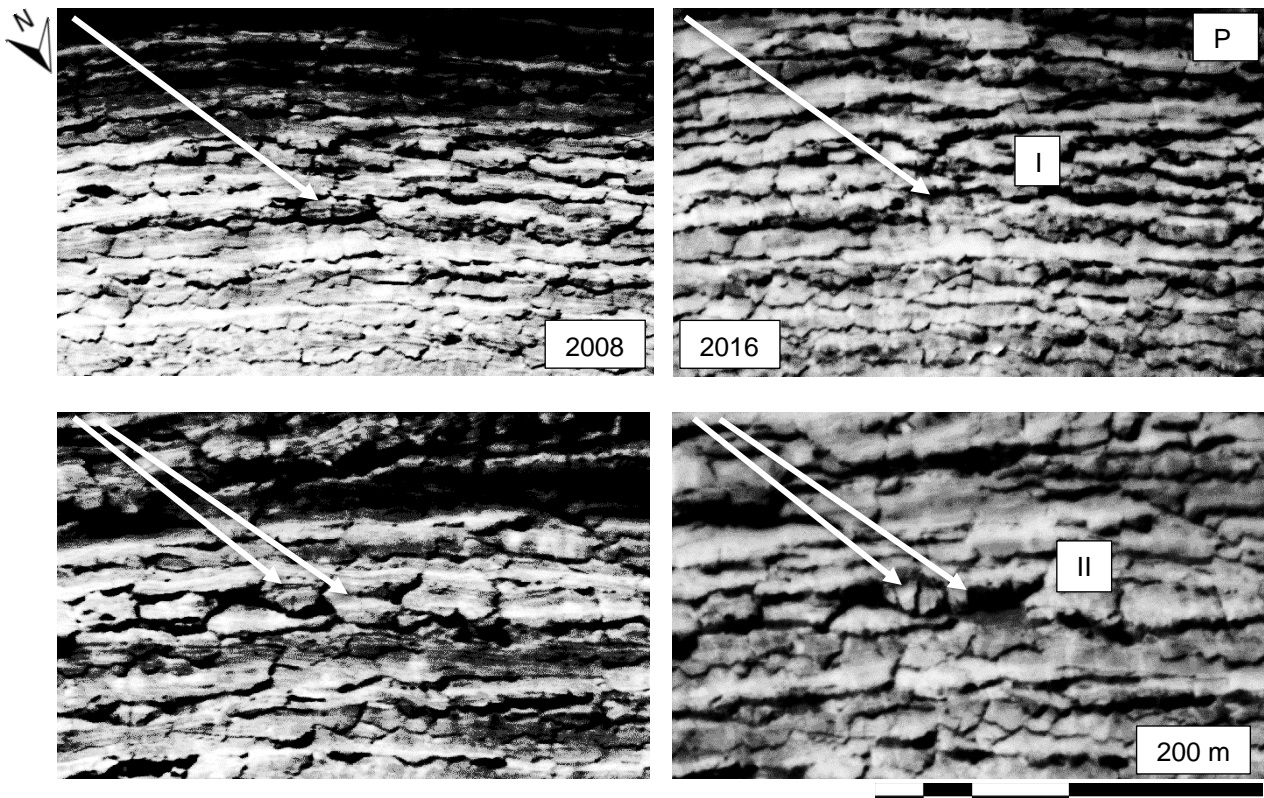
*Figure 58: Exemplary failures, which have been identified and marked in the cliff's P tile (cf. 56), indicated by white circles and arrows. Displayed are features such as block failures and growing fractures (raw data from HiRISE, n.d.).*

The results of the subtraction of DEMs in accordance to the DIC runs for the seasonal change detection in relation to small scale features is visualized in figure 59. As no DEM was derived for 2012, only three subtractions could be made, i.e. for 2007/08 to 2009/10, for 2009/10 and 2013/14, and for 2013/14 and 2015/16.
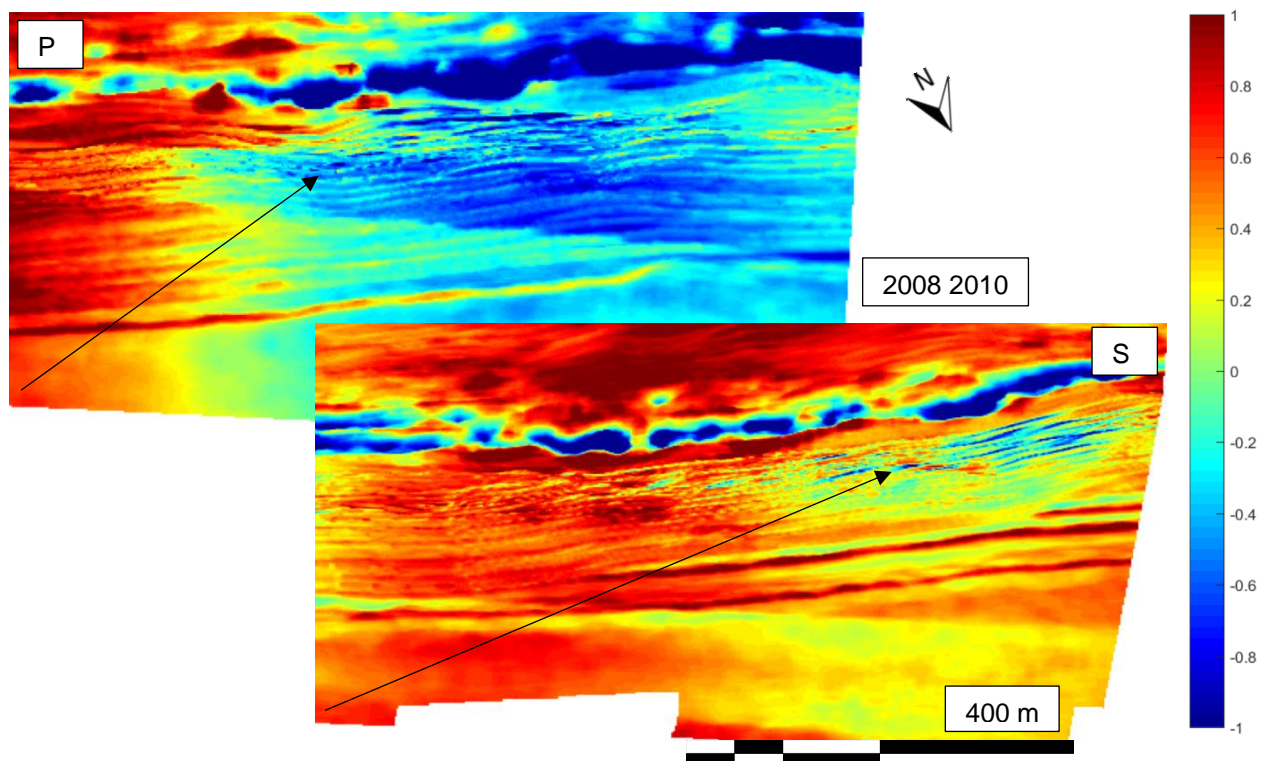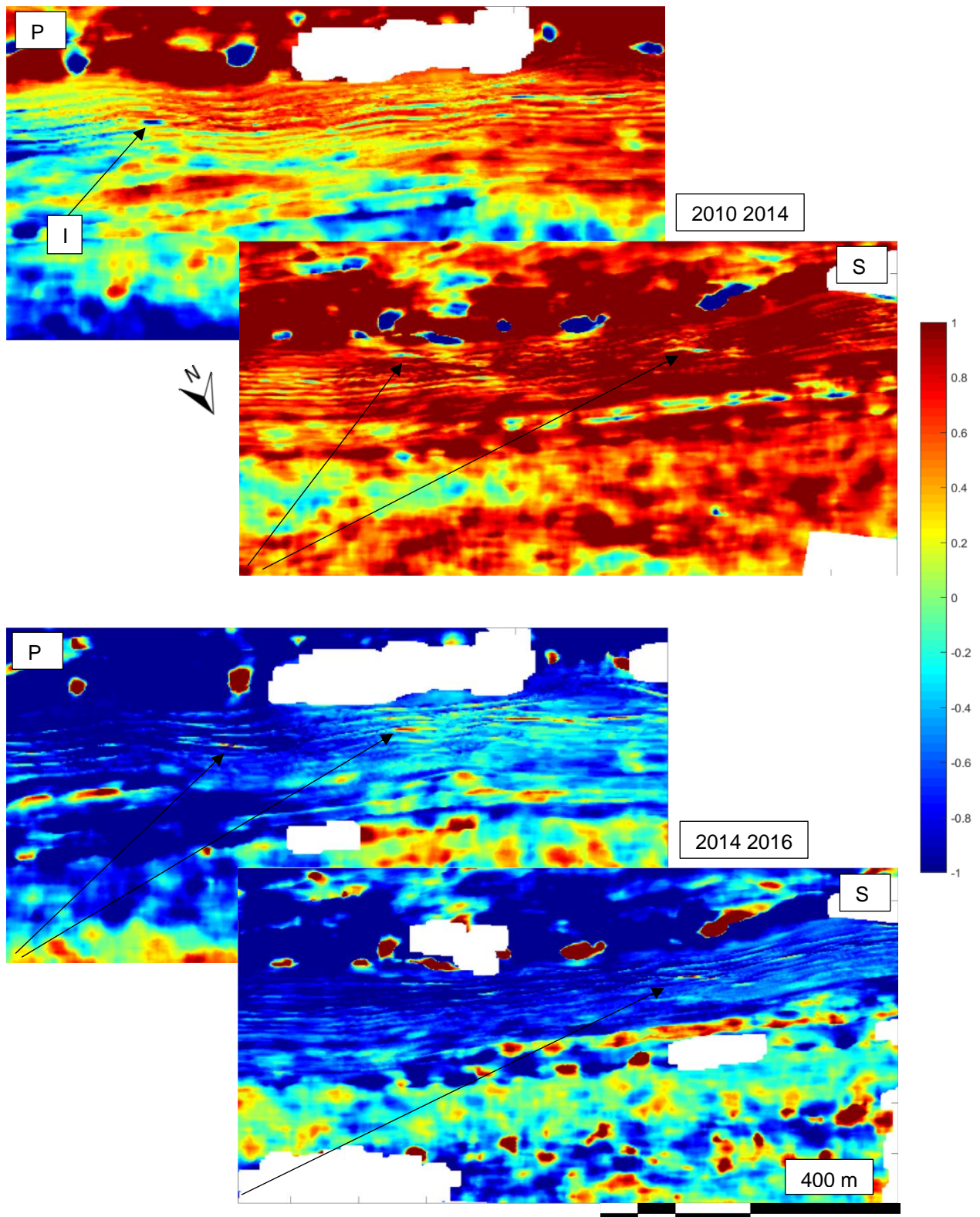
*Figure 59: Differential DEMs from the seasons 2008 to 2010, 2010 to 2014 and 2014 to 2016 for tiles P and S, scale is in [m]. Heavy noise can be recognized in all plots, particularly on the plateau and on the toe of the cliff. Location of instability I is marked, as well as presumed locations of other failures. Scale bar ranges only from +1 to -1 m to adapt the weighing of the color scale; locally, values can be higher or lower (raw data from HiRISE, n.d.).*

As the level of noise is significant and the quality resp. temporal resolution does not seem to be sufficient

to detect changes without large ambiguity, the same procedure has been performed for the maximum

temporal baseline with the DEMs 2007/08 to 2015/16 for tile P, to test whether the use of the maximum temporal baseline could reduce the ambiguity introduced by noise (figure 60).



*Figure 60: DEM subtraction of DEMs 2007/08 to 2015/16 for the P tile. Different types of noise and artefacts are visible, some is masked in white. Scale is in [m] difference between both DEMs, black arrow indicates distinct location of failure "I" from figure 56 (raw data from HiRISE, n.d.).*

Based on the results of the DIC analysis over the seasons as well as over the entire temporal timespan, all identified failures were counted and measured, when applicable in 3D using the DEM difference maps. As t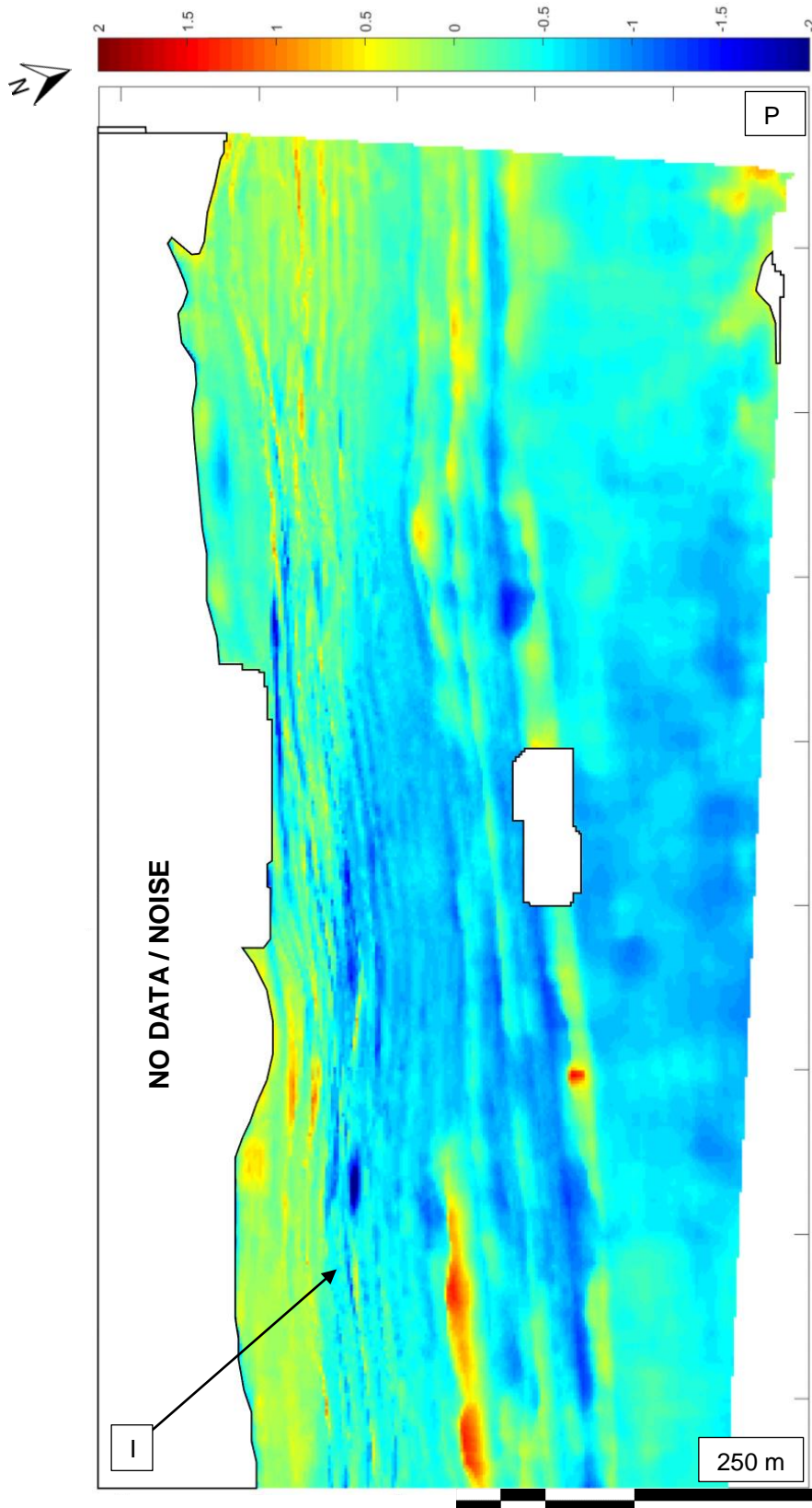he sensitivity and reliability of the DEM subtraction is limited, for most cases without respective signature in the DEM difference maps a conservative value of 1 m or smaller has been assumed, as the largest measured depth has been around 2 m (failure I in figure 56). Table 14 shows a summary of all measurements with their respective year of failure, including tile, area, estimated depth and estimated volume, while figure 61 illustrates the relative volume of eroded material for each season. The maps for P and S with all marked failures can be reviewed in the supplementary information section (S 17 & S 18).

*Table 14: Summary of all identified and measured cliff failures in tiles P and S with assumptions for the volume of the events.*

| P | Mean length [m] | Mean height [m] | Mean area [m²] | Mean estimated depth [m] | Mean estimated volume per failure [m³] |
|---|---|---|---|---|---|
| 2008 to 2010 | 10 | 8 | 80 | 0.8 | **64** |
| 2010 to 2012 | 10 | 6 | 60 | 0.9 | **54** |
| 2012 to 2014 | 20 | 6 | 120 | 1 | **120** |
| 2014 to 2016 | 11 | 8 | 88 | 0.8 | **70.4** |
| | | | | **MEAN / SEASON** | **77.1** |

| S | Mean length [m] | Mean height [m] | Mean area [m²] | Mean estimated depth [m] | Mean estimated volume per failure [m³] |
|---|---|---|---|---|---|
| 2008 to 2010 | 10 | 5 | 50 | 0.9 | **45** |
| 2010 to 2012 | 7 | 5 | 35 | 0.9 | **31.5** |
| 2012 to 2014 | 14 | 7 | 98 | 0.9 | **88.2** |
| 2014 to 2016 | 8 | 5 | 40 | 0.8 | **32** |
| | | | | **MEAN / SEASON** | **49.175** |

Figure 61 further displays the relative distribution of events on the observed timeframe, while the distribution of failure magnitude and quantity is illustrated in figure 62 using histograms.
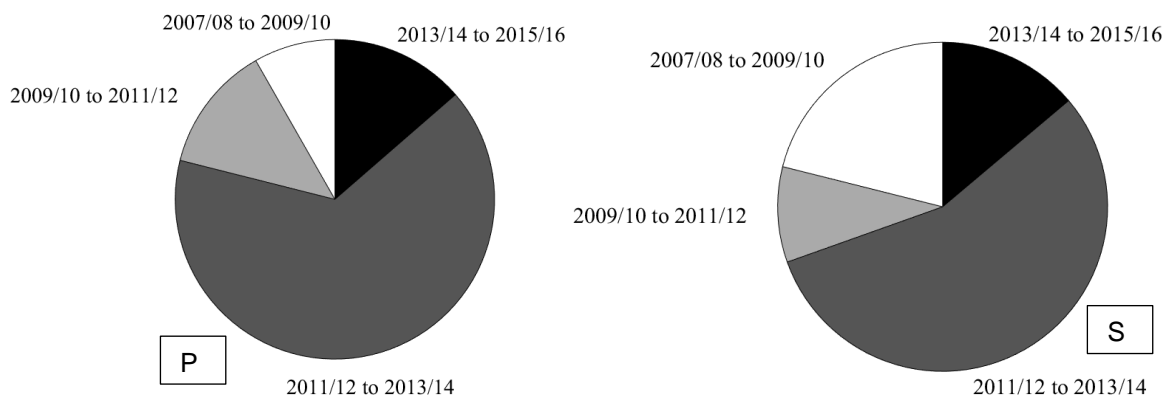


*Figure 61: Relative distribution of avalanche failure activity over the observed timeframe from 2008 to 2016 for the P (left) and S (right) tile.*
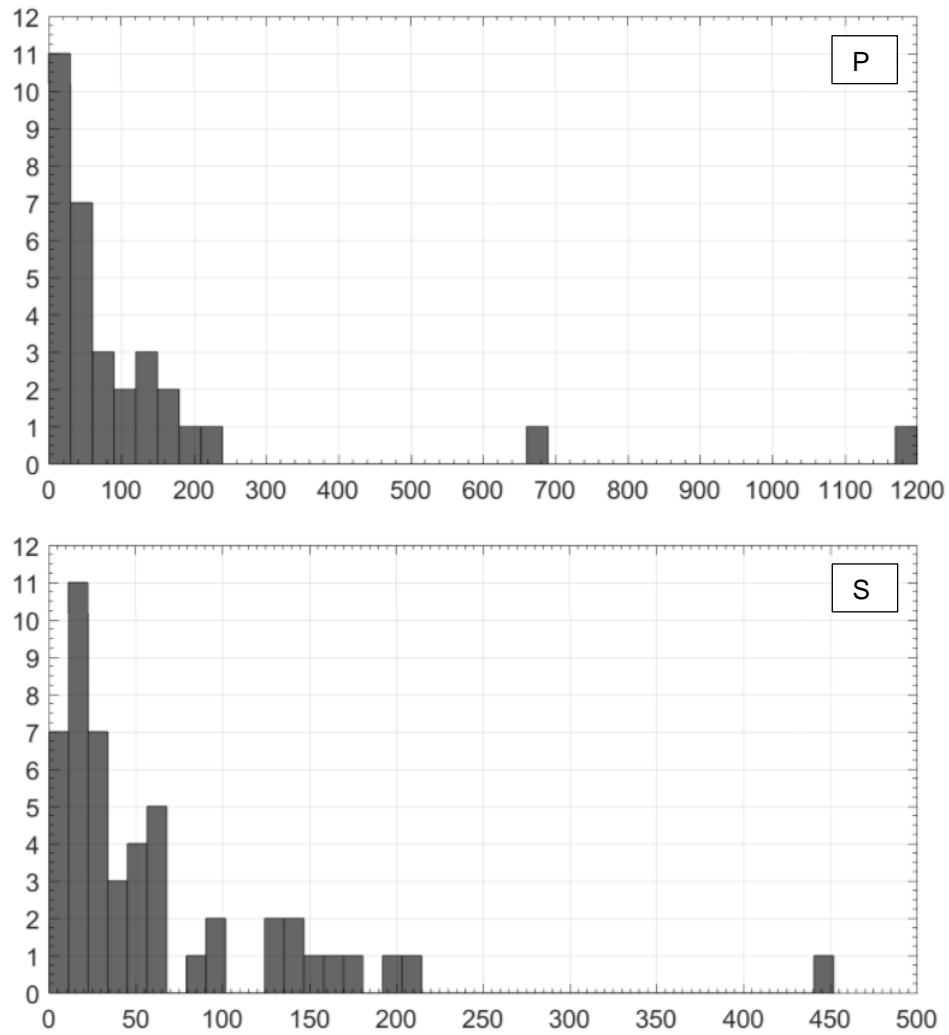
*Figure 62: Histograms showing the failure magnitude in cubic meters on the x axis and the failure quantity as running number on the y axis; tile P on top, tile S on the bottom.*

All gathered observations allowed the plotting of the measured event magnitude versus the respective time of failure, providing a certain trend of avalanche activity in magnitude and time, displayed by figure 63:
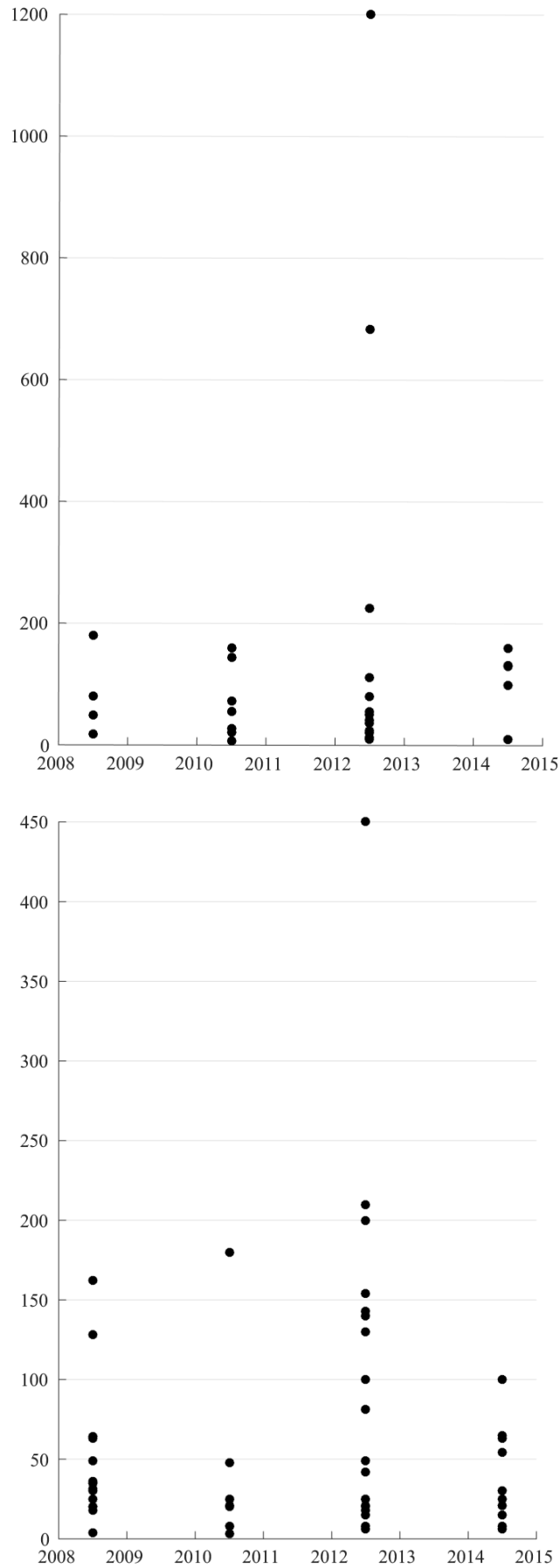
*Figure 63: Temporal distribution of avalanche events in relation to the magnitude, the x axis shows the date in [Earth years] and the y axis represents the magnitude in [cubic meters].*

## 5.4 Discussion

### 5.4.1 Discussion CTX camera

The intention of the application of CTX images during phase two was to investigate potential surface displacements occurring in places, that were not investigated in phase one and that supposedly show very slow movements, if existing at all. All three selected targets fulfill these criteria and the temporal baseline is close to its theoretical maximum, limited by the time in orbit of the satellite MRO. Still, the retrieved deformation matrices do not indicate any displacement, but entirely stable and static conditions for all three AoIs. This is positive, as it indicates a close to perfect quality of the produced orthoimages, with almost no entailed artefacts, despite the long temporal difference and the distinct relief in e.g. the Ascraeus Mons caldera. Only very slight distortions, potentially caused by insufficient camera parameter or position corrections are locally visible in the plotted NS component. Close to areas with high relief, as e.g. below the rim of Penticton Crater, noisy areas occur. These are caused by moving shadows due to a change in the illumination conditions and can be neglected, although they confirm that the DIC codes do detect small changes. Assuming the identified minimum sensitivity of FFT codes is equal to the used GSD of the input images (cf. equation 3.5-2), as found in the CdV case study (cf. figure 20), a non-sub-pixel DIC application would require a displacement of about 6 m during both observations. In the three investigated locations, this would result in displacement velocities of 0.6 to 0.8 m per Earth year.

The quality of the input images as well of the DIC output is sufficient and indicates that either the temporal baseline is still too small to detect surface changes, that the minimum sensitivity of the DIC algorithms is too poor, or that the CTX's GSD is too coarse, or a combination of all. Finally, the results could indicate as well that occurring deformations are slower than the calculated 0.6 to 0.8 m per year, required for a successful detection during the selected period, or that no current movement takes place on Mars's surface in these three specific locations. In the last case, the GLF close to Pentincton Crater could be considered as static and the volcanoes Ceraunius Tholus and Ascraeus Mons extinct or dormant, assuming that volcanic activity would cause deformations in the camera plane as well, instead of only vertical displacement. However, due to the coarse GSD of 6 m per pixel, the likely assumption is that Martian processes might be too slow to be detected with medium-resolution optical imagery. Still, future analyses of similar and other promising surface targets such as rift zones, volcanoes and GLFs could reveal different conclusions and insights and should be definitively performed during a follow-up investigation. A focus on Tharsis and Elysium Montes is assumed as most promising at this point, as they are expected to be the youngest volcanic provinces on Mars (cf. e.g. Tanaka et al., 2014).

### 5.4.2 Discussion HiRISE camera

Prior to DIC application and data investigation, quality control was performed by comparing two orthoimages, which have been derived by projecting identical input images over temporally-overlapping

DEMs. Figure 54 reflects the results of this procedure, which revealed a sufficient quality of the orthorectified images, derived with the described processing pipeline (cf. chapter 5.2). Almost the entire cliff AoI is shown in green, indicating completely stable conditions, as it is expected when comparing identical images. The contained noise along the edges of the images is presumably caused by edge and co-registration effects, while the noisy patch in image b) is introduced by a hole in the underlying DEM. Some minor mismatches are situated at the toe of the cliff, but are locally limited. They could be acquainted with differences in the underlying DEMs, as they are based on one overlapping, but also on one different input image, which have a certain difference in time, i.e. slight surface changes (e.g. frost patches) could cause those minor DEM differences. However, none of the observed features are assumed to influence the subsequent analysis in any way.

By exploiting the built multitemporal image stack with an FFT code over the described seasons, the influence of noise becomes apparent, presumably caused by rapid changes of the surface, e.g. by frost or dust. Figures 55 and 56 show that the plateau and the toe area are subject to heavy noise, which obstructs any further interpretation of the data. As expected, the use of the non-bundle adjusted 2012 acquisition introduced gradual noise patches (seasons 2010 to 2012 and 2012 to 2014), caused by the poor camera correction. Still, the actual AoI, i.e. the cliff itself, is free of any significant noise for all produced results, even over the maximum temporal baseline of 8 Earth years. Indicated deformations in this zone are therefore directly related to changes. Due to the rapid nature of the observed avalanche failures, DIC has not been able to measure any displacement, other than the occurrence of changes itself; therefore, DIC is operating as a change detection code, but without any possibility to reproduce deformation of the cliff over time. By applying the entire bandwidth of available temporal baselines from 1 day to 8 years of time difference, no further details can be retrieved from the dataset. This could be an indicator that the initiation of avalanches in this area is a particularly short-lived phenomenon without any detectable acceleration, occurring in a very limited time frame of minutes to hours. In order to measure a potential pre-failure displacement, a significantly finer temporal resolution of the image stack would be required, as well as a finer spatial resolution of the used imagery. Such a resolution cannot be reached with any orbiting sensor, i.e. a potential way of investigation would be the installation of a permanent monitoring sensor in front of the AoI, retrieving data with a very high temporal frequency in the order of hours or fractions of hours.

Still, DIC enables a detection of all occurred failures, which in turn allows a further quantitative investigation of the avalanche activity in this area. This analysis has been supported with the utilization of the implemented image subtraction code with results (figure 57) indicating all surface changes over the maximum temporal baseline. Due to the intrinsic properties of this procedure, the displayed changes include all occurred variations of the surface, including the significant alterations of the edge of the plateau and the toe area. Interestingly, DIC and image subtraction disagree in displaying noise on the plateau itself; the reason for that is yet unknown, but could be e.g. the thresholding of the applied binary mask. Although hampered by other surface changes, most DIC-derived failures could be identified in the binary masks as well. Apparently, frost activity is most prominent along the upper edge of the cliff, but too small in spatial extent to be unambiguously detected by DIC codes. As indicated by the binary mask and other results, the spatial distribution of the occurring surface changes appears to be situated

in elongated areas along the cliff. These features could be caused by artefacts in relation to slight changes in the illumination conditions, but could also represent true activity, concentrated at the edges of outcropping layers. However, such surficial activity could not be connected to mass wasting processes or avalanches, but could be small scale dislodging of surficial carbon dioxide frost, as proposed by NASA researchers (2015).

Ground-truthing, using the co-registered input images, confirmed most of the failures identified with DIC and image subtraction, as displayed in figure 58. Additionally, some changes of the cliff were detected by the FFT code, which have not been pointed out by DIC or the binary mask, indicating a limitation of the applied algorithm. As those additionally recognized features generally have a small spatial extent, a probable explanation could be that the GSD of the used HiRISE sensor is not sufficient enough to detect these small-scale differences. The SNR for FFT with 64 by 64 pixel windows was around 2 and reached a probability of ~ 68 % for a detected change to be correct, derived during the manual ground truthing. An application of search window sizes with 32 by 32 pixels and smaller significantly decreased the SNR below 1 and impeded any reliable further investigation, as indicated changes were likely to be just DIC mismatches. It is known that DIC codes produce a poorer SNR if performing runs with smaller search window sizes, but there is a way to define a loose threshold for the FFT code above which the algorithm performs reliably with a good accuracy, based on the input image GSD and the search window size, independent of the observed signal, i.e. the displacement in this case. In relation to formulae 3.5 - 1 and 3.5 – 2 and using observations made with different GSDs one could state that an appropriate SNR can be reached if

$$wi \; [pixel] = \; 0.45 * GSD^2 \; [m] - 8.4 * GSD \; [m] + 66 \qquad (5.4.2 - 1)$$

using a second degree polynomial fit. Figure 64 displays a linear fit as well as a shape-preserving interpolant, to visualize the relation between window size and GSD in the tested frame between 16 to 128 pixels and 0.25 to 15 m spatial resolution, using HiRISE and CdV aerial imagery (0.25 m), CTX (6 m), and HRSC (12.5 m).
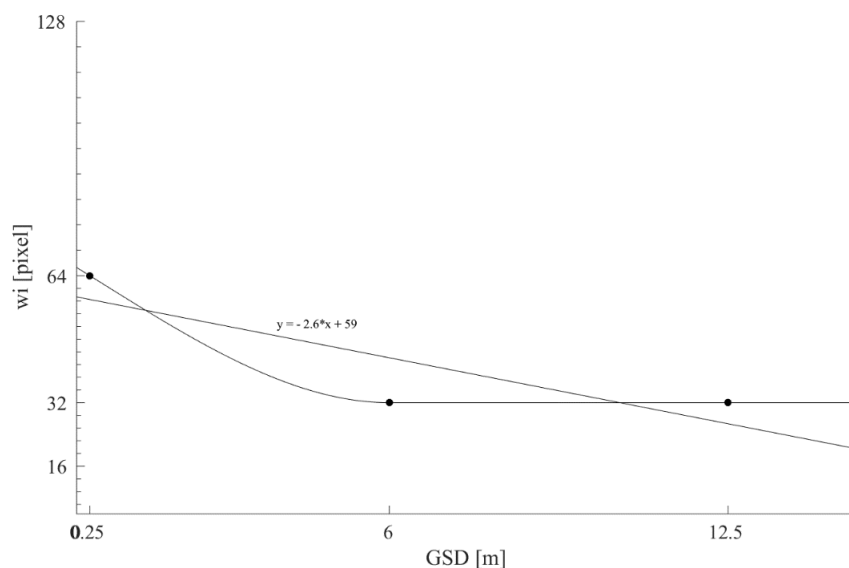


*Figure 64: Relation of GSD to wi in order to minimize the used search window, but optimize the SNR. Linear fit as well as a shape-preserving interpolant has been used.*

This equation could help to select a suitable search window size for a yet unknown bandwidth of GSDs, which produces the optimal SNR for the smallest possible window. However, further research and testing is required to confirm this finding and to extent this formulation to other DIC algorithms, such as NCC and COSI Corr.

The subtraction of seasonally derived DEMs was performed to obtain information about the vertical extent of the avalanche disposals. The results however show numerous variations of noise, which impede a reliable extraction of information: apparently, the scale of the noise is equal to the scale of the signal. These artefacts are probably introduced by differences during the stereo matching and the DEM meshing and are difficult to recognize in the output difference maps, which reduces the overall reliability of this data. It has to be kept in mind that the horizontal resolution of all DEMs is 5 m, which is likely to obstruct a detection of changes in the DEM, caused by failures with a small spatial footprint. Nevertheless, one distinct failure (I) with a large footprint in the P tile can be identified and suggests a vertical DEM difference of around 2 m, derived from a point measurement at its location. This suggests that all other failures have similar or smaller vertical extent, particularly if they have a smaller footprint. This finding is supported by several other locations in the differential DEMs, which were correlated with DIC-detected and verified failures, as indicated in figure 60. Although the precise vertical accuracy of the produced DEMs is unknown, it is assumed that the observed vertical differences are meaningful and representative.

By using the measured vertical differences, where applicable, or by assuming a depth with relation to the horizontal footprint, all identified failures were mapped and listed, as shown in table 14. Finally, these data allowed an estimation of the failed volume, by assuming a simplified box-shaped form of the failed blocks and slabs, ranging from 3 up to 1200 cubic meters. Hereby, as shown by figure 62, the majority of blocks are in the range of 0 to 200 cubic meters and have a slab or elongated form, according to recommendations by Kalenchuk et al. (2006). The temporal distribution of avalanches in figures 61 and 63 illustrates that the average magnitude of failures is around 100 cubic meters for both tiles and that the failure volume is equally distributed over tiles P and S in the AoI over the observed timespan. Still, the season from 2012 to 2014 shows an increase in the occurrence of extremely large events, with volumes of 1200, 450 and 684 cubic meters. In addition, the collapsed volume during this season increased, as the amount of failures increased, however, without increasing the mean volume of any one failure. This specific pattern could indicate a difference in the environment during that season, e.g. by varying atmospheric conditions. A potential way to verify such a proposal would be to exploit Mars Odyssey data, which is another Martian orbiter operated by NASA. One of its payloads is the Thermal Emission Imaging System (THEMIS), which enables estimates of the surface temperature. Potentially, the surface temperature of the AoI during the 2012 to 2014 season differed from the other monitored seasons, which could be a reason for the increased activity. This potential correlation between surface temperature and avalanche activity is particularly interesting, but requires more research. In addition, other potential causes for the increase in avalanche activity might be possible, such as marsquakes or recent micro-impacts, causing terrain motion. Seasonally, wind speeds in Mars's northern hemisphere can reach 100 m/s or more during global dust storms, as proposed by Mitchell et al. (2015), which could influence shallow surface changes as well. An investigation of this hypothesis would require a detailed

analysis of the atmospheric conditions during the 2008 to 2016 period, but could not be performed due to time limitations. Generally, the constant pattern of activity of the Rupes Tenuis cliff and the assumed direct correlation between activity and environmental and geological conditions can be compared to activity pattern of sites on Earth, such as in Surprise Valley, Jasper National Park in Canada, where Luckman (1976) showed that rockfall activity is dependent on micro-climatic conditions and the physical character of the observed cliffs.

Based on all findings and the underlying data such as multispectral imagery, radar profiles, DEMS and orthoimages, a basic conceptual kinematic model has been developed. The relatively small dimensions of the detected blocks as well as the low vertical extent suggest that mass movement is a shallow process. Such processes could develop faster than deeper seated features, potentially explaining the rapid evolution and failure of the avalanches as well as the difficulties to detect pre-failure deformation. Driven by visual observations, the proposed kinematic mechanism is a toppling of loose slabs and blocks of the cliff, which rotate around their center of gravity until they suddenly fail. Such a mechanism would help to explain the difficulties of a pre-failure DIC displacement detection, as most of the deformation occurs not orthogonal to the sensors LOS but vertically, which cannot be measured with DIC using orthorectified orbiter imagery. The loosening of slabs could be caused by seasonal thermal expansion cycles, induced by the Martian seasons as well as by direct sun illumination. The formation of cracks has been observed e.g. in figure 58 and is horizontally limited by the dimensions of the slabs. Vertically, crack propagation could be limited by the observed sub-horizontal layering of the cliff body, as visible in figures 42 and 41, which have an estimated mean vertical distance of around 2 m in the upper part of the cliff. These horizontal and vertical boundaries could explain the relatively constant mean dimensions of the observed failed blocks. The composition of the monitored cliff is not precisely known, but is assumed to consist of a water- dry ice and dust mixture, as indicated by figure 31. As proposed by Levrard et al. (2007) layers formation results from cap-wide climate processes and represents the incremental deposition and removal of water ice/dust material during a season, integrated over orbital timescales. The internal structure of the cliff could therefore be similar to layering of terrestrial glaciers, such as in the Northern latitudes, shown in figure 65.



*Figure 65: Glaciers on Svalbard, sub-horizontal layering of icy and dusty layers is visible. Glacier height from sea level is around 20 m in the left image. Person as scale in the right image.*

Falling blocks of ice and dust would easily disintegrate during their descent, as they repeatedly hit the cliff and would finally vanish upon impact into the talus cone. This mechanism would therefore explain why no disposed blocks or their fragments could have been identified in the talus area and why DIC results are decorrelated in this area, despite the reduced impact energy due to a lower gravitational acceleration. The occurrence of massive dust clouds, as imaged by HiRISE (cf. figure 32), could be explained by this type of collapse, as the complete disintegration of the dust-ice blocks upon impact on the cliff and the talus cone could produce significant amounts of particles and volatiles. The lower Martian gravitational acceleration and the lower density of the atmosphere is expected to further facilitate the formation of large dust clouds with extents that likely exceed sizes of dust clouds on Earth, caused by events of the same magnitude. However, excessive presence of water ice would mitigate dust clouds, as particles are expected to stick to the surface of ice blocks, based on experiences from Earth. Presumably, the superficial cover of seasonal dust on the cliff's face as visible in reddish colors in figure 41 significantly contributes to the formation of the observed clouds. Theoretically, this assumption could be verified by comparing RGB composites before and closely after a failure, where fresh scarps should appear in a different color or reflectance, because the underlying material is exposed and dust has not yet been deposited. The first step would be to identify the precise date of failure of a specific slab and to generate and visually compare the respective composite images. Due to time and data availability limitations, this procedure was not performed, but would be an interesting subject for future analysis. Due to the unknown composition of the cliff, a glacier-like behavior of the AoI cannot be excluded, which also includes the possibility that the observed mass wasting processes are in fact similar to calving processes, which can be observed on Earth. In addition, a large-scale or deep-seated deformation of the entire body cannot be excluded, as ice masses on Mars might be advance or retreat in the same way as ice bodies on Earth. A deeper analysis requires a detailed investigation of Mars's climatic past and present setting, however. Figure 66 summarizes and visualizes the proposed conceptual kinematic model for the monitored Rupes Tenuis cliff on Mars:

Surface frost/ frost features

Sub-vertical fracture growth caused by freeze
and thaw cycles

Toppling of instable slabs

Sub-horizontal layers
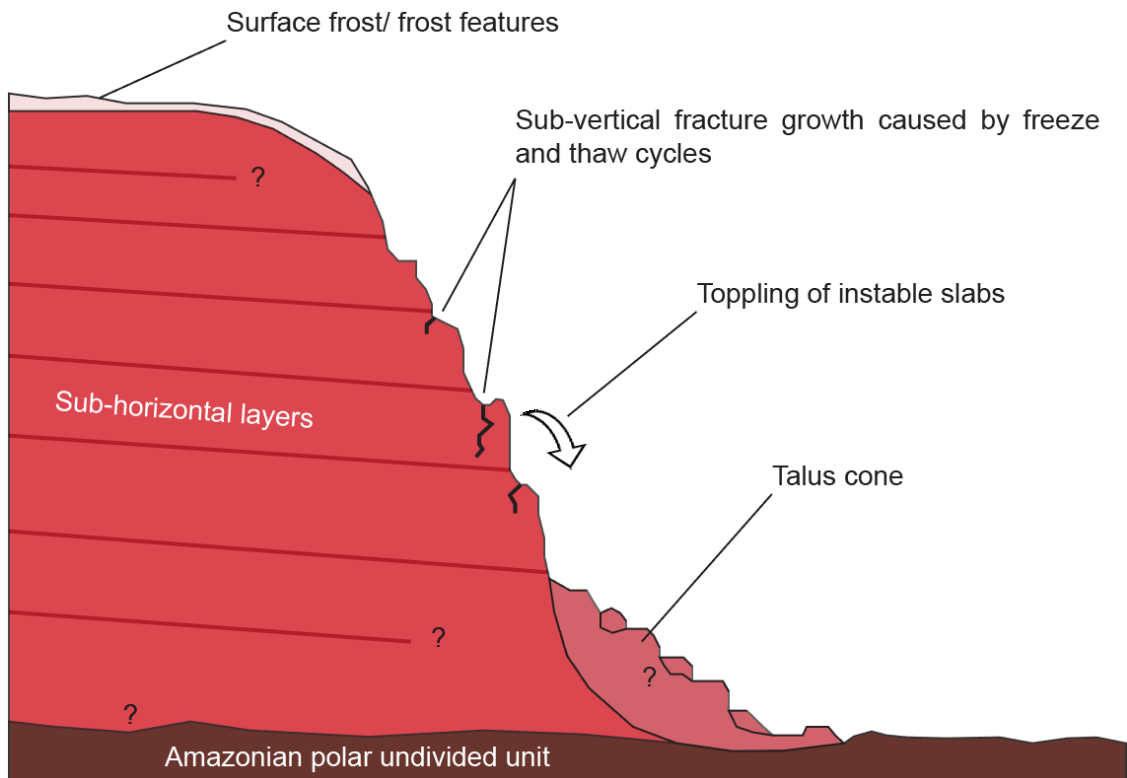
Talus cone

Amazonian polar undivided unit

*Figure 66: Proposed conceptual kinematic model for the Rupes Tenuis cliff. Dust-ice body superimposes the Amazonian polar undivided unit, contact properties can only be estimated using SHARAD data. Shallow surface frost features are subject to significant changes over the seasons and cause strong decorrelation during DIC analyses. Vertical fracture propagation is assumed to produce blocks, limited in size by the horizontal layering of the cliff body. The kinematic mechanism is proposed to be toppling, where loose blocks rotate around their center of gravity. Upon impact with the talus cone, failed slabs completely disintegrate and produce large clouds of dust particles and volatiles. Not to scale.*

By observing and investigating these processes under particularly difficult conditions on Mars, conclusions can also be drawn for remote sites on Earth. As ground truthing is not yet possible on Mars, the stability and reliability of the used techniques such as DIC is the first priority for any analysis to be meaningful. Subsequently, such established procedures can also be deployed on Earth in areas without any direct accessibility, such as the Northern and Southern latitudes or mountainous areas such as e.g. the Himalayas. Generally, the observed features and processes at Chasma Boreale on Mars seem to have several parallels to processes on Earth, although some questions remain unanswered for the moment. DIC as a technique to detect and quantify changes over time has proven as being effective but with strict limitations, defined by the data availability and quality as well as by the observed kinematic. Even if impeding influences such as a thick atmosphere or vegetation are absent on Mars, other factors such as frost- or dust induced surface alterations exacerbate or locally inhibit DIC utilization and therefore a comprehensive analysis.

# 6. CONCLUSION & OUTLOOK

Besides the interest to answer the predominant scientific questions of this thesis, another objective of this work was not only to apply DIC codes, but also to develop improvements of the state of the art procedures prior to application on Earth and Mars. One step has been to write and implement a Wallis filter into the DIC processing pipeline to optimize the pre-processing of the used imagery, which significantly enhanced the quality of the returned spatial offset information by two of the assessed DIC algorithms, while slightly improving the accuracy of the measurements at the same time. On the other end of the workflow, a 2D spatial vector filter has been established, which effectively and reliably removes noise from the DIC output matrices, while enhancing the accurateness of the performed DIC operation, achieving peak accuracy values during the performed CdV case study (chapter 2).

In order to assess and validate the accuracy of 3 different DIC algorithms in a controlled case study on Earth prior to the application on Mars, a systematic comparison of 3 codes, NCC, FFT, and COSI Corr, on one Wallis filtered and one non-pre-processed input image with 4 different post-processing filters was executed with a total of 144 runs. The results show that larger DIC window sizes are favorable to detect unknown deformation, due to their ability to return a better spatial coverage of the AoI. In addition, it was found that FFT codes generally achieve the best matching quality, while the overall minimum sensitivity of the tested DIC codes has been derived as ~ 25 cm. In direct comparison to GNSS measurements of the same area over the same time period, FFT codes delivered results with the highest accuracy and precision, while COSI Corr produced the poorest. Further, it has been found that oversampling during DIC only very slightly improves accuracy and only below a saturation threshold of ~ factor 8. With a computation duration of seconds per run, COSI Corr performed fastest for the CdV dataset and NCC completed last with processing times of up to 12 hours per run. Based on the performed case study, a recommendation by Ayoub et al. (2015) for search window selection has been modified to equation 3.5 – 1. Further, a formulation has been developed to estimate the minimum deformation which can be recognized by DIC using a given GSD (3.5 – 2); both formulae are particularly useful for a pre-application validation. Another result of the CdV case study has been that the use of different sensors with varying GSDs as well as the application of input data with a maximum temporal baseline in combination with differing search window sizes, starting from the recommendations given by formula 3.5 - 1, is proposed for a comprehensive exploration of unknown surface processes. Having an increased understanding of the performance of DIC codes under different conditions, the ability to foresee future failures with DIC could be attempted by exploiting high-frequency multitemporal image data, as it has been done e.g. by Manconi et al. (2016) for the March 14th, 2016 event in CdV (chapter 3).

During the first phase of the exploration of recent Martian surface processes, the applicability of the developed DIC pipeline from Earth has been successfully applied on NASA MRO and ESA MEX imagery. Previous results on Martian dune migration by Bridges et al. (2012) and Ayoub et al. (2014) were reproduced in other areas of Mars with comparable dune migration rates (around 1m in the literature versus 0.8 to 1.4 m in this work), using all three DIC codes. DIC application further indicated a

way to precisely measure dust and sand migration at a local scale, which could lead to the implementation of DIC algorithms to improve the spatial resolution of atmospheric models and to potentially install a frequent monitoring of sand behavior at certain points of interest, e.g. close to landers or rovers. During phase one, ~20 % of NASA's available HiRISE medium-resolution orthoimage database has been exploited, targeting AoIs across the planet. This procedure revealed that orthorectification quality of the image stacks is sufficient for DIC, except for areas with very high relief and therefore particularly difficult image processing conditions. The locally poor quality of the NASA orthoimages introduced fake offsets e.g. at AoIs close to the North Pole, which could only be distinguished from true deformation by using DEM hillshades for enhanced artefact recognition. All in all, during phase one, true slope or surface deformations other than dune migration have not been found on Mars, despite the utilization of different temporal baselines, promising AoIs and various sensor imagery (HiRISE, HRSC). The major critical factor was the available temporal baseline between images, which seems sufficient to detect fast surface changes such as moving dunes, but insufficient to expose slower processes, such as slope or tectonic deformations (chapter 4).

For the second phase of the exploration campaign on Mars with DIC, image processing pipelines for CTX and HiRISE level 0 imagery for DEM and orthoimage production have been developed and extensively tested, to extend the limitations defined by the sparse availability of appropriate DIC input imagery. Image processing has shown to be generally highly demanding in terms of operational and computational times, particularly for HiRISE imagery. Further, processing can produce significant errors such as stereo mismatching, poor DEM meshing and poor orthorectification, which is why a continuous quality control is vital to produce results with sufficiently high quality. In total, 18 selected CTX and HiRISE images from 4 different AoIs were successfully processed to 9 DEMs and 16 high- and 2 low quality orthoimages, while processing pipeline quality has proven to be sufficient for DIC with complete avoidance of the artefacts, found in the NASA imagery. Still, surface or slope deformations have also not been found using maximum time scales between 7.5 to 8.5 Earth years with CTX imagery for AoIs such as a GLF and volcanoes. This either means that no deformation occurs at these locations at present or that displacement is slower than the calculated 0.6 to 0.8 m per Earth year and therefore below the minimum DIC sensitivity of an application with medium resolution imagery, according to equation 3.5 – 2. In addition, ongoing displacements could occur outside of the CVP with a vertical component, which could also explain why no deformation has been detected, particularly in the volcanic provinces. However, avalanche activity at a Rupes Tenuis cliff close to Mars's North Pole has been monitored with processed HiRISE data over 8 Earth years using 10 orthoimages and 4 DEMs with DIC, binary mask change detection, DEM subtraction and ground truthing. The detected failures at the cliff were measured in terms of volume and date of occurrence. Observed volumes range from 3 to 1200 cubic meters with a seasonal average of 100 cubic meters per event. Avalanche activity has been increased in the time period from 2012 to 2014 due to an unknown reason with several extremely large volume events and a higher failure frequency, but the same mean volume per event.

Based on the previous investigation a conceptual kinematic model for the Rupes Tenuis cliff has been proposed. Failed blocks appear to have a short vertical extent and failure occurs rapidly as slabs rotate around their center of gravity, impeding detection with DIC codes as deformation is parallel to the LOS

of the sensor. The physical driver for slab loosening could be thermal expansion induced by seasonal environment variations and changes in the sun illumination onto the cliff. As derived by visual observations, crack propagation occurs sub-vertically, limited by the sub-horizontal layering of the ice-dust body. Falling blocks appear to disintegrate during their descent and their impact upon the talus cone, producing massive clouds of dust particles and volatiles, while leaving no large fragments in the debris at the toe of the cliff, suggesting direct parallels to glacial processes on Earth such as iceberg calving. As a further addendum to equations 3.5 - 1 and 3.5 – 2, formulation 5.4.2 – 1 has been developed for the FFT algorithm based on all performed runs with various sensors and GSDs (0.25 to 12.5 m) to derive the optimal search window size for FFT DIC applications, that delivers the best compromise between spatial coverage and SNR (chapter 5). Finally, table 15 provides a summary of the results obtained during the exploration of the Martian surface with DIC.

*Table 15: Summary of the results of the DIC exploration campaign on Mars.*

| Location | Geological context | Used sensor | Applied DIC code | Temporal baseline | Detected deformation |
|---|---|---|---|---|---|
| **Eastern Coprates Chasma** | Dune fields in valley | HiRISE | FFT, NCC, COSI Corr | 22 Earth months | **Dune migration with rates around 0.8 m/ Earth year** |
| **Ganges Chasma** | Dune fields surrounded by mountains | HiRISE | FFT, NCC, COSI Corr | 34 Earth months | **Dune migration with rates around 1.4 m/ Earth year** |
| **Unnamed crater close to Yaren Crater** | Crater slope with gullies and dunes | HiRISE | FFT | 21 Earth days | **Micro-scale dust and sand migration across slopes** |
| **Palikir Crater** | Impact crater | HiRISE | FFT | 22 Earth days | **None** |
| **Rupes Tenuis polar cliff (Phase 1)** | Terminal cliff of North polar layered deposits | HiRISE | FFT | 29 Earth days | **Fake deformation introduced by poor DEM** |
| **Inca City** | Seasonal processes close to South Pole | HiRISE | FFT | 5.5 Earth years | **Rapid surface changes caused by seasonal processes** |
| **Phlegra Dorsa** | Inflation feature | HiRISE | FFT | 36 Earth days | **None** |
| **Ganges Chasma** | Old landslide scarp and deposits | HRSC | FFT | 6 Earth days | **None** |
| **Eastern Hellas Planitia** | GLF in crater | CTX | FFT | 9.5 Earth years | **None** |
| **Tharsis Province** | Volcanoes in volcanic province | CTX | FFT | 7.5 Earth years | **None** |
| **Rupes Tenuis polar cliff (Phase 2)** | Terminal cliff of North polar layered deposits | HiRISE | FFT | 8 Earth years | **Detection and measurement of seasonal avalanche activity** |

The major scientific question of this thesis was whether there are recent slope or surface processes on Mars. Previous work has identified and quantified a limited amount of rapid changes of surface features such as migrating dunes and dust devils. Finally, images of ice and dust avalanches, such as imaged on a Rupes Tenuis cliff in 2008, showed a dynamic site of Mars for the first time. The contribution of this thesis to the planetary exploration of Mars was to examine, whether Mars's surface might be currently shaped by other, yet unknown processes, such as landslides or other mass wasting processes. By applying validated DIC codes in combination with imagery taken by different sensors, this work found that such ongoing deformations are either too slow to be detected or non-existent resp. currently inactive. The major limitation was the low frequency of available HiRISE acquisitions with sufficient quality and imaging geometry. However, by exploiting complementing change detection techniques in combination with data from various sensors, a comprehensive investigation of magnitude and frequency of avalanche events at a Rupes Tenuis cliff was performed, resulting in a detailed conceptual kinematic model that proposed several parallels between terrestrial and extra-terrestrial geological mass wasting processes. Contributions like this could help to get an understanding of the mechanisms that formed Mars in the past and will continue to form Mars in the future. Concurrently, these findings answer the second and the third scientific question of this work, whether potential recent deformations can be detected and measured using DIC and available satellite imagery, and whether predisposing and driving factors of slope or surface deformations on Mars are similar to the ones observed on Earth. Still, DIC as a technique to detect and quantify unknown changes over time on the surface of another planet or celestial body has been proven as being effective but with specific limitations.

Besides the numerous findings and conclusions of this work, a variety of promising goals for future investigations have been identified. As one of the initial intentions of this thesis, DIC code performance could be further enhanced by an implementation of an anticipating DIC algorithm, which uses rapid binary mask change detection prior to DIC application to automatically adapt window sizes to the expected resp. categorized level of change for each correlation cell, while optimizing its matching quality and operation time. In terms of DIC application, an open question is the detection of the linear feature in the NE of the CdV AoI, which would require a more sophisticated investigation with recent and more frequent image data, in order to assess whether the formation of a new, and for CdV uncommon, feature might express itself on the surface in the near or far future. In order to further validate formulation 5.4.2-1 and to extend its applicable range, additional tests with other air- or space-borne sensors and with other GSDs would be required.

Apart from Earth, follow-up large-scale processing and investigation of CTX and HiRISE imagery for particularly interesting sites such as Elysium and Tharsis province volcanoes or GLFs on Mars are expected to deliver interesting results, using the maximum available temporal baselines, particularly in the context of the arrival of ESA's ExoMars Trace Gas Orbiter (TGO) in Martian orbit several months ago, which could soon offer new ways to process Martian orbiter imagery, using its high-resolution, single-pass multiband DEMs. The exploitation of sophisticated computational resources or clusters would be a great asset for this intention, especially as processing pipelines are already in existence and fully operational. Also, a follow-up quantitative and qualitative assessment of FFT and NCC DIC codes for dune field migration monitoring on Mars for areas, where COSI Corr was already applied, could

further support the findings of the CdV assessment study. Potentially, it could be shown that COSI Corr, although widespread amongst researchers worldwide, could be complemented or even replaced by other DIC codes, possibly benefitting the exploration of planetary surface processes in general. Further, an attempt to correlate the activity of the monitored Rupes Tenuis cliff with surface temperature variations is interesting, yet challenging, as further data by the Mars Odyssey THEMIS instrument need to be processed and exploited. The exploration of other planetary or cometary surfaces such as e.g. Earth's Moon or Comet 67/ Tschurjumow-Gerassimenko with DIC is also of particular interest for future work.

Finally, insights of this work could be applied for current and future planetary exploration missions, in order to improve data acquisition strategies for an optimized data quality for change detection purposes. The immense potential of DIC and other change detection codes within the frame of such missions has yet to be exploited.

# 7. REFERENCES

Amann, F. (2006). Grosshangbewegung Cuolm Da Vi (Graubünden, Schweiz): Geologisch-geotechnische Befunde und numerische Untersuchungen zur Klärung des Phänomens. *Dissertation, Universität Erlangen-Nürnberg.*

Ayoub, F., Avouac, J.-P., Newman, C. E., Richardson, M. I., Lucas, A., Leprince, S., & Bridges, N. T. (2014). Threshold for sand mobility on Mars calibrated from seasonal variations of sand flux. *Nature Communications*, *5*, 5096.

Ayoub, F., Leprince, S., & Avouac, J. P. (2015). User's Guide to COSI-Corr. *California Institute of Technology.* http://www.tectonics.caltech.edu/slip_history/spot_coseis/pdf_files/cosi-corr_guide.pdf (Status: 10.08.2017).

Baltsavias, E. P. (1991). Multiphoto Geometrically Constrained Matching. *Dissertation*, *Institute for Geodesy and Photogrammetry, ETH Zurich.* https://www.ethz.ch/content/dam/ethz/special-interest/baug/igp/igp-dam/documents/PhD_Theses/49.pdf (Status: 08.08.2017).

Becker, K.J., & Anderson, J.A. (2013). ISIS Support for the MRO/CRISM Instrument, *Lunar Planet. Sci. XLIV*, Houston, Texas, Abstract #2366.

Casu, F., Manconi, A., Pepe, A., & Lanari, R. (2011). Deformation Time-Series Generation in Areas Characterized by Large Displacement Dynamics: The SAR Amplitude Pixel-Offset SBAS Technique. *IEEE Transactions on Geoscience and Remote Sensing*, 49(7), 2752–2763.

D'Errico, J. (2006). gridfit. External Matlab function, Release 2.0.

Ehlmann, B. L., Mustard, J. F., Murchie, S. L., Bibring, J.-P., Meunier, A., Fraeman, A. A., & Langevin, Y. (2011). Subsurface water and clay mineral formation during the early history of Mars. Nature, 479(7371), 53–60.

Bridges, N. N., Ayoub, F., Avouac, J. P., Leprince, S.,Lucas, A., Mattson, S. (2012). Earth-like sand fluxes on Mars. *Nature*, DOI: 10.1038/nature11022.

Carr, M. H., & Head, J. W. III. (2010). Geologic history of Mars. *Earth and Planetary Science Letters, 294*, 185-203.

Christensen, P. R., Engle, E., Anwar, S., Dickenshied, S., Noss, D., Gorelick, N., & Weiss-Malik, M. (2009). JMARS - A Planetary GIS. *American Geophysical Union, Fall Meeting 2009*, Abstract #IN22A-06.

Delacourt, C., Allemand, P., Berthier, E., Raucoules, D., Casson, B., Grandjean, P., Pambrun, C., & Varel, E. (2007). Remote-sensing techniques for analysing landslide kinematics: a review. *Bulletin de Société Géologique*, *178* (2), 89–100.

Guizar-Sicairos, M., Thurman, S. T., & Fienup, J. R. (2008). Efficient subpixel image registration algorithms. *Optics Letters*, *33* (2), 156–158.

Heid, T., & Kääb, A. (2012). Evaluation of existing image matching methods for deriving glacier surface displacements globally from optical satellite imagery. *Remote Sensing of Environment*, *118*, 339–355.

HiRISE. (n.d.). High Resolution Imaging Science Experiment Webpage. *University of Arizona, Lunar & Planetary Laboratory.* https://hirise.lpl.arizona.edu/index.php (Status: 08.08.2017).

HiRISE IC5. (n.d.). High Resolution Imaging Science Experiment Webpage, Spring in Inca City. *University of Arizona, Lunar & Planetary Laboratory.* https://www.uahirise.org/ESP_038299_0985 (Status: 08.08.2017).

HRSC DLR. (n.d.) Mars Express Webpage, HRSC Camera. *DLR, Institut für Planetenforschung.* http://www.dlr.de/mars-express/desktopdefault.aspx/tabid-290/944_read-1409/ (Status: 08.08.2017).

HRSC OLE. (n.d.). HRSC Orbit Location Extractor. *Freie Universität Berlin.* http://maps.planet.fu-berlin.de/ (Status: 08.08.2017).

Hubbard, B., Souness, C., & Brough, S. (2014). Glacier-like forms on Mars. *The Cryosphere*, 8(6), 2047–2061.

Image Explorer. (n.d.). Image Explorer Webpage. *Arizona State University.* https://viewer.mars.asu.edu/viewer/themis#T=0 (Status: 08.08.2017).

JHUAPL. (n.d.). Applied Physics Laboratory Webpage. *John Hopkins University.* http://crism.jhuapl.edu/instrument/design/overview.php (Status: 08.08.2017).

JPL. (n.d.). Marx Express Summary Webpage, NASA JPL. https://marsprogram.jpl.nasa.gov/express/ (Status: 08.08.2017).

Kalenchuk, K.S., Diederichs, M.S., & McKinnon, S. (2006). Characterizing block geometry in jointed rockmasses. *International Journalof Rock Mechanics and Mining Sciences* 43 (8), 1212–1225.

Regional deterministic characterization of fracture networks and its application to GIS-based rock fall risk assessment (PDF Download Available). Available from: https://www.researchgate.net/publication/229378829_Regional_deterministic_characterization_of_fracture_networks_and _its_application_to_GIS-based_rock_fall_risk_assessment [accessed Sep 12, 2017].

Leprince, S., Barbot, S., Ayoub, F., & Avouac, J.-P. (2007). Automatic and Precise Orthorectification, Coregistration, and Subpixel Correlation of Satellite Images, Application to Ground Deformation Measurements. *IEEE Transactions on Geoscience and Remote Sensing*, *45* (6), 1529–1558.

Levrard, B., Forget, F., Montmessin, F., & Laskar, J. (2007). Recent formation and evolution of northern Martian polar layered deposits as inferred from a Global Climate Model. *Journal of Geophysical Research: Planets*, 112(E6), E06012.

Lewis, J. P. (1995). Fast normalized cross-correlation. In *Vision interface*, *Vol. 10*, pp. 120–123.

Luckman, B. H. (1976). Rockfalls and rockfall inventory data: Some observations from surprise valley, Jasper National Park, Canada. *Earth Surface Processes*, 1(3), 287–298.

Manconi, A., Wolter, A., Amann, F. (2016). Measuring surface displacement from airborne imagery with Digital Image Correlation: insights from the Cuolm da Vi DSGSD. *Conference Presentation Poster. 14th Swiss Geoscience Meeting Geneva 2016.*

Mars Fact Sheet. (n.d.). Mars/ Earth Comparison. *NASA.* https://nssdc.gsfc.nasa.gov/planetary/factsheet/marsfact.html (Status: 08.08.2017).

McEwen, A., Dundas, C. M., Mattson, S. S., Toigo, A. D., Ojha, L., Wray, J. J., Chojnacki, M., Byrne, S., Murchie, S. L., & Thomas, N. (2014). Recurring slope lineae in equatorial regions of Mars. *Nature Geoscience,* 7, 53-58.

McEwen, A., & Eliason, E. (2007). Information for Scientific Users of HiRISE Color Products. *HiRISE Webpage manual.* https://www.uahirise.org/pdf/color-products.pdf (Status: 08.08.2017).

Michael A., M. A., Orteu, J.-J., & Schreier, H. W. (2009). Digital Image Correlation (DIC). In H. Schreier, J.-J Orteu, & M. A. Sutton, Image Correlation for Shape, Motion and Deformation Measurements (pp. 1–37). Boston, MA: *Springer US.*

Mitchell, D. M., Montabone, L., Thomson, S., & Read, P. L. (2015). Polar vortices on Earth and Mars: A comparative study of the climatology and variability from reanalyses. *Q J R Meteorol Soc.* 2015 Jan; 141(687): 550–562.

Mitchell, K. L., & Wilson, L. (2003). Mars: a geologically active planet. *Astronomy & Geophysics*, 44(4), 4–16.

Moreira, A., Prats-Iraola, P., Younis, M., Krieger, G., Hajnsek, I., & Papathanassiou, K. P. (2013). A tutorial on synthetic aperture radar. *IEEE Geoscience and Remote Sensing Magazine*, 1(1), 6–43.

MRO. (n.d.) JPL MRO Mission Webpage. *NASA.* https://mars.nasa.gov/mro/mission/instruments/ (Status: 08.08.2017).

NASA. (2015). Frost Avalanche on Mars. *NASA News Webpage.* https://www.nasa.gov/image-feature/frost-avalanche-on-mars (Status: 08.08.2017).

Olshausen, B. A. (2000). Aliasing. PSC 129 Sensory Processes. *University of Berkeley California Education Paper.* http://redwood.berkeley.edu/bruno/npb261/aliasing.pdf (Status: 08.08.2017).

Prost, G. L. (2013). Remote Sensing for Geoscientists: Image Analysis and Integration, Third Edition. *CRC Press.*

Scambos, T. A., Dutkiewicz, M. J., Wilson, J. C., & Bindschadler, R. A. (1992). Application of image cross-correlation to the measurement of glacier velocity using satellite image data. *Remote Sensing of Environment*, 42(3), 177–186.

Shean, D. E., Alexandrov, O., Moratto, Z., Smith, B. E., Joughin, I. R., Porter, C. C., Morin, P. J. 2016. An automated, open-source pipeline for mass production of digital elevation models (DEMs) from very high-resolution commercial stereo satellite imagery. *ISPRS Journal of Photogrammetry and Remote Sensing.* 116.

Smith, D. E., Zuber, M. T., Frey, H. V., Garvin, J. B., Head, J. W., Muhleman, D. O., Pettengill, G. H., Phillips, R. J., Solomon, S. C., Zwally, H. J., Banerdt, W. B., Duxbury, T. C., Golombek, M. P., Lemoine, F. G., Neumann, G. A., Rowlands, D. D., Aharonson, O., Ford, P. G., Ivanov, A. B., Johnson, C. L., McGovern, P. J., Abshire, J. B., Afzal, R. S., & Sun, X. (2001). Mars Orbiter Laser Altimeter: Experiment summary after the first year of global mapping of Mars. *Journal of Geophysical Research 106*, 23689-23722.

SVI Scientific Volume Imaging. (n.d.). Oversampling. https://svi.nl/OverSampling (Status: 08.08.2017).

Swiss Geoportal. (n.d.).Maps of Switzerland, SwissTopo, from https://map.geo.admin.ch (Status: 28.08.2017).

Tanaka, K. L., Skinner, J. A., Jr., Dohm, J. M., Irwin, R. P., III, Kolb, E. J., Fortezzo, C. M., Platz, T., Michael, G. G., & Hare, T. M. (2014). Geologic Map of Mars: U.S. Geological Survey Scientific Investigations Map 3292, scale 1:20,000,000, pamphlet 43 p.

Travelletti, J., Delacourt, C., Allemand, P., Malet, J.-P., Schmittbuhl, J., Toussaint, R., & Bastard, M. (2012). Correlation of multi-temporal ground-based optical images for landslide monitoring: Application, potential and limitations. *ISPRS Journal of Photogrammetry and Remote Sensing*, *70*, 39–55.

Walter, T. R., Legrand, D., Granados, H. D., Reyes, G., & Arámbula, R. (2013). Volcanic eruption monitoring by thermal image correlation: Pixel offsets show episodic dome growth of the Colima volcano. *Journal of Geophysical Research: Solid Earth*, 118(4), 1408–1419.

Wang, Z., Kieu, H., Nguyen, H., & Le, M. (2015). Digital image correlation in experimental mechanics and image registration in computer vision: Similarities, differences and complements. *Optics and Lasers in Engineering*, *65*, 18–27.

Whelley, P. L., & Greeley, R. (2008). The distribution of dust devil activity on Mars. *Journal of Geophysical Research, 13*.

Yun, S.-H., Zebker, H., Segall, P., Hooper, A., & Poland, M. (2007). Interferogram formation in the presence of complex and large deformation. *Geophysical Research Letters*, 34(12).

# 8. SUPPLEMENTARY INFORMATION
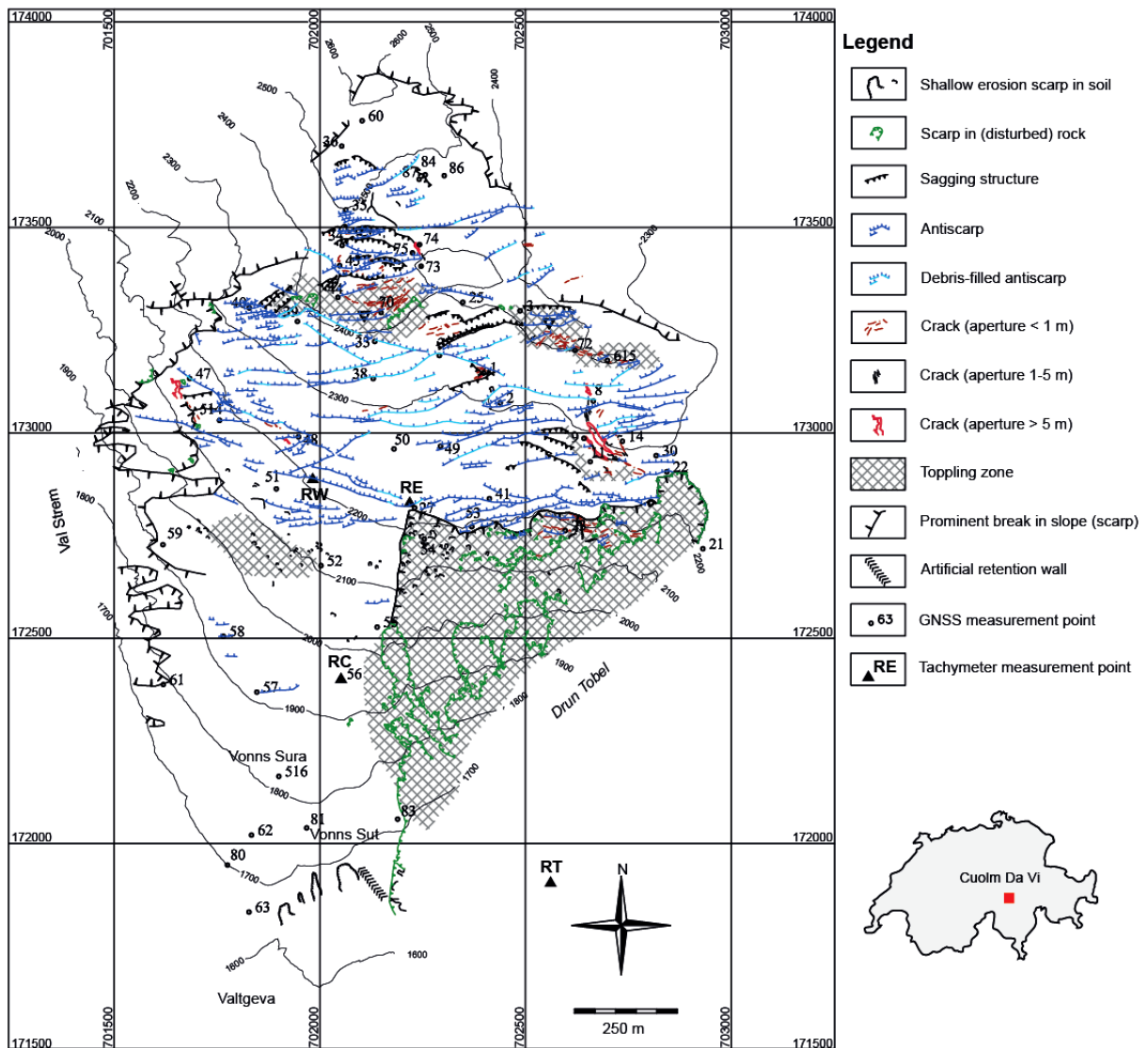


*S 1: Morphological map of CdV, indicating mapped surface structures as well as measurement points. The location of CdV in Switzerland is marked on the bottom right (from Manconi et al., 2016).*
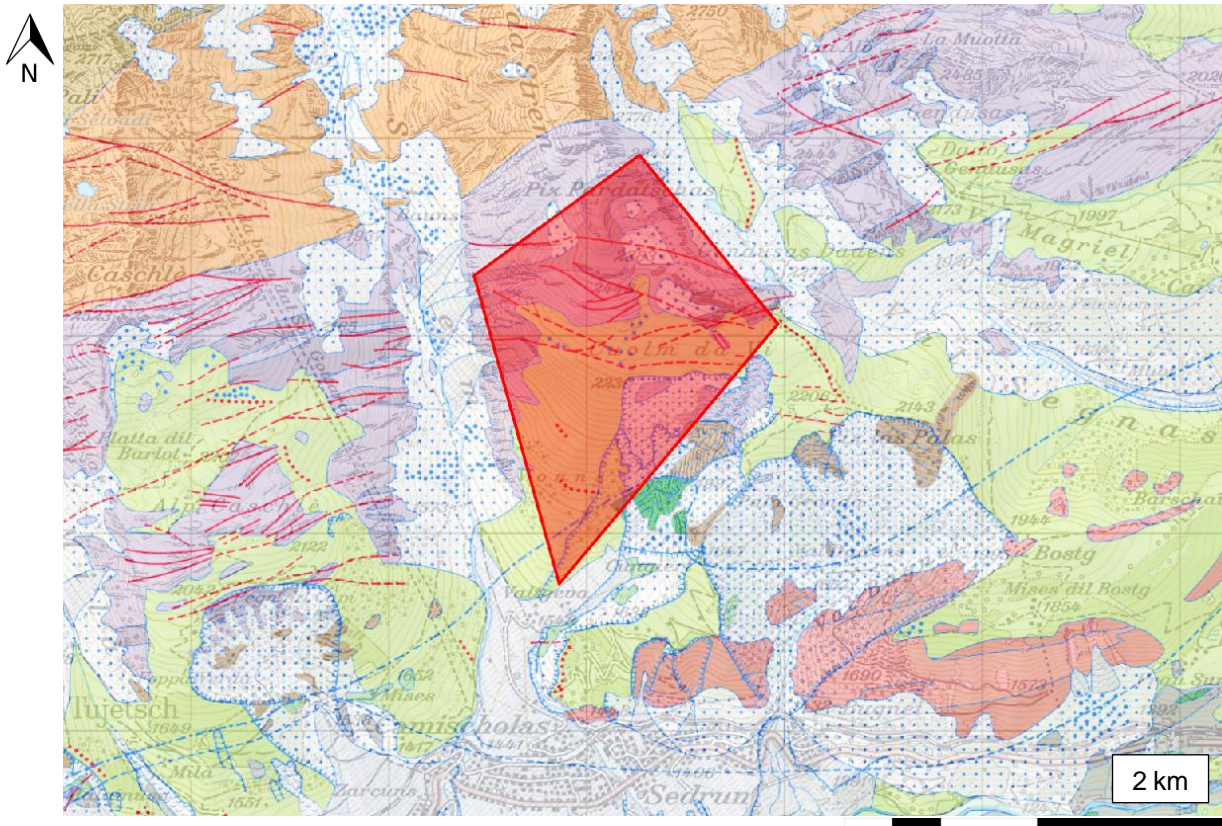
*S 2: Geological map from the CdV AoI with the same dimensions as the topo map in chapter 3.1, image coverage is marked in red. Major faults are marked with red lines, violet indicates Aar-Massive lithology, while greenish colors suggest quaternary moraine coverage and blue-white dots represent debris (Swiss Geoportal, n.d.).*



*S 3: Measurement of GNSS data in CdV, left image shows tripod with GNSS antenna and the execution of the antenna elevation measurement, right image shows the rock bolt (white arrow) which is used as marker for the respective GNSS point and above which the antenna is placed.*

*S 4: Photographs of CdV scarps from 1952 (top) and 2003 (bottom), the progression of the displacement is clearly visible (Amann, 2006).*
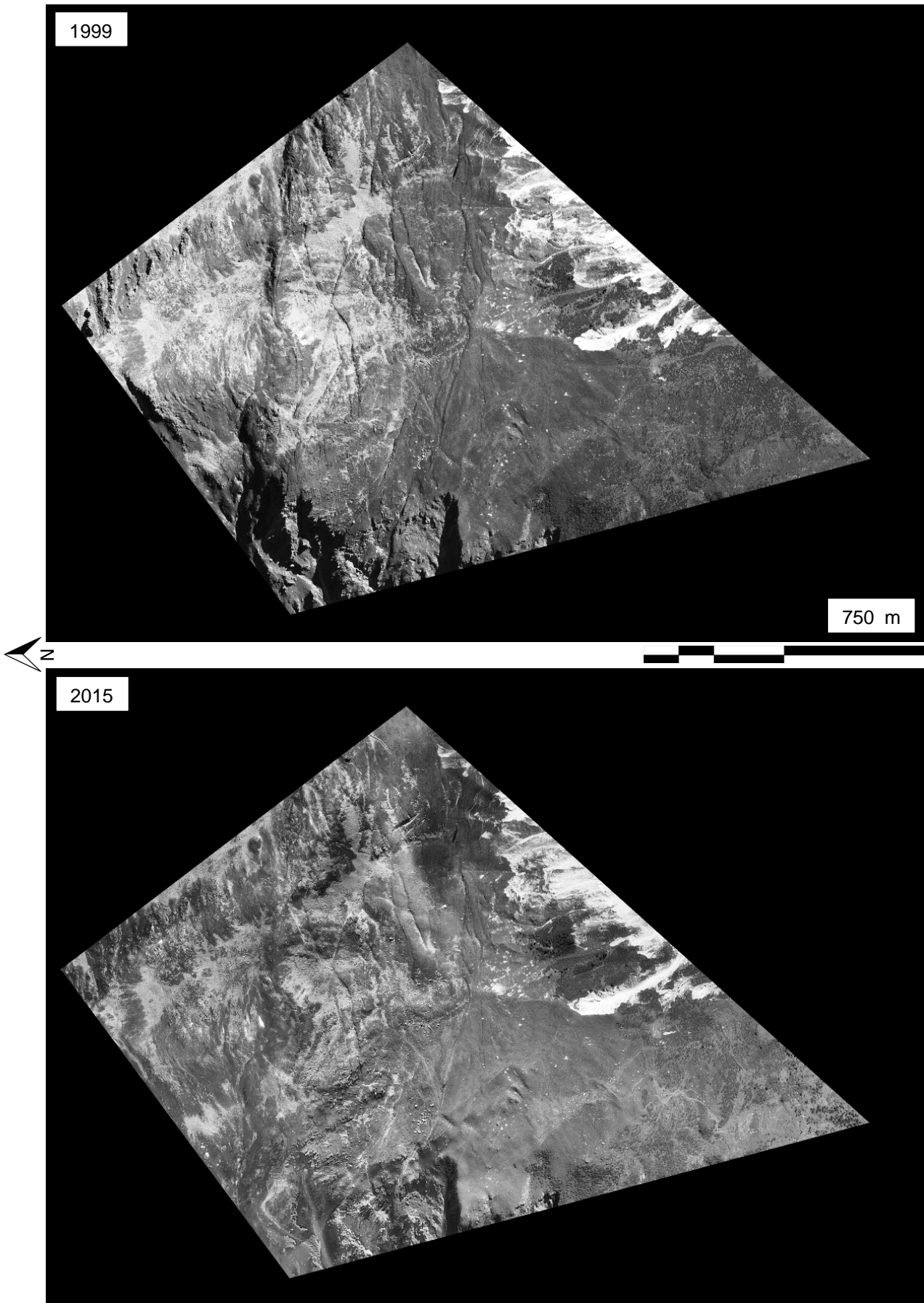
*S 5: CdV orthoimages from 1999 (top) and 2015 (bottom). Turned by 90° to optimize page space.*
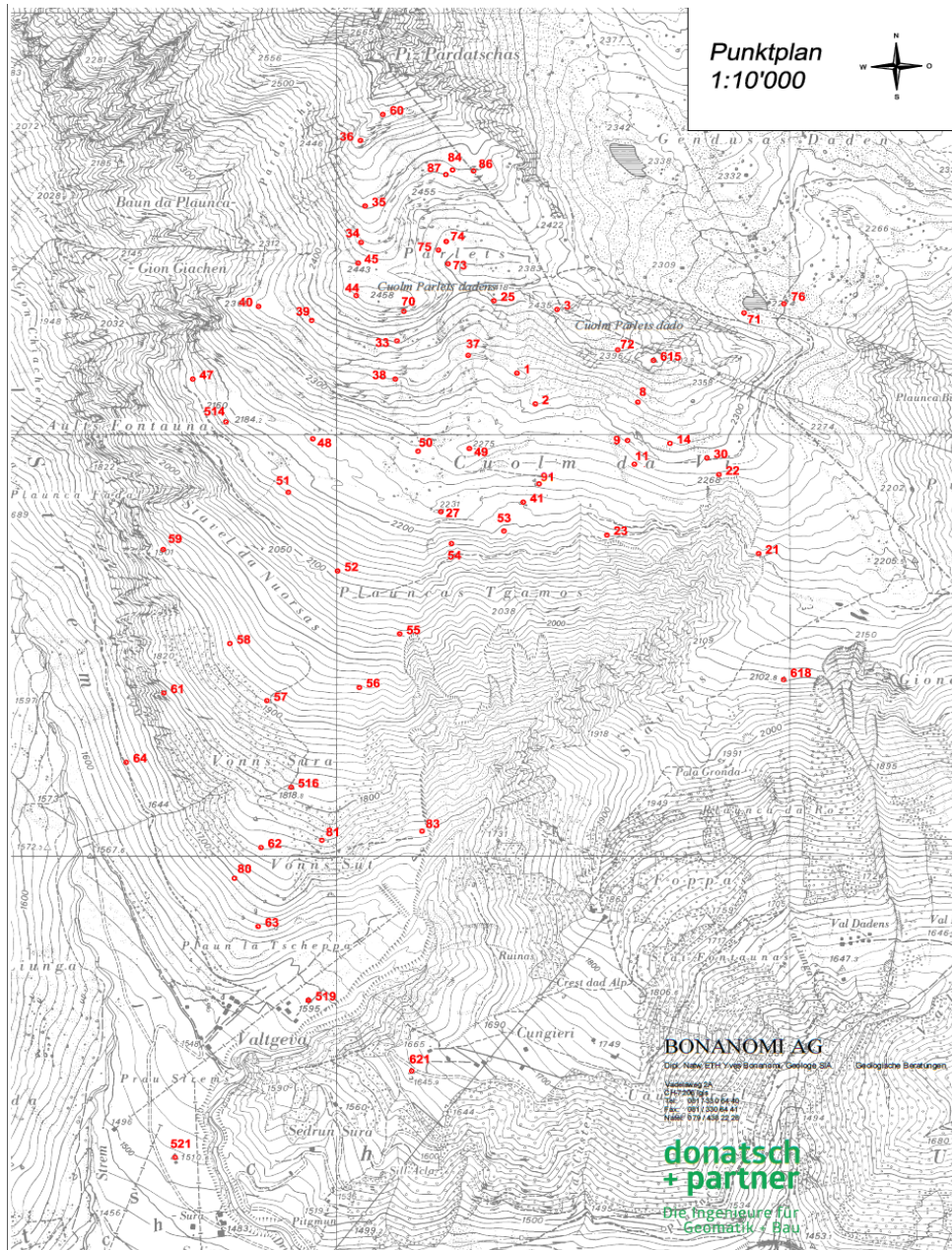
*S 6: CdV map with all GNSS measurement point locations („Punktplan").*

*S T 1: RMSE magnitude values for the selection in [m], whether 1, 4, or 12 points should be used for the quantitative comparison. 1 point is prone to noise, while 4 and 12 perform similarly; finally, 12 points were selected because of the better SNR and stability.*

|          | Points | Threshold | Vector | Median | Mean |
|----------|--------|-----------|--------|--------|------|
| **ORIGINAL** | **1**  | 1.01 | 1.01 | 1.02 | 1.08 |
|          | **4**  | 1.01 | 1.01 | 1.02 | 1.08 |
|          | **12** | 1.09 | 1.09 | 1.02 | 1.08 |
|          |        |      |      |      |      |
| **WALLIS** | **1**  | 1.75 | 1.01 | 1.04 | 0.99 |
|          | **4**  | 1.09 | 1.01 | 1.02 | 1    |
|          | **12** | 1.12 | 0.97 | 1.01 | 1    |

*S T 2: CdV NS DIC-output visualization for NCC on original and Wallis images with different window sizes as well as mean and threshold filter. Colorbar and coding are equal to the one used for DIC NS and EW output plotting before. Differences in color intensity are caused by different densities of the used search windows, 32 appears brighter than 128. North is up, not to scale.*
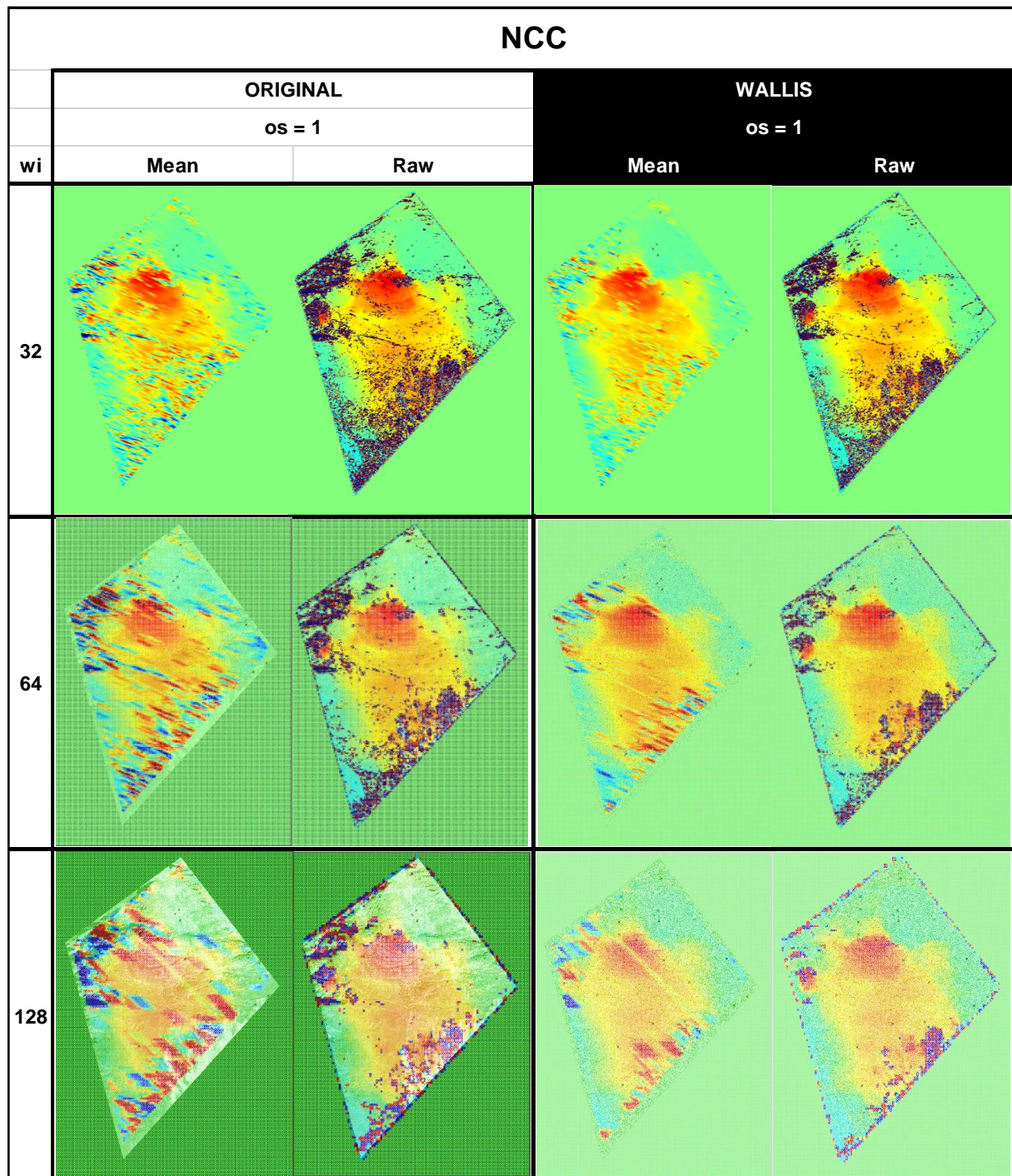
S T 3: CdV NS DIC-output visualization for COSI Corr on original and Wallis images with different window sizes as well as mean and threshold filter. Colorbar and coding are equal to the one used for DIC NS and EW output plotting before. Differences in color intensity are caused by different densities of the used search windows, 32 appears brighter than 128. North is up, not to scale.

*S T 4: CdV NS DIC-output visualization for FFT on original and Wallis images with different window sizes as well as mean and threshold filter. Colorbar and coding are equal to the one used for DIC NS and EW output plotting before. Differences in color intensity are caused by different densities of the used search windows, 32 appears brighter than 128. North is up, not to scale.*



| FFT | | | | |
|---|---|---|---|---|
| | ORIGINAL | | WALLIS | |
| | os = 1 | | os = 1 | |
| **wi** | **Mean** | **Threshold** | **Mean** | **Threshold** |
| **32** | | | | |
| **64** | | | | |
| **128** | | | | |

*S 7: Bar chart comparison of measured displacement (towards East with positive values, towards West with negative values) at all 23 points in [m] with GNSS in black and an exemplary DIC run with FFT wi 64 pixels and vector filtering in white. The dashed lines represent the apparent minimum sensitivity of FFT with this particular window size.*

*S T 5: RMSE magnitude values for the selection in [m], whether co-registration split and oversampling perform better or worse, for NCC, as well as different window sizes. Due to time constraints not all indicated runs could be performed and are intentionally left blank.*

| | | | NCC | | | | | | | |
|---|---|---|---|---|---|---|---|---|---|---|
| | **wi** | | **sp** | | | | | | | |
| | | | **1** | | **4** | | **16** | | **32** | |
| **co_os** | | | 1 | 4 | 1 | 4 | 1 | 4 | 1 | 4 |
| **ORIGINAL** | **64** | | 1.93 | | 1.77 | | | | 1.77 | |
| | **128** | | 6.77 | 5.46 | 5.46 | 5.46 | 4.93 | | | |
| | | | | | | | | | | |
| **WALLIS** | **64** | | 1.07 | | 1.32 | | 1.32 | | | |
| | **128** | | | | | | | | | |

*S T 6: RMSE magnitude values for the selection in [m], whether co-registration split and oversampling perform better or worse, for FFT, as well as different window sizes. Due to time constraints not all indicated runs could be performed and are intentionally left blank.*

| | | FFT | | | | | | | |
|---|---|---|---|---|---|---|---|---|---|
| | **wi** | **sp** | | | | | | | |
| | | **1** | | **4** | | **16** | | **32** | |
| **co_os** | | 1 | 4 | 1 | 4 | 1 | 4 | 1 | 4 |
| **ORIGINAL** | **64** | 1 | 1.09 | 1.09 | 1.09 | | | | |
| | **128** | 1.03 | | | 1.12 | | | | |
| | | | | | | | | | |
| **WALLIS** | **64** | 1.09 | 1.09 | 1.18 | 1.18 | | | | |
| | **128** | 1.34 | | | 1.37 | | | | |



*S 8: Spider and fan features, which occur during Martian spring and summer in the Southern latitudes, when subsurface ice melts, while building up a gas pressure, until the surface ruptures, throwing out debris (HiRISE IC5, n.d.).*
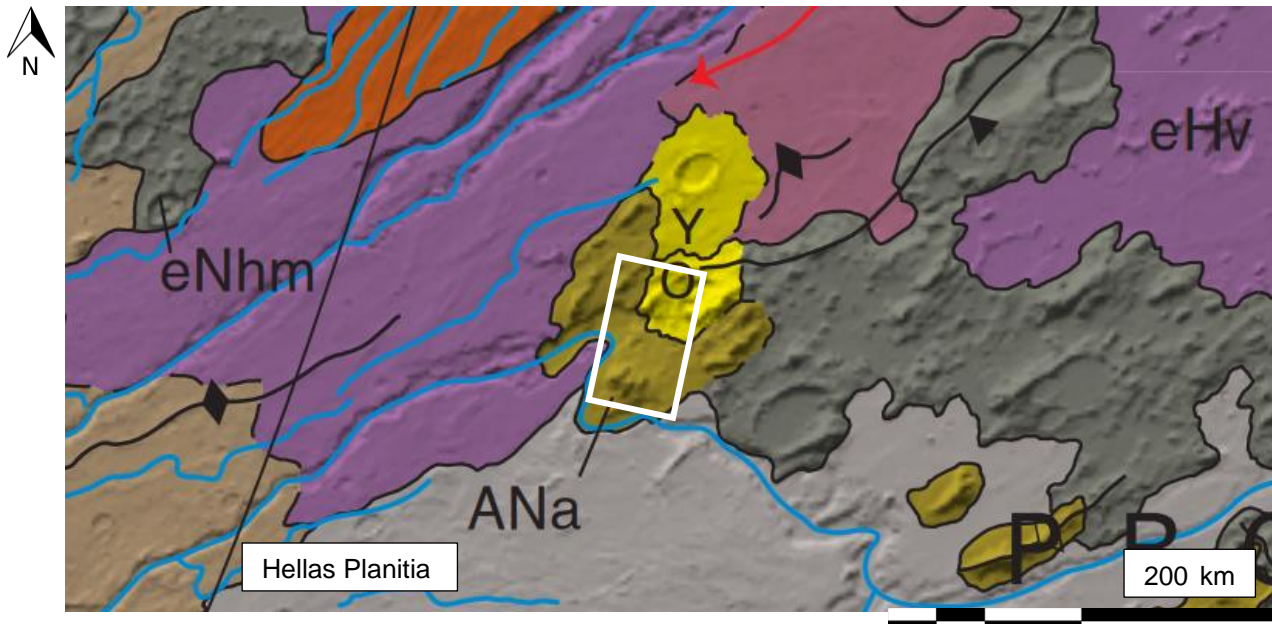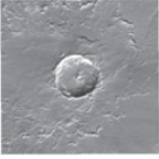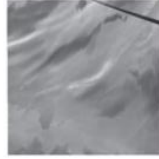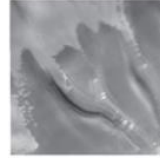
*S 9: Geological map for Eastern Hellas Planitia, where the GLF AoI is situated, marked by a white rectangle. Relevant geological units are the ANa, the Amazonian and Noachian apron unit, and the Ahi, the Amazonian and Hesperian impact unit (yellow), "Y" means younger part and "O" means older part of an intra-unit contact. For line symbol meanings and description of the units, refer to figures S 12 to S 14 (Tanaka et al., 2014).*
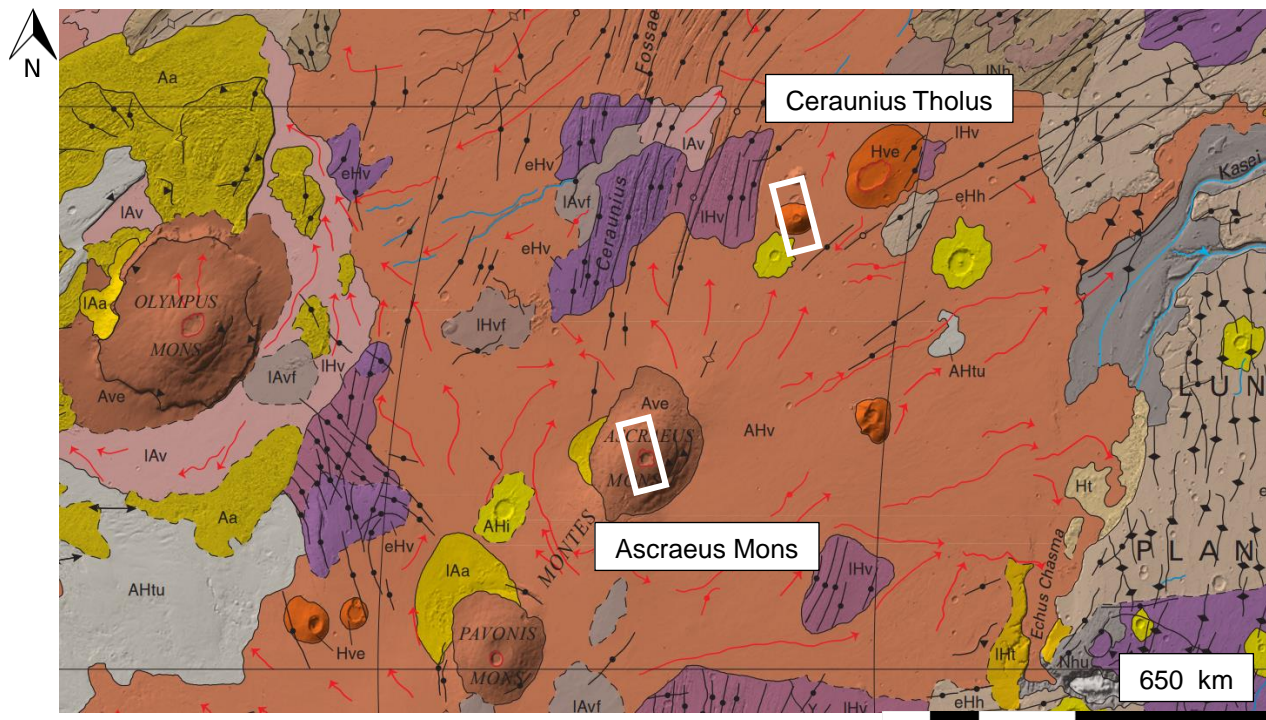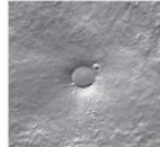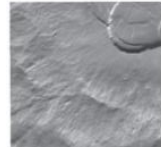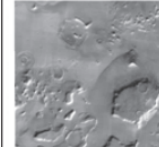


*S 10: Geological map for Tharsis Province, where the volcano and caldera AoIs are situated, marked by white rectangles. Relevant geological unit are the Ave, the Amazonian volcanic edifice unit, and the Hve, the Hesperian volcanic edifice unit. For line symbol meanings and description of the units, refer to figures S 12 to S 14 (Tanaka et al., 2014).*
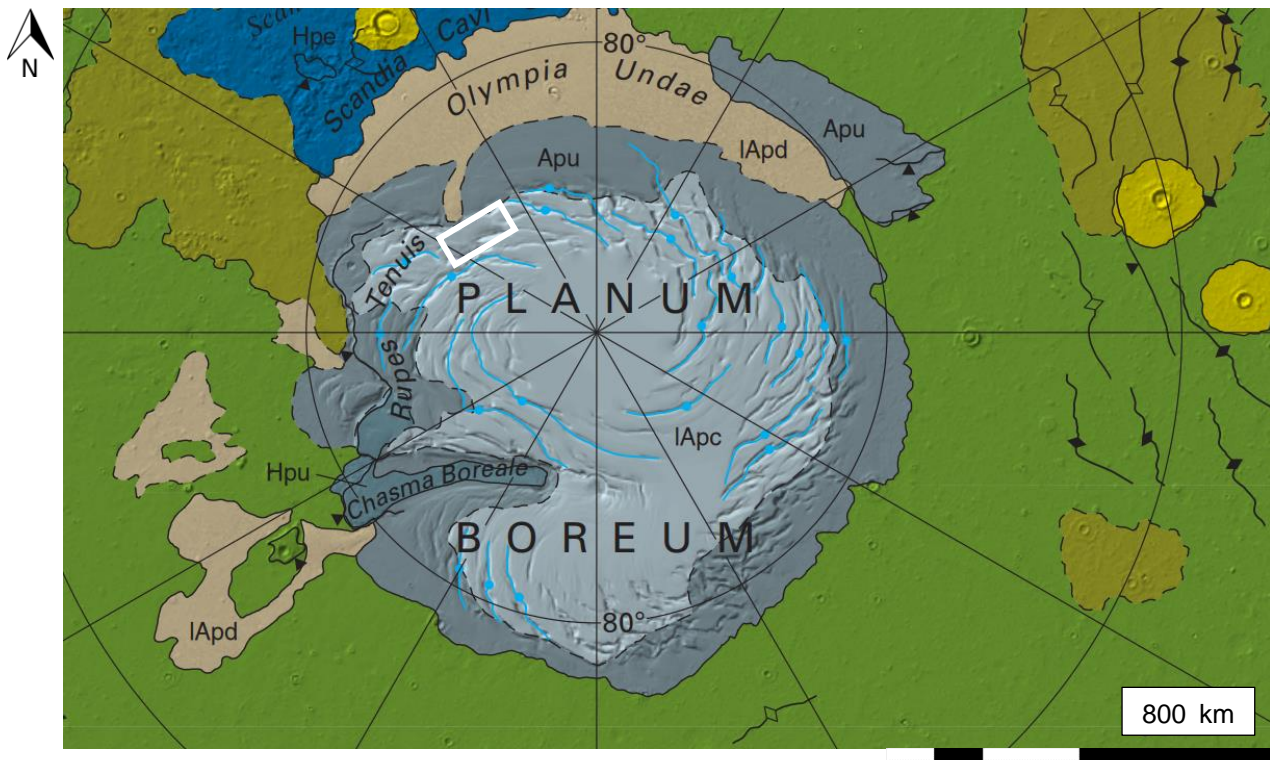
*S 11: Geological map for Planum Boreum, where the cliff AoI is situated, marked by a white rectangle. Relevant geological unit is the Apu, the Amazonian polar undivided unit. For line symbol meanings and description of the units, refer to figures S 12 to S 14 (Tanaka et al., 2014).*

## IMPACT UNIT

**AHi**

**Amazonian and Hesperian impact unit**—Craters with rims and surrounding blankets; some include single to multi-lobed blanket forms, dense secondary crater chains, and (or) central peak or pit. Blanket thicknesses of meters to a few hundred meters. (lat 23.17° N., long 207.77° E.)

Global occurrence. Superposes Noachian units; other unit superposition relations diverse. High kilometer-scale surface roughness; crater floors may be smooth to rough

Upturned, ejected, and brecciated target rocks and sediments, with local areas of impact melt. Post-impact mass-wasting and fluvial-lacustrine and eolian infill of craters common

## POLAR UNITS

[Mostly ice, dust, and other fines at polar latitudes; north polar outcrops occur within the northern lowlands and south polar outcrops are within the southern highlands. Some of the units have a relatively low dielectric constant consistent with water ice and water ice and dust mixtures]

**Apu**

**Amazonian polar undivided unit**—Plateaus hundreds of kilometers across at both poles. Moderate to high albedo. Meters-thick layers; some internal unconformities; local lower, mostly low-albedo deposits unevenly bedded or crossbedded. Exceeds 1,000 m thickness in places. (lat 80.97° N., long 0.00° E. and lat −83.15° N., long 64.91° E.)

Forms Planum Australe and upper part of Planum Boreum. Superposes units lHl, Hp, Hpe, Hpu, lNh, mNh, eNh, and most of Ap; overlain by unit lApc and, except for youngest part, by unit lApd. Tens-of-meters-thick layers in radargrams; modified by systems of spiral and aligned troughs

Water ice with minor amounts of dust intermixed and as lags; local lower sequences made up of frozen dunes with interbedded ice layers

## VOLCANIC UNITS

[Lava flows and pyroclastic deposits forming volcanoes. Flow fields erupted from fissures and centralized vents; may include local pyroclastic deposits. Most occurrences are likely basaltic, based on rheologic properties estimated from morphologic measurements. Lava plains display low kilometer-scale surface roughness]

*S 12: Legend Part I) for the Martian geological map by Tanaka et al. (2014).*

| Symbol | Unit description | Occurrence | Interpretation |
|---|---|---|---|
| Hve | **Hesperian volcanic edifice unit**—Shield-like edifices several tens to hundreds of kilometers across; made up of lobate flows meters to tens of meters thick and tens to hundreds of kilometers across, as well as dissected layers tens of meters thick. As much as few kilometers thick. (lat 24.65° N., long 146.80° E.) | Occurs at Tharsis and Elysium rises, Hadriacus Mons, and Apollinaris Mons south flank. Superposes unit eNhm; gradational with units lHv, lHvf, lHt, lHl, eHv, and HNt (Hesperian part); overlain by unit AHv. Some outcrops have summit calderas tens of kilometers across; some radiating valleys | Volcanic edifices composed of different combinations of lava flows and pyroclastic and volcaniclastic deposits. Modified by summit collapse from magma withdrawal and fluvial dissection in places |
| Ave | **Amazonian volcanic edifice**—Shield-like edifices hundreds of kilometers across; made up of lobate flows meters to tens of meters thick and tens to hundreds of kilometers across. Edifices several to more than ten kilometers high. (lat 18.89° N., long 225.86° E.) | Forms Olympus, Alba, Ascraeus, Pavonis, and Arsia Montes. Younger part superposes units Aa and AHtu; gradational with units lAvf, and AHv; overlain by unit lAa. Deformed by summit calderas tens to >100 km wide and circumferential scarp systems | Volcanic edifices composed of lava flows and possible volcaniclastic rocks. Deformed by summit collapse from magma withdrawal and gravity spreading of flanks |

**APRON UNITS**

| Symbol | Unit description | Occurrence | Interpretation |
|---|---|---|---|
| ANa | **Amazonian and Noachian apron unit**—Irregular knobs and mesas tens of kilometers across and aprons extending tens of kilometers from them. Aprons hundreds of meters thick. (lat –43.22° N., long 26.66° E.) | Occurs in Deuteronilus and Protonilus Mensae and east of Hellas Planitia. Noachian part gradational with units HNt, lNh, mNh, and eNhm and overlain by unit AHi. Amazonian part embays units AHv, lHv, lHvf, lHt, eHv, eHt, HNhu, lNh, mNh, and eNhm; gradational with HNt (Hesperian part). Aprons sparsely cratered, locally grooved and pitted, and in places display low-radar-dielectric constant | Ice-rich Amazonian materials derived from air-fall and mass-wasting erosion and transported by mass flow and underlying, relict Noachian highland materials. Modified by thermokarst processes |

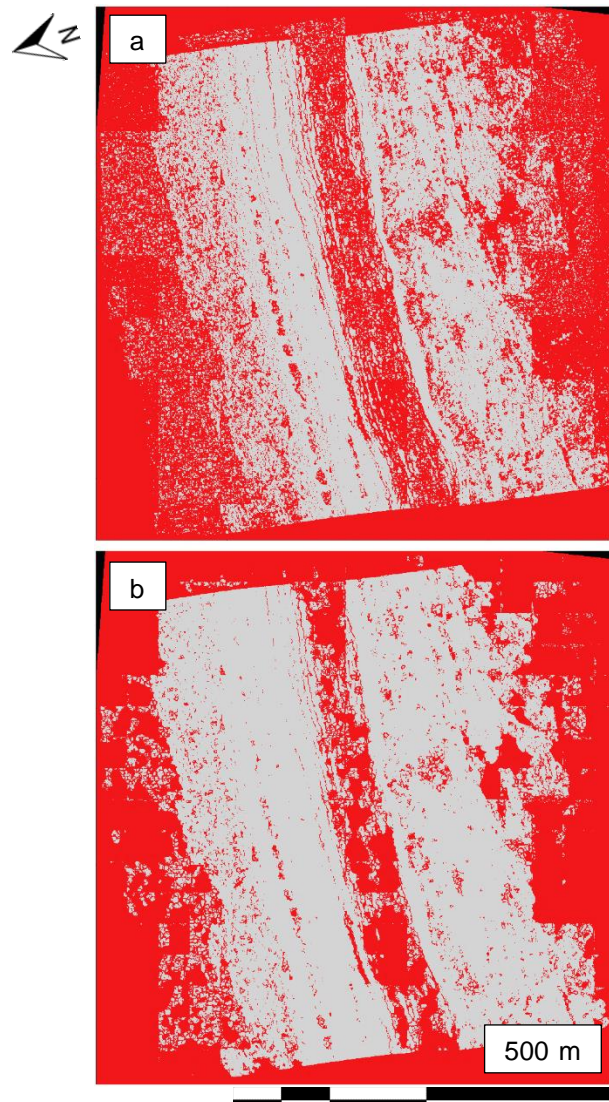*S 13: Legend Part II) for the Martian geological map by Tanaka et al. (2014).*

## EXPLANATION OF MAP SYMBOLS

[For each feature type, typical morphologies and process origins are indicated. See the "Global Structure Digital Attribute Table" in the GIS database for additional information on preservation state (fresh, subdued, partly buried, and buried) and width (broad, >10 km; narrow, <10 km)]

**Contact**—Solid where certain, dashed where approximate, concealed, or gradational; internal contacts mark where superposition relations identify "y" (younger) and "o" (older) divisions

**Wrinkle ridge**—Ridge, sinuous, crenulated; tectonic contraction

**Graben**—Trough, linear or sinuous, en echelon; tectonic extension

**Channel**—Trough, sinuous, floor sloping downhill, dendritic branching or anastomosing; fluvial erosion

**Scarp**—Sinuous, crenulated or scalloped; erosional, also tectonic or volcanic

**Lobate flow**—Lobate flow axis and trend; volcanic flow

**Crater rim**—Circular ridge and (or) scarp, associated inner depression and outer apron; impact

**Ridge**—Simple form; erosional or volcanic

**Spiral trough**—Arcuate, deeper at lower elevations, asymmetrical in cross section, equator-facing steeper slope; ablation due to wind and insolation

**Outflow channel**—Long, wide, sinuous channel floors, often braided with bars and islands along the reach; catastrophic flooding, local collapse, and mass wasting

**Yardangs**—Parallel, narrow, linear to curvilinear ridges, some areas showing multiple orientations; eolian erosion

**Pit-crater chain**—Linear series of circular to semicircular, isolated to overlapping pits, typically associated with a trough, collapse associated with tectonic activity

**Rille**—Sinuous, steep-sided trough, narrows in down-slope direction; volcanic erosion and possible collapse

**Caldera rim**—Ovoid scarp, outlines single or multiple coalesced partial to fully enclosed depression(s); volcanic collapse, related to effusive and possibly explosive eruptions

**Landing sites**—Locations of landed spacecraft. Labels include Viking 1 (Viking 1 Lander), Viking 2 (Viking 2 Lander), Pathfinder (Mars Pathfinder–Sojourner), MER A (Mars Exploration Rover A–Spirit), MER B (Mars Exploration Rover B–Opportunity), PHX (Phoenix Lander), MSL (Mars Science Laboratory–Curiosity)

*S 14: Legend Part III) for the Martian geological map by Tanaka et al. (2014).*

*S 15: GoodPixelMaps of the same area but with two different stereo correlation algorithms: a) using a parabola fitting code, and b) using a simple affine correlator with EM. Computation time for b) is increased by a factor of ~2-3, while results are slightly worse: although the result is less noisy, there are larger patches without any matching data, which will in turn lead to large holes in the DEM. a) produces smaller holes, which can be filled more easily and reliably (raw data from HiRISE, n.d.).*

*S 16: Qualitative comparison of DEM meshing grid, a) with 10 m resolution, b) with 40 m resolution. a) appears much smoother, but requires significant application of hole filling algorithms, which might lead to severe orthorectification errors. b) appears coarse, but returns much fewer holes and could be preferable for orthorectification. For this work, a 10 m grid was selected, to benefit from the better spatial resolution; potential drawbacks were avoided by a frequent and strict quality control procedure (raw data from HiRISE, n.d.).*
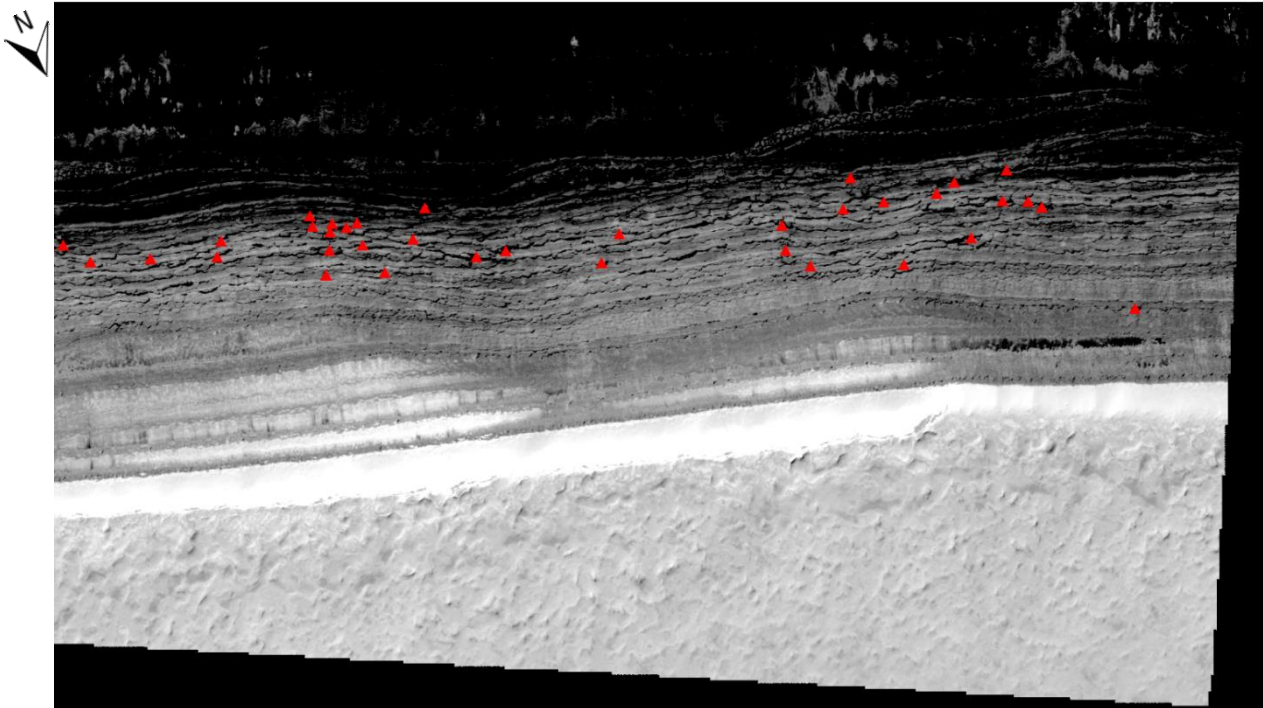
*S 17: Map of failures for tile P. Red triangles mark locations where failures occurred in the period from 2008 to 2016 (raw data from HiRISE, n.d.).*
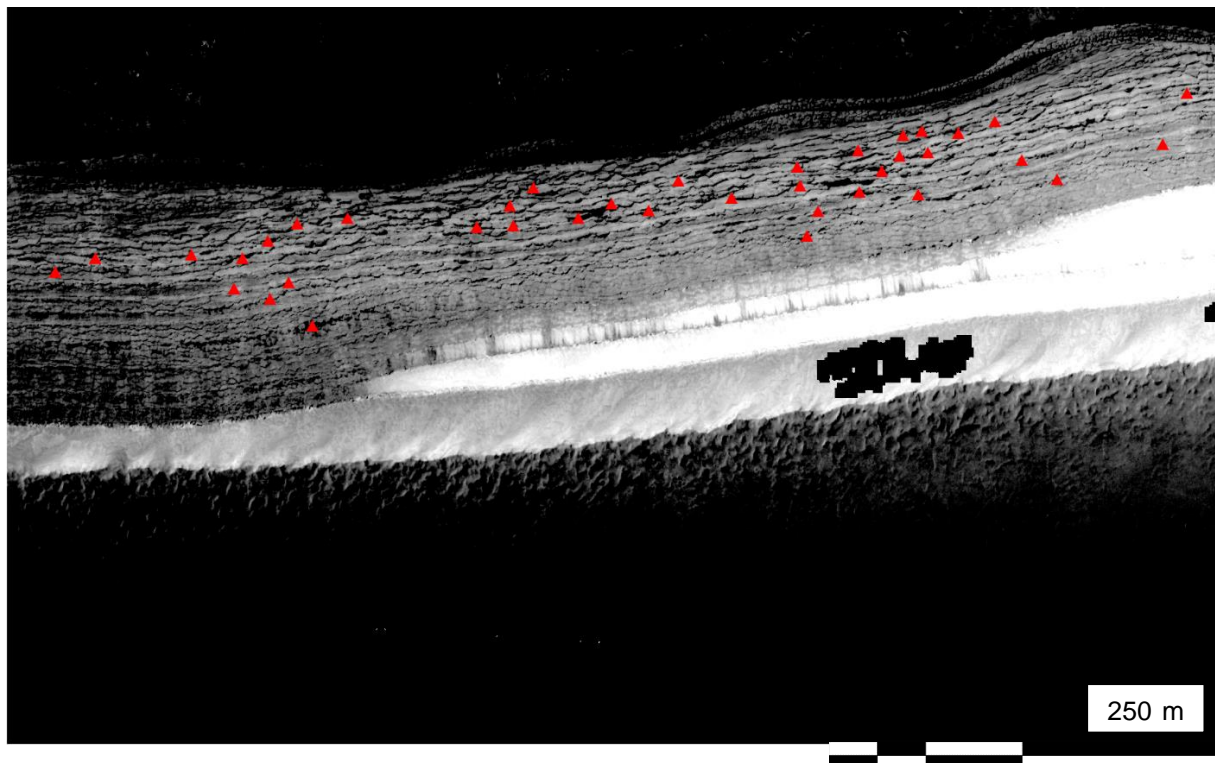


*S 18: Map of failures for tile S. Red triangles mark locations where failures occurred in the period from 2008 to 2016 (raw data from HiRISE, n.d.).*

*S T 7: Complete list of all identified and measured cliff failures in tile P with assumptions for the volume of the events.*

| P | Length [m] | Height [m] | Area [m²] | Estimated depth [m] | Estimated volume [m³] |
|---|---|---|---|---|---|
| **2007/08 to 2009/10** | 18 | 10 | 180 | 1 | 180 |
| | 9 | 9 | 81 | 1 | 81 |
| | 7 | 7 | 49 | 1 | 49 |
| | 6 | 6 | 36 | 0.5 | 18 |
| | | | | Σ | **328** |
| **2009/10 to 2011/12** | 7 | 6 | 42 | 0.5 | 21 |
| | 14 | 4 | 56 | 1 | 56 |
| | 16 | 10 | 160 | 1 | 160 |
| | 5 | 3 | 15 | 0.5 | 7.5 |
| | 9 | 8 | 72 | 1 | 72 |
| | 16 | 9 | 144 | 1 | 144 |
| | 7 | 3 | 21 | 1 | 21 |
| | 7 | 4 | 28 | 1 | 28 |
| | | | | Σ | **509.5** |
| **2011/12 to 2013/14** | 7 | 3 | 21 | 1 | 21 |
| | 38 | 18 | 684 | 1 | 684 |
| | 12 | 3 | 36 | 1 | 36 |
| | 14 | 3 | 42 | 1 | 42 |
| | 5 | 5 | 25 | 0.5 | 12.5 |
| | 75 | 3 | 225 | 1 | 225 |
| | 14 | 4 | 56 | 1 | 56 |
| | 10 | 5 | 50 | 1 | 50 |
| | 5 | 2 | 10 | 1 | 10 |
| | 14 | 3 | 42 | 1 | 42 |
| | 9 | 9 | 81 | 1 | 81 |
| | 14 | 8 | 112 | 1 | 112 |
| | 60 | 10 | 600 | 2 | 1200 |
| | 7 | 7 | 49 | 0.5 | 24.5 |
| | | | | Σ | **2596** |
| **2013/14 to 2015/16** | 7 | 3 | 21 | 0.5 | 10.5 |
| | 12 | 11 | 132 | 1 | 132 |
| | 11 | 9 | 99 | 1 | 99 |
| | 5 | 4 | 20 | 0.5 | 10 |
| | 13 | 10 | 130 | 1 | 130 |
| | 16 | 10 | 160 | 1 | 160 |
| | | | | Σ | **541.5** |
| | | | | **TOTAL** | **3975** |
| | | | | **MEAN / SEASON** | **993.75** |

*S T 8: Complete list of all identified and measured cliff failures in tile S with assumptions for the volume of the events.*

| S | Length [m] | Height [m] | Area [m²] | Estimated depth [m] | Estimated volume [m³] |
|---|---|---|---|---|---|
| **2007/08 to 2009/10** | 7 | 5 | 35 | 1 | 35 |
| | 18 | 9 | 162 | 1 | 162 |
| | 5 | 5 | 25 | 1 | 25 |
| | 5 | 4 | 20 | 1 | 20 |
| | 9 | 7 | 63 | 1 | 63 |
| | 16 | 8 | 128 | 1 | 128 |
| | 5 | 4 | 20 | 1 | 20 |
| | 16 | 4 | 64 | 1 | 64 |
| | 18 | 2 | 36 | 0.5 | 18 |
| | 9 | 8 | 72 | 0.5 | 36 |
| | 9 | 7 | 63 | 0.5 | 31.5 |
| | 8 | 1 | 8 | 0.5 | 4 |
| | 7 | 7 | 49 | 1 | 49 |
| | 6 | 5 | 30 | 1 | 30 |
| | | | | Σ | **685.5** |
| **2009/10 to 2011/12** | 5 | 5 | 25 | 1 | 25 |
| | 4 | 2 | 8 | 1 | 8 |
| | 3 | 2 | 6 | 0.5 | 3 |
| | 8 | 6 | 48 | 1 | 48 |
| | 7 | 3 | 21 | 1 | 21 |
| | 18 | 10 | 180 | 1 | 180 |
| | 5 | 4 | 20 | 1 | 20 |
| | | | | Σ | **305** |
| **2011/12 to 2013/14** | 7 | 7 | 49 | 1 | 49 |
| | 5 | 4 | 20 | 1 | 20 |
| | 6 | 3 | 18 | 1 | 18 |
| | 9 | 9 | 81 | 1 | 81 |
| | 5 | 3 | 15 | 1 | 15 |
| | 22 | 7 | 154 | 1 | 154 |
| | 7 | 6 | 42 | 1 | 42 |
| | 25 | 8 | 200 | 0.5 | 100 |
| | 7 | 3 | 21 | 1 | 21 |
| | 26 | 5 | 130 | 1 | 130 |
| | 20 | 10 | 200 | 1 | 200 |
| | 14 | 10 | 140 | 1 | 140 |
| | 13 | 11 | 143 | 1 | 143 |
| | 5 | 5 | 25 | 1 | 25 |
| | 30 | 15 | 450 | 1 | 450 |
| | 42 | 20 | 840 | 0.25 | 210 |
| | 4 | 3 | 12 | 0.5 | 6 |
| | 4 | 4 | 16 | 0.5 | 8 |
| | | | | Σ | **1812** |
| **2013/14 to 2015/16** | 10 | 10 | 100 | 1 | 100 |
| | 5 | 5 | 25 | 1 | 25 |
| | 9 | 7 | 63 | 1 | 63 |
| | 10 | 3 | 30 | 1 | 30 |
| | 4 | 4 | 16 | 0.5 | 8 |
| | 4 | 3 | 12 | 0.5 | 6 |
| | 9 | 6 | 54 | 1 | 54 |
| | 12 | 5 | 60 | 0.25 | 15 |
| | 9 | 7 | 63 | 1 | 63 |
| | 7 | 3 | 21 | 1 | 21 |
| | 13 | 5 | 65 | 1 | 65 |
| | | | | Σ | **450** |
| | | | | **TOTAL** | **3252.5** |
| | | | | **MEAN / SEASON** | **813.125** |